Imperial College London

THESIS

THE EFFECTS OF SURFACE TEXTURE IN RECIPROCATING BEARINGS

Author:

Sorin-Cristian VLĂDESCU

Supervisors:

Dr. Thomas REDDYHOFF

Prof. Andrew OLVER

A report submitted in fulfilment of the requirements

for the degree of Doctor of Philosophy

in the

Tribology group

Department of Mechanical Engineering

February 2016

DECLARATION OF AUTHORSHIP

I, Sorin-Cristian Vladescu, declare that this thesis titled, 'THE EFFECTS OF SURFACE TEXTURE IN RECIPROCATING BEARINGS' and the work presented in it are my own.

I confirm that:

- This work was done wholly or mainly while in candidature for a research degree at the Imperial College of London.
- Where I have consulted the published work of others, this is always clearly attributed.
- Where I have quoted from the work of others, the source is always given. With the exception of such quotations, this thesis is entirely my own work.
- I have acknowledged all main sources of help.
- Where the thesis is based on work done by myself jointly with others, I have made clear exactly what was done by others and what I have contributed myself.

Signed:
_____

Date:
_____

IMPERIAL COLLEGE LONDON

ABSTRACT

Faculty of Engineering

Department of Mechanical Engineering

Doctor of Philosophy

THE EFFECTS OF SURFACE TEXTURE IN RECIPROCATING BEARINGS

by Sorin-Cristian VLĂDESCU

In recent years, interest in reducing friction in internal combustion engines has grown significantly. This has mainly been due to stricter regulatory standards, with emission targets set as low as 95g of CO_2/km from 2020 onwards. As a result, motor vehicle manufacturers have been focusing investment on energy efficient technologies with the aim of reducing fuel consumption. As part of this drive, the reduction of friction between the piston rings and cylinder liners is gaining considerable attention. A potentially effective way of doing this is to apply laser texturing to piston liner surfaces. However, little is understood about the mechanisms by which pockets affect friction, primarily because of the lack of reliable experimental measurements.

In this study, the influence of surface texture on film thickness and friction force was measured simultaneously in a convergent-divergent bearing under different lubrication regimes, closely replicating an automotive piston ring-bore conjunction. This was achieved using a reciprocating sliding test rig, designed to control all operating parameters with a high degree of accuracy.

Various pocket shapes were assessed in order to understand the beneficial or detrimental effects of surface texture under various operating conditions. This showed unequivocally that pockets are able to reduce friction in the mixed regime and increase friction under full film conditions. After the optimum pocket shape had been determined, various spatial parameters (depth, breadth, separation) were tested, under different lubrication regimes, in order to characterise the influence of geometry. A key finding here is that optimum pocket geometry varies along the length of the stroke. Next, film thickness was measured using a modified version of the ultra-thin film optical interferometry approach. The results here agreed with the friction data by showing how pockets increase film thickness in the mixed and boundary regime and decrease film thickness in the full film regime. Furthermore, through transient measurements, a number of insights into mechanisms by which surface texture reduce or increase friction were obtained.

In addition, cavitation in the ring-liner pairing was investigated, as well as various aspects of pocket behaviour, such as orientation, location relative to reversal and the influence of steady state versus transient sliding. Finally, wear tests were conducted under highly loaded conditions which led to an understanding of the interactions between laser surface texture and wear behaviour.

ACKNOWLEDGEMENTS

A very special thanks to my friends from the Tribology group. They are amazing people who turned this PhD into the best job of my life. Alessandra, Antonio, Yasunori, Aleks, Yannis, Johan, Pawel, Francesco, Yuta, Harriet, Nico x2, Leimei and Oana, thank you all.

Sincere and warm thanks to my family: to my brother Catalin for his artistic suggestions on the looks of this thesis and to my beloved mother Natalia for her unconditional love, communicated over the physical distance that this achievement implied.

Finally, a most deserved mention to my father, Mircea and my girlfriend, Ioana. I thank my father for his invaluable technical advice and unreserved support to pursue this path; I owe you. To Ioana, who by now knows more about Tribology than I do, for making all of this possible and for being an unending source of trust. From showing me the PhD advert to providing precious advice on written style, she was always there. I dedicate this thesis to both of you.

CONTENTS

LIST OF FIGURES

9

LIST OF TABLES

Chapter 1

INTRODUCTION

1.1   Project background

Problems of energy security and climate disruption are becoming increasing serious. In fact, global energy demand is forecast to rise by 37% over the next 25 years [1], while emissions from machines consuming fossil fuels are expected to outweigh the savings from renewables to such an extent that avoiding a catastrophic 2°C rise in average temperature will demand exceptional efforts [1].

To combat these issues, governments are imposing progressively stringent regulations – such as the EU limit of 95g of CO_2/km as the average emission on all new models of passenger car by 2020 [2] – to encourage manufacturers to increase energy efficiency. However, innovative technology is needed to make such achievements possible.

One of the most direct ways to increase energy efficiency is to reduce mechanical friction through improved lubrication, since friction is responsible for a significant proportion of wasted energy in all machines. In the case of automobiles for instance, friction losses constitute 11.5% of the total fuel energy [3], of which the piston–cylinder system accounts for 45% and the crankshaft bearings account for 19% [4]. An approximate breakdown of these losses is shown in figure 1.1.
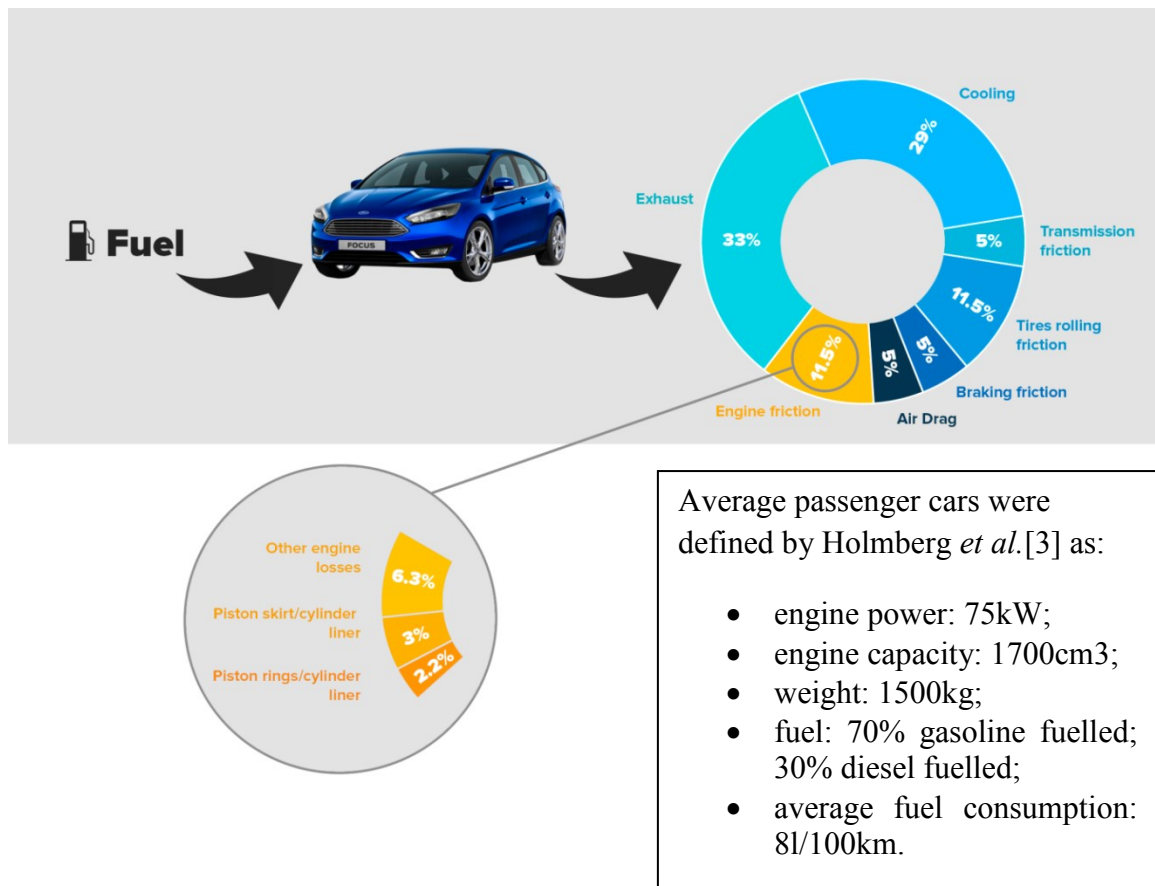
FIGURE 1.1: Fuel energy dissipation in passenger cars, as approximated for a speed of 60 km/h (after [3,4])

A further reason for seeking improvements in lubrication is that a single strategy can benefit a range of different machines. Several approaches have been recently introduced to reduce engine friction losses, including:

i) The adoption of Low Viscosity Oils (LVO) to reduce hydrodynamic engine losses, as this has been shown to lower the engine power required to achieve a specific set of operating conditions [5,6]. The disadvantage of this approach is that, as a result, mixed and boundary lubrication conditions are becoming increasing dominant in IC engines. However, this trend is prevalent, therefore other friction reduction methods are required to compensate for these harsher conditions.

ii) The introduction of start and stop vehicle operation, to limit engine running time to the necessary time periods.

iii)   The application of **surface texture** to engine components as a means of reducing friction losses. Surface texturing is defined as the application of micro pockets of various shapes and sizes, forming different patterns, to the component in question. As reviewed in Chapter 2, numerous efforts have been made to apply surface texture to engineering components in order to control friction and wear.

Applying texture – *i.e.* features such as dimples or pockets – to the surface of engineering components is an obvious way to modify friction and has been investigated since the 1960s [7]. The impact of this approach can be significant, with friction reductions of over 40% demonstrated in laboratory controlled tests [8], and evidence suggests that it translates to measurable improvements in overall engine performance [9]. Compared to other energy saving solutions, surface texture is cheap and simple to implement. It does not require components to be redesigned and can be incorporated easily into existing and future technologies.

Despite the potential rewards, surface texturing has largely eluded practical applications. The reason for its limited uptake is that, despite the simplicity of the concept and the intense attention it has received, the effect of textured surfaces on friction is a highly challenging subject to study. This is because texture interacts with, and hence complicates, frictional processes, which themselves depend on interactions between surface and lubricant chemistry, fluid and contact mechanics that are not always well understood. This is the case particularly under the transient conditions found in piston liner contacts, where surface texture may offer the greatest benefits. The bulk of existing research resulted in considerable confusion, with texture effects reported intermittently as being beneficial [10], detrimental [11,12] or negligible [13]. A further oversight of recent studies is that it is generally concerned with the overall effect on friction that results from the transit of many pockets through the contact, rather than observing each pocket individually to elucidate the mechanisms that are occurring.

In summary, the application of surface texture has the potential to provide a much needed improvement in automobile energy efficiency; however, the highly complex conditions and mechanisms through which texture reduces friction need to be better understood.

1.2   Research goals

After reviewing the most relevant experimental results in the area of microtexturing bearing surfaces reported over the last half century, it becomes evident that the addition of texture can have both beneficial and detrimental effects on friction. In a number of cases, greater load support and/or thicker lubricating film values were reported when testing bearing surfaces with specific micro textured patterns. Despite these achievements, much of the previous experimental work has been limited to studying the effect of texture geometry on friction reduction, *i.e.* the shape and configuration of features. In the process, the importance of, and interactions between texture and other variables and operating conditions have so far been largely overlooked.

This research aims to improve the understanding of how textured surfaces reduce friction and increase load support in a reciprocating line contact simulating the piston ring–cylinder liner pairing. For a better understanding of the underlying mechanisms of friction reduction, measurements of film thickness, friction force and cavitation pattern are performed all in situ and simultaneously.

One of the primary goals of this study is to understand the lubrication conditions under which surface texture can be most advantageous. To achieve this, a new test apparatus was developed to allow the accurate controlling of all operating conditions at all times. The beneficial or detrimental effects of pocketed surfaces are accurately assessed by comparing all the results obtained using the textured specimens against a non-textured reference.

Textured patterns comprising various shapes and orientations are investigated at the same time while simultaneously assessing the effects of surface texture upon friction and film thickness response under all lubrication regimes. The optimal pattern shape and orientation are subsequently employed for a parametric study of surface texture, in which various combinations of pocket breadths, depths and densities are assessed.

Furthermore, the study aims to shed light on the mechanisms by which surface pockets cause a reduction in friction by observing the transient response as pockets pass through a sliding contact. A related issue is the evaluation of the effects that various pocket geometries have on wear behaviour, and the understanding of what precise role 'lubricant replenishment' plays in the variation of film thickness and frictional response.

A secondary focus of this project is determining cavitation behaviour in the contact between piston ring and cylinder liner. The cavitation pattern is qualitatively evaluated when a textured pocket passes through the reciprocating contact, with an emphasis on the particular case encountered at the reversal point. Moreover, various effects of pockets in reciprocating bearings are investigated to highlight the effects on friction force of textured features at reversal point, sliding velocity and squeezed film at the end of the stroke.

Overall, the results of this research are expected to lead to the recommendation of an optimum shape and geometry of the texture pattern (suitable for high volume production), as well as the appropriate placement along the stroke, which can be ultimately used in internal combustion engines to achieve reductions in friction and consequently fuel consumption and CO_2 emissions.

1.3 Thesis outline

The structure of this thesis is outlined below:

Chapter 2 provides a literature review, which highlights the most important work undertaken in this area of research to date, and is a crucial step to ensure existing knowledge is built upon and the significant gaps in past research are adequately bridged. A number of studies concerning the use of surface texture in sliding contacts are explored with a focus on the key conclusions regarding the influence of micro-features on friction, film thickness and wear.

Chapter 3 introduces the reciprocating test rig developed as part of this project, detailing its key features and explaining the rationale behind component selection and design decisions. Each sub-system is presented individually, alongside calibration specifications.

Finally, the experimental procedure is detailed and the repeatability of friction and film thickness measurements demonstrated.

Chapter 4 focuses on the first set of results of the experimental work. The main aim of this chapter is to present experimental results and assess them to determine the optimum shape and orientation of the pockets that constitute the textured surface. In addition, the beneficial or detrimental effects of texture in boundary, mixed and full film regimes are found from tests performed under a range of lubricant viscosities and applied normal loads, in order to vary the lambda value. Finally, the influence of micro-texture on cavitation in the ring–liner pairing is assessed qualitatively.

Chapter 5 describes the parametric study aimed at defining the relationship between the geometric parameters of the surface texture (*i.e.* pocket breadth, pockets depth, texture density) and friction coefficient, keeping constant the pattern shape and orientation previously deemed optimal. For a more intuitive practical correlation with the lubrication regimes encountered in the IC engine, all results are plotted as master Stribeck curves.

Chapter 6 presents the results obtained after simultaneously measuring film thickness and friction force. The effect of textured features was investigated while varying lubrication regimes, a phenomenon which often occurs in IC (internal combustion) engines over a single cycle.

Chapter 7 sheds light on the mechanisms responsible for significant reductions in friction while the bearing operates under mixed and boundary lubrication conditions. Both the transient effects of particular micro-features entering the contact as well as the overall effect of the textured pattern along the stroke are investigated and the results interpreted.

Chapter 8 is dedicated to the final set of results presented throughout this thesis – the study of the effects of micro-feature geometries on lubricant replenishment and wear behaviour immediately after reversal point. The chapter displays and interprets correlations between friction force, oil replenished to the contact and wear volume.

Chapter 9 summarises the conclusions and achievements of the current research and suggests a range of open questions to be investigated going forward.

Chapter 2

SURFACE TEXTURE IN TRIBOLOGICAL CONTACTS – A REVIEW

2.1   Introduction

It is well-known that surface texturing can improve tribological performance in a multitude of circumstances. Whether in the case of fish using surface texturing to reduce drag whilst moving through water or on plants leveraging the "lotus leaf" effect to achieve self-cleaning, textured surfaces have already proven their effectiveness in nature. These natural occurrences have inspired the artificial texturing of surfaces in various engineering applications.

Typically, surface features are created in engineering applications through laser texturing (also known as LST, or laser honing). However, due to the high manufacturing costs and long duration necessary for LST, alternative texturing methods for tribological surfaces are increasingly developed. In a recent study, Costa and Hutchings [14] investigate and classify the existing texturing techniques, exploring a variety of high potential, innovative methods which may be employed in the future.

Due to its vast array of advantages, surface texture is currently being applied to various components in modern IC (internal combustion) engines. Figure 2.1 illustrates this process applied on a cylinder liner by Gehring [15] - the first company to offer LST technology applications commercially. This approach is not limited to cylinder liners − for instance, figure 2.2 shows texture applied to various other components from modern internal combustion engines [16].
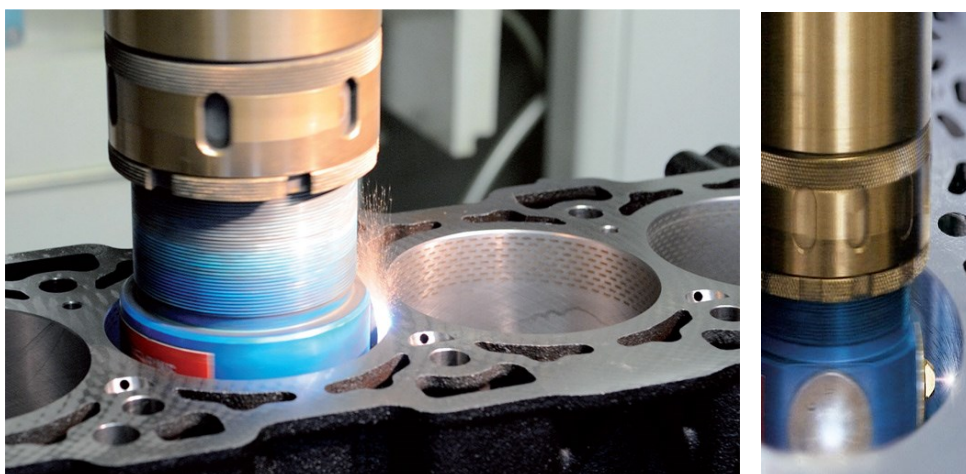
FIGURE 2.1: A laser honing operation performed on a cylinder liner [15].
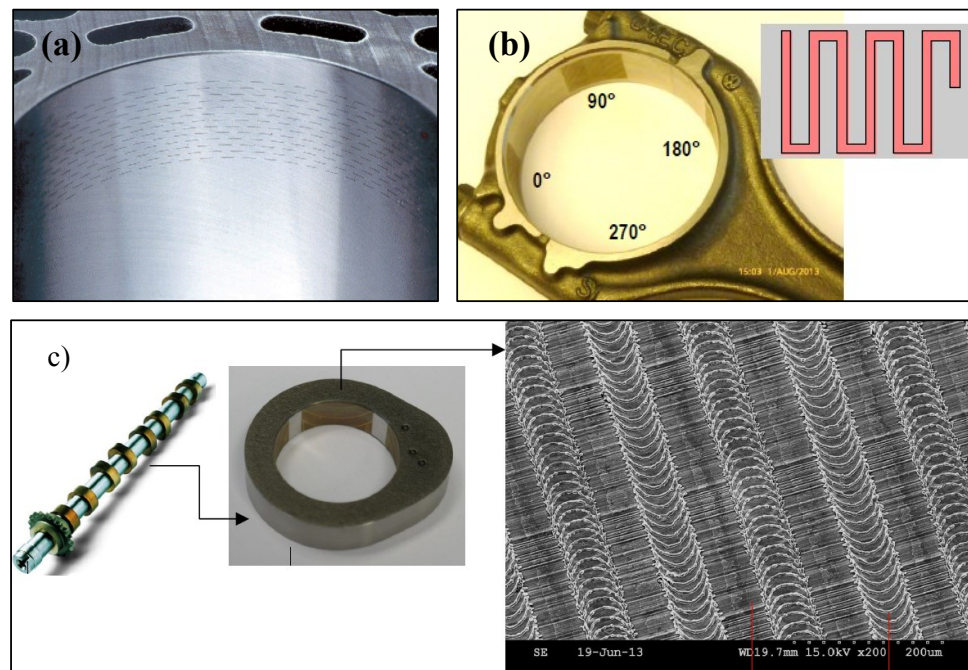
FIGURE 2.2: Laser Surface Texture applied to (a) cylinder liner; (b) connecting rod and rod cap; (c) cam [16].

Various beneficial effects of surface texture on tribological performance have been hypothesised in the academic literature. The main advantages of surface texture demonstrated in research are *i)* sliding fiction force reduction [9,10,17–25] by increasing load support, *ii)* significant wear reduction by acting as "debris traps" under dry and boundary lubricating conditions [20,26–30] and *iii)* prevention of starvation (insufficient oil present at the inlet) by acting as a secondary lubricant reservoir [20,26,31–34]. In addition, a recent study by Greiner et al. [35] suggests the ability of surface texture to reduce static friction by a factor of two, provided an optimum dimple diameter is selected. This is of considerable interest to designers of modern IC engine components intended to endure frequent start and stop periods, such as crankshaft bearings and piston ring-cylinder liner pairings.

The concept of "micro-irregularities" was first introduced in a tribological context by Hamilton and Allen in 1966 [7,36]. They pointed out that the addition of 'asperities and depressions' to one face of a parallel rotary-shaft face seal can improve the load support capabilities of the seal. Nevertheless, the vast majority of research investigating the performances of textured bearings was carried out in the last two decades. The study of micropockets was brought back in focus by Tønder [37,38] who primarily researched the

effects of texture addition to both moving and stationary bearing surfaces. His research showed that the optimal positioning of texture is in the vicinity of the bearing's inlet. Two phenomena were indicated as potential explanations. On the one hand, the texture reduces fluid leakage from the contact by creating resistance. On the other, a "virtual step" is created, similar to the abrupt change in film thickness used in Rayleigh step bearings.

Various subsequent analytical and experimental studies into the effect and performance of textured bearings were carried out in the last decade with increasing frequency [39]. The majority of these studies investigated the effects of patterned surfaces in hydrodynamic, full film conditions [13,40–44], whilst fewer tested the effects of geometric patterns under elastohydrodynamic lubrication [45,46] and boundary and/or mixed lubrication [11,30,47–49].

This chapter reviews research into the effects of surface texture on tribological performance. The main mechanisms by which laser surface texture has been suggested to reduce friction typically arise from the fact that pockets act to bring lubricant into the contact, increasing pressure and hence film thickness. In the mixed and boundary lubrication regime, this can result in lower friction as solid on solid contact is reduced, while under full film conditions (where the surfaces are completely separated), this may lead to lower friction since a thicker films reduce strain rate. It should be noted however that other explanatory mechanisms have also been proposed, which include debris trapping, lubricant replenishment, and static friction reduction.

The chapter is laid out to address individually each of the mechanisms through which surface texture reduces friction. Before discussing the tribological consequences of deliberately adding texture to surfaces, Section 2.2 explores the effects of natural roughness and those of plateau honing. Next, the four main sections of the chapter (2.3-2.5) review research into the effects of texture on sliding friction, wear, lubricant replenishment and finally static friction. Section 2.6 investigates possible methods of measuring lubricant film thickness in textured linear bearings under different lubrication regimes. Finally, Section 2.7 discusses practical aspects of applying surface texture before Section 2.8 summarises the key conclusions of the literature review.

2.2   Effect of plateau honing on sliding friction

Before focusing exclusively on the effects of laser surface texturing, it is worth briefly summarising early research into the effect of modified roughness. In plateau honing, asperity peaks are removed by an abrasive tool, resulting in a flat surface scattered with valleys. Work by Jeng et al [50] showed that this approach is beneficial to piston ring lubrication, as shown in figure 2.3. Two phenomena explain the improved lubrication: firstly, honing increases the lambda ratio of the contact so that it operates to the right on the Stribeck curve and secondly, the valleys act as oil reservoirs and delay the onset of starvation.
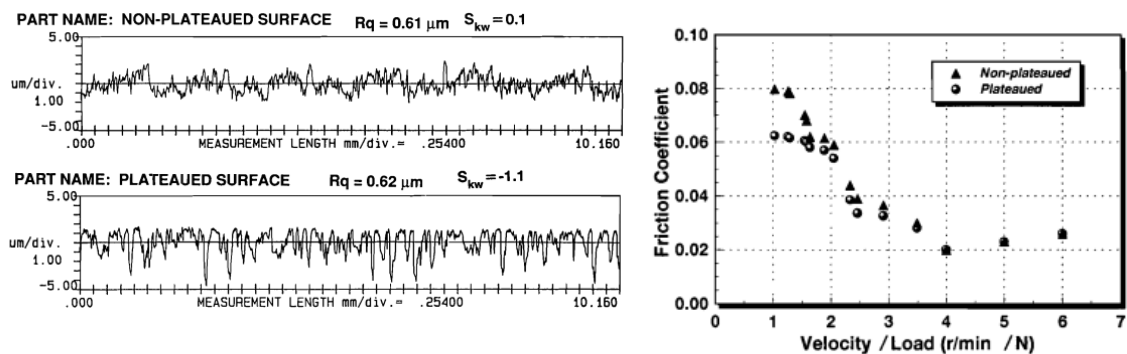
FIGURE 2.3: Effect of plateau honing on a) surface topography, b) friction coefficient [50].

The work of Jeng provided a verification of the effect of plateau honing, taking into account the different lubrication regimes. A natural step forward from the work of Jeng and Willis was to investigate how the surface honing parameters affect cylinder friction. A key parameter of interest is the cross-hatching angle, which is manipulated by altering the speed to feed ratio of the honing tool. Bolander *et al.* [51] concluded through an experimental and analytical investigation using a reciprocating test rig that the cycle average friction coefficient decreased when reducing the cross-hatching angle, as shown in figure 2.4. Specifically, a 25% reduction in average friction coefficient is observed when the angle is reduced from 90º to 20º.
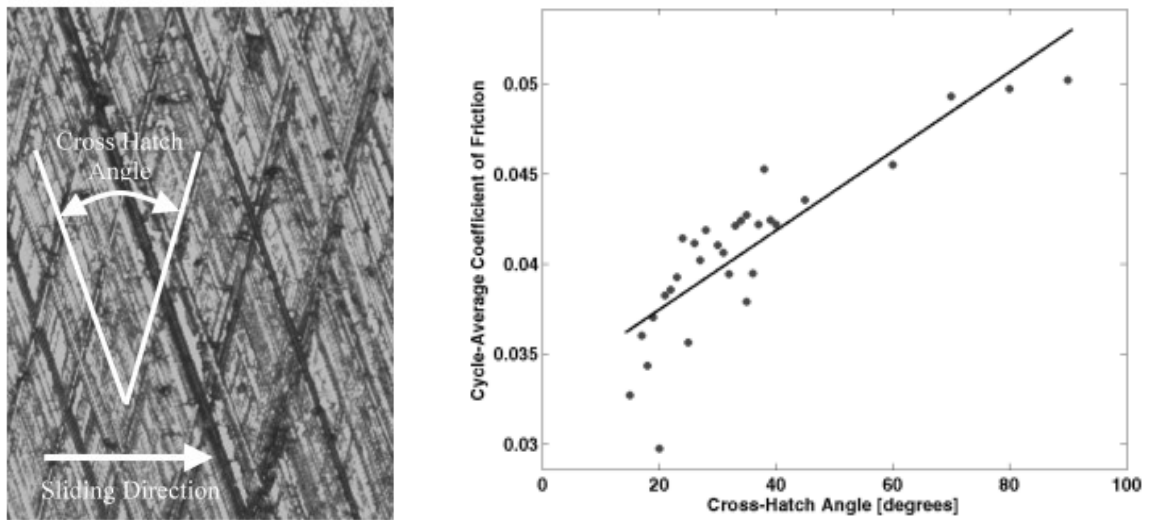
FIGURE 2.4: a) Photograph of honed surface defining cross-hatch angle, b) relationship between cross-hatch angle and average friction coefficient [51].

This result is supported by similar findings by Mezghani *et al.* [52] using the two dimensional Reynolds equation and the Swift-Streiber boundary condition. However, Mezghani predicted that in fact two distinct minima are produced at 40-45° and 115-130° (figure 2.5), which correspond to commonly used hatch angles produced by plateau and slide honing respectively. This is also in agreement with several other studies reviewed in this chapter, in that linear grooves/pockets are most effective when they are aligned transverse, rather than parallel, to the sliding direction.
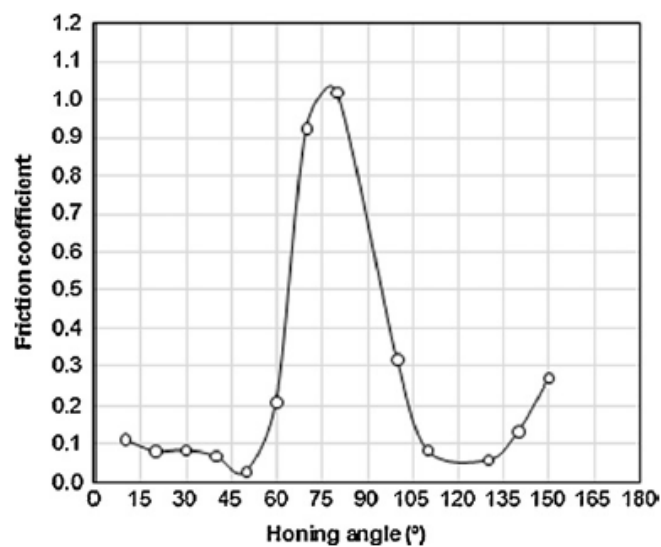
FIGURE 2.5: Predicted variation in friction coefficient with honing angle [52].

It has been concluded elsewhere that 45º is an optimal cross hatching angle [53]. Furthermore, the size of the grid produced by the honing process and determined by the honing angle directly affects the hydrodynamic pressure, and hence the friction coefficient. Cross hatching at approximately 45º produces a balance between grid size (*i.e.* plateau length) in the sliding direction, and the circumferential direction.

A limited amount of work has focussed on the effect of groove width on friction of honed liner surfaces and results have been somewhat contradictory. Considerably less effort has been devoted to the investigation of groove density effects on cylinder liner friction. Generally a balance must be reached between low groove density, whereby less hydrostatic pressure is generated (as this cannot be generated in the grooves due to the groove clearance, and only acts on the plateaued surfaces), and high groove density, whereby the viscous shear effect is amplified (again, the shear force will have a greater effect on the plateaued surfaces).

2.3   Effect of Surface Texture on Sliding Friction

The following section summarises the findings of studies looking at the effect of texture on friction. The majority of research initiatives to date have been carried out on lab-based tribometers, with the exception of two complete engine studies. The section concludes with a discussion of the mechanisms suggested to account for friction reduction behaviour.

2.3.1   Evidence of Surface Texture Reducing Sliding Friction

Several major contributions to surface texture research have been made by Etsion and co-workers (Israel Institute of Technology). For almost a decade, the researchers experimented with and theorised on a wide variety of bearing geometries and rig settings. For example, Ryk and Etsion showed the effectiveness of texture in reducing friction in "*reciprocating automotive components*", specifically piston rings [17]. To achieve this, they employed a reciprocating test rig (figure 2.6a) to measure the friction force between a piston ring segment and cylinder liner segment (figure 2.6b). Laser surface texture was

applied to the piston ring in the form of micro dimples with the following parameters: dimple diameter 72 μm, dimple depth 7.5 μm and dimple density 50% (figure 2.6c). This resulted in reductions of average friction force of up to 25% when comparing laser surfaced specimen with a smooth reference over a wide range of crankshaft angular velocities (figure 2.6d).
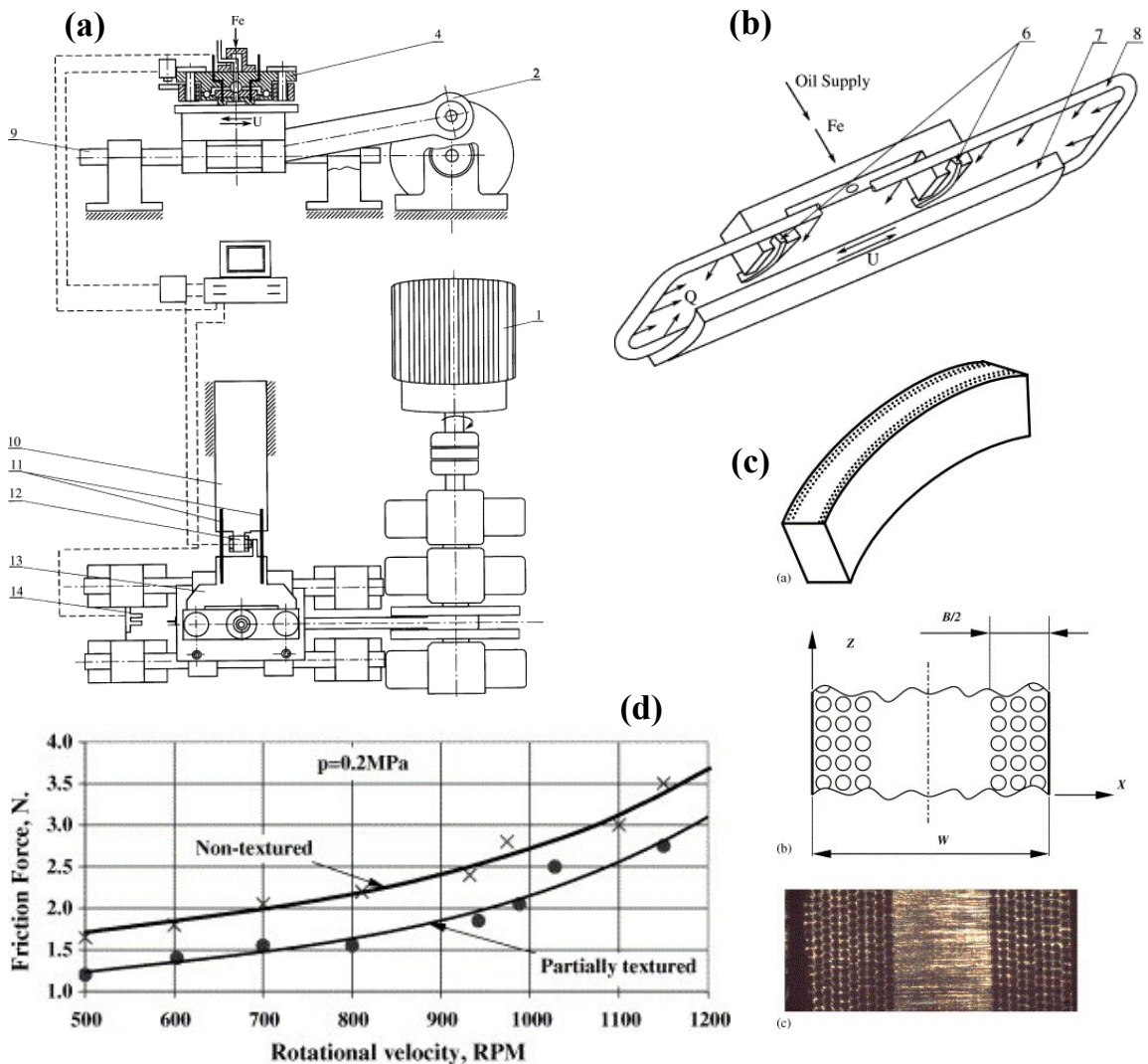
FIGURE 2.6: (a) Reciprocating test rig; (b) Schematic of the two counterpart specimens' assembly; (c) Partial LST piston ring; (d) Friction force vs. angular velocity for textured and untextured specimens [17].

The same test rig was employed in a further study to measure the friction force under fully flooded conditions for various angular velocities [8]. This time the counterpart specimens were parallel flat surfaces simulating flat piston rings and cylinder liner (figure 2.7a), so that the obtained experimental results could be compared against an analytical

model developed by the same group and detailed in [54]. Although the validity of this model was later questioned by Fowell *et al.* [23,24] and Ausas *et al.* [55,56], who employed a mass conserving cavitation algorithm and demonstrated that load support had been over-predicted in Etsion's non-mass conserving approach, the experimental results are relevant to piston ring-cylinder liner bearing due to the conformal nature of the contact.
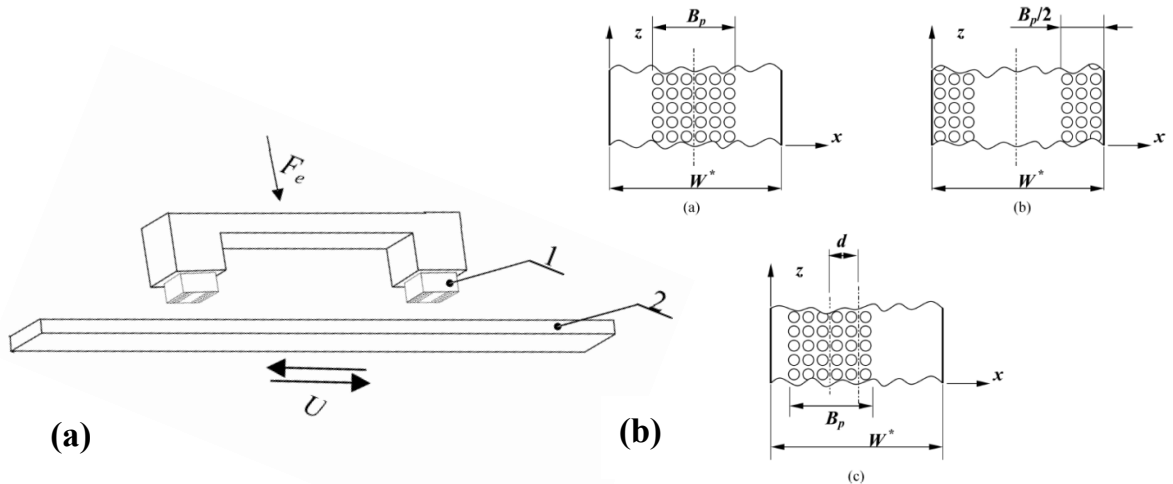
FIGURE 2.7: (a) Schematic of the two counterpart specimens; (b)Textured specimens with different locations of the pocketed area [8].

Partially and fully textured specimens (*i.e.* varying proportions of contact area coverage as shown in figure 2.7b) were compared with the non-textured case and reductions in friction of 25% and 40% respectively were recorded, as well as good correlations with the theoretical predictions for crank rotational velocities between 500 and 900 rpm. Figure 9 shows these results in terms of friction force vs. angular velocity for two selected external normal pressures: 0.1 and 0.5 MPa.
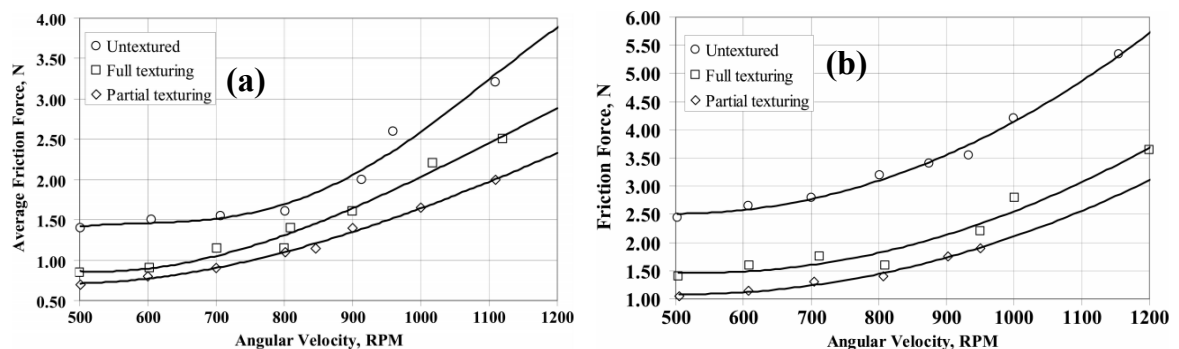
FIGURE 2.8: Average friction force variation vs. angular velocity: (a) external normal pressure 0.1 MPa; (b) external normal pressure 0.5 MPa [8].

More recently, dynamometer tests were carried out on a real IC engine, as described by Etsion *et al.* [18]. A naturally aspired 2,500 cm^3 Ford Transit engine (figure 2.9a) was used to evaluate the effect of laser surface texturing on fuel consumption, when texture is partially applied to the upper set of piston rings. Under these conditions, it was discovered that fuel consumption for partially LST chrome coated piston rings was up to 4% lower than in the case of corresponding non-textured conventional barrel-shaped piston rings. The author states that the mechanism by which friction reduction occurs is the *"collective effect of the dimples that provide an equivalent converging clearance between nominally parallel mating surfaces"*.
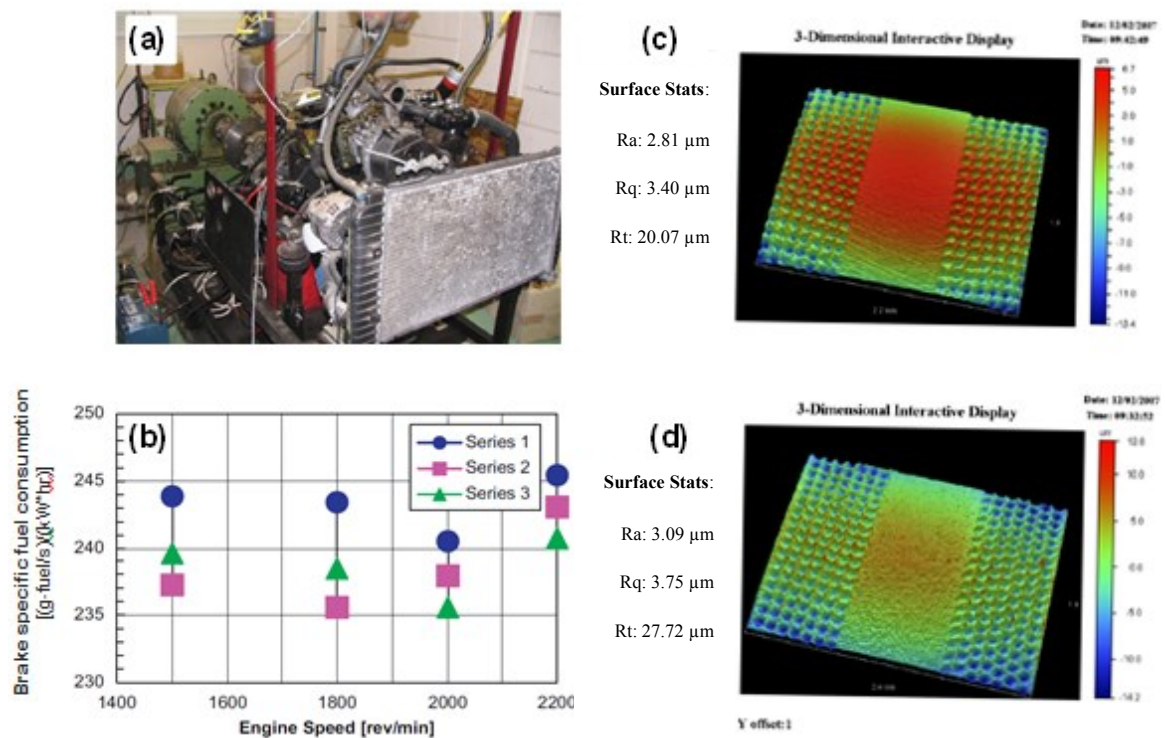
FIGURE 2.9: (a) Photograph of engine on test bench; (b) Effects of texturing and coating on engine specific fuel consumption for three piston ring configurations: Series 1: non-textured barrel-shaped Cr-coated, Series 2: flat Cr-coated LST-treated, Series 3: flat uncoated LST-treated; (c) Partial laser surface textured cylindrical Cr coated piston ring; (d) Partial laser surface textured cylindrical uncoated piston ring [18].

It is worth mentioning that the engine speed of 1800 rev/min, where the highest difference between non-textured and LST-treated piston rings was achieved, also corresponds to that of the maximum torque. The effect of LST on exhaust gas composition was also investigated; however, no traceable change between textured and non-textured piston rings was recorded. Figure 2.9(b) shows the variation of engine

specific fuel consumption versus engine speed for three piston rings configurations: non-textured barrel-shaped Cr-coated, flat Cr-coated LST-treated and flat uncoated LST-treated.

Further proof of friction reducing performance of LST in an actual IC engine has been provided by Rahnejat *et al.* [9]. The authors used a single-cylinder test engine (figure 2.10(a)) to study variations in torque for three cylinder liner configurations: a standard liner, a diamond like coated (DLC) liner, and a laser-etched textured liner (figure 2.10(b)). Improvements of up to 4.5% could be observed when using the laser-etched textured liner, compared to the standard liner (similar to findings from Etsion). Figure 2.10(c) shows the variation in torque percentage for the two modified liners (DLC and laser-etched) throughout the entire engine speed range.
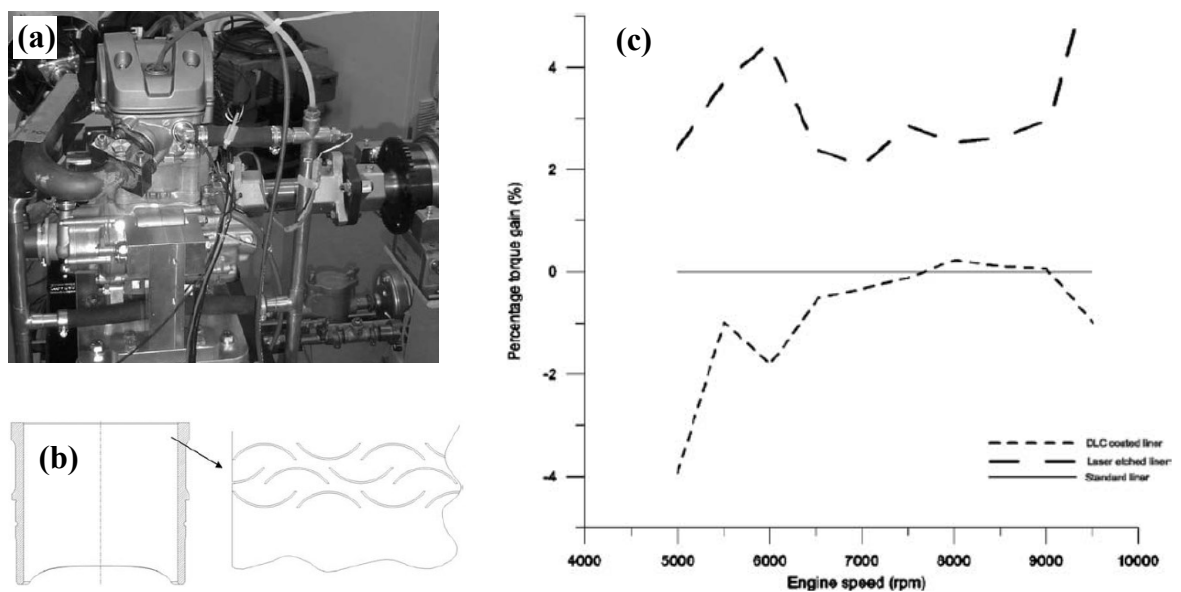
FIGURE 2.10: (a) Test engine; (b) Laser-etched cylinder liner; (c) Variation in torque percentage for the modified liners vs. the standard one [9].

Researchers from Argonne National Laboratory in the US studied the effects of pocketed surfaces under mixed and boundary lubricated contacts. Kovalchenko *et al.* [19] conducted tribological experiments using the pin-on-disc apparatus presented in figure 2.11(a). Frictional responses for various pocketed surfaces (figure 2.11(b)) were compared with the results obtained for the plain surface.
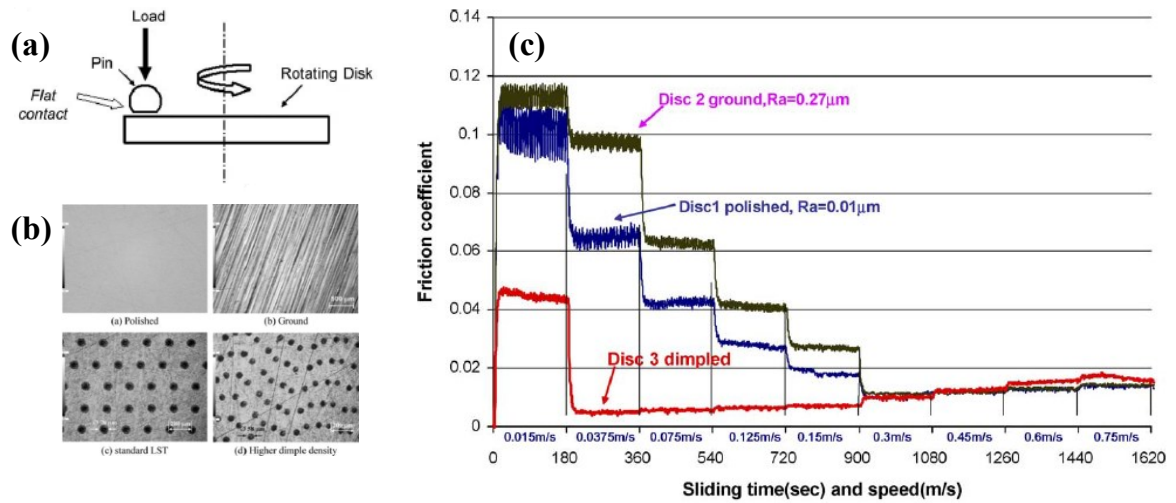
FIGURE 2.11: (a) Schematic representation of the pin-on-disc configuration; (b) various test specimens; (c) friction coefficient variation for different sliding speeds – oil viscosity: 54.8 cSts [19].

These tests were conducted using a range of sliding speeds (0.015 to 0.75 m/s) and nominal contact pressures (0.16 to 1.6 MPa). Significant differences between the friction behaviour of textured and plain bearings were observed particularly at low speeds when comparing the ground, polished, and laser surface textured specimens (figure 2.11(c)). Finally, the authors concluded that *"LST can be used to reduce friction in oil-lubricated tribological components that are operating under a boundary lubrication regime"*. This observation is in general agreement with several other studies and is further investigated in the current research: texture is most effective at reducing friction when contacts operate in the mixed and boundary regime, whereas texture generally appears to have little effect on hydrodynamic friction.

Similar results were reported a few years later by Borghi et al. [20] who investigated the effect of LST when used in high-performance engine applications. These researchers used nitrided steel discs, textured with arrays of circular dimples 100 μm in diameter, 50 μm in depth and with 40% surface density (figure 2.12(a)). Friction force tests were performed using a pin-on-disc test rig and Stribeck curves were generated for both the textured and non-textured specimens by varying the sliding speed (from 0.01 to 0.12 m/s) and the nominal contact pressure (1 to 10 MPa) (figure 2.12(b)). The most significant effects of LST on friction coefficient and wear were recorded when using a *"single drop"*

lubrication approach (*i.e.* a small quantity of Shell Helix Ultra commercial lubricant) at high normal applied load and over an extensive sliding time.
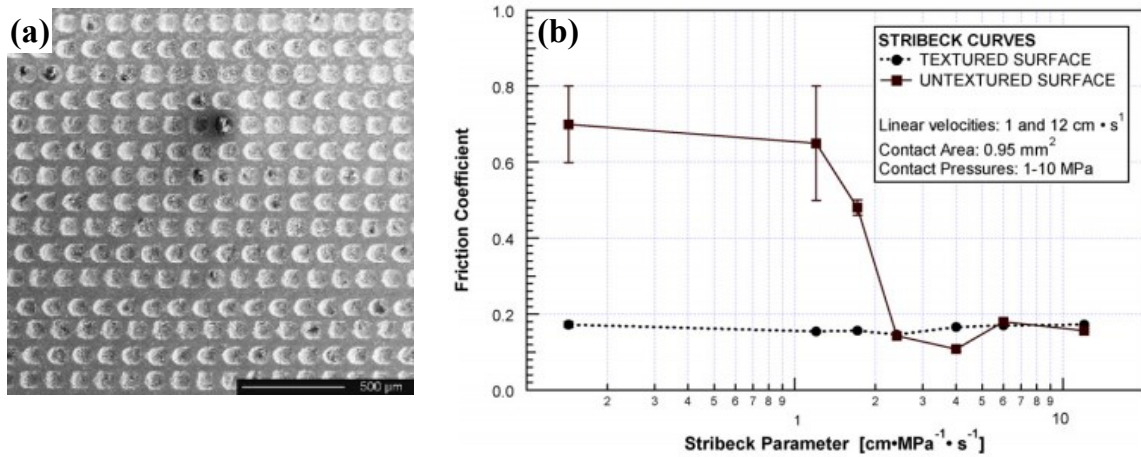
FIGURE 2.12: (a) Textured specimen with dimpled pattern; (b) Stribeck curves for both the textured and untextured specimen [20].

In 2014, Braun *et al.* [10] also investigated the efficiency of LST in friction reduction under mixed lubrication conditions. Tests were again conducted using a flat-pin-on-flat-disc configuration (figure 2.13(a)), with circular dimples applied to the surface of the pin. The dimple diameters ranged between 15 to 800 μm while the area density and the depth to diameter ratio were kept constant at 10% and 0.1 respectively. Tests were performed varying the speed of the disc in order to control the lubrication regime. The authors found a "*severe*" dependence of friction reduction on dimple diameter. Different oil temperatures and viscosities require different dimple diameters to achieve a maximum reduction in friction force *e.g.* the optimal dimple diameters were 40 and 200 μm for the tests at 100 and 50 °C, respectively (figure 2.13(c)). The researchers were however unable to demonstrate a general relationship between optimal dimple size and oil temperature. No clear correlation was observed between sliding velocity and optimal dimple diameter although velocity had a demonstrated effect on the extent of friction reduction.
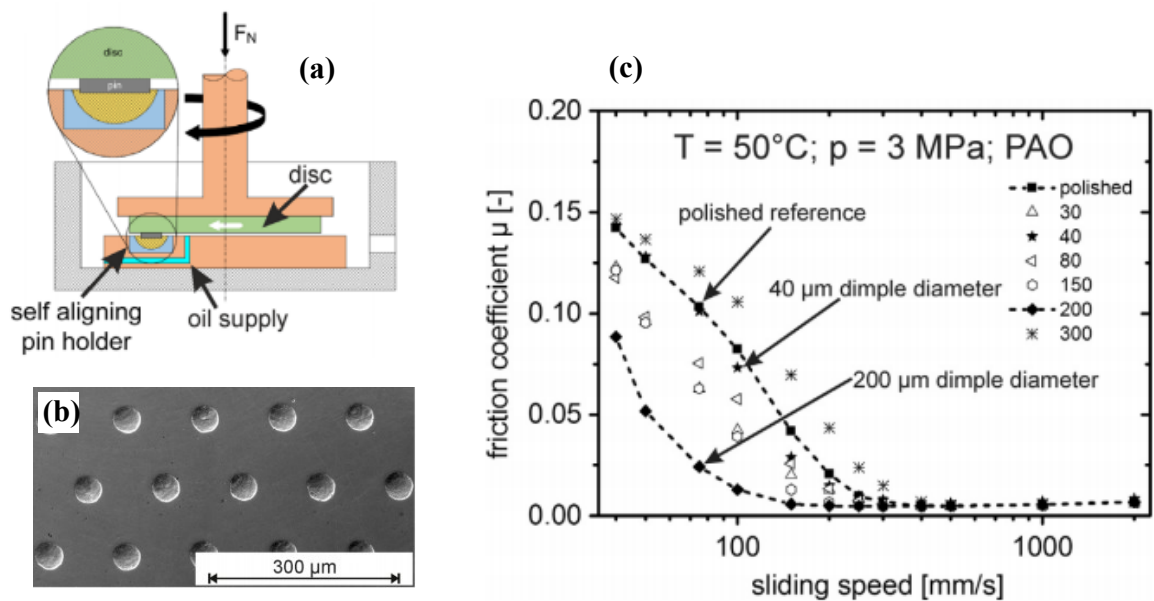
FIGURE 2.13: (a) Pin-on-disc testing setup comprising a self-aligning pin holder; (b) SEM image of a textured specimen with dimple diameter of 40 μm; (c) friction coefficient variation with sliding speed at oil temperature: 50°C [10].

The importance of this very recent study is enhanced by its attempt at understanding and hence optimising the underlying mechanisms involved in texture friction reduction. These were investigated by controlling the applied texture geometry, leading to the following outcomes. Firstly, the authors found that the depth-to-diameter relationship had a limited impact on friction. This is in contradiction to previous research on elastohydrodynamic contacts, where the depth-to-diameter ratio was a significant factor [46]. This discrepancy may suggest that the ratio is important in elastohydrodynamic contacts where piezo-viscous effects come into play, but less so in nominally conformal, low pressure contacts. As mentioned, a strong dependence of friction reduction on dimple diameter was demonstrated. However, no positive relationship between friction reduction and dimple circumference was found (*i.e.* dimple edge perpendicular to the sliding directions), which is contrary to the theory that pockets act as miniature step bearings. Instead, the research concluded that pockets cause a change of flow which builds up the pressure. An optimum dimple diameter was also found, which lead to an 80% reduction in friction.

Despite the incontestable value of this research, the results cannot be used to predict optimum dimple geometry for other applications due to the fact that the optimum dimple diameter varies as a function of operating conditions. In the authors' words, *"**the data**

39

also highlight that research for one set of texturing parameters being optimum in all applications and for all operation points most likely will be futile. Rather, in each new case, the textures need to be optimized." At the most, it can be concluded that the optimum dimple diameter may increase with lubricant viscosity, which is supported by several other studies [57–59]. This is supported by the fact that, in a study Wang *et al.* [57] who attempt to find the optimum dimple geometry for a hydrodynamic pad bearing, a different optimum pocket geometry was predicted.

Wang et al. [21] employed a ball-on-disc tribometer (figure 2.14(a)) to investigate the effects that triangle-shaped dimples with various coverage ratios (figure 2.14(b)) have on friction coefficient while placing the bearing under various lubrication regimes. Stribeck curves were plotted for all the investigated pocketed surfaces, various geometric parameters of the dimples (*i.e.* depth, size, direction and coverage ratio) being tested throughout the experiment.
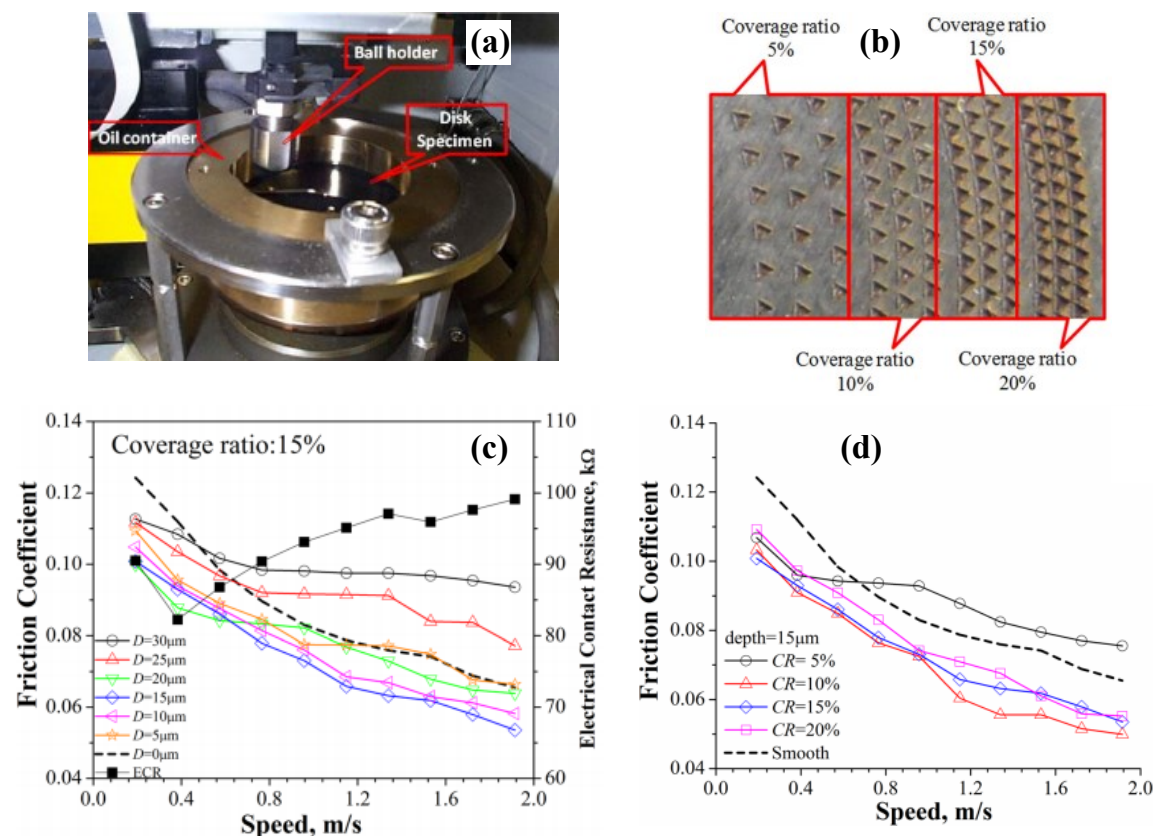
FIGURE 2.14: (a) Ball-on-disc test rig; (b) Textured specimen with various coverage ratios; (c) Friction coefficient variation for different dimple depths – coverage ratio: 15%; (d) Friction coefficient variation for different coverage ratios– dimple depth: 15 μm [21].

40

Results showed that distinct friction behaviours are associated with the presence of dimple arrays of different sizes, depths and coverage ratios. In comparison to non-textured surfaces, the friction coefficient varied with dimple depth, firstly decreasing then increasing when dimple depth was reduced from 30 μm to zero whilst coverage ratio and size were held constant. The lowest friction coefficient appeared at a dimple depth of approximately 10 to 15μm (figure 2.14(c) – plotted for a constant coverage ratio of 15%), before finally approaching that of the non-textured surface as dimple depth declined below 10 μm. Plotted for a constant dimple depth of 15 μm, the coverage ratio of texture had a similar effect on friction – a ratio of approximately 10% generated the lowest friction coefficient (figure 2.14(d)).

Duarte et al. [60] employed a novel texturing technique based on laser interference metallurgy to study the tribological performance of various pocketed surfaces comprising features such as lines (figure 2.15(a)), dimples, and *"crosslike"* patterns. Significant improvements in tribological performance of the tested bearings were observed when surfaces comprising features were compared against the smooth reference, especially under starvation conditions (figure 2.15(b)). Moreover, the authors concluded that *"produced structures are strong and robust increasing lubricating film lifetime, even under mixed lubrication conditions, where a part of the periodic structure is lost"*.
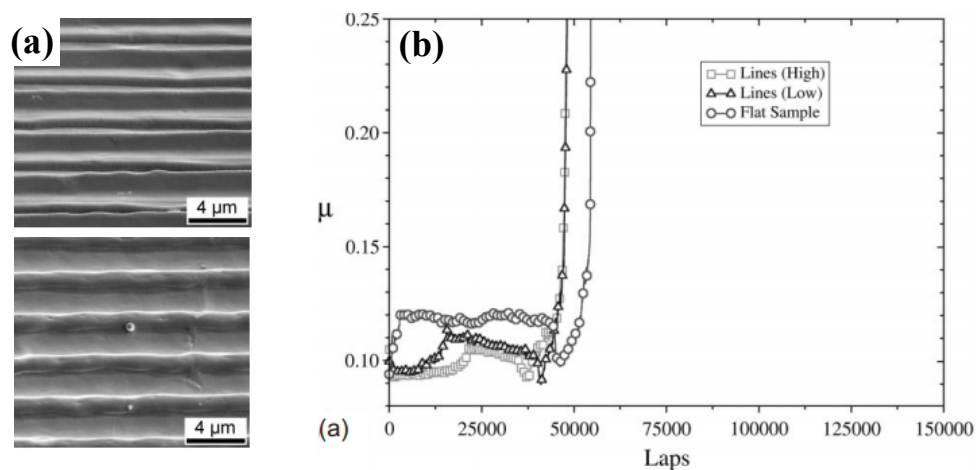
FIGURE 2.15: (a) SEM images of the line-like patterns; (b) Friction coefficient vs number of laps for different line-like and flat samples [60].

Lu and Khonsari at Louisiana State University investigated the effects of dimples on Stribeck curves in a project conducted in collaboration with Caterpillar Inc. [22]. Their

findings are particularly relevant to this review since the contact studied is nominally hydrodynamic (having a conformal geometry) and tests are carried out under a range of speeds with particular emphasis on the mixed regime. Furthermore, the dimpled bushings were obtained using two alternative methods to laser texturing (namely machining and chemical etching – figure 2.16(a)) and were tested varying load, velocity and dimple dimensions.

The authors conclude that "*the so-called secondary lubrication effect in the dimpled area is the main mechanism responsible for improvement of performance*". More oil is thus retained in between dimples, which causes friction to be lowered. Friction results recorded using circular dimples of different dimensions, as well as dimples obtained using different processes, were compared against results obtained using a conventional smooth bush (figure 2.16(b-c)). In agreement with the majority of reported studies, the benefit of surface texture is only apparent in the mixed and boundary regimes.
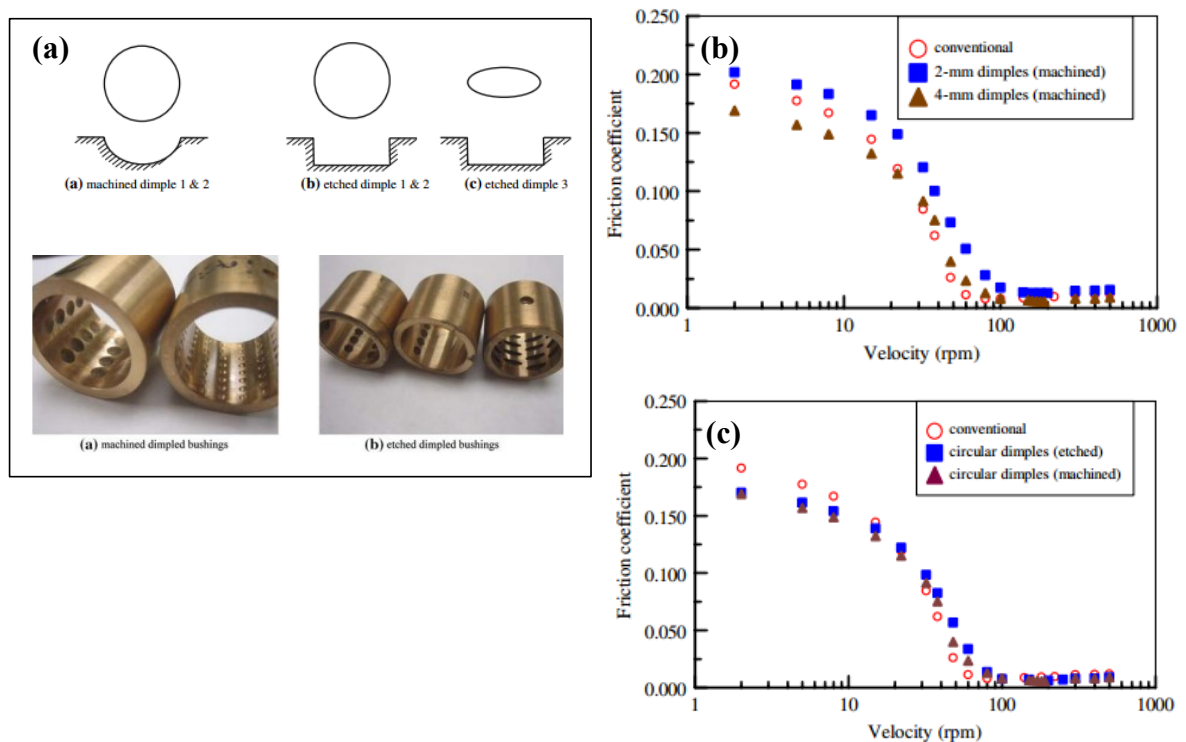
FIGURE 2.16: (a) Dimpled specimens obtained using different processes; (b) Stribeck curves showing the effect of dimple diameter – 890 N load; (c) Stribeck curves presenting the effect of texturing process – 890 N load [22].

Costa *et al.* [13] successfully employed a capacitance technique to measure minimum film thickness in a reciprocating line contact with one surface containing a micro-textured pattern. Several pattern types were tested and it was concluded that for a given load the addition of specific texture patterns can increase the minimum film thickness in the reciprocating contact (figure 2.17).
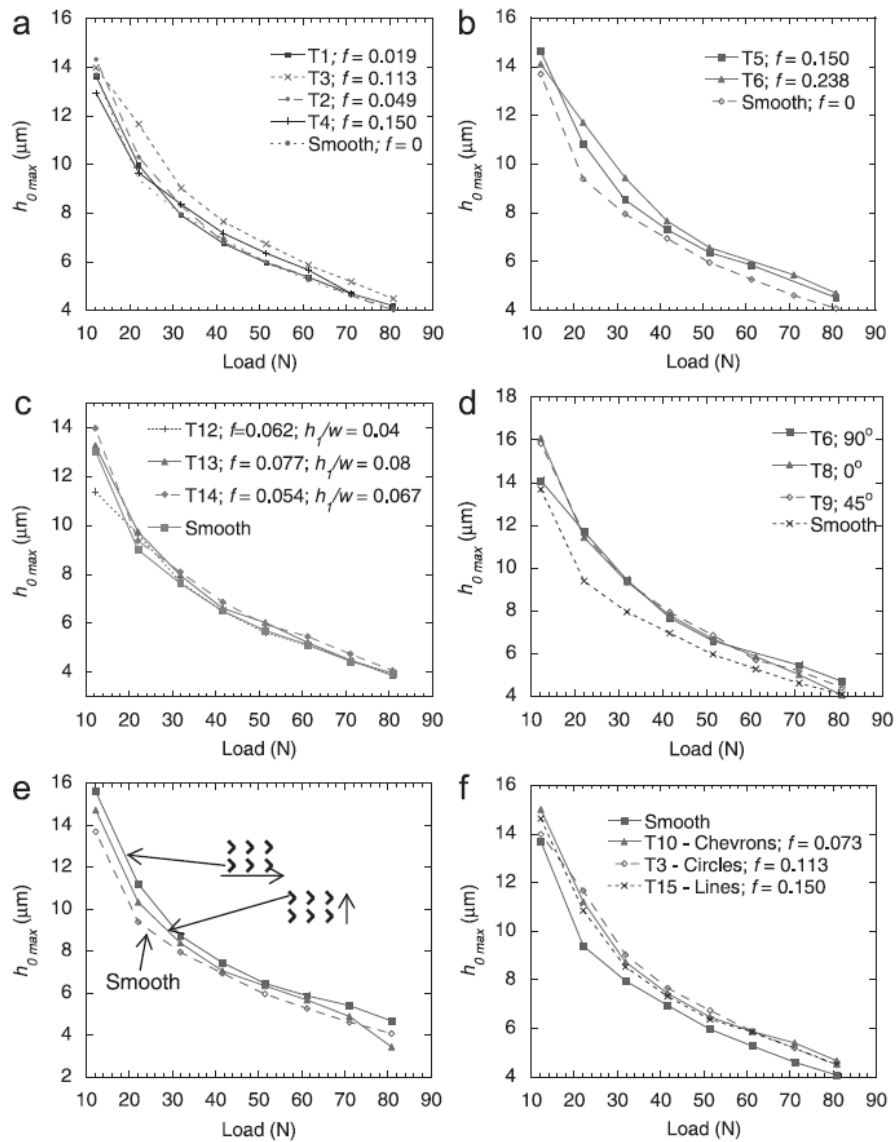
FIGURE 2.17: Effect of various textured patterns upon minimum film thickness in a hydrodynamic reciprocating contact [13].

Costa and Hutchings' experiments showed that the shape and orientation of patterns has a direct influence on film thickness, with chevron patterns pointing along the sliding direction being most effective configuration. Conversely, measurements using grooved textures gave the lowest fluid film thickness. Moreover, clearly asymmetric behaviour of

the samples was observed during acceleration versus deceleration over the course of the reciprocating sliding tests. As a result of the squeeze-film effect, film thickness consistently registered higher values when the samples were decelerating. Another noteworthy observation from their study was that features larger than the elastic contact width resulted in lower film thickness values when compared to smooth test samples.

The use of laser textured surfaces has also been investigated intensively at Imperial College over the last decade. A study conducted in the framework of a PhD program by Manzoor [61] led to the development of a novel experimental test rig capable of studying the variation of friction, load and film thickness present between a rotating glass disc and a loaded flat or textured pad. Manzoor made a worthwhile contribution to the current state of knowledge on the use of hydrodynamic lubricated micro-textured bearings. He found that textures with a single large pocket placed near the inlet or the outlet of the contact exhibit favourable load support and film thickness values over a wide range of convergence ratios, reducing friction by up to 6% when compared to a plain experimental pad (figure 2.18).
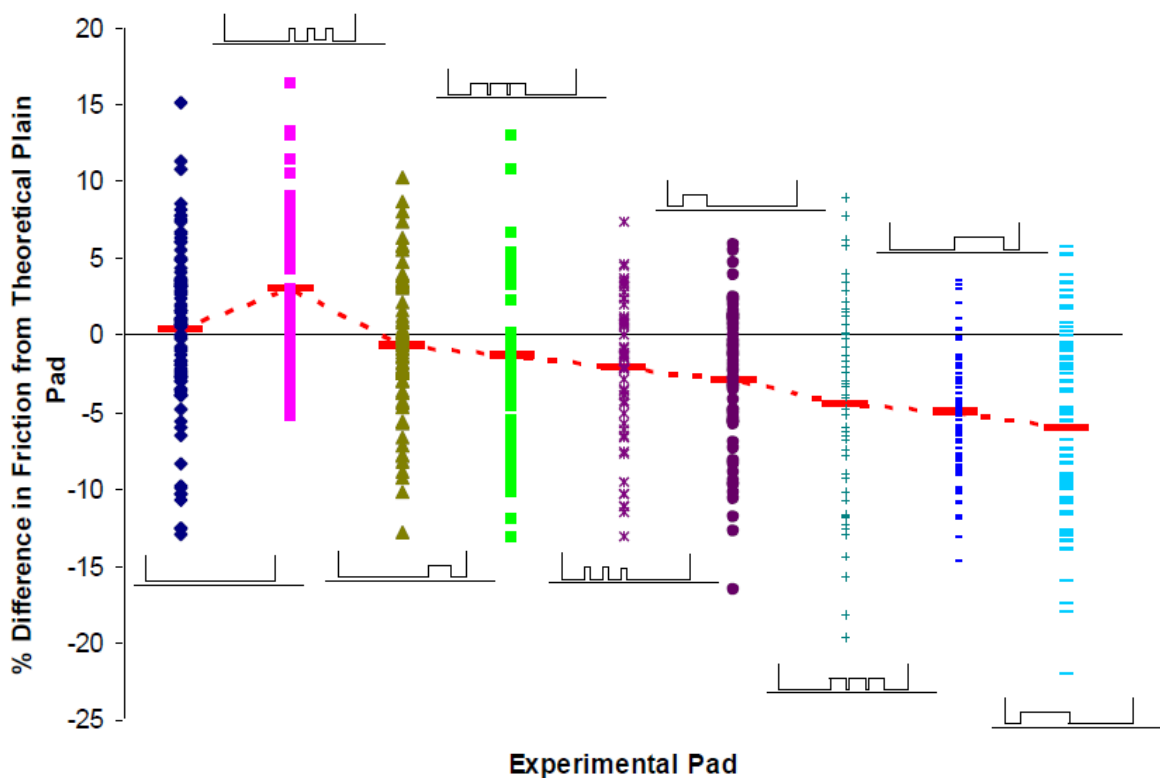
FIGURE 2.18: Percentage difference in friction compared to equivalent theoretical non-textured pad for all patterns tested [61].

A final study worth referring to in this section is the work of Scaraggi *et al.* [25]. The authors used a commercial CSM pin-on-disc tribometer and applied the texture to the pin specimen (figure 2.19 (a)). Contrary to the majority of previous research, the results of this study show texture to significantly reduce friction in the hydrodynamic regime (figure 2.19 (b)). This area may be worth further investigation to confirm the possibility that this particular texture configuration results in a different friction mechanism that is effective under full film conditions.
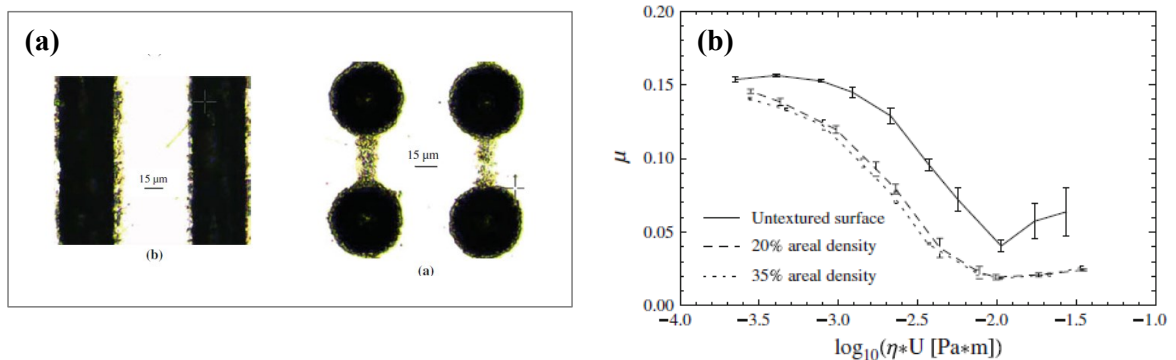
FIGURE 2.19: (a) Optical micrographs of surface texture on pin specimen, (b) Stribeck curve showing the effect of texture (and texture density) on friction [25]

2.3.2   Effect of surface texture on static friction

Modern IC engines featuring start and stop functions by definition spend longer periods of time under static conditions. During these periods no liquid film is present between the surfaces (true solid-solid contact occurs) so that on start up the contact is subject to static friction (*i.e.* a peak in friction at the onset of sliding required to shear the conjunctions which had time to form between the two surfaces). Yet another potential benefit of applying texture to the surface of components, particular under start stop operation, is that it may serve to reduce this static friction.

Although, for the reasons explained above, this is of significant interest to motor vehicle manufacturers, the influence of laser surface texturing on static friction has been largely overlooked. Only one recent study has focussed on this area whereas the effect of surface texture on dynamic friction and wear has enjoyed an exponential increase in the number of technical publications during the last decade. The study in question was undertaken by

Greiner *et al.* [35] who employed a custom build tribometer described in detail in [62] to study the influence of dimple depth and diameter on static friction. Laser textured samples with dimples of various diameters (20, 50, 75, 100, 150 and 200 µm respectively) and depths varying between 10 and 65 µm were tested (figure 2.20(a-c)). Values of static friction force were recorded for a speed of 1 µm/s and a normal applied load of 10 N.
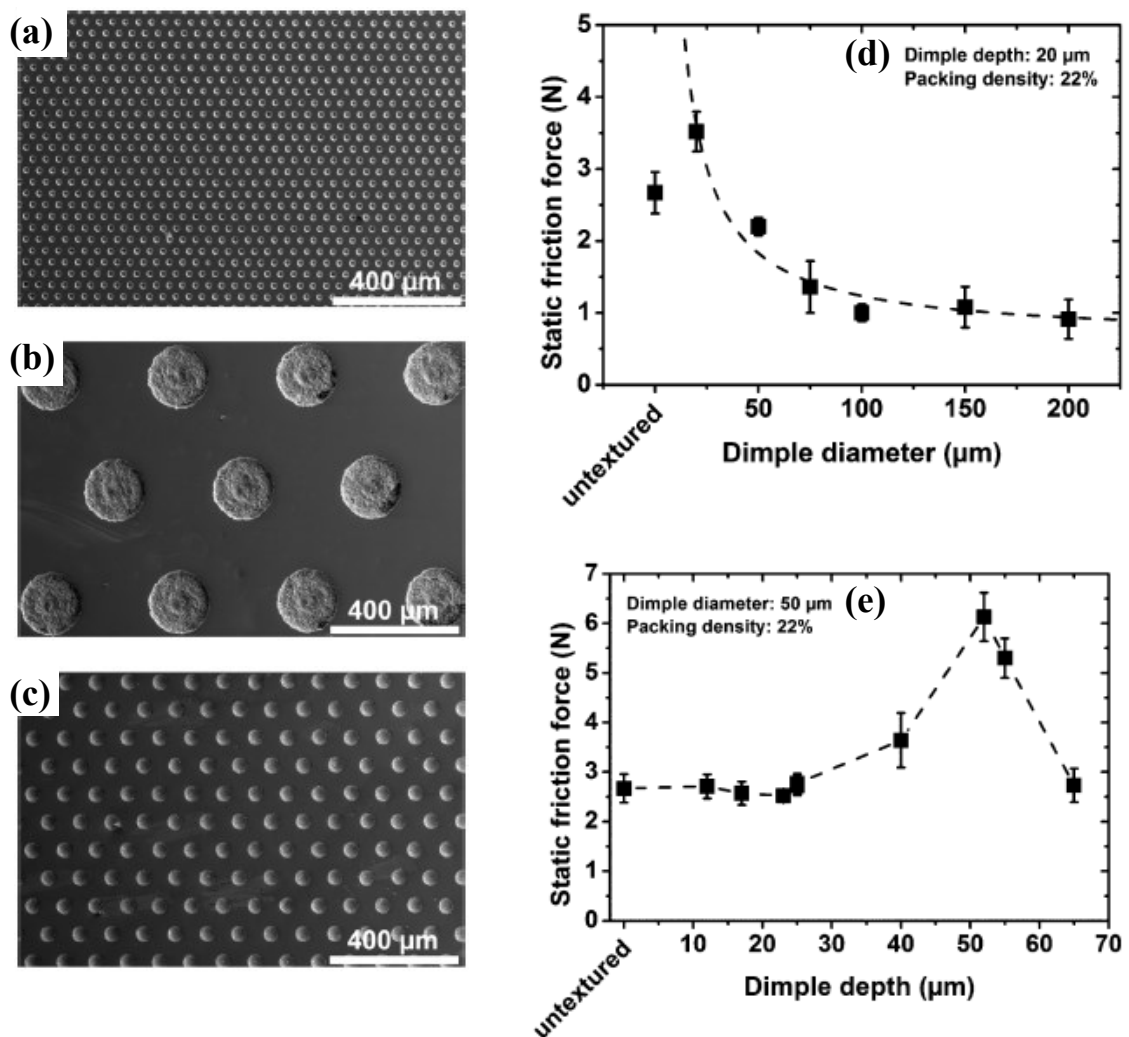
FIGURE 2.20: (a-c) Optical images of the pocketed surfaces with different dimple diameters: (a) 20 µm; (b) 200 µm; (c) 50 µm. (d) static friction force variation as a function of dimple diameter; (e) static friction force variation as a function of dimple depth [35]

Counterintuitively, results showed that static friction force decreases with increasing dimple diameter (figure 2.20(d)), *i.e.* the smallest dimple diameter specimen (20 µm) exhibited higher static friction forces than the non-textured specimen. According to the

researchers, the result is of *"high relevance as it indicates that there is indeed contact splitting for dimpled surfaces under a tribological load, similar trend being reported for the adhesion of elastomeric samples* [63]*"*.

The way in which dimple depth influences static friction force was also investigated for a range of depths between 10 and 65 μm (here, the dimple diameter and density were kept constant throughout these experiments at 50 μm and 22% respectively). The resulting variation in static friction is shown in figure 2.20 (e) with a peak of 6.13 N reached at a dimple depth of 52 μm. However, the authors do not discuss this behaviour and it is difficult to understand the physical reasons why static friction would vary as a function of pocked depth.

2.3.3   Mechanisms by which surface texture affects friction

This subsection outlines different mechanisms proposed as explanations for the observed reductions in friction associated with surface texture. In more than five decades since the first studies exploring the correlation between micro-features and friction, surprisingly few authors have attempted to investigate and explain the mechanisms responsible for optimised tribological performance of textured surfaces.

Tønder [37,38] was among the first authors to investigate possible mechanisms of friction reduction in lubricated bearings after concluding that surface texture is most effective if placed close to the bearing's inlet. The following two mechanisms were provided as possible explanations for the observed decrease in friction. Firstly, texture can create resistance, acting to prevent fluid from escaping the contact. Alternatively, the patterns generate a *"virtual step"* which resembles the discontinuous change in film thickness found in Rayleigh step bearings.

Studying the behaviour of transverse roughness in EHL lubricated contacts, Morales-Espejel [64] and Greenwood [65] suggested that, in the bearing's inlet region, each asperity peak entering contact zone behaves as a flow exciter that closes and opens the inlet to allow varying amounts of fluid to enter. This phenomenon is possible as both pressure and roughness deformations are low in the vicinity of the inlet. Years later,

Morales-Espejel, Tripp and co-workers [66] showed new interesting phenomena through which surface texture can affect load support and consequently friction force. They observed that, under EHL lubrication conditions, oil is released from the pocket under pressure, as a result of elastic deformation of the material in the contact area. This mechanism can also contribute to significant friction reduction in boundary and mixed lubrication regimes.

Olver and Fowell [23,24] identified a new mechanism of hydrodynamic lubrication termed *"inlet suction"*, and demonstrated how parallel and low convergence, micro-pocketed bearings, can generate load support. The authors observed that the reduction of pressure below atmospheric values in the pocket inlet leads to lubricant being sucked into the bearing. They thus provided an alternative explanation to fluid entrapment for the mechanism responsible for transporting lubricant into the bearing at low convergences.

Finally, recent theoretical studies by Chong *et al.* [67] who employed a numerical model based on a modified Elrod's cavitation algorithm [68] found that the *"pre-reversal"* cavitation is sealed off by the lubricant and forms a bubble at the inlet. Although the cavitation bubble is gradually absorbed by the lubricant film, the inlet is starved. It was then postulated that surface pockets may bring lubricant into the starved region and hence reduce friction. There appears to be uncertainty in the literature regarding the presence of cavitation in piston-liner contact and its interaction with surface texture. For this reason, cavitation is reviewed in the Section 4.3.5 and its interactions with surface texture are studied experimentally as part of this project (see Chapter 4).

One other means by which surface texture can improve tribological performance is by increasing the supply of oil to the inlet of the contact, especially under starved conditions. This would have the effect of increasing film thickness and hence reduce friction and wear.

Under starved lubrication conditions, the lack of lubricant leads to the two sliding components being covered by separate oil films which only merge into a meniscus close to the contact. This reduced quantity of oil entering the contact can occur due to high sliding speeds but other factors such as viscosity, surface tension or reciprocating

behaviour can also result in thinner than expected oil films. Fortunately, textured cavities have been shown to act as a secondary source of lubricant, which flows back to the contact region *"replenishing"* the oil film and hence limiting starvation [26,32,33]. In other words, in such situations, the texture features act as lubricant micro-reservoirs that help to replenish the contact inlet [14].

Chiu [32] was the first to investigate lubricant *"replenishment"* behaviour. Specifically, he related the oil flow back into the track to lubricant surface tension, viscosity, and rolling speed [69]. Since this initial approach more than four decades ago, other studies have investigated the possibility that textured pockets can act as lubricant retention reservoirs.

Blatter et al. [31] investigated the reservoir mechanism through which surface texture continuously provides lubricant to the surfaces in contact by running pin-on-disc tests for three different disc patterns: polished, *"rough"* grooves (separation: 20 μm, width: 11 μm, depth: 4 μm) and *"fine"* grooves (separation: 20 μm, width: 3 μm, depth: 2 μm). Friction coefficient and wear tests were performed for all three specimens, leading to the results shown in table 2.1. The *"fine"* textured specimen resulted in the minimum friction coefficient and wear rate, coupled with the longest sliding life. The researchers attributed this boost in performance to the fact that *"the full oil reservoir in the fine grooves remains available for lubrication"* and they concluded that *"the much longer sliding life of patterned samples reflects the potential of microscopic grooves to store the lubricant and to replenish the sliding track with fresh oil"*.

TABLE **2.1**: Summary of the pin-on-disk test results for smooth and laser pocketed surfaces [after [31].

Pattern	Reservoir capacity	Minimal friction coefficient	Sliding life (revolutions)	Ball wear rate (10^{-18} m^2/N)
none	small	0.05	155,920	2.6
rough	large	0.05	660,650	2.5
fine	medium	0.02	>5,800,000	1.8

In a more recent study, Borghi *et al.* [20] examined the chemical composition of textured and non-textured surfaces using Energy Dispersive Spectroscopy (EDS). Results showed

significant quantities of Mg and Ca inside the dimples (table 2.2) demonstrating the retention of lubricant. This provided an explanation for the reduction in both friction and wear afforded by the textured surfaces, a phenomenon that is most pronounced under mixed lubrication and harsher sliding contact conditions.

TABLE 2.2: Summary of the Energy Dispersive Spectroscopy results [20]

	C (at.%)	O (at.%)	N (at.%)	Ca (at.%)	Mg (at.%)	Ni (at.%)	Cr (at.%)
Untextured steel (raw surface)	$5-6$	$1-2$	$7-9$	$-$	$-$	$3-4$	$1-2$
Untextured steel (wear track)	$2-3$	$4-7$	$-$	$-$	$-$	$2-3$	$1-2$
Textured steel (wear track outside dimples)	$5-9$	$2-3$	$7-8$	$-$	$-$	$2-3$	$1-2$
Textured steel (wear track inside dimples)	$28-30$	$20-25$	$-$	$5-6$	$6-7$	$-$	$-$

Finally, Krupka *et al.* [34] investigated the effects of micro-dimples in EHL and mixed lubrication regimes. They measured film thickness as various micro-dimples passed through a lubricated non-conformal contact between a steel ball and a glass disc. As shown in figure 2.21, under mixed lubrication conditions, the array of micro-dimples is entrained into the contact and increases film thickness.
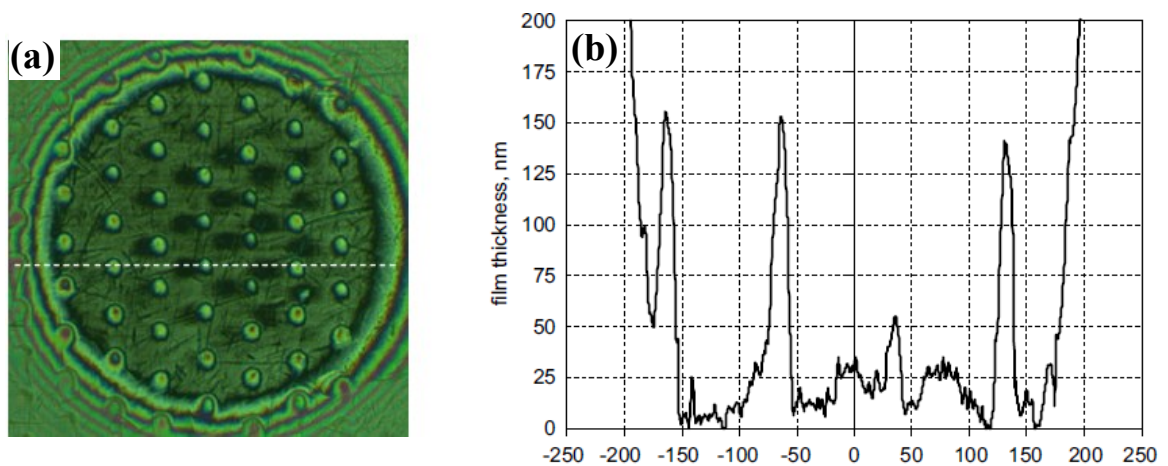
FIGURE 2.21: (a) Interferometry image of the ball-on-disc contact under mixed lubrication conditions; (b) film thickness profile showing the effects of various micro-dimples passing through the point contact [34].

Wear was also assessed by analysing surface topography after testing. It was revealed that the textured specimens showed no discernible surface wear, while the non-textured

showed distinct abrasion marks. Again, the researchers concluded that pockets can act as oil reservoirs capable of supplying lubricant into the contact region and overcoming starvation.

2.4   Effect of surface texture on wear

This section represents an overview of research into the impact of structured surfaces on wear, with a focus on tests performed under lubrication conditions similar to those typically encountered at top dead centre in IC engines applications.

It is generally accepted in the technical literature that surface texturing contributes to the removal of debris from the contact and thus inhibits wear processes under dry conditions (*i.e.* decelerates or delays the onset of wear). The beneficial effects of this phenomenon can also be observed in lubricated contacts, especially under mixed and boundary lubrication conditions [26].

Relatively new techniques such as Scanning Electron Microscopy (SEM) have allowed researchers to investigate the morphology and chemistry of surfaces immediately after performing tribological tests, as well as debris behaviour and the degradation of texture. The first to focus on this aspect of pocketed surfaces was Zum Gahr [27] who carried out wear tests on plain and micro-textured steel/oxide-ceramic and self-mated oxide-ceramics sliding pairs (figure 2.22(a, b)). Reductions in friction due to texture were noted when tribological tests were performed with both steel/oxide-ceramic and self-mated oxide-ceramics pairs (figure 2.22(c, d)).

The authors noticed that *"short-time"* (instantaneous) spikes in friction force appeared after 50 m of sliding for the non-textured specimens and related this to wear particles being trapped inside the contact area. However, for the dimpled textured specimens, such peaks in friction did not occur until after 400 m of sliding (figure 2.22(d)). They attributed this improved performance of the textured specimens to *"the capability of the micro-dimples to gather wear debris from the contact area"*. SEM micrographs were recorded for the worn micro-textured specimens after the 900 m sliding tests were completed. These graphs reveal low quantities of wear debris in the pockets of the crosshatched recesses, but large amounts of partially compressed to layers wear debris

collected inside the dimple shaped micro-pockets. The researchers concluded that the spikes in friction signal observed after a 400 m distance of sliding were caused by detached layers or groups of small wear particles which had accumulated in the micro-dimples.
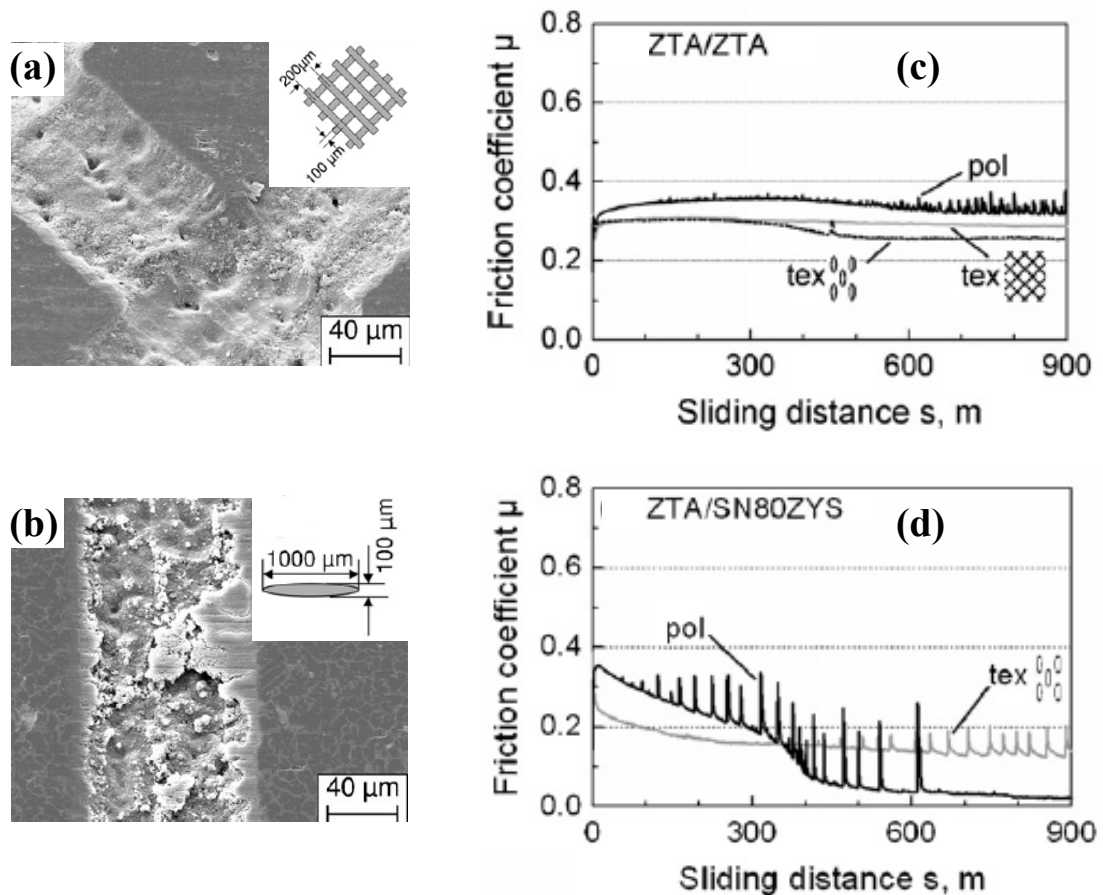
FIGURE 2.22: (a) Crosshatch textured specimen; (b) textured specimen with grooves normal to the direction of sliding; (c) friction coefficient vs. sliding distance of self-mated ZTA (SN80) ceramic and smooth specimen; (d) friction coefficient vs. sliding distance of ZTA/SN80ZYS and smooth specimen [27].

Borghi et al. [20] also examined the interior of micro-textured pockets using an SEM (figure 2.23) after performing the tribological tests described in the previous section of this study. The different wear tracks observed on the textured and non-textured surfaces were explained by the fact that wear debris accumulated between pin and disc (the "white" signal visible on the SEM images). In the case of the non-textured surface, debris is found covering the entire wear track (figure 2.23(a) and figure 2.23(b)), whereas this only accumulates inside the dimples on the textured specimen (figure 2.23(c)). The "white" signal apparent in the SEM image of one dimple in isolation is explained by the

presence of irregular particles which moved from the contact region and inside the cavity. Wear is thus reduced due to the migration of debris from the contact area between pin and disc and into the dimples which act as collectors.
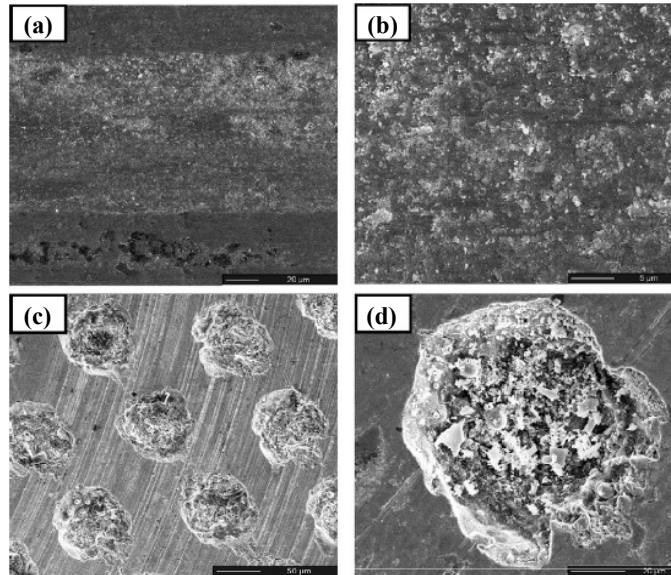
FIGURE 2.23: Secondary Electron Microscopy of (a) plain specimen (b) detail of the plain specimen; (c) micro-textured specimen and (d) detail of a dimple from the textured pattern [20].

Probably the first study regarding the ability of micro-topography to entrap wear debris in a tribological dry contact was conducted by Varenberg *et al.* [28] on a flat-on-flat experimental setup. The researchers studied various aspects regarding the role of oxide wear debris in a fretting test, with particular emphasis on how the removal of wear debris from the contact area and into the micro-textured pockets occurred. In fact, they were able to describe schematically the underling mechanisms by which waste is collected inside textured features. This is shown in figure 2.24(a) where the four stages of the filling mechanism can be seen, alongside an optical microscope image of an intermediary stage (i.e. stage 2 or 3), in figure 2.24(b).
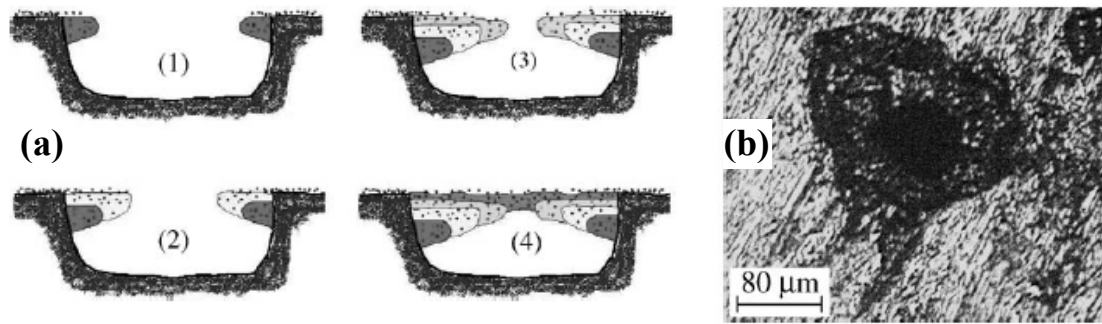
FIGURE **2.24**: (a) Schematic representation of the pocket filling mechanism; (b) optical microscope image of an intermediary filling stage [28].

Figure 2.24 clearly shows how the pocket filling takes place: starting at the rim, followed by the centre and finally the base. Another important finding of this study is that the filling mechanism can lead to either reduced or increased damage; depending on the dominant wear mechanism − *i.e.* pockets reduce damage if adhesive wear is dominant and increase damage if abrasive wear is dominant.

Although Varenberg's study is not directly related to the IC engine contact, the mechanism documented by the researchers is accepted in the literature as the main way in which surface texture can help to accommodate wear particles and reduce damage [20,41]. In fact, in a liquid lubricated contact, this mechanism can lead to a near doubling of fatigue life [29].

Pettersson and Jacobson investigated the influence of surface texture on wear under starved and lubricated boundary conditions [11,30]. They also concluded that recesses can remove debris from the contact zone and hence delay or decelerate wear [30]. Based on a series of ball-on-plane reciprocating sliding tests using different texture geometries, the researchers grouped the tested textures into two categories: *"low friction and no measurable wear"* and "high friction and severe wear*"*. They concluded that *"successful textures were those having the smallest tested grooves or squares and an orientation perpendicular to the sliding direction"*.
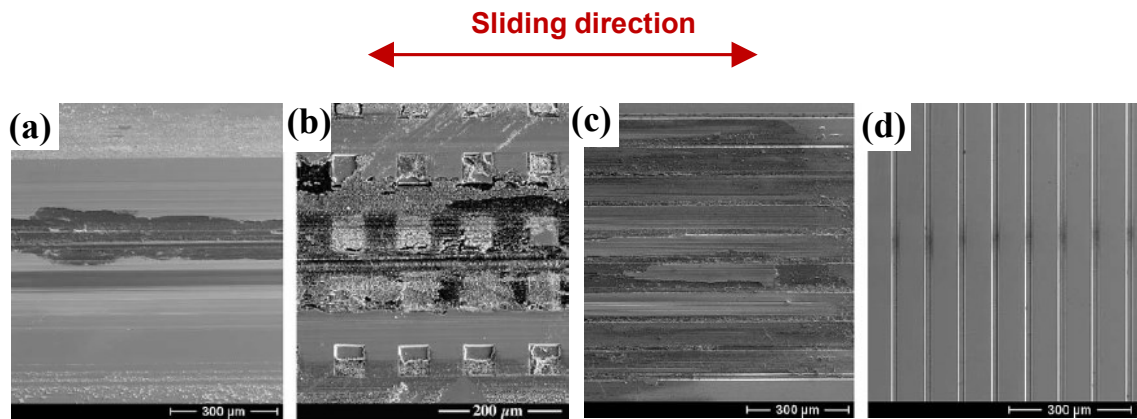
Sliding direction

FIGURE 2.25: SEM images showing influence of surface texture on wear under starved boundary lubrication: (a) non-textured; (b) square depressions; (c) grooves horizontal to the direction of sliding; (d) grooves normal to the direction of sliding [30].

The plain surface, as well as the textured surfaces with grooves parallel to the direction of sliding exhibited significant wear (figure 2.25(a-c)). This may either have been because such pockets are unable to provide sufficient lubricant to the contact zone, or because they are not able to collect all of the debris. Conversely, even after 200.000 cycles, no observable wear was recorded on the textured specimen comprising grooves normal to the sliding direction (figure 2.25(d)).

2.5   Cavitation

The phenomenon of cavitation is reviewed in this section since it is prevalent in piston-liner contacts and is believed to cause lubricant starvation. This is relevant to the current study since the effects of lubricant starvation can be alleviated by the presence of surface pockets (see Section 4.3.5).

Often encountered when a lubricant film separates two surfaces in relative motion, cavitation occurs due to the lubricant's inability to sustain sub-ambient pressures [70]. This leads to the fluid's transition from liquid form to gas-liquid mixture (gas pockets form inside the lubricant), potentially leading to changes in the anti-symmetric pressure distribution occurring in the vicinity of surface asperities.

Whereas the first to suggest the film rupture boundary condition was Gümbel in 1921 [71], the multiple cavities regions were first formulated mathematically by Swift (1931)

[72] and Stieber (1933) [73]. Since this first suggestion of film rupture, considerable efforts have been made to investigate cavitation behaviour in various types of bearings both numerically and experimentally. With regard to the theoretical investigation a sequence of papers by Jacobson and Floberg [74], Olsson [75] and Floberg [76,77] were published between 1957 and 1974, a series of papers referred to collectively as the JFO theory boundary conditions. This theory was the first attempt at defining the reformation boundary conditions necessary to express closed cavities and the related change in expected load-carrying capacity.

More recently, using a numerical model based on a modified Elrod's cavitation algorithm [68], Chong and Teodorescu [67] found that although cavitation decreases considerably in close proximity of the top dead centre (TDC) and bottom bead centre (BDC) (figure 2.26(a)), it does not disappear altogether (figure 2.26(b)).
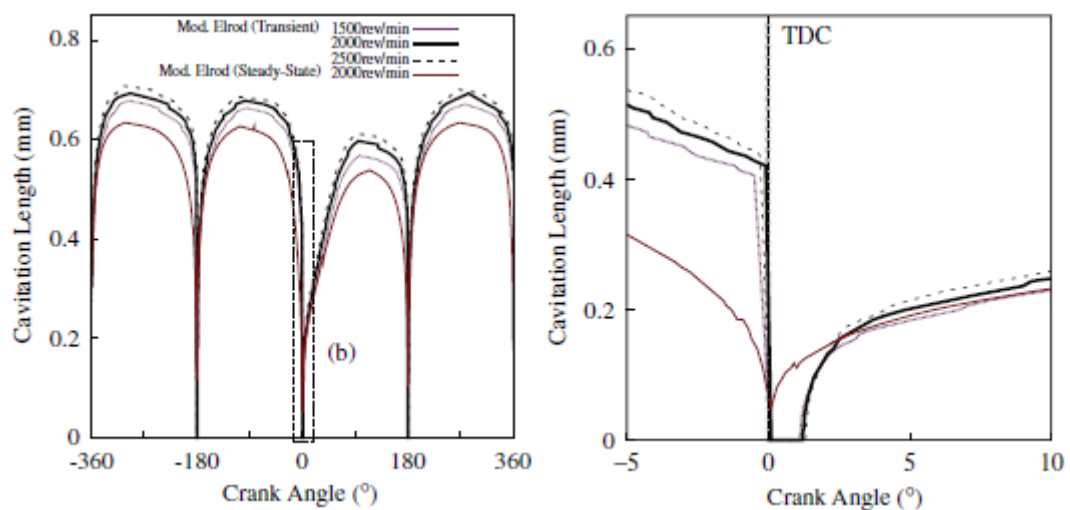
FIGURE 2.26: Variation of cavitation length versus crank angle. a) for a complete engine cycle; b) in the vicinity of TDC [67].

Chong and Teodorescu [67] also found that *"the 'pre-reversal' cavitation is sealed off by the lubricant and forms a bubble at the inlet. Although this is gradually absorbed by the lubricant film, before it fully vanishes, the inlet is starved"* (figure 2.27). This consequently leads to thinner lubricant films and higher friction forces. However, in a very recent study [78], after developing a 1D model to analyse the squeeze film lubrication effects in a reciprocating contact replicating the piston ring-cylinder liner

contact, Taylor concludes that *"around reversal positions, the whole of the piston ring is covered with oil, and there is no cavitation"*.
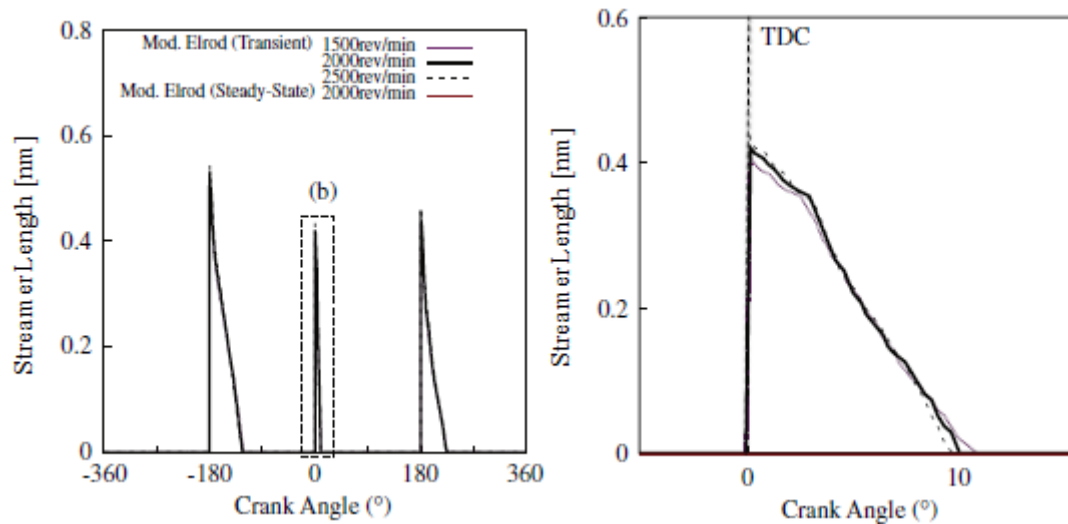
FIGURE 2.27: Variation in length of the inlet bubble formed by the pre-reversal cavitation versus crank angle. a) for a complete engine cycle; b) in the vicinity of TDC [67].

Various experimental contributions to the understanding of film rupture and pressure variation in the cavitated region were made by Dowson *et al.* [79,80] and Etsion and Ludwig [81], both groups relying on both photography techniques and pressure measurements. Arcoumanis *et al.* [82,83] have also qualitatively documented the cavitation pattern variation in reciprocating piston ring-cylinder liner assemblies while simultaneously measuring the lubricant film thickness in the reciprocating contact, either by employing a capacitance technique [82] or a laser induced fluorescence technique [83]. In the most recent study on this topic, Tang *et al.* [84] employed a digital holographic microscope to perform, for the first time, accurate measurements of the cavitation bubbles generated in a sliding linear contact replicating the ring-liner pairing. In this way, closed cavitation streamers were observed when a plane glass was driven by a bi-directional translation stage against a cylindrical lens.

Tests were performed using a gear oil at room temperature while keeping the load and the sliding speed constant. Phase maps captured with the help of a CCD camera were processed to reveal, for the first time, thickness measurements of the cavitation bubbles.
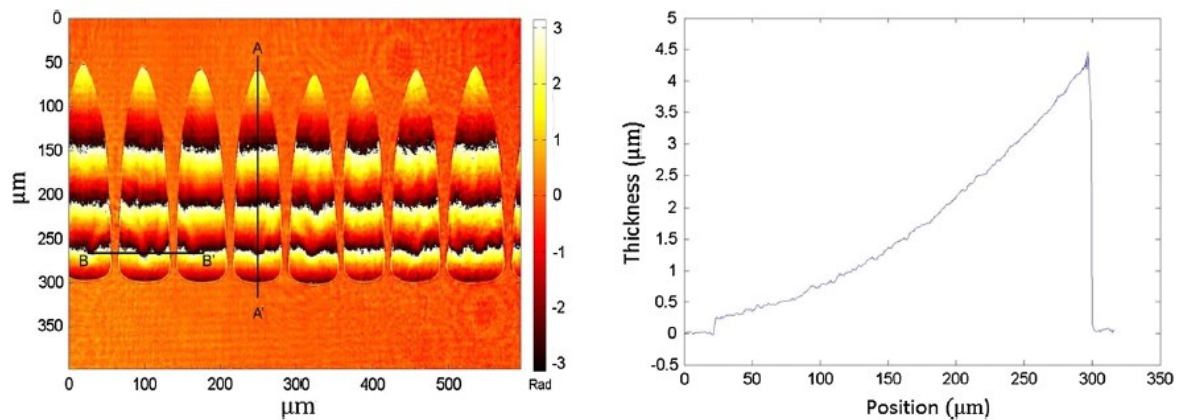
FIGURE 2.28: a) Phase map presenting the cavitation streamers; b) Thickness variation of one streamer along A-A' [84].

Figure 2.28 shows that close to the outlet of the contact the thickness of the cavitation streamers is around 0.3 μm, increasing to approximately 4.5 μm at the furthermost point from the contact outlet.

This literature review reveals a general lack of knowledge regarding the interaction between surface texture and cavitation pattern, with no experimental studies having been carried out to date. Moreover, despite its importance, cavitation itself is poorly understood, with recent studies unable to agree as to whether cavitation is even present at reversal [67,78]. Since at reversal point the gas-filled outlet becomes the inlet and therefore reduces the supply of oil causing starvation [67], cavitation in reciprocating contacts is a phenomenon of great interest where micro-texture can prove to have a beneficial effect.

One of the aims of the current research is to experimentally investigate the precise effects of surface texture on cavitation pattern and their impact on friction and wear behaviour.

2.6 Film thickness measurements in textured bearings

Film thickness is a key parameter necessary to understand in sliding contacts and its measurement is necessary to analyse and understand tribological behaviour. With the notable exception of Costa and Hutchings [13] previously mentioned, simultaneous measurement of film thickness and frictional response of textured interfaces in boundary

and mixed lubrication regimes has so far largely escaped attention, possibly due to the difficulty in measuring film thickness in a sliding contact under exceptionally thin film conditions. The techniques used to measure film thickness in textured contacts under different lubrication regimes are briefly reviewed below.

- **Optical interferometry** has been employed as a tool to measure lubricant film thickness since the 1960s [85]. In 1996, Cann et al. developed the Spacer Layer Imaging Method (SLIM) [86], which, combined with high-performance video cameras allowing automatic colorimetric imaging of interference images and film thickness mapping of mixed and boundary lubricated contacts below 150 nm. In 2001, Spikes et al. employed SLIM to study asperity film formation for the first time in detail [87]. Here, film thickness maps were obtained for ball specimens with transverse and longitudinal ridges as well as for arrays of small bumps. The optical interferometry technique was later applied to oil film thickness mapping of microtextured bearing surfaces, typically using ball-on-disc tribometers. Mourier et al. [46] who analysed the effects on lubricant film thickness of isolated micro-cavities passing through an elasto-hydrodynamic (EHD) point contact. This showed that, under pure rolling conditions, there are no significant changes in film thickness as the dimple passes through contact. However, under rolling-sliding conditions, two different effects of the micro-cavity passing through contact were observed: *i)* deep cavities (7 μm) tend to decrease the oil layer locally as the pocket enters the contact, while *ii)* shallow dimples (1.3 μm) exhibit the opposite effect, increasing the lubricant film thickness when the bearing operates under EHD regime.

  In a similar study employing pocketed steel balls on glass discs, Krupka et al. [88] also analysed the effect of texture depth on thin EHD lubrication films. Optical interferograms and cross-section profiles of the film thickness were plotted for various textured surfaces with micro-dents depths varying between 560 nm and 1900 nm. Similar to Mourier's observations, the authors concluded that deep micro-dents lead to a reduction in oil film thickness downstream the leading edge. Furthermore,

a slightly reduced pocket depth again led to a reduction in measured friction. The same group also used a thin film colorimetric interferometry technique to observe the behaviour of shallow micro-dents under mixed lubrication conditions [34]. Here, results showed a significant local increase in oil film thickness as shallow micro-dents (depths between 200 and 300 nm) passed through the mixed lubricated contacts as well as a qualitative reduction in wear when textured specimens were employed.

Another study involving oil film thickness measurement by optical interferometry worth mentioning is the work by Kaneta et al. [89]. They built a reciprocating test apparatus which enabled simultaneous measurements of friction force and lubricant film thickness in a line contact. Although the main purpose of the study was to observe the influence of cross sectional shape and stroke length of the rubber seal upon friction force and film thickness, a surface defect in the shape of a dent was also investigated. In this case, a local increase in film thickness was observed downstream from the dent.

These studies show that optical interferometry is a powerful technique to measure film thickness under mixed and boundary conditions. However, under the reciprocating conditions present in an automotive piston-liner type contact, the reliance on a semi-reflective coating on that transparent specimen is problematic due to issues of wear.

- **Laser Induced Fluorescence (LIF)** is a technique commonly used to determine lubricant film thickness in a tribological contact. Based on the photo-excitation of a fluorescent dye, this technique proves difficult to use in conjunction with textured surfaces, as additional light from the deeper pockets distorts film thickness measurements. However, LIF has proved reliable when measuring oil film thicknesses in non-textured lubricated contacts (*e.g.* [90,91]), and imaging the cavitation pattern encountered at the outlet of tribological contacts [92]. LIF has been applied to automotive contacts by Dearlove and Cheng [93] who simultaneously measured mid-

stroke lubricant film thickness and friction force in a single piston ring-floating liner non-textured assembly. Although the frictional behaviour was found consistent with Stribeck diagrams while running in both hydrodynamic and mixed regimes, the authors reported difficulties in calibrating the LIF signal.

- **Ultrasonic Sensing** has been developed over the last decade as a tool to measure film thickness in tribological contacts (*e.g.*[94,95]) and has recently been applied in IC engine cylinder liner applications by mounting elements to the cylinder wall [96,97]. Although this approach has the advantage of being non-invasive (it can be used on actual components without requiring a transparent window), it has disadvantages in terms of spatial resolution (which is typically larger than piston-liner contact area) and minimum measurable film thickness of around 50 nm (despite showing potential to distinguish asperity and liquid stiffness under mixed lubrication conditions [98]).

In conclusion, optical interferometry is an effective technique for measuring film thickness under boundary conditions; however its reliance on optical coatings usually limits its application to rolling conditions in order to preserve the semi-reflective coating. In order to overcome this limitation and study the effect of surface texture on film thickness in a piston-liner type contact, this study uses a modified version of the standard optical interferometry technique which will be later detailed in Chapters 3 and 6.

2.7 Application of surface texture

This review has reported numerous potential benefits of surface texture on bearings in automotive start stop situations. The obvious next step is to explore how texture can be applied in practice. By far the most commonly used method in the reviewed studies is laser surface texturing, primarily due to its ability to produce complex geometries. For instance, a laser with a femtosecond pulse can create features with depths and diameters as small as 200 and 20 nm respectively [14,46]. Laser texturing, however, poses two

main disadvantages. Firstly, material pile up may occur around the features, which needs to be removed by further machining. Secondly, laser texturing is a costly operation, which may not be an issue for research set-ups but could preclude its application in mass produced components. This is exemplified by the fact that laser texturing is currently only employed in high performance vehicles such as those used in Formula 1 or Le Mans races [99].

Alternative texturing methods have been employed in certain studies. For example, chemical etching was used by Lu *et al.* in [22], though this method may not be applicable when aiming at complex geometries. Laser interference texturing is a further alternative, which offers a speed advantage but limits the possible size of features that can be applied [60]. A third, recently introduced, technique to be applied to tribological contacts is micro-casting [58].

An in depth assessment of the relative cost of these methods is beyond the scope of this review. However a recent study by Hutchings [14] puts forward several alternatives and lower cost solutions available for large volume production of cheap components.

2.8   Summary of review

This chapter provided an overview of the current state of knowledge regarding the tribological benefits of surface textured bearings. Effects of surface texture on sliding friction, wear and lubricant replenishment, as well as various mechanisms of friction reduction, film thickness measurement techniques and the implications of cavitation were briefly reviewed. The aim has been to bring together research on surface texture, leading to the following conclusions:

- In the majority of cases, texture proves effective in reducing friction in the mixed and boundary regime, whereas in the hydrodynamic regime fewer improvements are shown. A notable exception is the recent work by Scaraggi and co-workers [25], who shows a considerable reduction in friction in the hydrodynamic regime. The specific contact conditions may be worth further investigation to confirm the

possibility of a particular texture configuration resulting in friction reduction under full film conditions.

- Few studies appear to have given in-depth consideration of the effect of different texture configurations on friction; the main exceptions being Braun *et al.* [10], who tried to optimise dimple diameter. However, these authors concluded that texture geometry needs to be optimised for the specific conditions being tested and that an attempt to draw generic design rule for texture at this stage would prove futile; the most generic conclusion drawn was that optimum dimple diameter decreases with increasing viscosity.

- Numerous friction measurements have been made on textured bearings. However, very few studies of reciprocating textured bearings employ film thickness measurements, mainly due to the difficulty in performing such measurements under mixed and boundary conditions. As a result, there remain uncertainties regarding the mechanisms by which surface pockets affect friction.

- There is general agreement that textured features act as *"debris traps"* under boundary lubricating conditions and in doing so greatly reduce wear. The ways by which surface texture reduces friction is less clear, with a number of mechanisms proposed, but little experimental evidence to support them.

- Although only one study has been carried out to date in this regard, it was demonstrated that static friction can be reduced by a factor of 2, provided an optimum dimple diameter is selected (whereas detrimental effects of a similar magnitude result if incorrect dimple depths are chosen).

- Cavitation in piston-liner contacts has received considerable attention, however there remains confusion in this area. For instance, recent studies have been unable to agree as to whether cavitation bubbles exist at reversal point; moreover, the impact that surface texture has on cavitation at reversal has not been investigated prior to the current research.

- The majority of existing studies used lasers to produce textured features, however, alternative methods were employed in a limited number of cases, namely laser interference metallurgy, microcasting, machining and chemical etching.

This all shows there is still a lack of knowledge in the area of microtextured bearings with important issues such as the impact of surface texture on film thickness and cavitation, the impact of feature shape and geometric parameters, as well as the influence of texture at reversal still insufficiently understood. Furthermore and perhaps most importantly, the mechanisms by which surface texture acts to reduce the frictional response are still unknown, none of the theoretically suggested mechanisms being yet supported by experimental evidence. The current research addresses these aforementioned shortcomings to a large extent, by designing, making and testing apparatus to measure, in situ and simultaneously, friction force and film thickness as well as cavitation pattern in textured and non-textured reciprocating contacts.

Chapter 3

EXPERIMENTAL DEVELOPMENT AND METHODOLOGY

3.1 Introduction

This research project focuses on the reciprocating contact between a top piston ring and the counterpart cylinder liner in an IC engine. An optical reciprocating test rig was designed and built to accurately replicate the interaction between these two elements inside the engine and study the various effects that surface texture has on lubricant film thickness, friction force and cavitation pattern. A key objective was to perform all measurements in situ and simultaneously, while accurately controlling all operating conditions at all times.
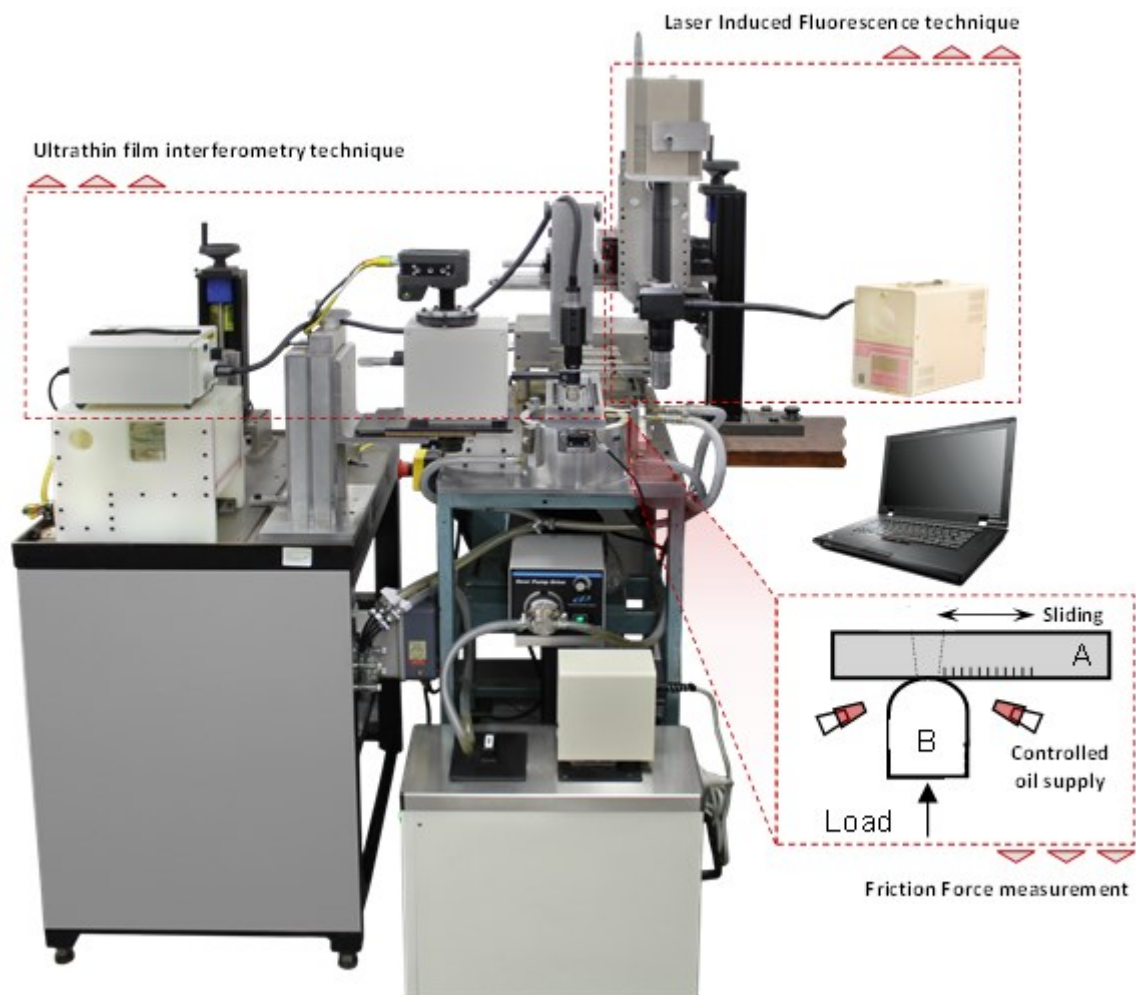
FIGURE 3.1: In-house developed reciprocating test rig.

The test rig used in the project is shown in figure 3.1. This was built using a motor and drive system from a previous project, started by Dr Aswad Manzoor. Various aspects of the rig development which were carried out to ensure a consistent and repeatable operation will be described in detail in this Chapter. Furthermore, new additional systems such as the film thickness interferometry technique, and the triggering and lubrication control systems were designed and installed on the rig in order to ensure the accomplishment of the initial objectives.

As opposed to standard ball-on-disc tribometers, there is no knowledge of any commercially available test rig capable of simultaneously measuring friction, film thickness and cavitation in a transient linear contact. As argued throughout this chapter, such research set-ups are difficult to achieve, mainly because various measurement techniques must be interconnected and integrated in the same assembly. A certain degree of emphasis must be placed on the measurement of nanometre scale film thicknesses which proved to be a significant challenge in transient linear contacts.

The most important limitation of the current set-up is the use of a single ring, whereas pistons in IC engines commonly have three or in some cases more rings. Moreover, the piston skirt comes in direct contact with the liner in the real scenario [100]. In other respects however, the rig accurately replicates piston liner contact conditions.

The following sections provide a detailed explanation of the test rig assembly and the main systems and measurement techniques developed and attached on the initial structure, as well as their controllability and calibration. The test specimens are introduced and the experimental procedure detailed. Finally, the chapter concludes with evidence of repeatability over time for both friction force and film thickness tests, under different lubrication conditions.

3.2   Reciprocating test rig

3.2.1   Rig description

Figure 3.1 shows the three main areas of interest on the rig: the Friction Analysis System, the Laser Induced Fluorescence (L.I.F.) System and the Optical Interferometry System. These measurement techniques together with the mechanical part of the rig are described below.

The Friction Analysis System is used to achieve measurements of friction between the contacting surfaces – a convex AISI 52100 steel pad with a width of 2 mm and the counterpart fused silica specimen – by employing a low capacity isometric load cell, in direct contact with a special holder mechanism. This holder mechanism was designed to allow for the measurement of friction force on the one hand, and the self-alignment of the steel test specimen on the other, as described in detail below.

The silica plate, simulating the cylinder liner of an IC engine, reciprocates relative to the steel specimen, via a cam mechanism responsible for controlling amplitude and sinusoidal velocity profile, thus accurately replicating the piston's motion. Two steel shims allow for the displacement of the upper part of the specimen holder away from or towards the load cell. As the specimen holder deflects due to friction forces in the reciprocating contact, a voltage differential is recorded. This voltage output, proportional with the specimen deflection, is fed into the data acquisition system (DAQ).

The reciprocal motion of the fused silica pad along two linear bearings is ensured by an electric motor which drives the adjustable stroke cam mechanism. A continuous and smooth sliding movement of the silica plate at both ends of the stroke is ensured by employing two centrifugal governors. As a result of governor inertia, the silica plate holder is forced to continue its reciprocating motion every time one of the dead centres is reached, changing its direction. The main structural features of the reciprocating test apparatus are shown in figure 3.2.
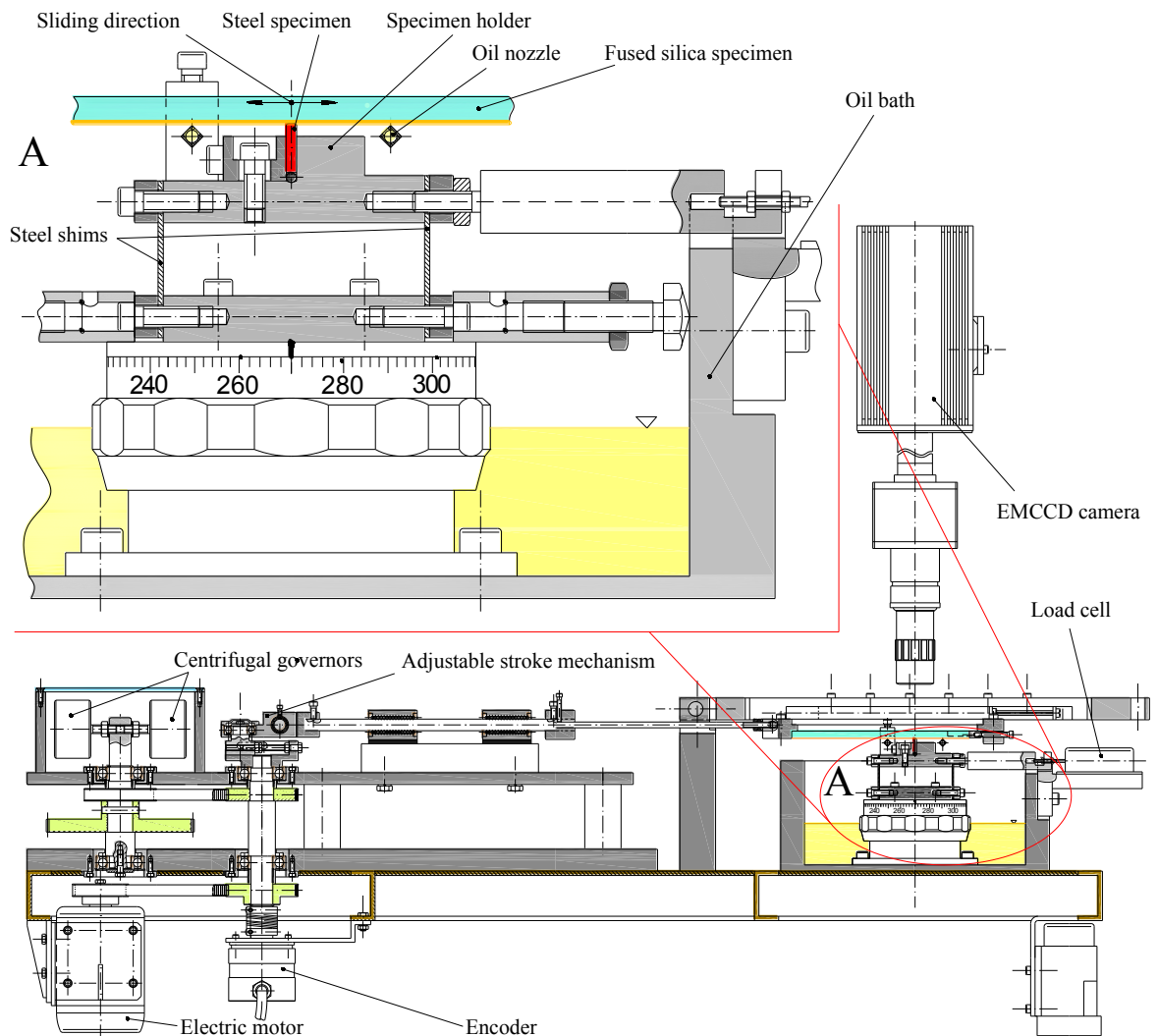
FIGURE 3.2: Schematic representation of the reciprocating test rig.

The reciprocating speed is measured by a 9 bit rotary position encoder, fixed securely to the bottom of the cam mechanisms' shaft and used to determine both the angular position and velocity of the shaft. An NI 6343 X Series data acquisition device (figure 3.3) transmits the signal from the encoder to the computer. This model was selected for two main reasons: *i)* high sampling rate and resolution; *ii)* 23 Digital Input/Output lines available, a feature necessary to integrate the new triggering system.

FIGURE 3.3: National Instruments 6343 X Series data acquisition device.

The software package LABVIEW is used to import and translate the DAQ output for further analysis in an integrated programme developed specifically for this reciprocating rig with the help of Dr Mark Fowell and Dr Simon Medina. This custom code allows for instant visualisation of friction force and rig speed.

One important feature of the reciprocating rig is the low capacity (450 grams) isometric load cell, which significantly increases accuracy of friction force monitoring during tests. The decision for this update was made taking into consideration that future reciprocating tests will be undertaken at very low speeds (1 to 5 Hz), moving the experiment away from dynamic characteristics to resemble a quasi-static force measurements application. Due to this limitation of speed, it was not recommended to make assessments using a piezoelectric force sensor, as a strain gauge type load cell would be best suited. One consequence of the limitation created by low frequency was that, despite being under constant applied load, the piezoelectric sensor had the tendency to continuously return to its nominal position (since the measurement signal generated by this type of sensor decays over time), thus diminishing the accuracy of measurements.

In order to replace the piezoelectric sensor with the new low capacity load cell, an adjustable platform with a corresponding pushing rod was designed. Figure 3.4 shows the friction system conversion from the piezoelectric sensor design (a) to the new isometric load cell assembly (b and c).
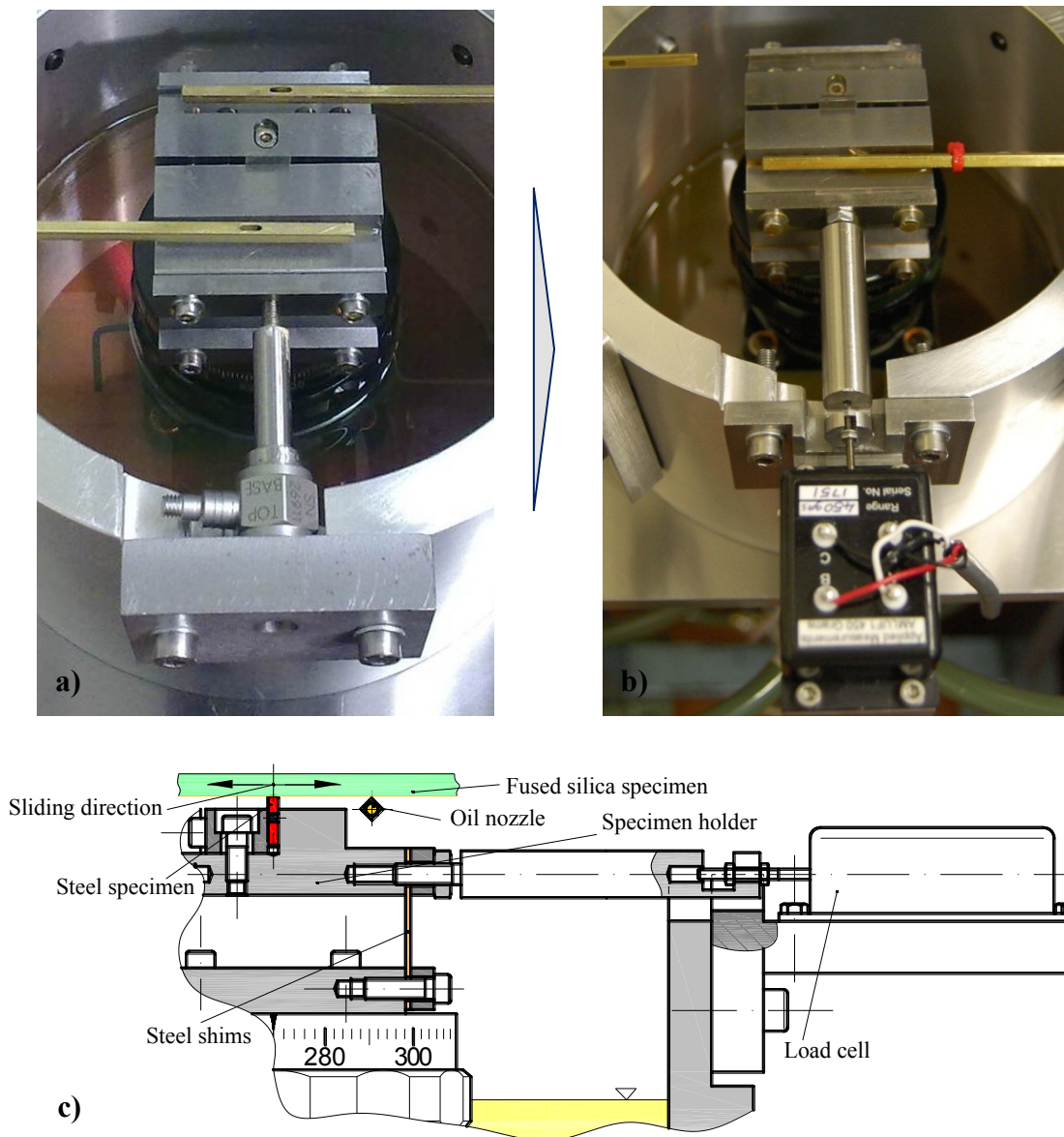
FIGURE 3.4: Fiction measurement system redesign from the piezoelectric sensor assembly (a) to the low capacity load cell assembly (b and c).

A second important upgrade to the friction measurement system was the replacement of the initially acquired height-adjustable rotary stage (figure 3.5(a)), which was found after the initial tests to be the source of small errors due to the clearance present in the large thread allowing the height adjustment. To solve this problem, the adjustable stage was replaced with a specially designed block of steel (figure 3.5(b)).
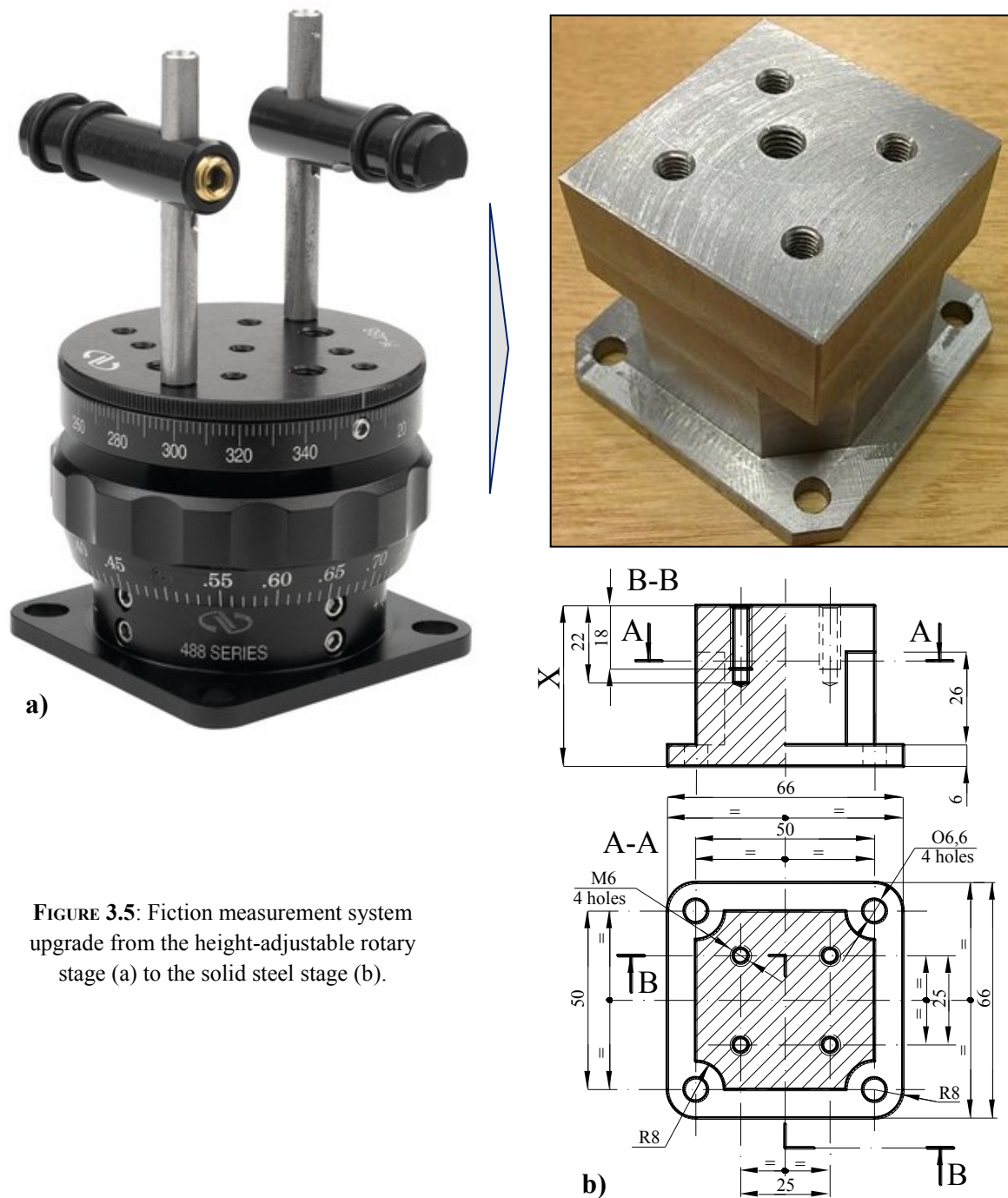
FIGURE 3.5: Fiction measurement system upgrade from the height-adjustable rotary stage (a) to the solid steel stage (b).

Since the new solid stage was no longer ensuring a perfect alignment of the two specimens in the normal direction, the self-adjusting mechanism was also modified. Changes to the way the steel pad is locked into its holder were implemented, with the newly designed mechanism (figure 3.6(a)) allowing for both the adjustment on the normal direction (of the steel pad against the counterpart fused silica), and also for the steel pad to follow the silica pad along the entire stroke length, consequently avoiding incorrect

positioning between the two specimens (as schematically illustrated in figure 3.6(c)). The accurate construction of the small pin and hole were achieved by employing Electrical Discharge Machining (EDM) technique.
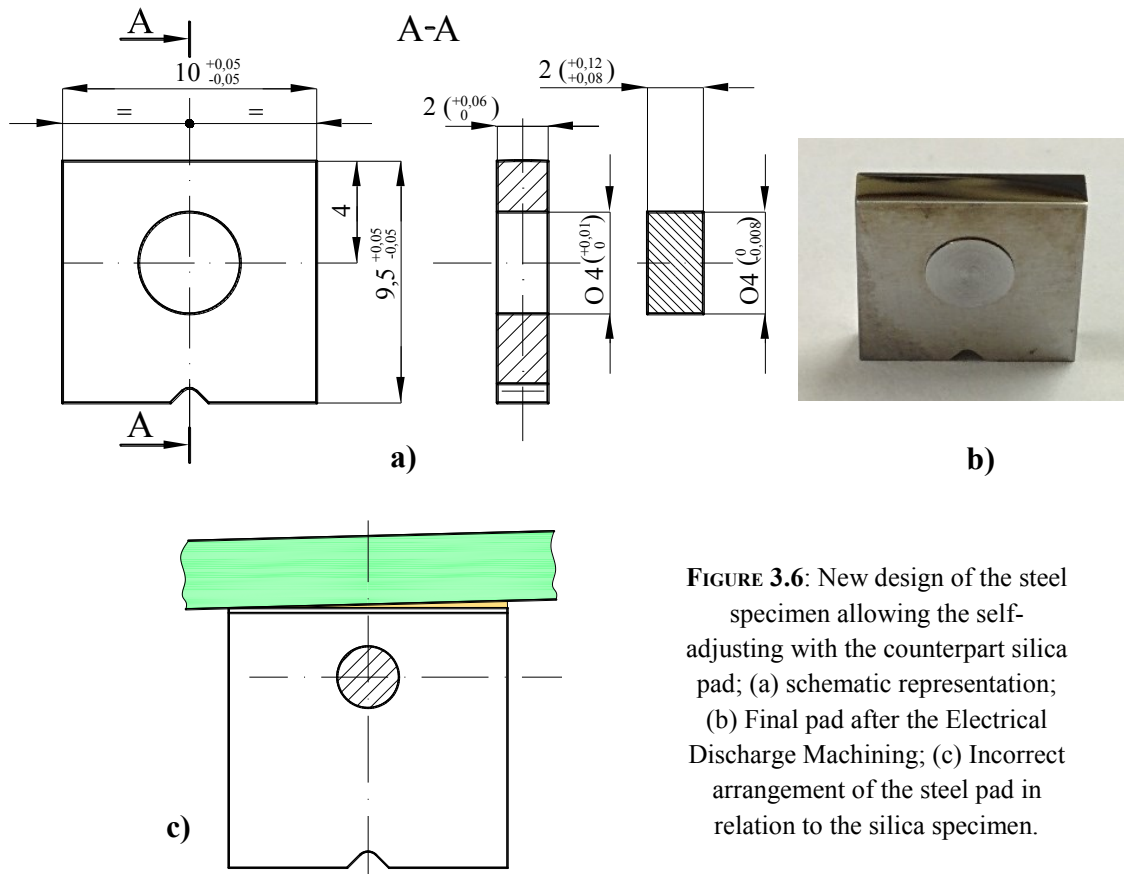
FIGURE 3.6: New design of the steel specimen allowing the self-adjusting with the counterpart silica pad; (a) schematic representation; (b) Final pad after the Electrical Discharge Machining; (c) Incorrect arrangement of the steel pad in relation to the silica specimen.

The operating normal load can be varied between 10 N and 160 N using multiple dead weights attached to the silica pad specimen holder.

3.2.2   Peripheral lubrication – Oil supply

The oil is supplied directly to each side of the contact area by two nozzles, attached to the oil bath. This arrangement prevents inlet starvation, supplying a sufficient rate of SAE 40 fully formulated oil to the reciprocating contact. Initial experimental tests revealed that the most critical operating parameter is the oil temperature. Even a slight change in the oil temperature, and consequently viscosity, can dramatically alter the measured friction values. It is for this reason that the oil supply system was carefully redesigned to accurately control the oil temperature over a broad range. The initial temperature control

system, comprising two cartridge heaters installed in their designed locations inside the oil bath (figure 3.7(a)) and controlled using a Fuji PXR459 temperature micro-controller (figure 3.7(b)) was abandoned due to the inability to control the oil temperature and consequently its viscosity. More precisely, the oil bath, manufactured from aluminium, proved very difficult to stabilize oil temperature over time, which created significant differences in frictional response during initial tests. Furthermore, the oil bath, always in direct contact with the isometric load cell, would expand rapidly when heated (or contract when the cartridge heaters shut off), placing additional tension or exerting compression forces onto the load cell, consequently at times even driving the load cell signal out of range. Figure 3.7 (c) shows the initial oil temperature control set-up.
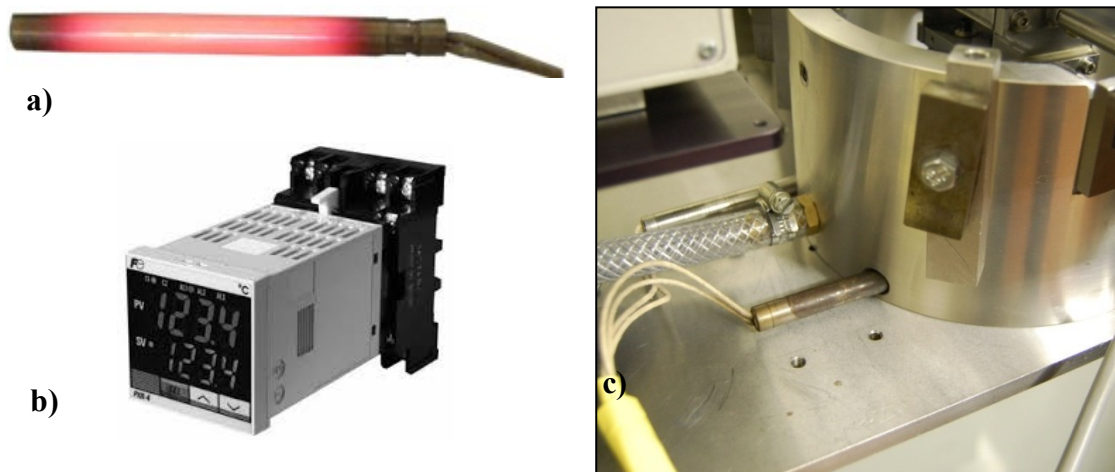
FIGURE 3.7: Initial oil temperature control set-up: a) cartridge heater; b) Fuji PXR459 temperature micro-controller; c) cartridge heaters installation inside oil bath.

The new oil system designed to replace the initial set-up is presented in figure 3.8. More precisely, a Thermo Scientific SC150 immersion circulator was installed in the reciprocating rig system to precisely control the oil temperature between +10°C and +150°C with a temperature stability of 0.2°C. A Cole-Parmer gear pump is used to transport oil from the immersion circulator to the reciprocating contact while at the same time controlling the oil flow rate. Finally, an additional peristaltic pump is employed to return the oil from the rig's oil bath to the immersion circulator. The new oil temperature controlling set-up allows for the assessment of textured and non-textured bearing configurations to be carried out under all lubrication regimes: boundary, mixed and full film. A handheld Fluke 62 MAX infrared thermometer was used as a backup means of

monitoring the temperature inside the heating circulator bath as well as the temperature of the lubricant in the vicinity of the contact.
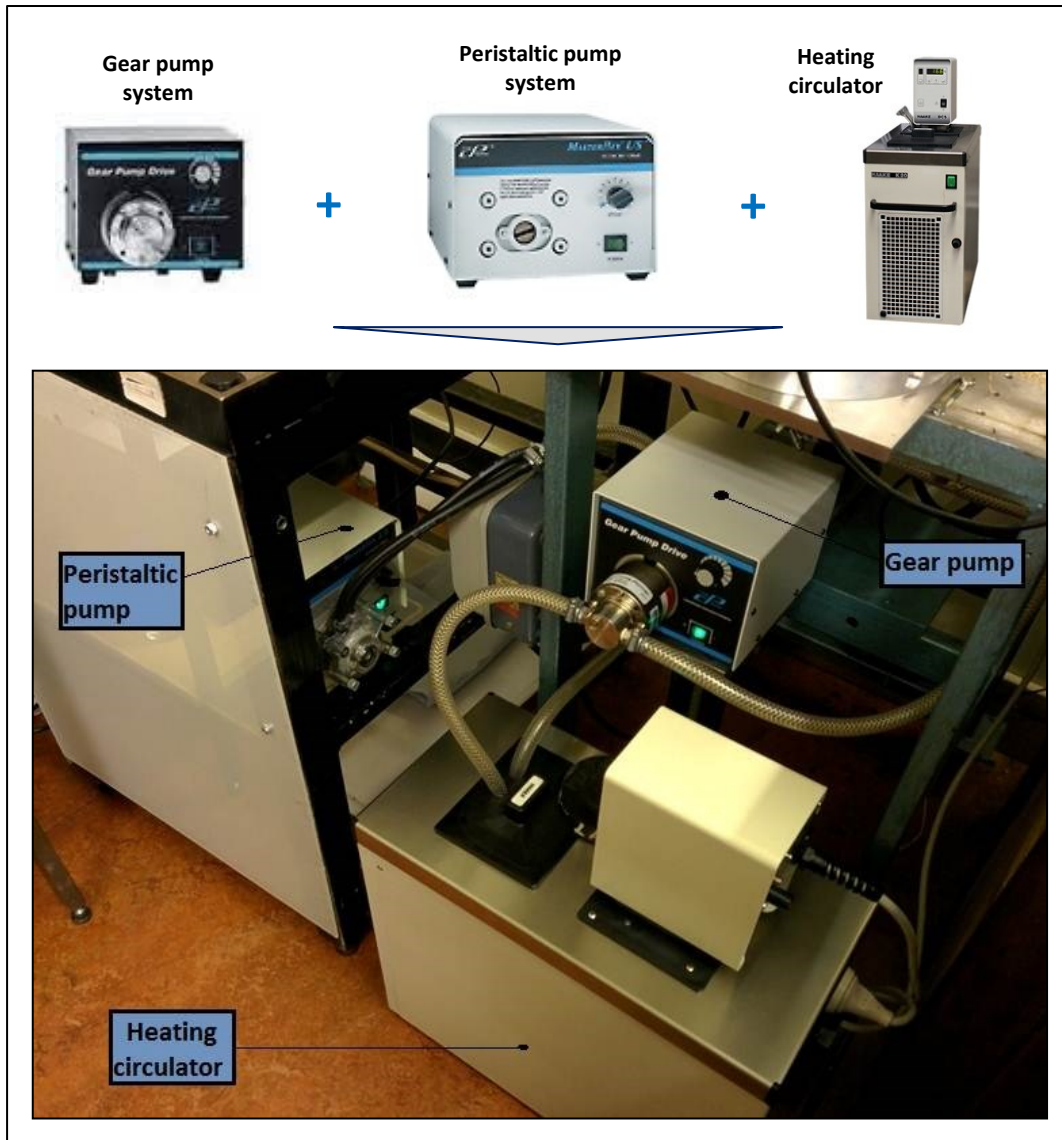
FIGURE **3.8**: New oil temperature control system comprising heating circulator, gear pump and peristaltic pump.

3.2.3   Triggering system

Film thickness and frictional response for individual textured and non-textured specimens are accurately identified at any location along the stroke of the silica pad using a 9 bit trigger designed and manufactured in-house (figure 3.9). Moreover, the trigger system allows for the imaging of texture features moving through the contact as well as a precise evaluation of cavitation in the vicinity of end strokes. This electronic circuit enables both

the high-speed camera used for interferometry measurements, and the EMCCD camera used for cavitation visualisation using fluorescence, to be triggered with precision equal to 0.7 degrees of crankshaft revolution (corresponding to a distance of 111.2 µm along the stroke).
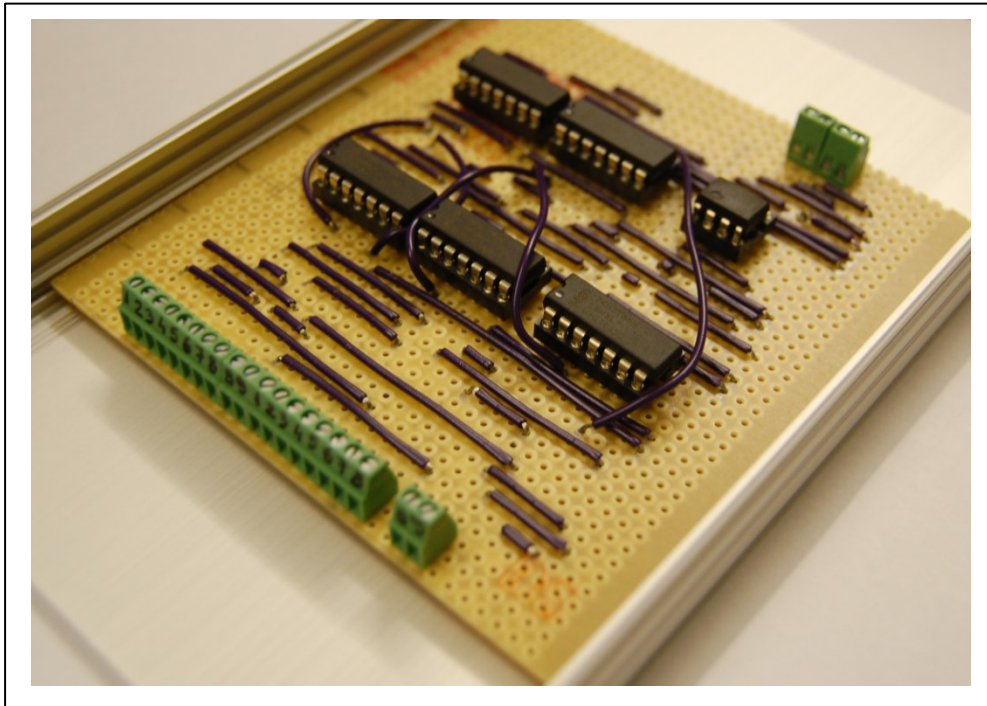
FIGURE 3.9: Nine bit trigger system designed and manufactured at Imperial College.

Visual proof of the accuracy of the trigger system is shown in figure 3.10, where four captured images are at the same triggering point over four consecutive reciprocating strokes of the silica plate. Evident in the top left corner of the figure are two small cavitation streamers, captured each time in the exact same location.
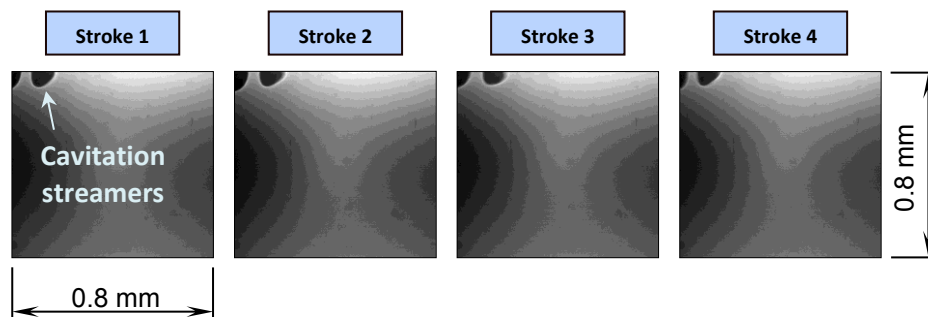
FIGURE 3.10: Four different cavitation images captured at the same triggering point over four different strokes.

76

Subsequent to the trigger manufacturing and the new DAQ acquisition, the electrical diagram of the reciprocating rig was redesigned and the electrical links/connections between the different components were reconstructed. A detailed image of the electrical connections made for the installation of the new trigger and DAQ into the rig system is presented in figure 3.11.
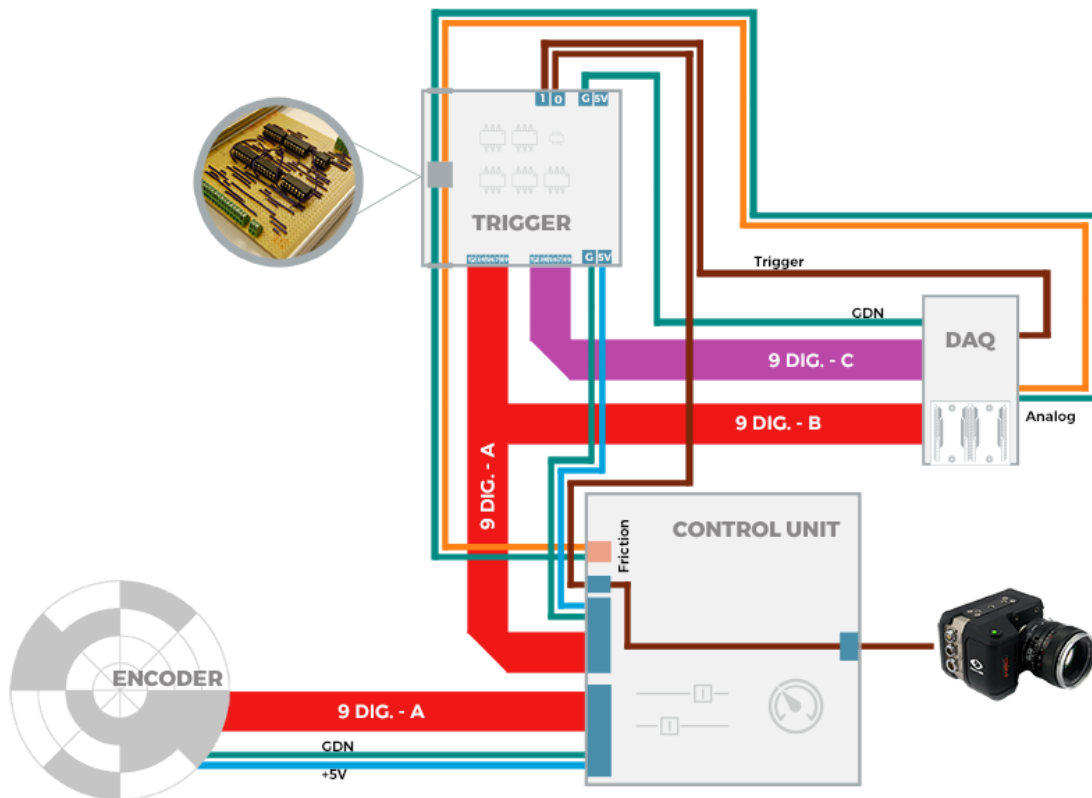
FIGURE 3.11: Schematic representation of the rig's electrical diagram – the interconnections of the 9 bit trigger system, rotary encoder and data acquisitions system.

3.3 Film thickness measurements – Ultrathin film interferometry technique

A key requirement in this study was the measurement of oil film thickness in addition to friction force, in both full film and mixed lubrication regimes. To achieve this, a variation of the optical ultrathin-film interferometry technique was devised allowing sub 50 nm film thickness to be monitored, without using a silicon spacer layer. Optical interferometry was chosen due to its ability to accurately quantify nanometre scale film thicknesses. This technique typically involves reflecting light off the top and bottom of an

oil film and calculating its thickness based on the wavelength at which constructive or destructive interference occurs and fringe order (*i.e.* the number of complete wavelengths between the two rays).

The method to achieve this is outlined schematically in figure 3.12 and involves positioning an optical microscope above the stationary ring specimen and focussing through the transparent reciprocating pad. The lower surface of the pad specimen is coated with a 570 nm semi-reflective chromium coating so that light from the microscope undergoes a division of amplitude when it is incident to the oil film. A spectrometer slit captures the interfered reflected beam and disperses it by wavelength before it is recorded by a high speed video camera.
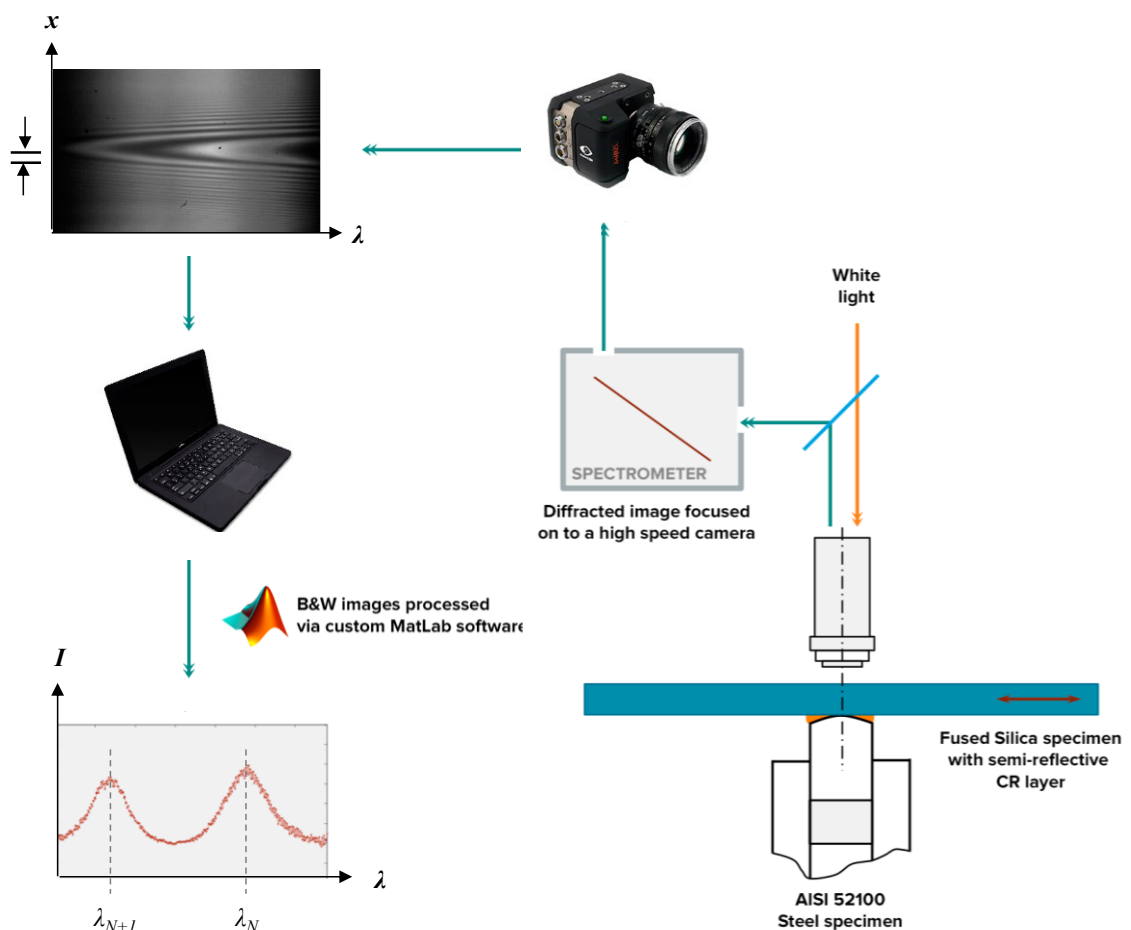
FIGURE 3.12: Schematic diagram of the interferometry set-up.

In figure 3.12, an example output image from the spectrometer is shown in the top left corner, where wavelength, λ, is on the *horizontal* axis and distance along the contact is on the *vertical* axis. Here, lighter and darker regions represent constructive and destructive interference respectively. As detailed in Appendix C, this image is then processed in Matlab to remove erroneous spectral variations (that arise from the optical system), before being averaged over its central region to give the variation in intensity versus wavelength, shown in the bottom left of the figure. The peaks in this graph result from constructive interference of light at specific wavelengths. Chapter 6 explains in detail the modifications to the standard ultra-thin film interferometry technique that are necessary for the type of contact being studied.

3.4 Cavitation visualisation – Laser Induced Fluorescence technique

A technique based on the photo-excitation of a fluorescent dye, Laser Induced Fluorescence (LIF), is employed in this research for the visualisation of cavitation pattern along the reciprocating stroke. The high sensitivity optical imaging system set-up comprises three main components, illustrated in figure 3.13:

- *Light Source* – Ultraviolet Spot Light Source Hamamatsu LightningCure L8222, with electronically controllable shutter and 150 watt Mercury-Xenon arc lamp;

- *Microscope* – composed from a main tube, a beam splitter and a 10x magnification Mitutoyo objective;

- *Camera* – CCD QuantEM 512SC from Photometrics, with Electron Multiplying Gain, a crucial feature in our low light setup.
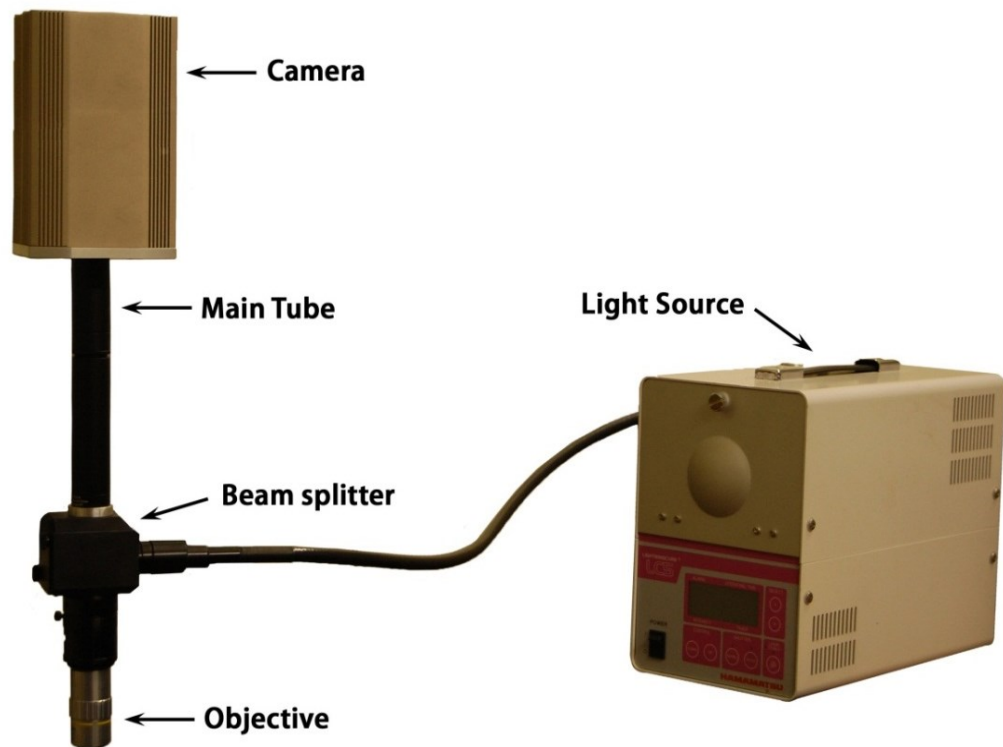
FIGURE 3.13: Laser Induced Fluorescence (L.I.F.) microscope system.

Light Source

Financial considerations were the primary reason behind the selection of Mercury-Xenon bulbs as the light source employed in the current research among sufficiently adequate alternatives to Laser. Despite the generally accepted knowledge that a laser light source should be used in L.I.F. systems, more common lamp/bulb alternatives such as ultraviolet (U.V.) or blue light are often used in practice. While lasers are indeed preferred due to the high intensity of a precisely known wavelength, components such as mercury-xenon or black light-blue bulbs, as well as U.V. lamps, emit the necessary wavelength spectrum required for a multitude of naturally fluorescent hydrocarbon oils and are associated with significantly lower costs.

Microscope system

A beam splitter is situated between the camera, light source and microscope objective, connected to these components through pieces of tubing. The splitter operates by

reflecting light waves from the light source via a dichroic mirror (a piece of glass made of semi-transparent material and positioned at a 45 degree angle) onto the specimen and filtering the emitted fluorescent light which reflects upwards into the camera. Light from the light source enters the beam splitter through an exciter (band pass) filter which only allows the transition of wavelengths within a specified value range. The fluorescent light emitted by the excited specimen passes through a second filter, the emission (long pass) filter, which stops wavelengths below a specified value from passing through, before entering the camera. The minimum wavelength for the emission filter is selected to ensure that only the light-induced fluorescence from the dye/lubricant mixture is ultimately captured by the camera, whereas all light from the light source is prevented from travelling upwards. The components which make up the beam splitter are presented in Figure 3.14:
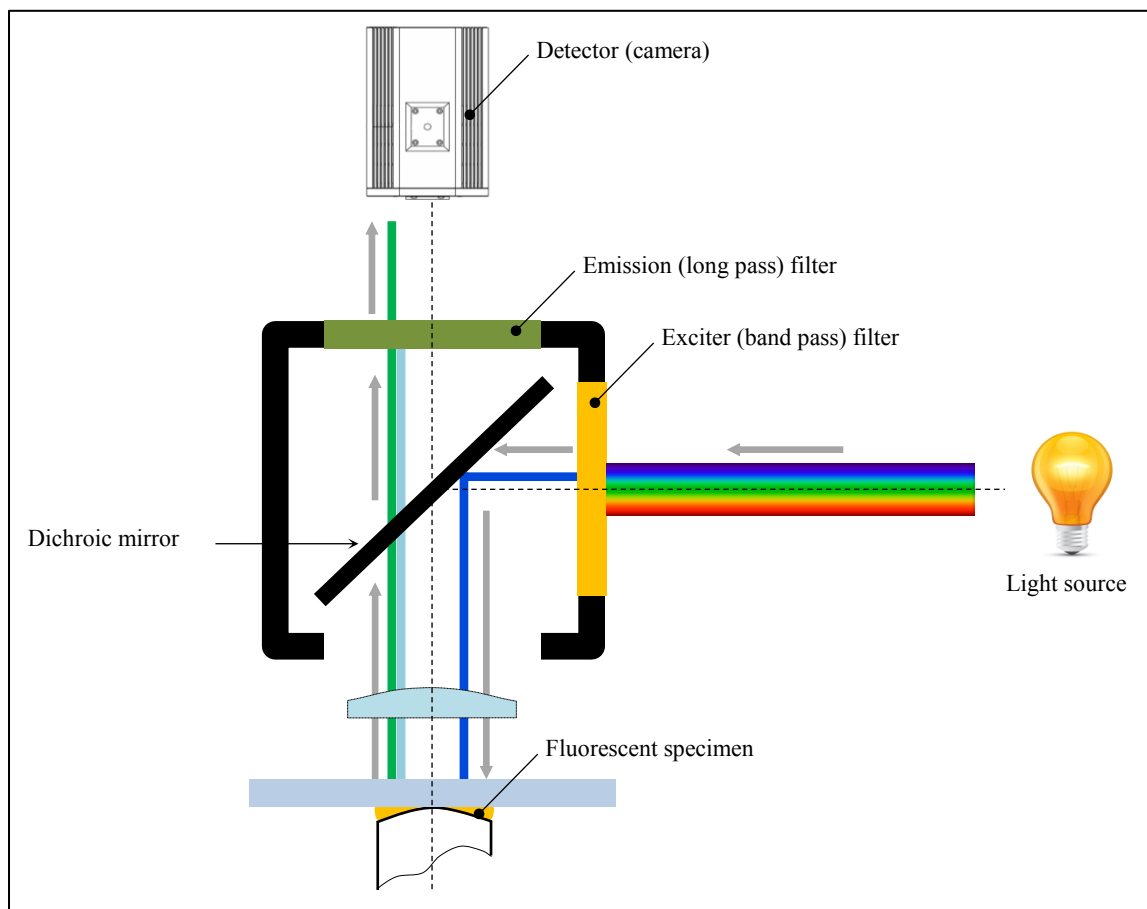
FIGURE 3.14: Schematic representation of the fluorescent cube and the light path inside the microscope.

Camera

Ensuring the camera adequately meets each and every scientific criterion specified below (especially as these are often interdependent) was a crucial prerequisite for successfully performing tests:

- Cooling – the camera is equipped with cooler sensors, recommended for high sensitivity applications such as L.I.F. to ensure a lower level of noise.
- EM gain – a particular type of CCD amplifies the charge stored before "read-out" stage, offering the advantage of signal amplification whilst minimising noise. Similarly to the cooling requirement, this is crucial in a low light setup.
- Dynamic range – the camera must be able to detect both low and high light intensities simultaneously at any moment in time.
- Sensitivity – the sensor on the camera must be able to detect a minimum light intensity even at high frame rates.

Cameras which meet the criteria above and are particularly well suited for high sensitivity applications by employing cutting-edge CCD technology are generally expensive. After careful consideration, the QuantEM:512SC camera from Photometrics was chosen for this study, as it *"employs an advanced CCD technology called 'impact ionization' to achieve charge multiplication gain above the read noise. As a result, the camera offers unparalleled sensitivity even at high frame rates. QuantEM cameras are most suited for high speed and/or low-light level imaging applications such as single molecule fluorescence, ion imaging, and adaptive optics. With the traditional readout amplifier, the QuantEM can also be used for standard fluorescence and imaging applications requiring higher dynamic range."*

Fluorescent Dye

Due to the high quantity of dye required to blend with 7 litres of oil, a commercially available oil tracer was chosen, the *"Dye-Lite"*. This entails two distinct ingredients, Perylene and Napthalimide, each with different absorption characteristics which are easily

visualised with any UV or Blue light system. Dye-Lite was furthermore deemed suitable after considering the potential interference with the working properties of the host oil such as its viscosity.

The combined absorption profile of Dye-Lite is shown in figure 3.15.
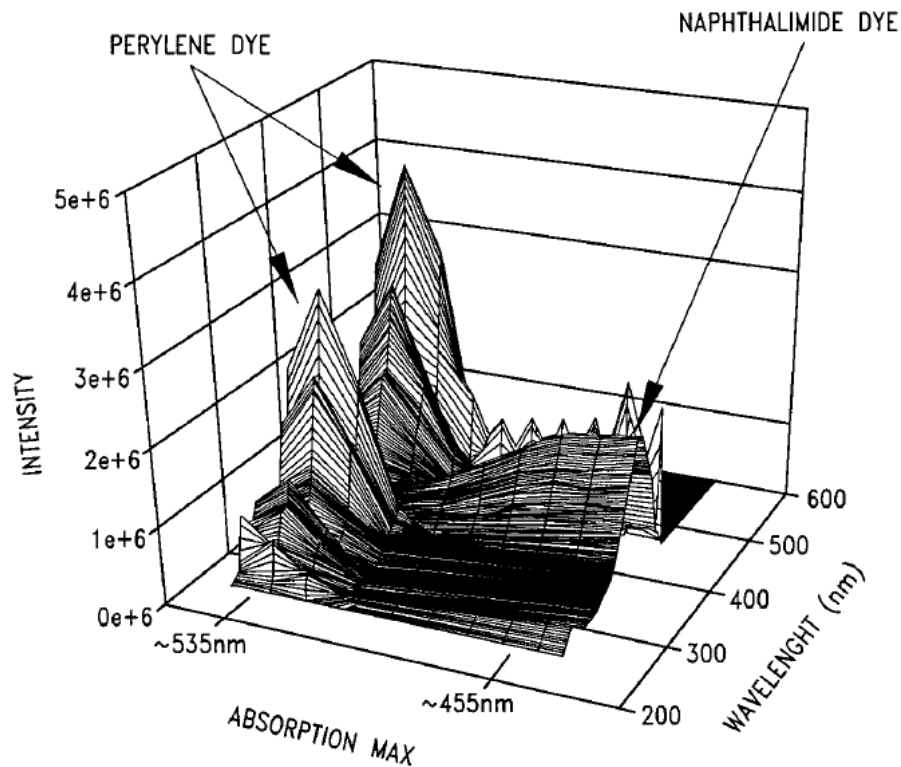
FIGURE 3.15: The absorption spectrum for 'Dye-Lite' [61].

The L.I.F. technique was initially considered as a secondary film thickness assessment to complement measurements achieved using optical interferometry, in addition to its usage in cavitation measurements. However, initial tests revealed inaccurate measurements of film thickness, which were subsequently explained by a motion blur left after the pocket passed through the contact. This motion blur distorts film thickness measurements for certain textured patterns, in certain crankshaft positions (*i.e.* when a pocket is too close to the contact at the time when the fluorescent image is captured).

Some of the images exemplifying the aberrations in film thickness values captured while employing L.I.F. technique to measure oil film thickness are presented in figure 3.16.
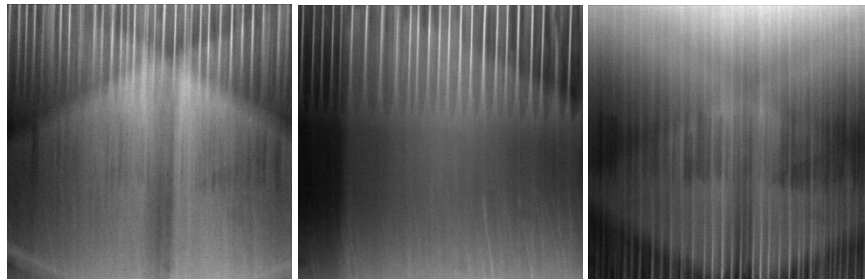
FIGURE 3.16: Measurement aberrations (blurring) obtained while employing Laser Induced Fluorescence technique to determine lubricant film thickness.

It was therefore decided that throughout this study the Laser Induced Fluorescence technique will only be employed to visualise and evaluate the cavitation pattern. In order to allow for secondary film thickness measurement using the fluorescence technique in future work, the texture of the silica specimens will be adapted to leave a non-textured 1 mm length corridor/strip along the centre of the specimen, where images can be taken (see section 3.7 for details).

3.5 System calibration

3.5.1 Friction calibration

To calibrate the friction sensor, a series of known masses are used to displace the steel pad holder in both tangential directions (tension/compression) in order to accurately define the relationship between distance travelled by the pad holder and equivalent voltage. Two steel shims allow the upper part of the steel specimen holder to move away from (tension) or towards (compression) the load cell, always in direct contact with the specimen holder through a connecting rod. Incremental masses (from 50 to 400 g) are hung from a fine cotton thread, connected to a calibration steel pad via a simple loop. As shown in figure 3.17, the cotton thread is directed outside the oil bath using one low friction pulley for compression (figure 3.17(a)) and two low friction pulleys rigidly attached to the oil bath for tension (figure 3.17(b)).
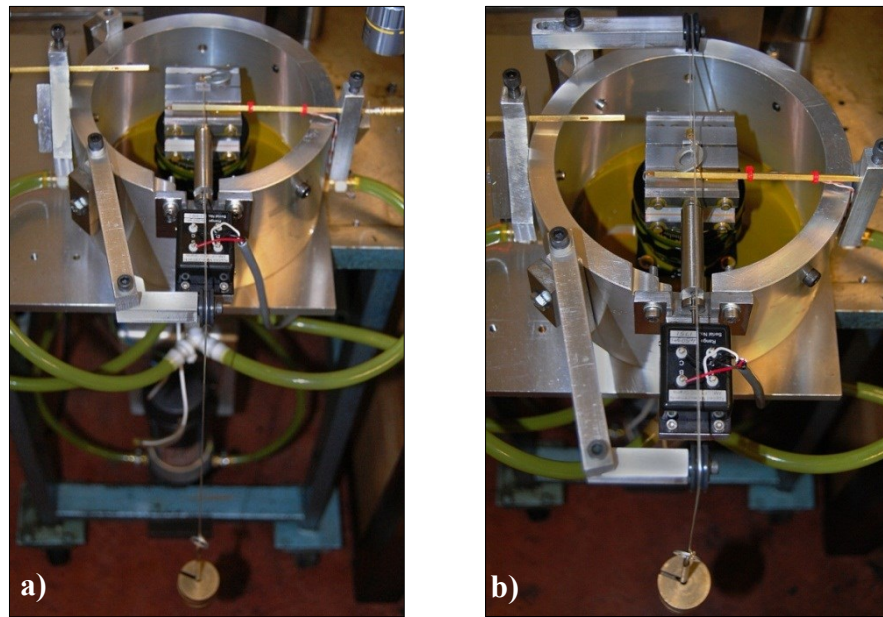
FIGURE 3.17: Removable friction calibration jig assembly for compression (a) and tension (b).

Voltages are recorded for the entire cycle, loading up and down for both tension and compression. The average values are used to determine the equation relating voltage output to frictional force. During testing, this equation is applied to determine of frictional response for any given voltage. Typical friction calibration relationships are presented in figure 3.18 for both tension and compression for a thickness of the steel shims of 0.8 mm. This particular thickness was selected to enable the measurement of frictional response for all test conditions and all lubrication regimes, while staying within the ±10 V range of the load cell.
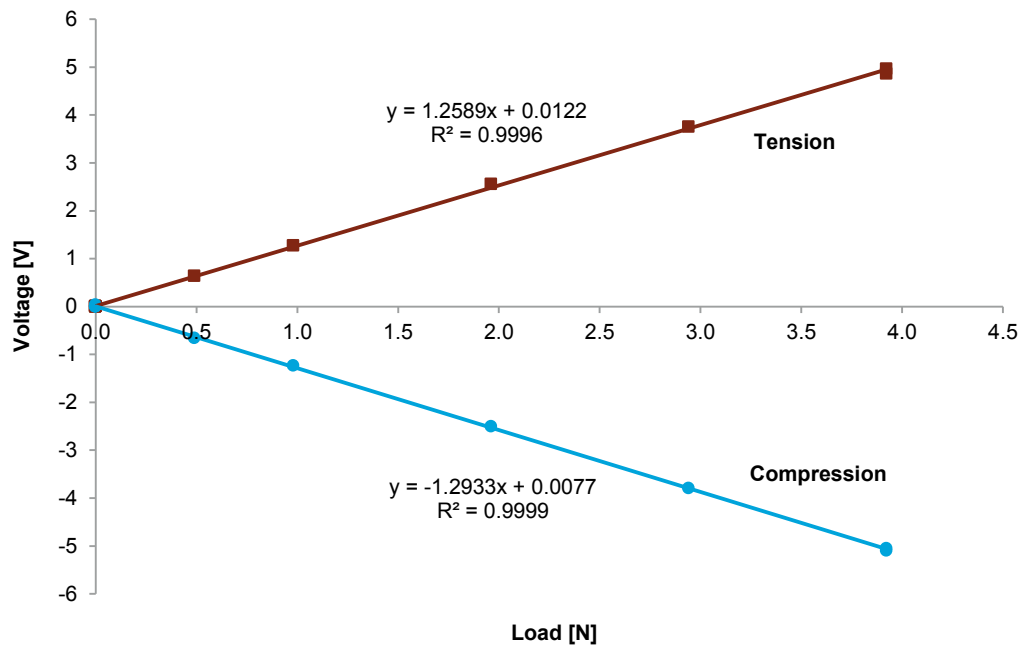
FIGURE 3.18: Typical friction calibration relationships for both tension and compression.

3.5.2   Interferometry calibration

Prior to the beginning of each testing session, accurate spectrometer calibrations were carried out. The importance of the spectrometer calibration must be highlighted, as this allows the wavelength of the interference peaks and consequently the oil film thickness to be accurately determined during testing.

The wavelength of light to pixel position calibration is performed by employing a low pressure mercury lamp. Subsequent to an initial 2 minute warming up period, the mercury lamp is fixed on one side of the reciprocating rig, facing the spectrometer. For this wavelength to pixel calibration, the 250 μm spectrometer' slit is replaced with a 100 μm one. Figure 3.19 presents the alignment of the spectral assembly.
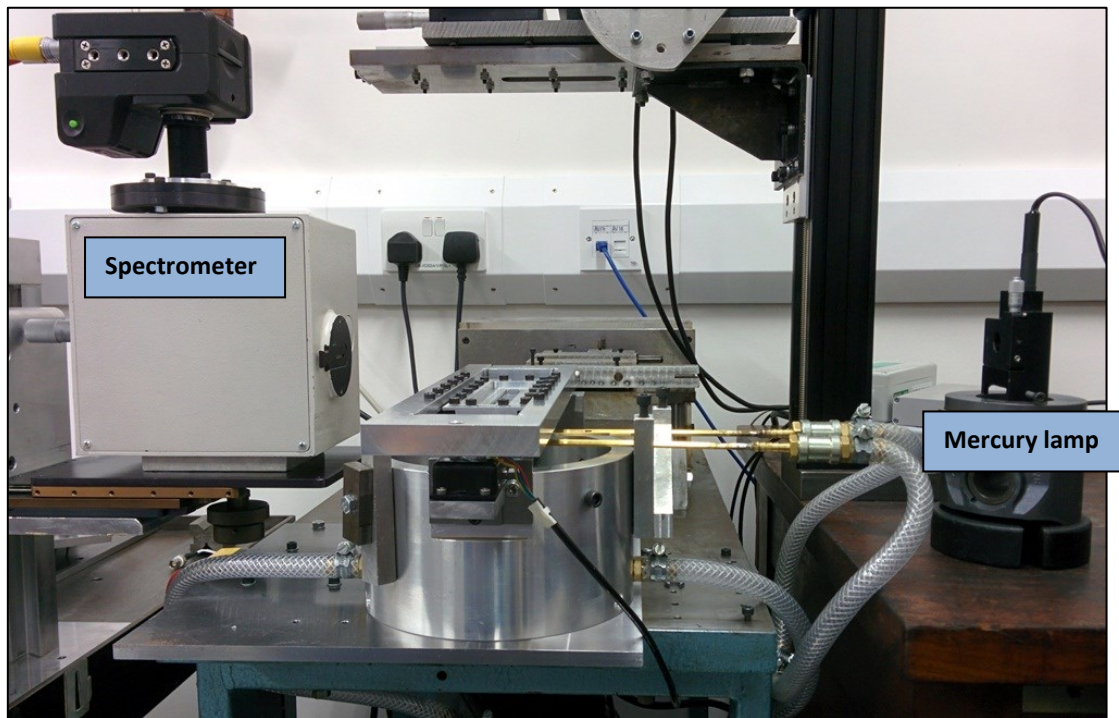
FIGURE 3.19: Spectral assembly for the wavelength to pixel calibration.

By adjusting the spectrometer's wavelength micrometer, the two brightest mercury lines in the visible range are positioned in the middle of the screen. The mercury lamp position is adjusted in order to obtain sharp spectral lines and a screenshot is grabbed (figure 3.20 (a)). The average intensity across the y axis in figure 3.20 (a) is consequently plotted against x axis' pixel position, as schematically presented in figure 3.20 (b).
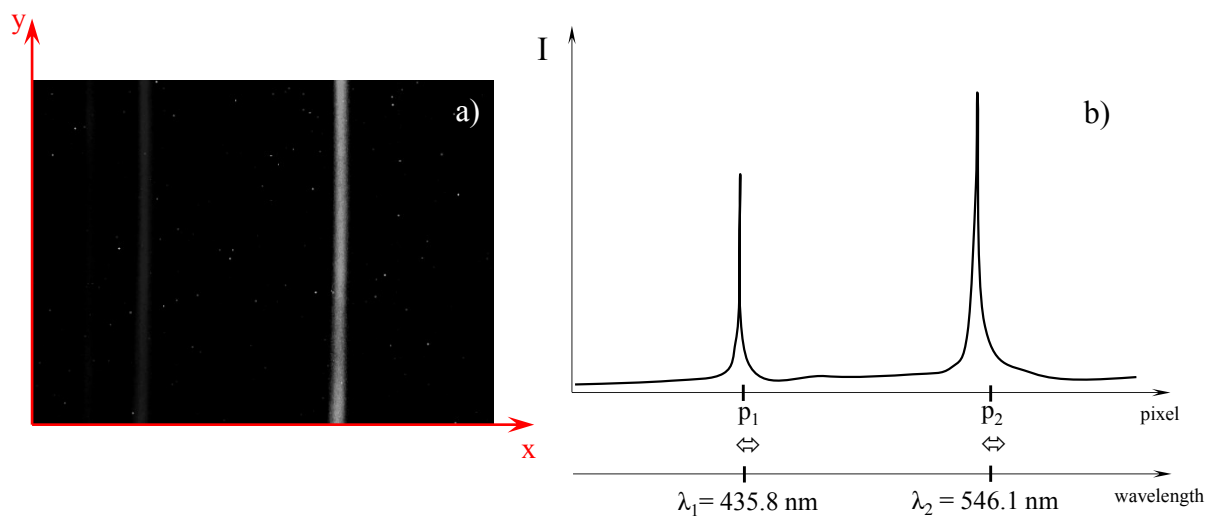
FIGURE 3.20: Intensity to pixel calibration image (a) and schematic representation (b).

The spectrum is consequently analysed using MatLab software, via a code specifically created for this purpose (Appendix C). As the wavelengths of light of the two mercury lines are known values (λ_1 = 435.8 nm and λ_2 = 546.1 nm) and the relationship between wavelength and pixel position is linear, the *slope* (A) and the *y intercept* (B) are determined. These two designated constants of the linear equation are consequently employed in a separate MatLab code (Appendix C) to process the interferometry images captured during reciprocating tests. The wavelength of light, λ, will be calculated according to the formula below, using the pixel position values, p, and the A and B constants:

$$\lambda = A \cdot p + B \tag{3.1}$$

3.6   Lubricants

A number of iterations were required to establish the optimal lubricant to be used, a key step in the research. Initial tests performed using mineral base oil revealed that, when running under mixed and boundary conditions, wear scars appear on the fused silica specimen. This behaviour had a negative impact on the repeatability of the frictional response. It was consequently decided that a new lubricant was needed to achieve accurate test repeatability. A lubricant well characterized in the mixed-boundary regimes will allow repeatability both throughout the full duration of a testing session as well as over different testing sessions. After carefully investigating different candidates, a fully formulated Shell Helix 10W40 lubricant containing anti wear additives was employed in all tests performed throughout this research, with one exception – to study of the impact of surface texture on wear behaviour (Chapter 8), in which instance the initially selected base oil, with no additive pack, was used.

The new, fully formulated oil was selected to have similar viscosities as the initial base oil. A SVM 3000 viscometer developed by Anton Paar (figure 3.21) was employed to determine the viscosity at various temperatures for each lubricant used throughout this research. Figure 3.22 presents the viscosity variation as a function of temperature for both the fully formulated oil as well as the mineral base oil.
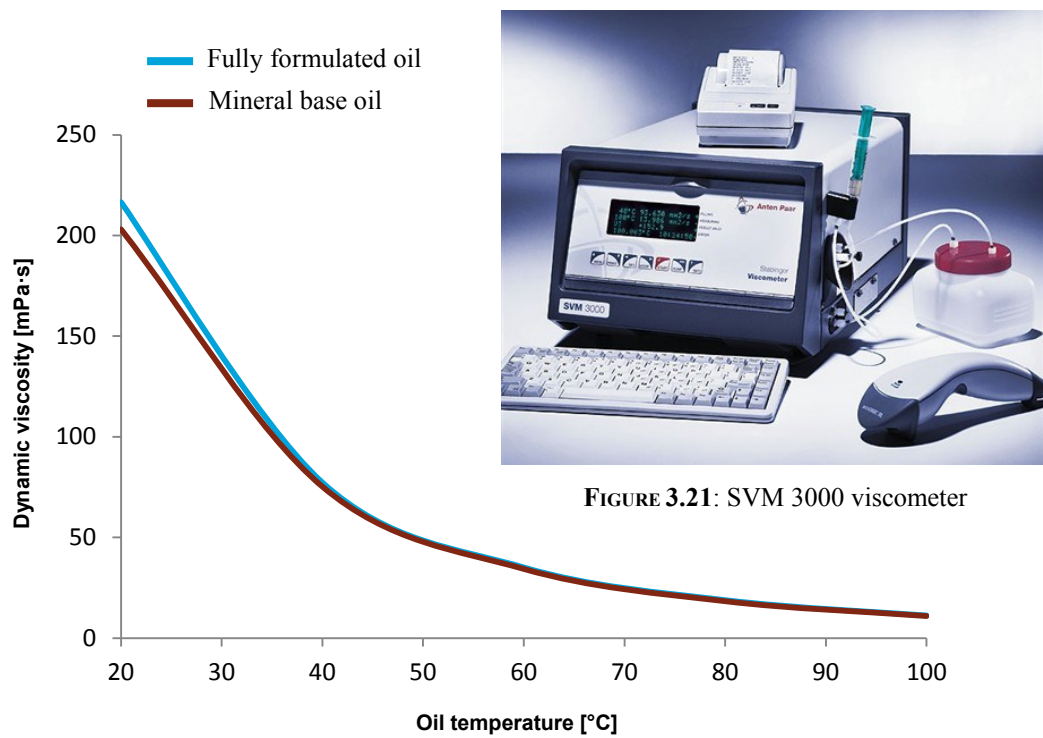
FIGURE 3.21: SVM 3000 viscometer

FIGURE 3.22: Dynamic viscosity variation with temperature for the two lubricants used in this study.

Over the duration of the testing session, the two lubricants were employed at different temperatures and consequently different viscosities, in order to place the sliding bearing under various lubrication regimes. In each chapter detailing test results (*i.e.* Chapters 4 to 8) the viscosity of the lubricant at the temperatures used in that particular test are presented upfront. However, for easy reference, the complete matrix detailing all properties of these two lubricants are presented in tables 3.1 (fully formulated oil) and 3.2 (base oil).

TABLE 3.1: Properties of the fully formulated engine oil at the desired temperatures used during the various test sessions

Oil Temperature [ºC]	*Fully formulated engine oil (Shell Helix 10W40)*		
	Dynamic viscosity, η [mPa·s]	Kinematic viscosity, ν [mm^2/s]	Density, ρ [g/cm^3]
10	401	460	0.872
20	216	250	0.866
40	77	90	0.853
60	35	42	0.841
80	19	23	0.828
100	11	14	0.816

TABLE 3.2: Properties of the mineral base oil at the desired temperatures used during the wear behaviour test session.

Oil Temperature [ºC]	Mineral base oil		
	Dynamic viscosity, η [mPa·s]	Kinematic viscosity, ν [mm²/s]	Density, ρ [g/cm³]
20	203	243	0.835
40	75	91	0.823
60	34	42	0.810
80	18	23	0.798
100	11	14	0.786

After determining the properties of the lubricants, the fully formulated oil containing anti-wear additives was characterized using a Mini Traction Machine (MTM2) developed by PCS Instruments (figure 3.23).
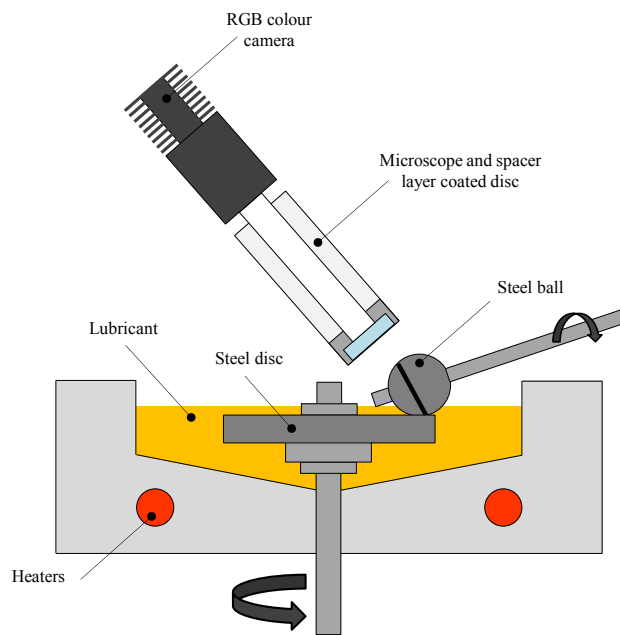
FIGURE 3.23: Schematic of Mini Traction Machine (MTM2) with 3D-SLIM (after [101]).

The MTM2 rig produces a mixed sliding and rolling contact between a ball and a disc. By individually driving the ball and the disc, the slide-roll ratio (SRR) can be controlled. For the current lubricant characterisation a SRR of 100% was selected (*i.e.* the disc speed of 240 mm/s is three times that of the ball speed), which combined with the selected loads (31 N and 50 N) and lubricant temperature (100 ºC), will allow the contact to pass

through all lubrication regimes. Three sets of measurements were performed for each test condition, before and after a one hour time step at constant lubricant temperature and applied load (figure 3.24).
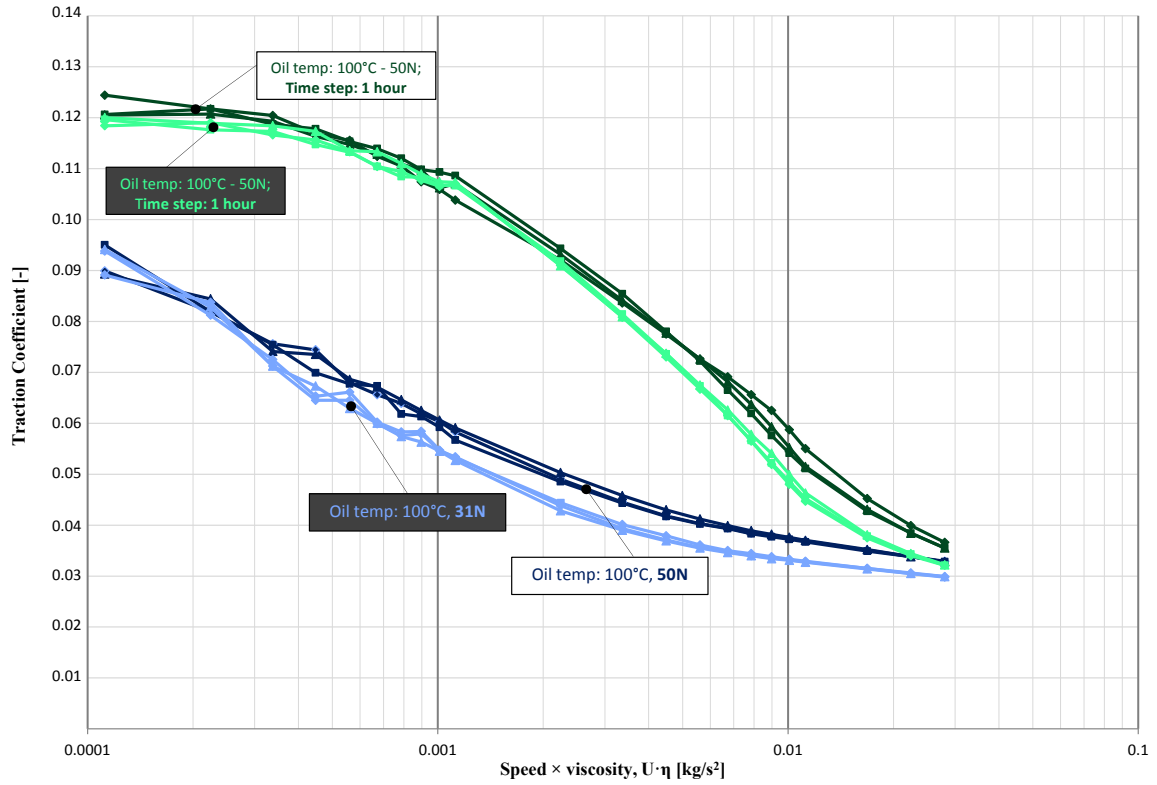
FIGURE 3.24: Stribeck curves for SRR 100% with varying lubricant temperatures and applied loads. Tests performed before and after a one hour time step.

The 3D-SLIM optical interferometry system was mounted on the MTM2 to analyse if the selected fully formulated oil has the ability to form a tribofilm on the specimens' surface, which will later protect the specimen against wear. The additive film was measured during the one hour time step and as presented in figure 3.25, where it can be observed that after 20 minutes of test a complete tribofilm was formed on the ball specimen.
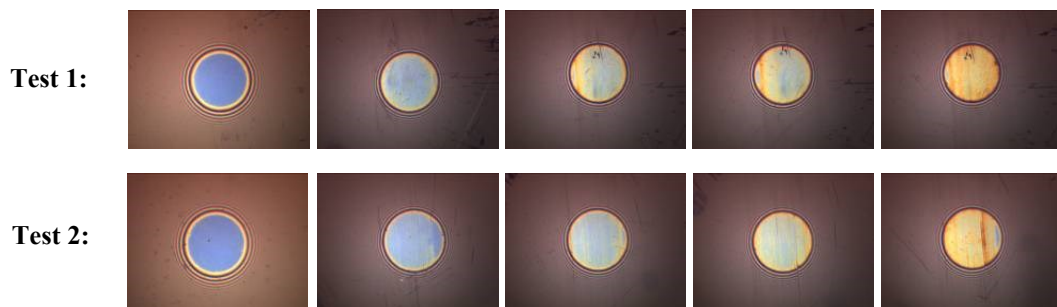
FIGURE 3.25: MTM2 3D-SLIM optical images captured during the 20 minutes time step.

The MTM2 SLIM test helped conclude that the fully formulated oil represents a viable selection in order to avoid wear and, as shown in Section 3.9, achieves repeatable friction data.

3.7   Test specimens and their controllability

A 10×10×2 mm rectangular steel pad (AISI 52100) was manufactured and fully hardened at 850 HV. A minimum stock of 0.15 mm was subsequently removed by grinding the pad on all sides. One surface of the 2 mm width side was ground at a 40 mm radius and curved in the sliding direction, resulting in a convex form closely replicating the IC engine piston ring. The exact dimensions and the geometrical constrains are presented in figure 3.26.
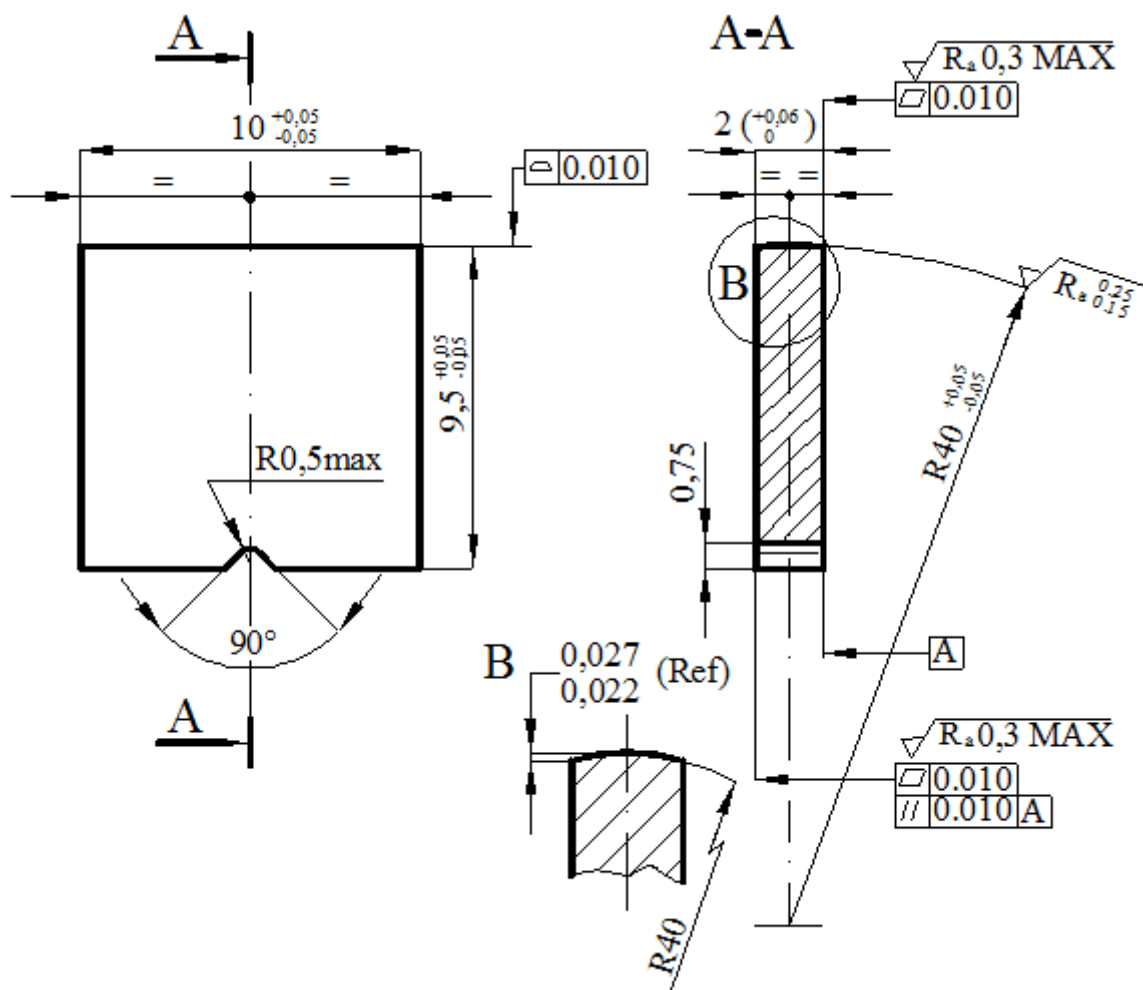
FIGURE 3.26: AISI 52100 steel specimen (all dimensions in mm).

Following the grinding, a mirror-polished convex surface was achieved along the length of the pad using a specially designed polishing jig (figure 3.27). Featuring two hard shoulders at both sides of the steel specimen, this ensures a correct finish along the length of the 10 mm convex side and thus an accurate contact along the length of the contact.
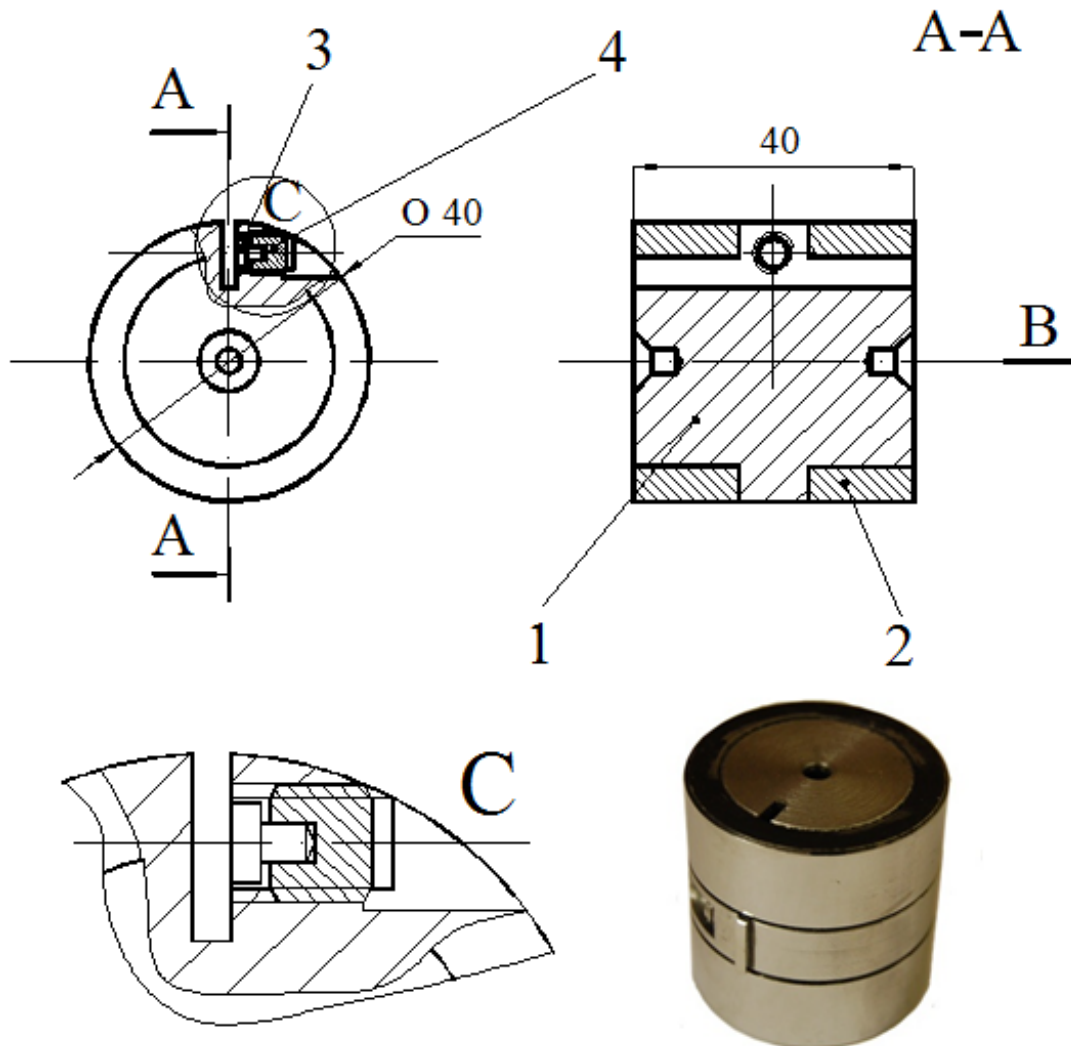
FIGURE 3.27: Steel test pad polishing jig.

As previously presented in Section 3.2, to ensure correct loading along the length of the contact, when switching between the textured and the non-textured fused silica specimens, the steel pad was fitted with a self-aligning mechanism. This consisted of a hole, through which a 4 mm diameter pin was positioned with a +80μm tolerance that resulted in a continuous self-adjustment with the counterpart silica specimen.

As accurate mirror-polishing of the convex surface of the test pad was crucial to achieve adequate film thickness measurements, this procedure was carefully controlled. To ensure a high quality of the polished surface, a synthetic short nap polishing cloth and a 0.25 µm monocrystalline water based diamond spray were used for the surface processing. A three dimensional surface plot of the convex part of the steel pad specimen is depicted in figure 3.28 as recorded by the Veeco Wyko NT9100 optical profiler.

Surface Stats:
Ra: 12.29 nm
Rq: 15.79 nm
Rt: 215.14 nm

Measurement Info:
Magnification: 20.30
Measurement Mode: VSI
Sampling: 487.78 nm
Array Size: 640 X 480
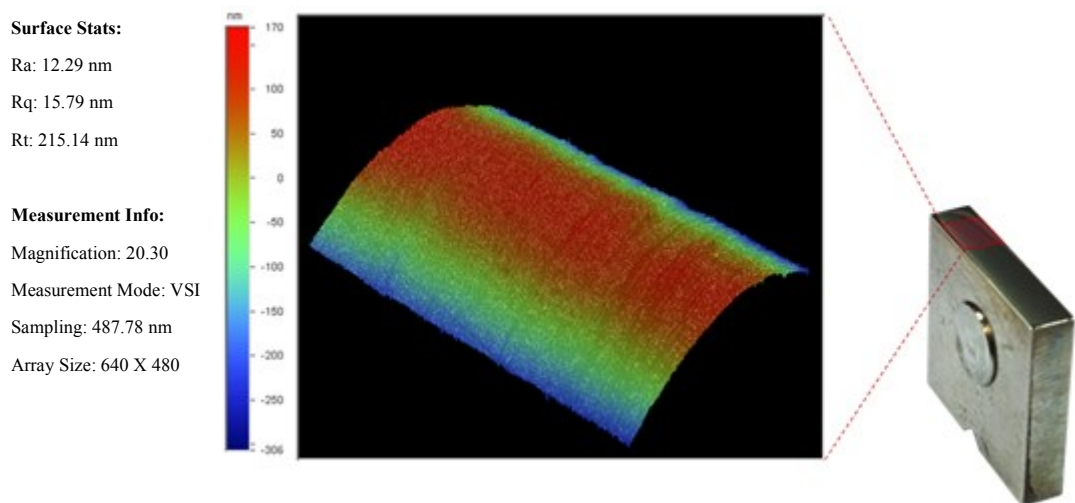
FIGURE 3.28: Three dimensional surface plot of a convex AISI 52100 steel specimen; roughness average Ra=88 nm, curvature radius 40 mm.

The counterpart specimens were manufactured from a HPFS Standard Grade fused silica material, due to its elastic modulus (72.7 GPa) being higher than normal glass for improved friction measurement, and its excellent optical qualities for improved fluorescence image quality.

The surface texturing was performed on the 124 × 15 × 5 mm rectangular fused silica specimens using an ultrafast picosecond laser, emitting optical pulses with duration of 10 picoseconds. The other performance parameters selected for the laser texturing were: a frequency of 10 kHz, wavelength of 355 nm, power of 5 micro joules. Such short pulse durations are vital in order to ablate micron sized portions from a surface before the material has time to undergo significant thermal changes. The non-textured fused silica pad had the same outer dimensions as the textured specimens.

Throughout this research, the surface texturing process took place in two stages. Firstly, various textured patterns and pocket shapes were tested in the initial phase of the research. The five different pocket shapes selected on the basis of expert advice received from computational collaborators (Dr Simon Medina and Dr Mark Fowell) are depicted in figure 3.29. Considering the 28.6 mm stroke length, each pattern was applied on a 30 × 12 mm area of the fused silica, so that on each specimen two different patterns can be fitted.

FIGURE 3.29: Pocketed fused silica test pads employed in the first stage of the research.

Once the optimal pocket shape has been determined, the second stage of the research switches focus to varying the pockets geometry in order to accurately determine the importance of pocket depth, breadth and density on film thickness and friction force under different lubrication conditions. In order to optimise the number of specimens used due to financial considerations, each blank fused silica specimen hosted two separate textured areas with different geometrical characteristics. Whilst pocket length and lateral distance between pockets on the fused silica specimens were kept constant for all the specimens (as depicted in figure 3.30), the depth, breadth and separation of the pockets were varied to achieve the parametric study of surface texture.

Since different geometries and densities of the pockets were employed throughout this study based on the various effects and mechanisms of surface texture which were investigated, these selected geometries and densities will be presented at the beginning of each chapter discussing experimental test results. Similarly, although the variability in

average roughness (Ra) of the AISI 52100 steel specimens employed throughout the research was less than 3 nm, since different samples were used for each set of results, the roughness parameters will be detailed at the beginning of each chapter.
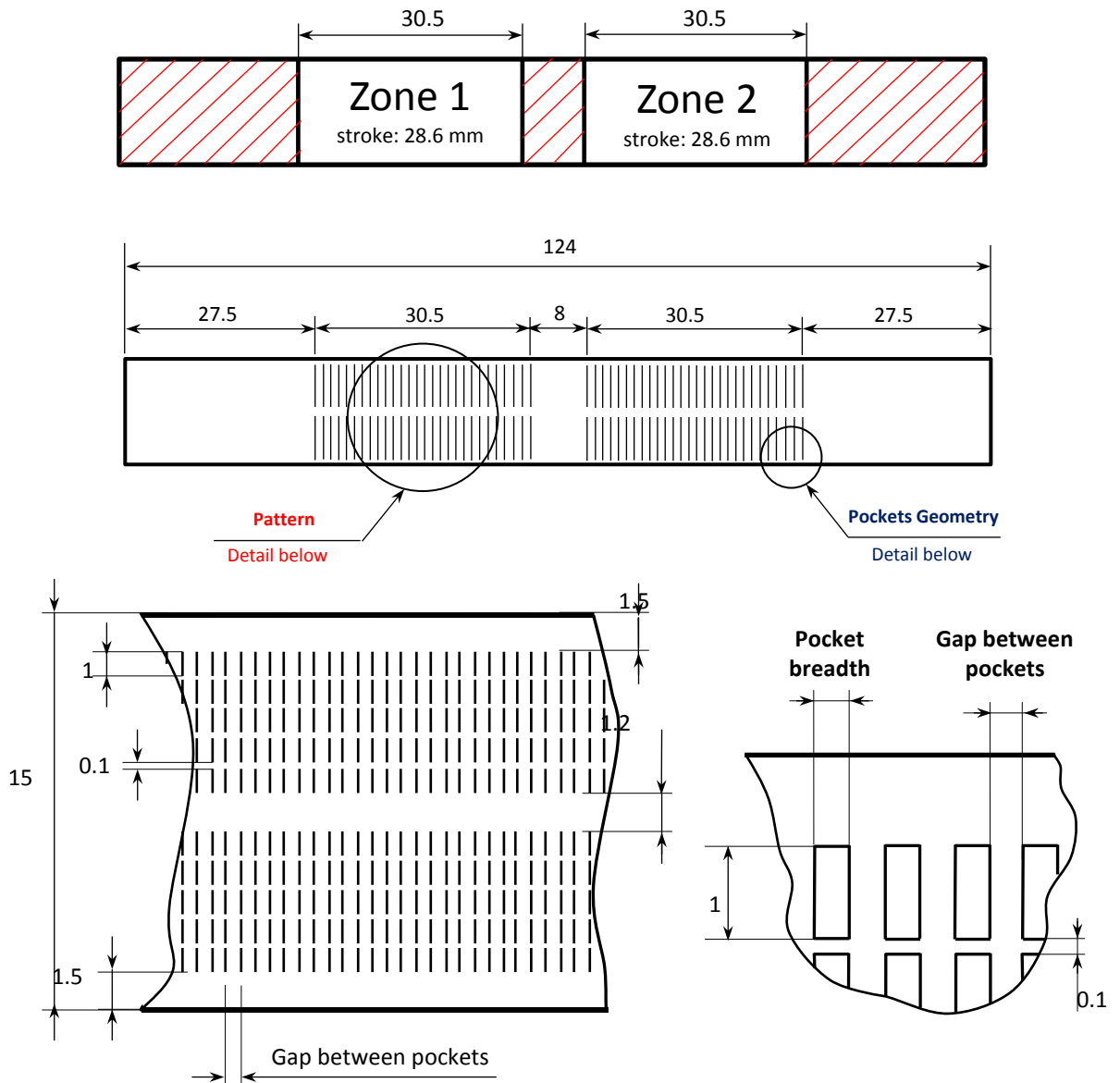
FIGURE 3.30: Geometrical configuration of the textured fused silica specimen.

3.8   The test procedure

The following section details the key steps of the test procedure carried out for all tests. Accurate calibrations of friction and interferometry sub-systems were performed prior to every testing session. In order to calibrate the friction load cell, a series of known masses were used to displace the steel pad holder in both tangential directions (tension/compression) so as to accurately define the relationship between distance travelled by the pad holder and equivalent voltage. During the calibration, voltage measurements were recorded as the sensor was loaded and unloaded in both tension and compression. The average values obtained from this procedure were used to determine the equation relating voltage output to frictional force. As described previously, spectrometer calibration was also performed at the beginning of the testing session.

The fused silica and the steel specimens were soaked in toluene and isopropanol and all traces of solvent were dried out using a heat gun. Following the cleaning procedure both specimens were fixed inside their corresponding holders on the reciprocating rig. Dead weights were attached to the silica pad specimen holder to generate an operating normal load and self-adjust the two counterparts one against the other.

To stabilize the temperature of the fully formulated lubricant together with the temperature of various parts of the rig which were in direct contact with the heated lubricant, the oil temperature control system was switched on, the desired temperature selected and the system left to run for approximately 30 minutes prior the commencement of the test. The interferometry microscope setup was subsequently placed at the desired location outside the contact area, in a position where more than two fringes are visible (*i.e.* approximately 1 mm outside the line contact).

The final step before starting a test was to connect the isometric load cell with the steel specimen's holder, by tightening the two nuts located on the load cell's screw against the connecting rod. This operation needed to be performed after the temperature of the different parts of the system was stabilized (*i.e.* the oil bath and the steel specimen holder) so that a zero line of the friction sensor could be easily maintained. Subsequently, the

LabVIEW program was switched on and the triggering position along the stroke was set. The program also allowed the visualisation of rig speed and real-time friction data.

Once all the steps described above were completed, the rig's motor was switched on and a test speed was selected. After a 15 minute running-in period, the speed was reduced to 0.1 Hz and an interference video was captured in order to accurately determine the out of contact curvature along the entire stroke length. The starting point of the recorded video was the triggering position previously chosen. Following the saving of the video file on the interferometry system's computer, the speed was increased again at the initial test value and a new interferometry video clip was recorded simultaneously with the corresponding frictional data. Again, the starting point for the data acquisition was the selected triggering position. Upon completing the recording and saving of the acquired data, the speed was increased to the next desired step, and the procedure repeated.

Once all the desired tests at different speeds were completed for a certain normal load, the load was increased and the procedure repeated starting with the capturing of a new out of contact curvature associated with the new applied normal load. A new out of contact curvature needed to be determined due to the different elastic deformation of the linear contact (see Section 6.2 for details of the out of contact curvature).

Following the completion of the entire matrix of loads and speeds, the oil temperature was increased to the next desired value and the matrix repeated. Finally, the test procedure for all *speed-load-oil temperature* combinations was repeated for all non-textured and textured specimens compared throughout this research.

Subsequent to successful simultaneous measurements of friction force and film thickness, the cavitation pattern variation was investigated. To do this the lubricant was removed from the heating circulator and the selected fluorescent dye added to the lubricant at a concentration of 2% of the total fluid mass. To ensure a homogenous mixture of the oil and dye, the fluid was blended using a magnetic stirrer for the duration of one hour. After being mixed thoroughly, the lubricant was poured back into the heating circulator, the desired test temperature set and the lubricant system run again for 30 minutes. For

consistency of results, during this 30 minutes period, the CCD camera and light source of the L.I.F. techniques were switched on and left running. This ensured the camera reached the temperature corresponding to optimal performance and the mercury-xenon lamp increased light output to steady optimal intensity. Subsequently, the microscope system was positioned on top of the linear contact and the rig's engine restarted. The desired *speed-load-oil temperature* parameters were selected and a series of fluorescent images were captured in the desired positions along the stroke (*i.e.* mid-stroke, reversal point, pocket passing through contact, etc.). The entire cavitation test procedure was repeated for various textured and non-textured fused silica specimens.

3.9   Measurements repeatability

Accurately controlling all operating conditions at all times was perhaps the most important aim of the current research. It is for this reason that significant effort was directed at designing and building a reciprocating rig which could ensure that all the results were closely reproducible, both in time during one test as well as from one testing session to another. Without such a careful design, it would have not been possible to differentiate between the performance of plain and textured surfaces, since both are heavily dependent on contact conditions. Multiple improvements were made to the test apparatus in order to reach this goal, the vast majority of them previously presented in sections 3.2 and 3.3. This effort proved effective, as friction and film thickness measurements were repeatable to within 0.1 N and 25 nm respectively, over a period of months.

To demonstrate this outcome, repeat tests are presented in figure 3.31 for both plain and textured silica specimens, under one combination of test conditions (crank angular velocity: 3 Hz, normal load: 50 N, oil viscosity: 18.8 mPa·s). The variation of friction force, both over time and between tests performed on different days, (while switching between specimens) was analysed. Figure 3.31 shows negligible variation in results over time. Furthermore, it can be seen that the contact operates in mixed/boundary lubrication conditions due to the reduction of friction with increasing speed. In addition, the substantial reduction in friction caused by the presence of surface pockets is evident.
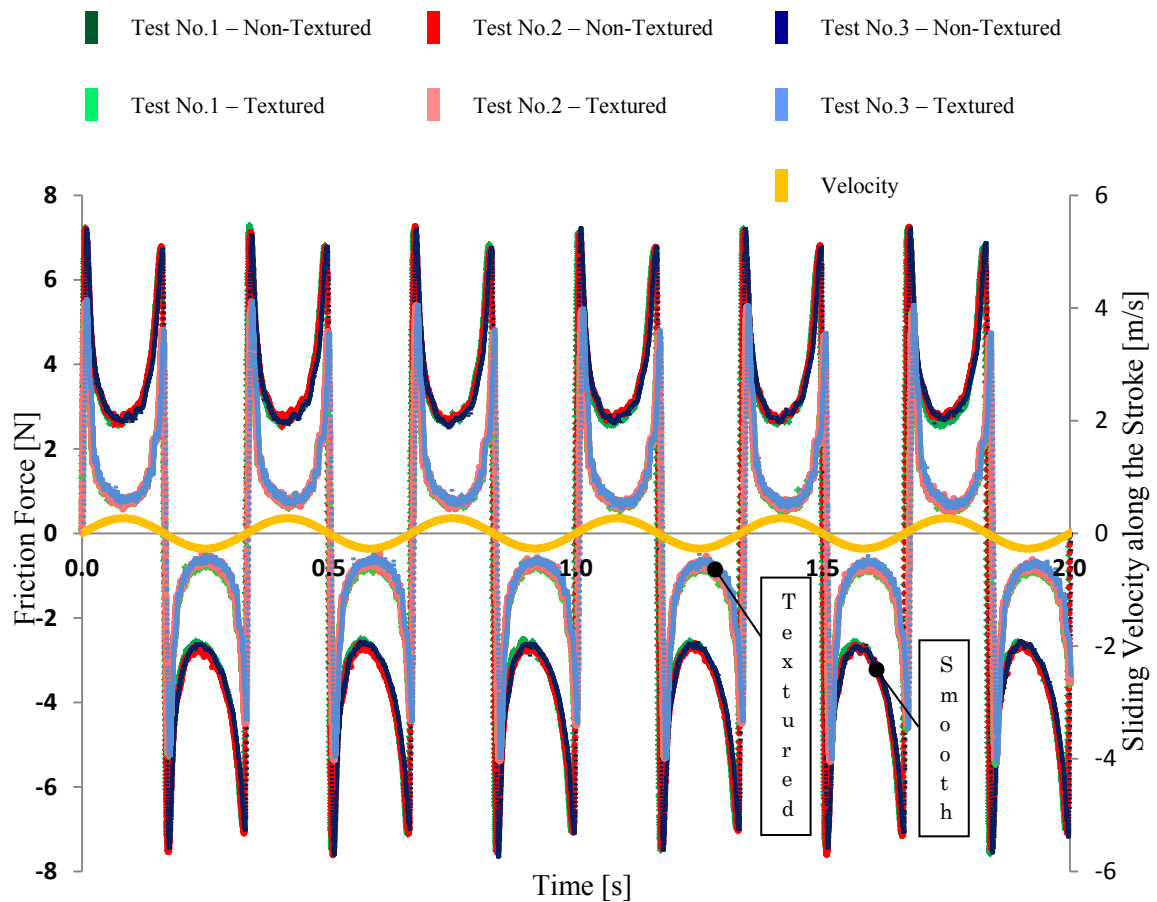
FIGURE 3.31: Friction force over time for both textured and non-textured specimens (measurements obtained on different days). Test conditions: crank angular velocity: 3 Hz, normal load: 50 N, oil temperature: 80°C.

Before starting the simultaneous film thickness-friction force test sequence, repeatability and stability over time were assessed and confirmed for each of the two parameters. Figure 3.32 demonstrates repeatability over time for both friction force and film thickness tests, showing performance graphs for three non-consecutive measurements. These were obtained using the non-textured specimen for one combination of test conditions (crank angular velocity: 3 Hz, normal load: 30 N, oil temperature: 15°C). As opposed to the friction repeatability results presented in figure 3.31, where the contact was operating in mixed/boundary lubrication conditions, figure 3.32 shows that the contact operates under hydrodynamic regime (*i.e.* friction force, generated by the shearing between layers of lubricant, increases with speed).

It can be seen from figure 3.32 that the variation in measured film thickness is not identical for every stroke; with strokes two and four showing lower values than one and three. This erroneous variation is due to a slight rolling rotation of the pad. Measures, such as using high tolerance linear bearings and the self-aligning mechanism, were put in place to reduce this effect but it was not possible to remove it entirely.

In order to check the validity of these measurements, film thickness was calculated for the relevant test conditions at the midpoint along stroke (this position was chosen so as to negate transient variations due to squeeze film effects). Specifically, Dowson and Toyoda's central film thickness equation for a line contact [102] was used and the result is shown in the figure. It is clear that the calculation matches the measurement very well and thus provides some validation for this new interferometry approach.
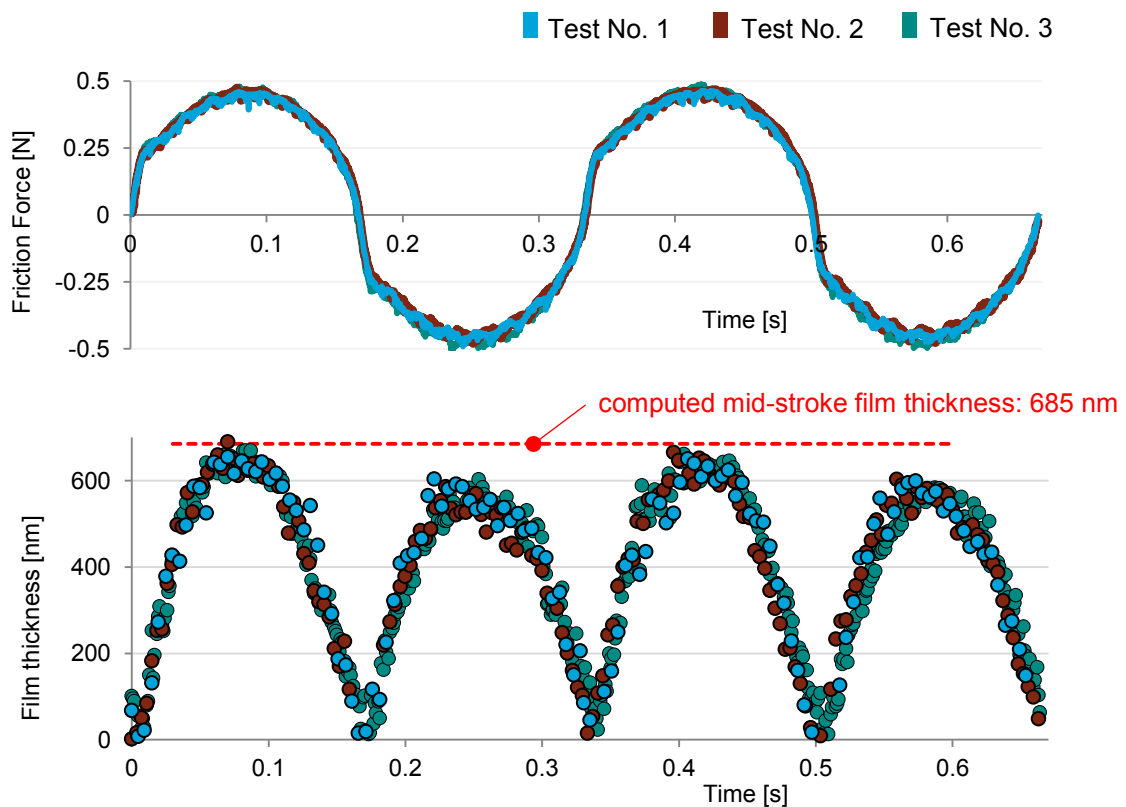
FIGURE 3.32: Stable friction force over time for the non-textured specimen; repeatability between three different tests. Test conditions: crank angular velocity: 3 Hz, normal load: 30 N, oil temperature: 15ºC.

3.10   Summary

This chapter described in detail the test apparatus designed in-house and used throughout the current research, along with the techniques to calibrate the friction and film thickness sub-systems. The main features of the reciprocating rig, which through their redesign allowed for accurate repeatability and stability over time, were also presented. Most notably, a modification of the conventional ultra-thin film optical interferometry was introduced, which allows nanometre film thicknesses to be measured in a textured line contact operating in a non-steady state. Finally, the adopted geometries of the test specimens as well as their controllability were introduced and the experimental procedure for simultaneously measuring friction force, film thickness and cavitation thoroughly described.

Chapter 4

THE EFFECTS OF TEXTURE IN RECIPROCATING CONTACTS – INFLUENCE OF PATTERN SHAPE

4.1   Introduction

The first course of action was to understand how various surface texture shapes and orientations can influence bearing performance and, more importantly, under which lubrication conditions texture is most advantageous. Using the reciprocating test apparatus, five textured specimens with different pocket shapes and orientations were assessed and compared with a non-textured reference specimen. Test conditions were varied in order to place the bearing under different lubrication regimes.

Corresponding friction force data for all five textured configurations and one non-textured specimen is presented in this chapter. The beneficial or detrimental effects on friction coefficient of the various textured shapes were investigated as a function of the lubrication regime in which the contact operates. In addition, the impact of textured features partially or completely entrapped inside the elastic contact area was assessed for both hydrodynamic and mixed lubrication regimes, leading to important conclusions regarding the positioning of pockets relative to the elastic contact zone.

Furthermore, various additional effects of pockets in reciprocating bearings were investigated, highlighting the impact on friction force of pattern direction, sliding velocity and squeezed film at the reversal point. The impact of the five textured patterns on cavitation was qualitatively investigated while accurately capturing various features passing through the linear contact. Important conclusions regarding the impact of laser surface texture on starvation at the end of stroke were deduced. Finally, the chapter concludes with test results revealing the influence of applied normal load on cavitation patterns.

4.2   Test specimens and experimental procedure

The 2 mm width of the fully hardened AISI 52100 steel specimen, closely replicating the piston ring, was ground for this initial study at a 40 mm radius, curved in the sliding direction to result in a convergent-divergent form. A high degree of emphasis was placed on mirror-polishing the convex surface of the steel test pad accurately, this procedure

being crucial to film thickness measurements and fluorescence observation. A high quality of the polished surface and an accurate radius along the length of the pad were obtained (as depicted in figure 4.1) by employing a specially designed jig in conjunction with a 0.25 μm monocrystalline water based diamond spray.

Surface Stats:

Ra: 12.29 nm

Rq: 15.79 nm

Rt: 215.14 nm

Measurement Info:

Magnification: 20.30

Measurement Mode: VSI

Sampling: 487.78 nm

Array Size: 640 X 480
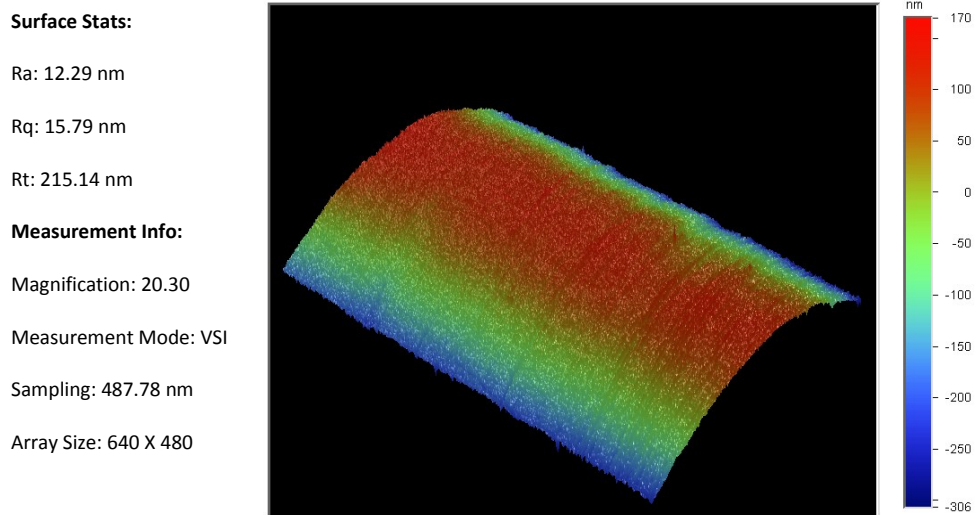
FIGURE 4.1: Three dimensional surface plot of a convex AISI 52100 steel specimen; roughness average Ra=88 nm, curvature radius 40 mm.

Geometries displaying identical features repeated at regular intervals were laser textured into the fused silica specimens, for a variety of distinct shapes. The pocket depth and breadth were kept as constant as possible for a more accurate comparison between different shapes and orientations. Figure 4.2 shows the three-dimensional optical profiles of the textured and non-textured samples as recorded by the Veeco Wyko NT9100 optical profiler. The five pocketed fused silica specimens selected for this research are further detailed in Table 4.1. As previously mentioned, the various textured patterns and pocket shapes selected for this initial phase of the research were chosen on the basis of expert advice received from computational collaborators [44]. The criteria for the selection were (1) the predicted increase in load support and (2) the hypothesised decrease in friction.

105
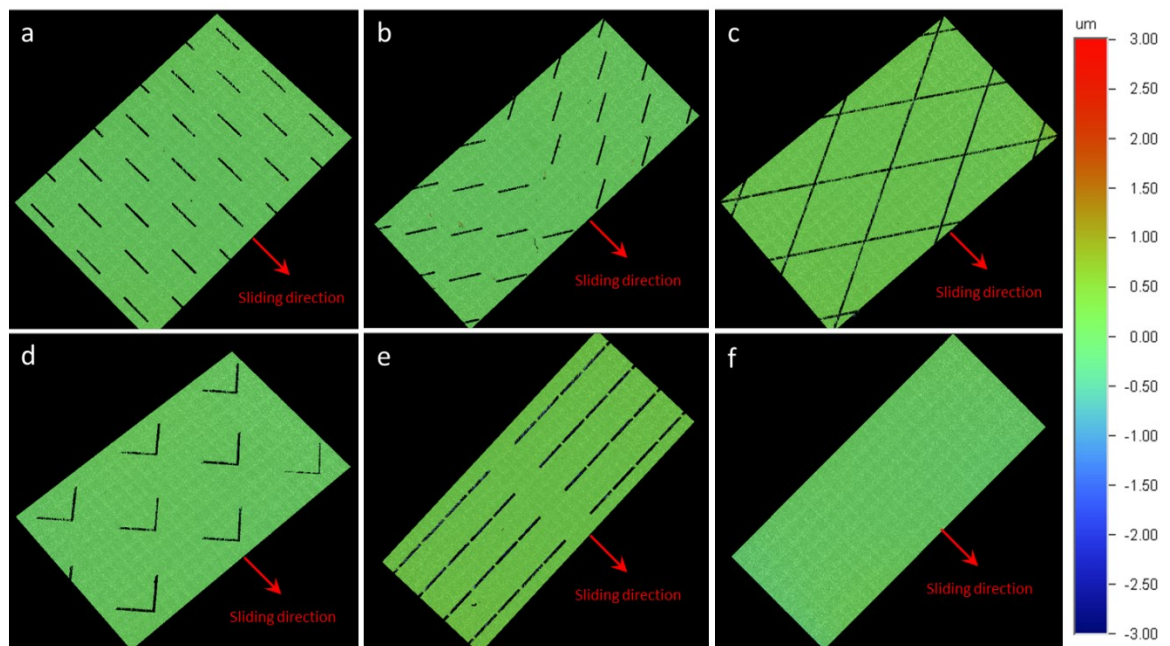
FIGURE 4.2: Three dimensional surface plots of fused silica specimens with different textured patterns: (a) Parallel Grooves - PlG; (b) Angular Grooves - AnG; (c) Crosshatch - Xh; (d) Chevrons - ChV; (e) Transverse Grooves - TrG; (f) Smooth.

TABLE 4.1: Geometric parameters of the pocketed fused silica specimens.

	Sample shape				
	Crosshatch	**Chevron**	**Angular Grooves**	**Parallel Grooves**	**Transverse Grooves**
Sample name	Xh	ChV	AnG	PlG	TrG
Sample profile					
Feature breadth [µm]	60	60	60	60	80
Feature depth [µm]	8.5	8	8	8.5	8
Feature spacing [mm]	2.3	1.5	1.5	0.95	1.05
Sample sliding orientation					

Reciprocating sliding tests were conducted to compare the textured and non-textured silica pads sliding against the mirror-finished stationary steel pad counterpart, while

varying engine speed and applied load. The relative reciprocating motion between the two counter-bodies took place with a controlled amplitude (stroke length) of 28.6 mm.

Tests were repeated while controlling the temperature, and consequently the viscosity, of the SAE 40 fully formulated oil. Table 4.2 shows the complete range of temperatures and the corresponding viscosities used to perform tests, as well as the computed values for mid-stroke film thickness and lambda ratio for a convergent-divergent non-textured bearing of identical geometry. Prior to film thickness calculation, Johnson's method [103] for a line contact was employed to determine the type of contact condition which applies to each case. This showed that, for all three test temperatures, the contact operates under elastic-piezoviscous conditions. By consequently assuming both elastic deformation and lubricant pressure-viscosity increases, mid-stroke film thickness was calculated using Dowson and Higginson's equation for a line contact. The determined values of film thickness were then used to calculate the three lambda values shown in table 4.2, which suggested that the contact operates in either boundary, mixed or full film regime, depending on oil temperature. For the purpose of the current discussion, the contact conditions are referred to by the following calculated lambda values: $\lambda = 0.9$ signifies the boundary regime, $\lambda = 2.2$ the mixed regime, and $\lambda = 6.4$ the full film lubrication regime. It should be noted that these values are approximate since they pertain only to the non-textured case – the exact film thickness in the textured contact is unknown.

TABLE **4.2**: Properties of the fully formulated engine oil at the desired temperatures used during the test session, along with calculated film thickness and lambda ratio for the non-textured contact mid-stroke.

Load, W [N]	Crank angular velocity, [rpm]	Oil Temperature [ºC]	Oil properties			Film thickness (mid-stroke), h_o [nm]	Lambda Ratio, Λ [-]
			Dynamic viscosity, η [mPa·s]	Kinematic viscosity, ν [mm²/s]	Density, ρ [g/cm³]		
50	180	15	274	315	0.8689	573.3	6.4
		45	62	73	0.8502	202.2	2.2
		80	19	23	0.8283	88.1	0.9

Frictional force between steel pad and moving fused silica pad was acquired using a specially developed LabVIEW code. In situ, cavitation zones were recorded concurrently with friction using the LIF observation technique.

4.3   Results and discussion

Multiple series of friction tests were carried out for all five textured configurations and the non-textured reference pad. The results are graphically depicted for various engine speeds, applied loads and oil viscosities, with the extent of friction reduction resulting from the various pocketed surfaces being analysed for each different test condition.

Figures 4.3, 4.4 and 4.5 show the friction force variation when the contact is operating in full film, mixed and boundary lubrication regime respectively. In each case the effects of the various textured pattern shapes on friction force are compared to the smooth case. Figure 4.6 summarises the change in friction force over a complete cycle for every regime.

The textured-to-smooth difference is further investigated for a range of normal loads, varying from 10 to 100 N, passing through the three lubrication regimes. The resulting performances of each surface texture shape are finally shown together in figure 4.7. This graph also enables performance comparison between different pattern orientations, for grooves positioned perpendicular, parallel and at a 60 degree angle relative to the sliding direction.

Figure 4.9 shows friction force variation with velocity along the stroke over one full cycle. The resulting curves for smooth and transverse grooves textured (pattern TrG) specimens are plotted for the three lubrication regimes.

Finally, zones of cavitation were observed throughout the reciprocating tests, using the fluorescence technique described previously. An example showing the variation in the cavitation pattern with normal load for the smooth specimen is presented in figure 4.11.

4.3.1   Influence of surface texture under various lubrication conditions

Figures 4.3 to 4.5 show the relationship between friction force and stroke angle, for a constant crank angular velocity of 3 Hz and a normal load of 50 N. The only variation in test conditions is oil temperature (and consequently oil viscosity), which is varied from 15°C to 45°C and 80°C respectively (see Table 4.2). Friction force graphs are plotted for two complete revolutions of the adjustable stroke rotating mechanism (equivalent to four strokes of the silica pad).
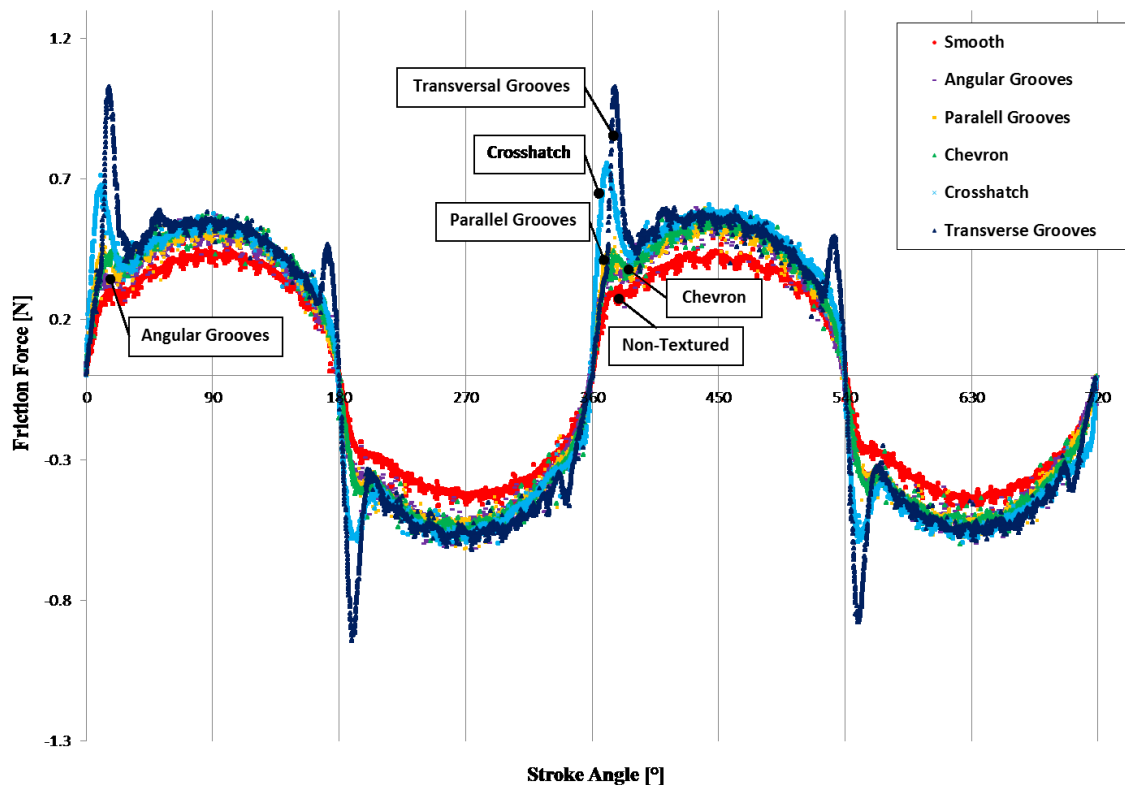
FIGURE 4.3: Friction force comparison between all textured and non-textured samples under the full film lubrication regime (test conditions: angular velocity: 3 Hz, load: 50 N, oil temperature: 15°C, λ = 6.4).
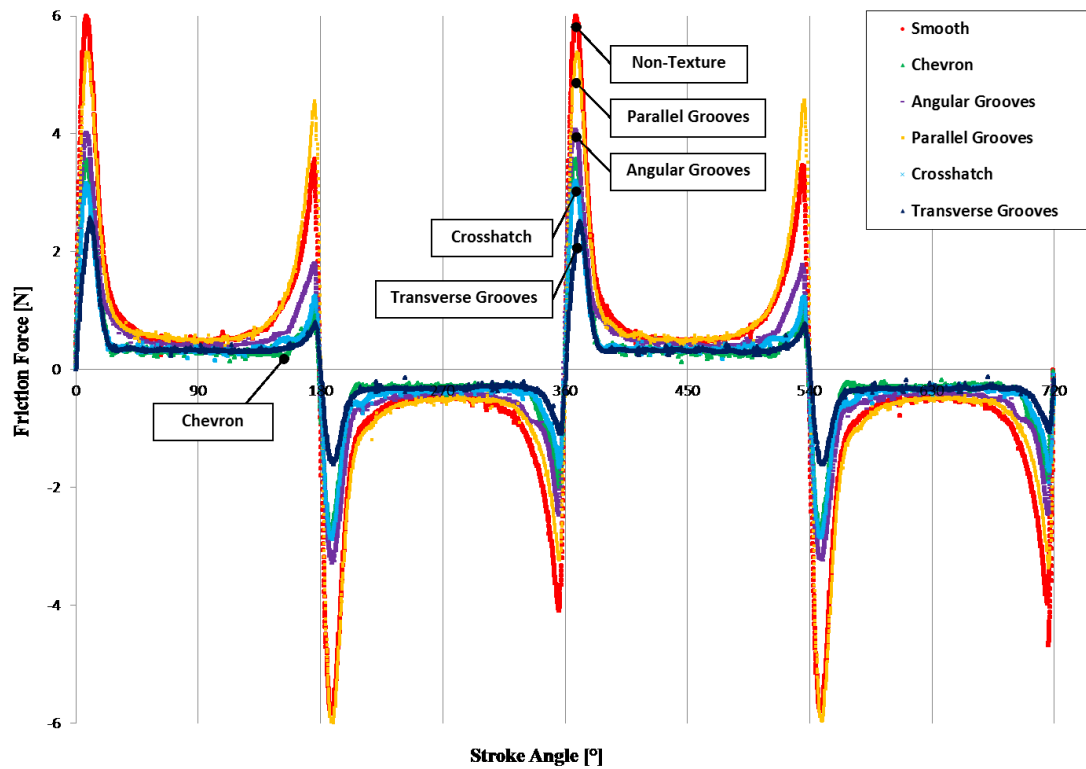
FIGURE 4.4: Friction force comparison between textured and non-textured samples under the mixed lubrication regime (test conditions: angular velocity: 3 Hz, load: 50 N, oil temperature: 45°C, $\lambda = 2.2$).
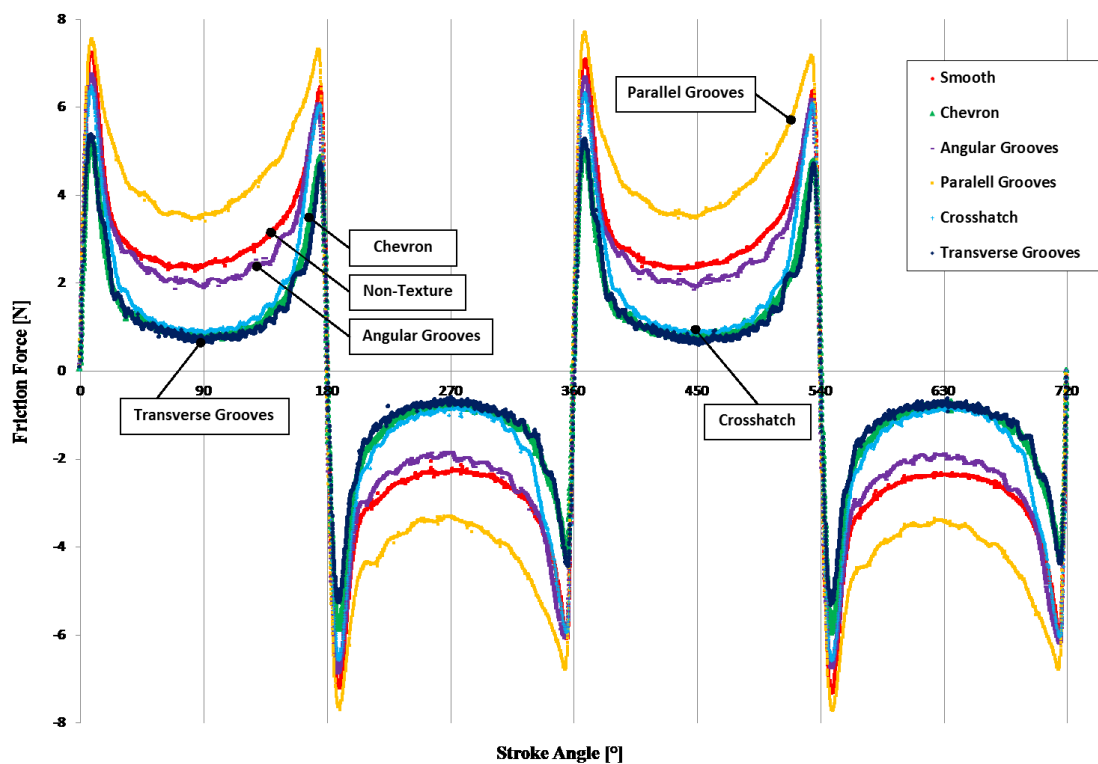
FIGURE 4.5: Friction force comparison between all textured and non-textured samples under the boundary regime (test conditions: angular velocity: 3 Hz, load: 50 N, oil temperature: 80ºC, $\lambda = 0.9$).

110

Figure 4.3, showing test results where oil viscosity was held constant at 273.6 mPa·s, clearly illustrates the full film lubrication regime (*i.e* when the lambda value for the smooth specimen at mid stroke is $\lambda_{smooth,\ mid\text{-}stroke}$ = 6.4), where the bearing remains lubricated along the entire length of the stroke. It can be observed that, as opposed to the boundary lubrication regime (Figure 4.5), friction force increases towards the middle of the stroke. Without taking into account the spikes at reversal in the case of test pads Xh and TrG, which are due to reverse motion taking place on a pocketed area (as later discussed in Chapter 7), all the tested texture shapes present the highest friction mid-stroke, in the exact location where the sinusoidal sliding velocity has the highest value. This is explained by the fact that, in full film lubrication regime, friction force is created by the shearing between the oil layers inside the contact – as a result, the higher the velocity, the higher the friction force (note: film thickness also increases with velocity and thus acts to reduce friction, however this effect is outweighed by the increase in lubricant shear).

When performing tests close to the mixed lubrication regime ($\lambda_{smooth,\ mid\text{-}stroke}$ = 2.2), friction force had its highest value immediately after reversal, probably due to the squeeze film effect [104], and decreased greatly after that. As depicted in figure 4.4, a central plateau of almost uniform friction force is achieved along a large portion of the reciprocating stroke. This suggests a complete fluid film had formed, since the well-established EHL theory predicts that traction does not vary strongly as a function of velocity.

In contrast to the full film regime, the boundary lubrication regime ($\lambda_{smooth,\ mid\text{-}stroke}$ = 0.9), shows friction force to be at its highest values at the ends of the stroke (figure 4.5), where, due to insufficient lubricant entrainment, friction is dominated by asperity contact. Friction decreases towards the middle of the reciprocating stroke, as the increasing sliding velocity acts to entrain more oil between the surfaces, reducing asperity contact.

When investigating the effect of surface texture within the sliding contact and comparing the performance of various texture patterns against a non-textured specimen, the experimental study shows that the impact of surface texture on friction force varies between the three regimes.

Under full film conditions, all surface textures tested generated higher friction force – Figure 4.3 suggests that the plain pad is advantageous compared to any of the textured specimens. Friction force was significantly higher for test pads Xh and TrG when compared to the non-textured sample; however, a close match between friction curves for all five textured specimens is observable, with a minimal improvement in the case of pad AnG, which exhibits the lowest friction.

With regard to the friction force measurements near the mixed regime ($\lambda_{smooth,mid\text{-}stroke} = 2.2$), textured specimens Xh, ChV and TrG showed marginally superior performance when compared to the reference smooth pad. However, Figure 4.4 suggests increased improvements for the pocketed surfaces towards both ends of the stroke. A 62% reduction in average friction force along one cycle was observed when comparing the best performing pocketed specimen, TrG, with the plain sample.

Finally, when the bearing ran in boundary lubrication regime, friction reductions of up to 51% were observed (when comparing the laser surface textured samples with the smooth reference), with chevron and transverse grooves patterns displaying the best performance. Friction force is also significantly decreased by the textured patterns on test pads Xh and AnG, whilst pad PlG appears to be the only instance resulting in higher friction force than in the case of the plain specimen.

Figure 4.6 compares the friction force under each of the regimes, generated by the textured pad with grooves normal to the direction of sliding (TrG). Close to mid-stroke it is clear that friction is lowest when the contact is at the transition between full film and mixed regimes.
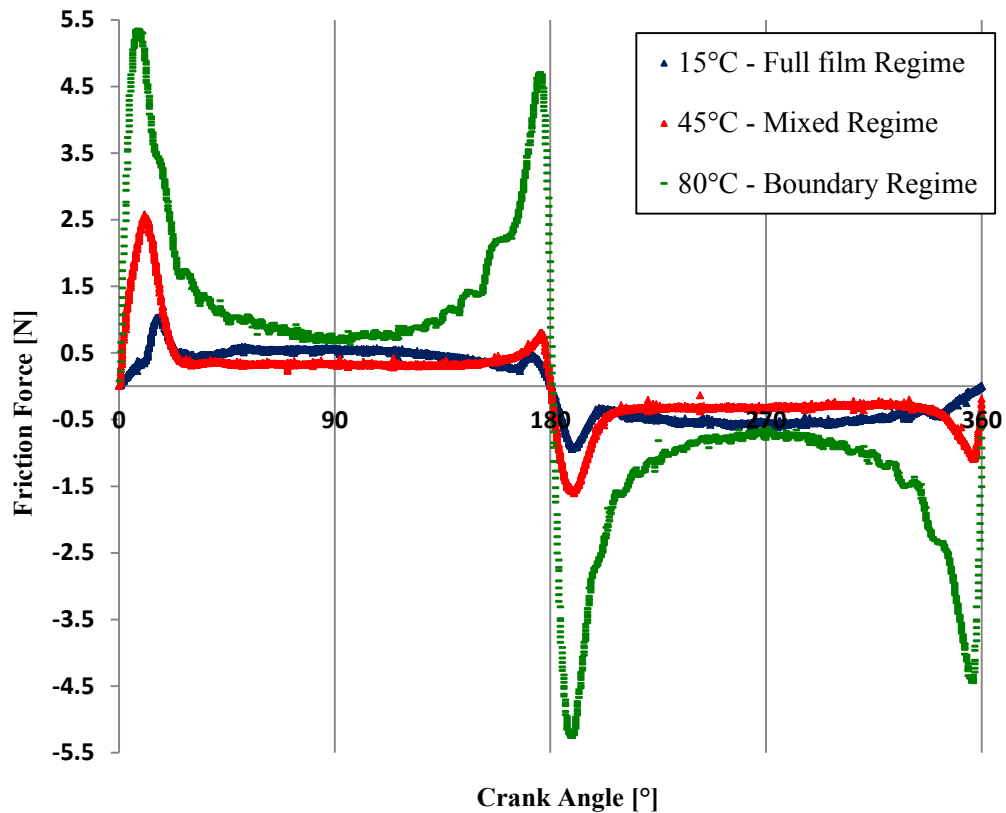
FIGURE 4.6: Three forms of friction force measured in the reciprocating test rig using a textured specimen with grooves orientated transversal to the direction of sliding (crank angular velocity: 3 Hz, normal load: 50 N).

4.3.2 Variation of power loss for different surface texture shapes

The effect of the various patterns can be observed in figure 4.7 where average power loss values for one complete cycle are plotted against applied normal load. Power loss in a reciprocating bearing as a result of bearing friction can be expressed as:

$$P = \int FU \qquad (4.1)$$

where F is the friction force and U the speed of the moving surface. Tests were carried out at a higher crank angular velocity of 4 Hz, while the oil temperature was maintained at 60°C (oil viscosity: 35.095 mPa·s). The speed and viscosity test parameters were set so that the variation of applied normal load could place the reciprocating bearing under all lubrication regimes.
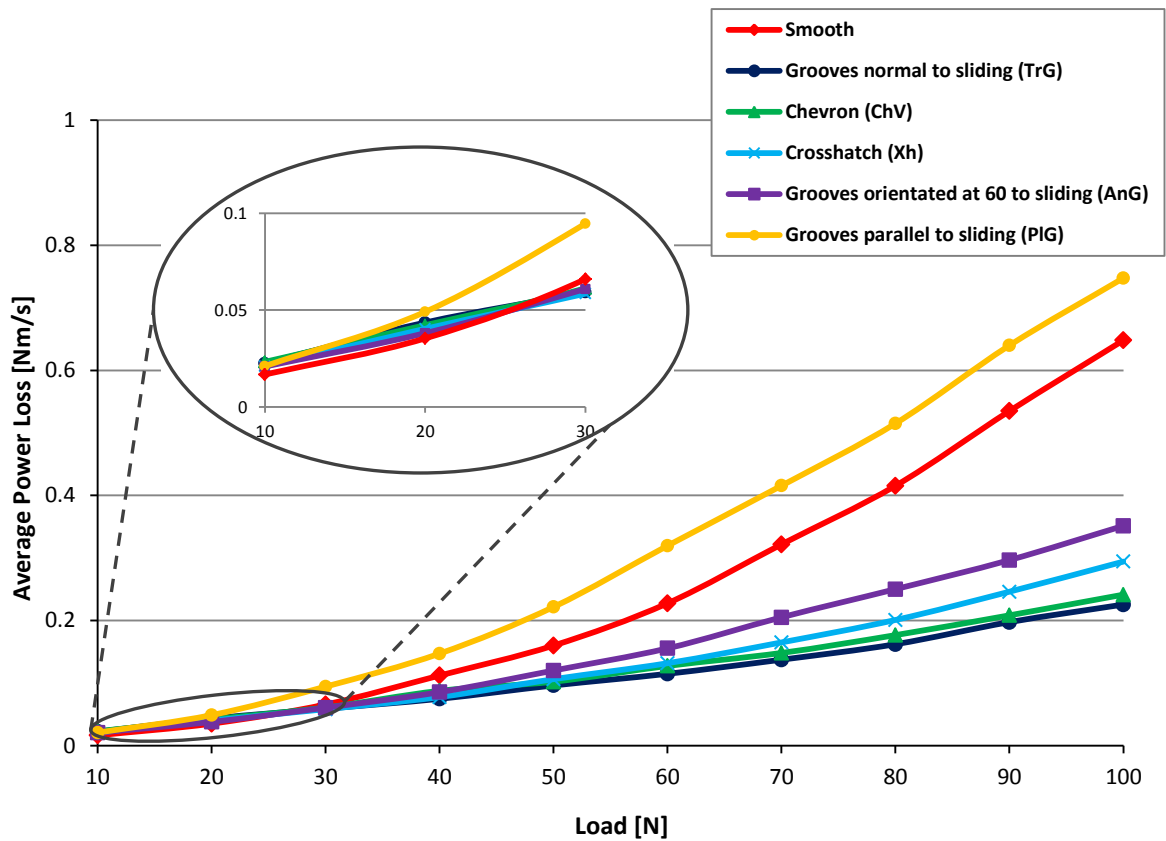
FIGURE 4.7: Average power loss variation vs. load for all textured and non-textured fused silica specimens (test conditions: crank angular velocity: 4 Hz, oil temperature: 60°C).

This is consistent with the observations presented in figures 4.3 to 4.5, where incremental reductions in friction are observed as the applied load increases and the contact is shifted from the full film to boundary, passing through the mixed lubrication regime. Furthermore, at relatively low loads, between 20 and 30 N, there is almost no difference between the textured specimens and the smooth reference pad, the latter actually performing best when a 10 to 25 N normal load is applied. However, as the load increases, significant differences between the smooth sample and different patterns emerge, improvements in average power loss of up to 55% being recorded when comparing the plain sample with the transverse grooves pad over the entire range of applied loads.

In the mixed (Figure 4.4 - $\lambda_{smooth, mid\text{-}stroke} = 2.2$) and boundary (Figure 4.5 - $\lambda_{smooth, mid\text{-}stroke} = 0.9$) regimes, experimental pad TrG proved to be the best performing textured pattern over the entire range of normal loads (40 to 100 N), closely followed by the chevron pattern. Table

114

4.3 summarizes the percentage reductions in average power loss for all textured patterns tested when compared with the plain reference, for the entire range of normal applied loads, 10 – 100 N.

TABLE **4.3**: Percentage change in average power loss along the entire range of applied normal loads (10 – 100 N).

	Sample shape				
	Crosshatch	**Chevron**	**Angular Grooves**	**Parallel Grooves**	**Transverse Grooves**
Average Percentage Decrease/Increase	-47%	-52%	-38%	+25%	-55%

4.3.3 The effect of the contact width to features width ratio and that of pattern orientation

The specimens containing grooves orientated at 60°, normal and parallel to the sliding direction (figure 4.8) were employed to investigate the effects of pattern orientation relative to direction of travel. The associated friction comparisons can also be observed in figures 4.3 to 4.5 and figure 4.7, for all lubrication regimes.

Under low temperature full film conditions, there was no significant difference in friction between the different pattern orientations. However, in both mixed and boundary regimes the test results clearly displayed that grooves orientated perpendicular to the direction of sliding (sample TrG) showed the most beneficial friction behaviour, for all test conditions (crank angular velocities, oil temperatures and applied loads). The sample with grooves parallel to the sliding direction (sample PlG) exhibited the worst performance in all tests, being the only textured pattern with average friction values per cycle higher than the smooth specimen. The 60° angled grooves pattern (sample AnG) performed significantly better over the whole range of tested loads, when compared with the non-textured and parallel grooved specimens, but considerably worse than the normal oriented grooves (TrG).
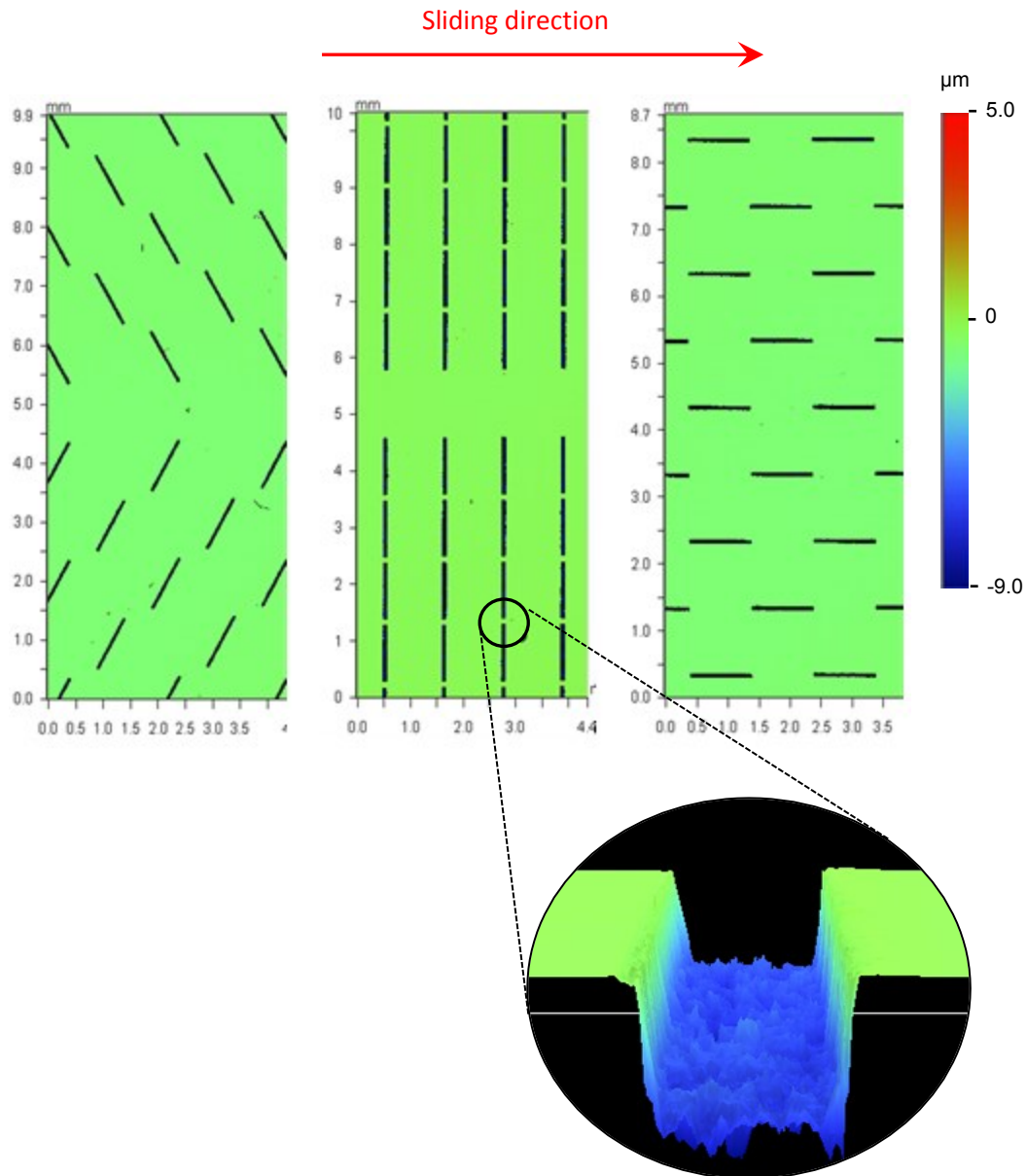
FIGURE 4.8: Two dimensional surface plots of fused silica specimens exemplifying the relative orientation of grooves in relation to the direction of sliding.

These results may be explained by the fact that, if grooves are longer than the contact zone in the sliding direction (as on samples AnG and PlG), pockets will have a tendency to allow high pressure oil to leave the contact zone, resulting in the oil film collapsing. This will inhibit oil film building after reversal and hence reduce the film thickness throughout the stroke, causing a higher shear rate in the oil film and increased asperity contact. Not only are friction losses increased and load support capability reduced, but this approach also results in higher wear rates. This is in agreement with both Costa *et al.*

[13] and Pettersson *et al.* [30] who previously studied the effects of pattern orientation and suggested that, especially for higher normal loads, grooves parallel to the sliding direction generate higher friction forces and lower oil film thicknesses when compared with transverse grooves.

In contrast, if the texture has individual features with dimensions smaller than those of the contact zone, they will be entirely contained within the conjunction for a period during their transit and little pressure-induced flow will be possible. This is the case, for example, with grooves positioned normal to the direction of travel (TrG).

4.3.4   Influ ence of sliding velocity on friction force

Figure 4.9 shows friction force for the best performing pocketed specimen (TrG) and the smooth reference pad plotted against sliding velocity, for each lubrication regime (note: this is the same data as shown in figures 4.3 to 4.5, but plotted differently – similar to the film thickness vs. speed graphs obtained by Costa *et al.* [13]). As expected, these plots have the form of Stribeck curves, but are asymmetrical with respect to increasing and decreasing speed. This difference is due to squeeze film effects, which act to reduce changes in film thickness as the pad accelerates and decelerates. This again agrees with observations of film thickness by Costa *et al.* [13] which were similarly asymmetric with respect to acceleration direction. It is interesting to note that the effect of the squeeze film on friction is most pronounced in the mixed regime, as opposed to the full film regime where increasing and decreasing speed of the smooth pad show identical friction (figure 4.9(a)). These plots further confirm the conclusions from figures 4.3 to 4.5 that friction reduction occurs only in the boundary and mixed regimes and that the texture at reversal is detrimental (figure 4.9(a)). Furthermore, figure 4.9(b) seems to show that the textured specimen enters the full film regime at a lower speed that than the smooth specimen, which suggests that the effect of texture is to boost entrainment.

It is also interesting to note that the difference in friction between the textured and smooth pad remains constant over most of the speed range (Figure 4.9(c)). This is mainly because the contact is so far into the boundary regime and it is only in the mixed/full film regime that the results converge.
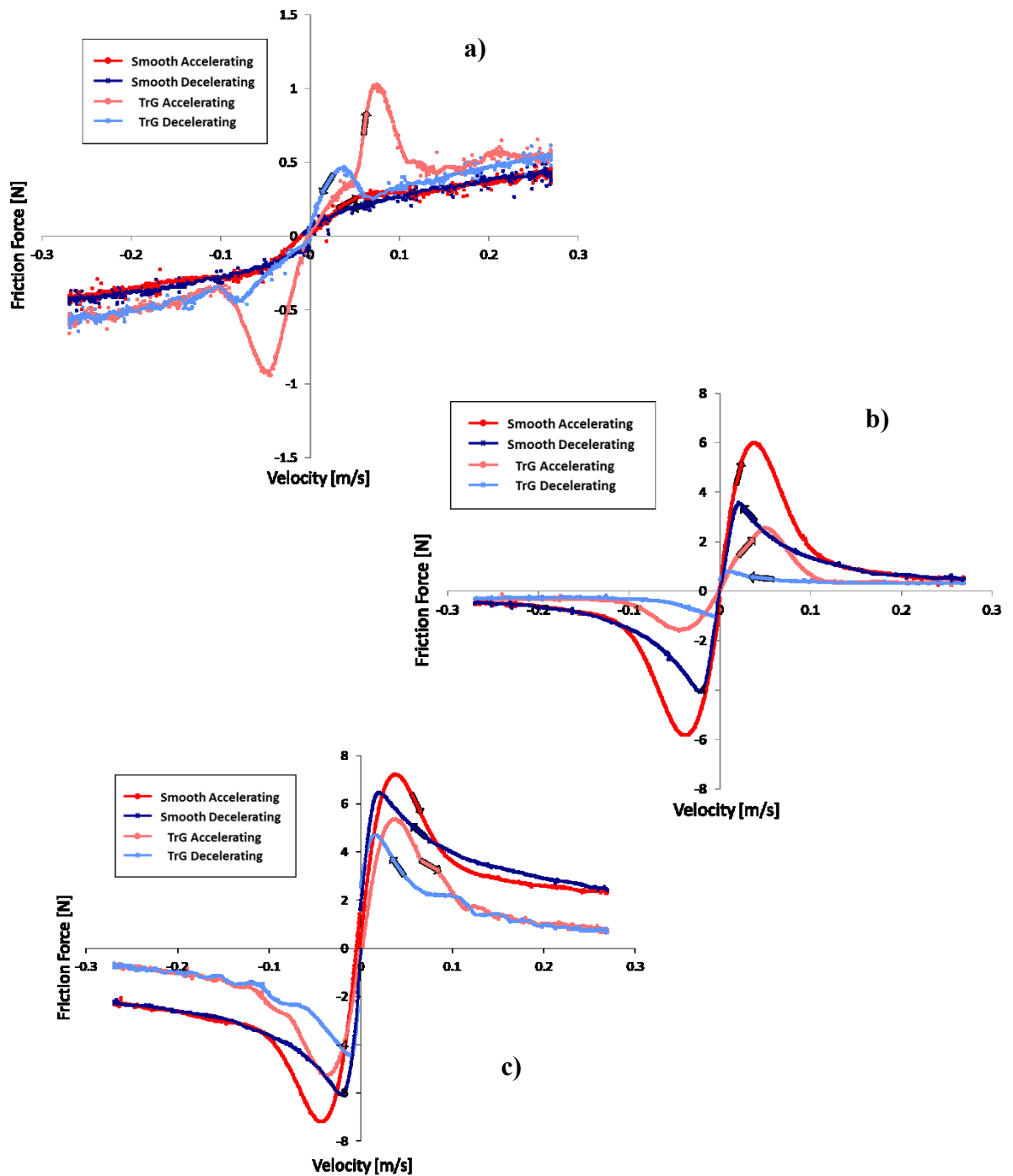
FIGURE 4.9: Friction force profile variation between accelerating and decelerating portions of the stroke for both a smooth specimen and a textured one: (a) full film regime – oil temperature 15ºC; (b) mixed regime – oil temperature 45ºC; (c) boundary regime – oil temperature 80ºC.

From each plot in figure 4.9 it can be seen that, above a certain speed, the friction when accelerating equals that when decelerating. Under these conditions (which correspond to crank angles between 30° and 150°), it can be assumed that squeeze film effects are

negligible. These portions of friction data can therefore be plotted against speed×viscosity in order to produce a master Stribeck curve, as shown in figure 4.10. Here, results for both the smooth and the textured specimen with grooves normal to the sliding direction (TrG) are plotted, along with sketched best fit curves. This figure shows even more clearly that the textured specimen outperforms the smooth specimen in the boundary and mixed regime, but is detrimental when a full film separates the surfaces. It can also be argued that the effect of surface texture on the TrG specimen is to shift the Stribeck curve to the left (compared to the smooth specimen), possibly suggesting enhanced fluid entrainment.
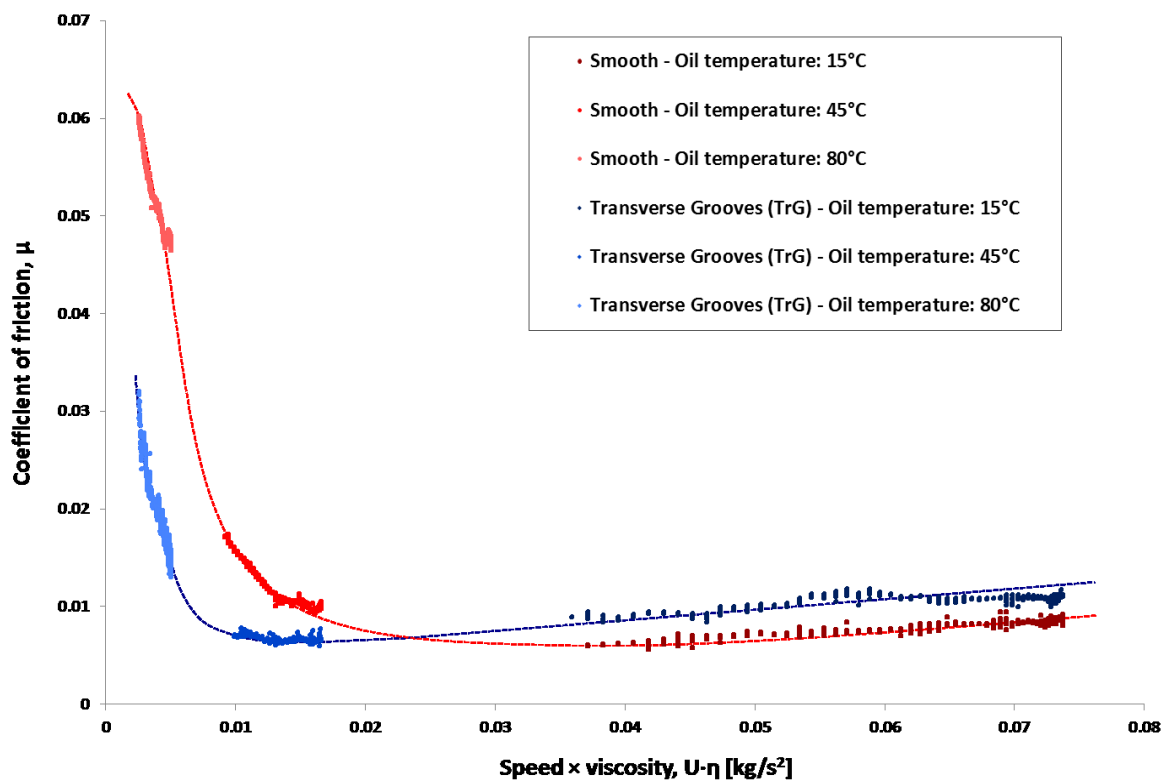
FIGURE 4.10: Stribeck curves showing friction behaviour for the three lubricant temperatures used in this study: 15°C, 45°C and 80°C.

119

4.3.5   Influence of load and texture on cavitation

Finally, a 2% mass concentration of the commercially available oil tracer dye selected for this research was mixed into the fully formulated oil. Then, by employing the L.I.F. microscope system, fluorescent images of the non-textured bearing were captured for a range of normal loads.

The qualitative results obtained in this way offer clear visualisation of the cavitation from the reciprocating contact. Figure 4.11 shows the presence of 6 to 7 cavitation bubbles at an applied load of 10 N. Then, as the load increases to 20 N and 40 N, the number of cavitation striations increases to ca. 11-13 and 34-38 respectively. For the maximum applied load of 80 N, between 70 and 80 different cavitation striations are recorded on the same 0.8 mm length of the contact. This variation of cavitation streamers per unit length for different applied load conditions is in agreement with analyses by Dowson and Taylor [105,106] which show that, as minimum film thickness declines with load, the number of cavitation streamers consequently increases.

These results highlight the possibility of using the current experimental setup to study the effect of oil properties (such as surface tension) on cavitation behaviour.
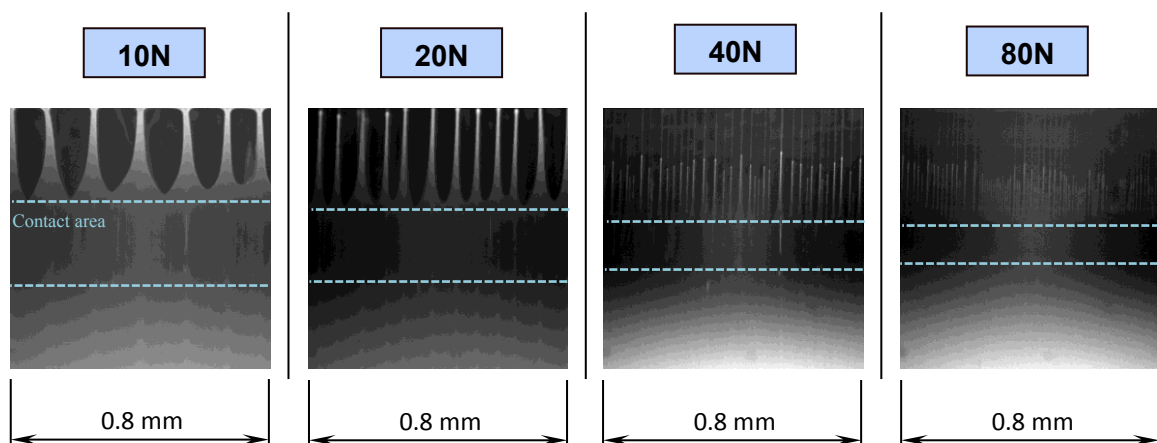
FIGURE 4.11: Cavitation pattern variation for different applied loads.

Furthermore, the trigger system enabled the response of the cavitation pattern to individual silica pad texture features to be imaged as a single textured region passes

through the contact. Figures 4.12(a) to 4.12(c)[1] give a set of fluorescent images of a pocket passing through the contact, captured at each 0.7 degree of crankshaft revolution using test pads AnG, PlG and test pad ChV, respectively.
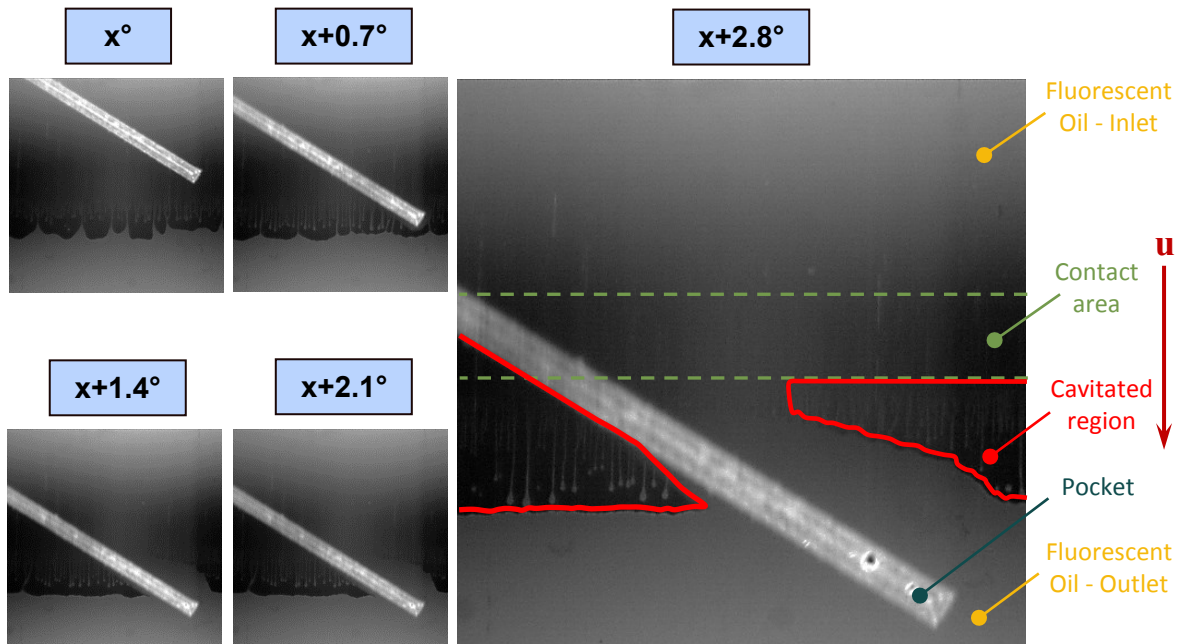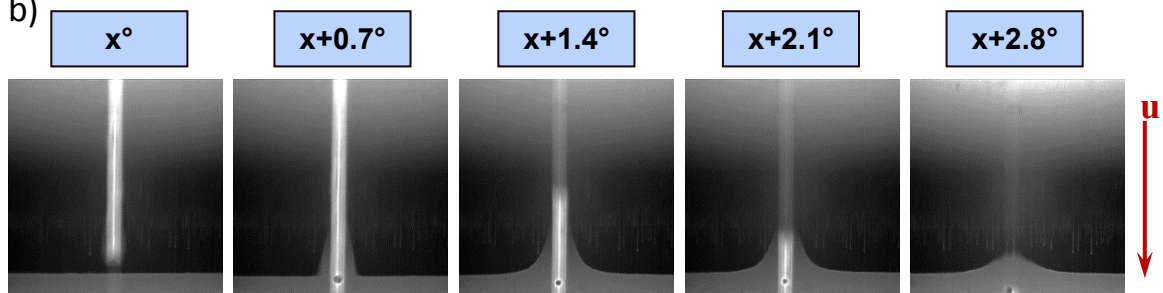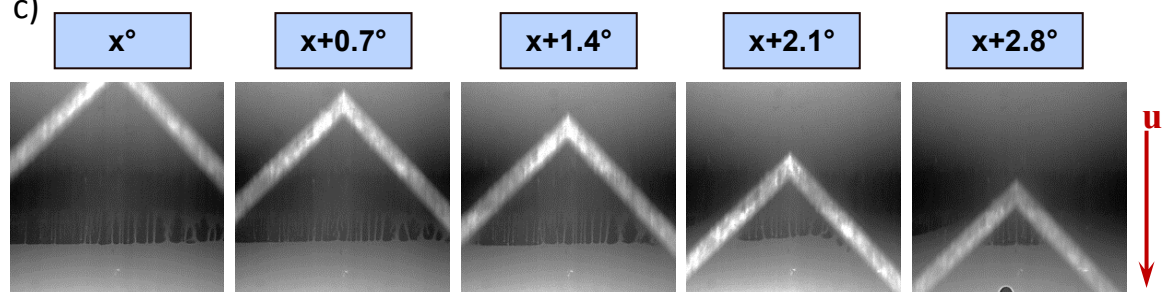
FIGURE **4.12**: Pocket passing through contact captured at a step of 0.7 degree of crankshaft revolution: a) test specimen AnG; b) test specimen PlG; c) test specimen ChV. **u** is the direction of the sliding silica pad relative to the stationary contact,

---

[1] In Figures 4.12(a) – 4.12(c), x equals a particular value of the crankshaft's position, in degrees.

In all three cases, once the pocket emerges from the cavitated region it is seen to transfer fluid back into this region. This observation suggests that in the full film lubrication regime, where friction is given by the shearing of the lubricant, textured specimens will give higher friction when compared with a plain one due to increased amounts of lubricant shear. This finding agrees with results shown in sections 4.3.1 to 4.3.2. Conversely, in mixed and boundary lubrication regimes, the cavitated region may reduce lubricant entrainment immediately after reversal, causing starvation. Therefore, pockets that bring oil into the cavitated region may aid lubricant entrainment and hence reduce friction under these conditions. This is in agreement with results shown in Figure 4.4 immediately after reversal. For a better observation of the mechanism through which pockets bring oil into the cavitated region, hence providing lubricant and prevent starvation, the image capture at *x+2.8°* in figure 4.12(a) was processed and plotted using a thermo scale in figure 4.13.
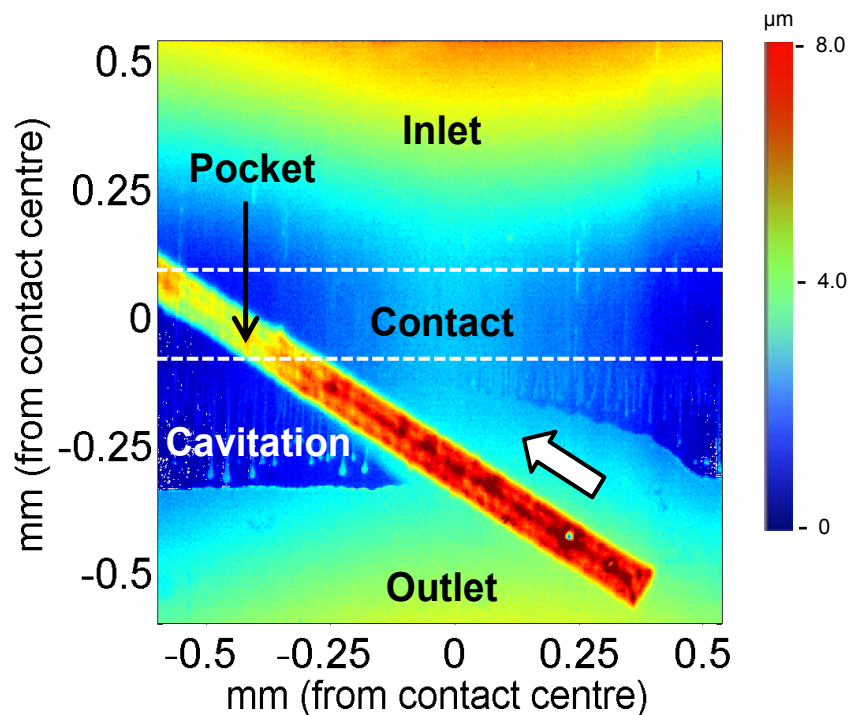
FIGURE 4.13: Influence of surface texture at reversal point.

It can be easily observed how the inclined groove acts to break the cavitated region, allowing the oil to reach the outlet of the contact. If the situation presented in figure 4.13 is considered to be the reversal moment, the lubricant already existent at the outlet can

form a film inside the contact immediately after reversal takes place, thus avoiding starvation and consequently the appearance of wear.

This hypothesis is tentative and further investigation of the effect of surface texture on cavitation will be the subject of ongoing work. Furthermore, it is not suggested that this is the only mechanism by which surface texture affects friction. For instance, in the boundary and mixed regime, it is also possible that the Tripp effect [66] (*i.e.* lubricant being squeezed out of the pocket due to elastic deformation of the component in the contact region) plays an important role. In fact, transient results in Chapter 7, demonstrate that another friction reduction mechanisms must be occurring.

4.4   Conclusions

The convergent–divergent bearing was placed under different lubrication regimes by altering test conditions to assess five different textures, with varying pocket shapes and orientations and compare them with a non-textured reference. Reciprocating sliding tests revealed that surface texture can have either beneficial or detrimental effects on friction reduction depending on the lubrication regime that the contact operates in. Significant observations include:

- In low film thickness contacts, surface texture can improve friction performances along the entire length of the stroke. Reductions in friction of more than 50% were achieved when operating in the boundary lubrication regime, the textured pad with grooves perpendicular to the sliding direction being the top performer. It can be concluded that, as the lubricant film decreases and consequently directs the bearing towards the mixed lubrication regime, laser surfaced textures becomes increasingly beneficial, demonstrating the greatest reduction in friction when the bearing operates in the boundary lubrication regime. Conversely, as observed when analysing the pocketed surface with grooves parallel to the direction of sliding (PlG), texture can in fact be detrimental along the entire length of the Stribeck curve, when compared with a smooth, non-textured specimen.

- Surface texture can alter the performance of the convergent-divergent bearing when running in thick film friction contacts. In this full film lubrication regime, the reference smooth specimen achieved the lowest average friction along one full cycle.

- Although the friction force does not vary considerably along the central stroke plateau when running in mixed regime, surface texture shortly after reversal can significantly reduce friction by helping to build the oil film within a shorter distance from the reversal point.

- Textured samples with pockets which can be entirely trapped in the contact zone (*e.g.* TrG) performed better than textured samples comprising pockets longer than the contact zone in the direction of travel (*e.g.* Xh, AnG), the latter having the tendency to collapse the oil film by allowing the pressurized oil to escape from the contact zone. As a consequence, pattern orientation is essential when pockets are larger than the contact width.

- Asymmetries in friction variation between the samples' acceleration and deceleration zones were detected predominantly in the mixed regime, whereby the friction is higher when the samples were accelerating, as a consequence of the squeeze film effect occurring shortly after reversal.

- Of all textured shapes tested in this study, grooves perpendicular to the direction of sliding showed the highest level of effectiveness for all mixed and boundary regime tests, closely followed by the chevron pattern. Grooves parallel to the sliding direction were the least effective, performing worse than the smooth reference pad in all three lubrication regimes.

Chapter 5

PARAMETRIC STUDY OF SURFACE TEXTURE

5.1   Introduction

Once the criteria for effective pocket shape were identified (*i.e.* rectangular features, that fit within contact area and have their long axis transverse to sliding textured), the next step of the research was to identify the ideal geometric parameters of the textured features. A series of specimens comprising variations of the best performing textured shape (TrG − grooves normal to the direction of sliding) were employed to study the influence of pocket depth, breadth and density on friction force.

Specimens were textured with varying density, depth and breadth and again tested under a range of conditions, placing the bearing under different lubrication regimes. Each geometrical parameter was varied and tested independently, while keeping the other two constant. The measurements were finally used to determine the criteria for varying pocket spacing, depth and breadth along the stroke.

Although the data were obtained under reciprocating transient conditions, friction data presented in this chapter will be plotted as Stribeck curves, to give an optimum visualisation of the impact of each geometric parameter under various lubrication regimes. In addition, in certain cases, the variation in friction with stroke angle is presented. Comparing the two methods of visualisation reveals the importance of varying the pocket characteristics along the stroke.

5.2   Test specimens and experimental procedure

All tests assessing geometries employed an AISI 52100, 850 HV fully hardened, 2 mm width specimen, similar to that presented in Chapter 4, to replicate the piston ring. This was ground at a 41 mm radius and mirror polished to obtain a smooth surface, whose main roughness values are presented in figure 5.1.
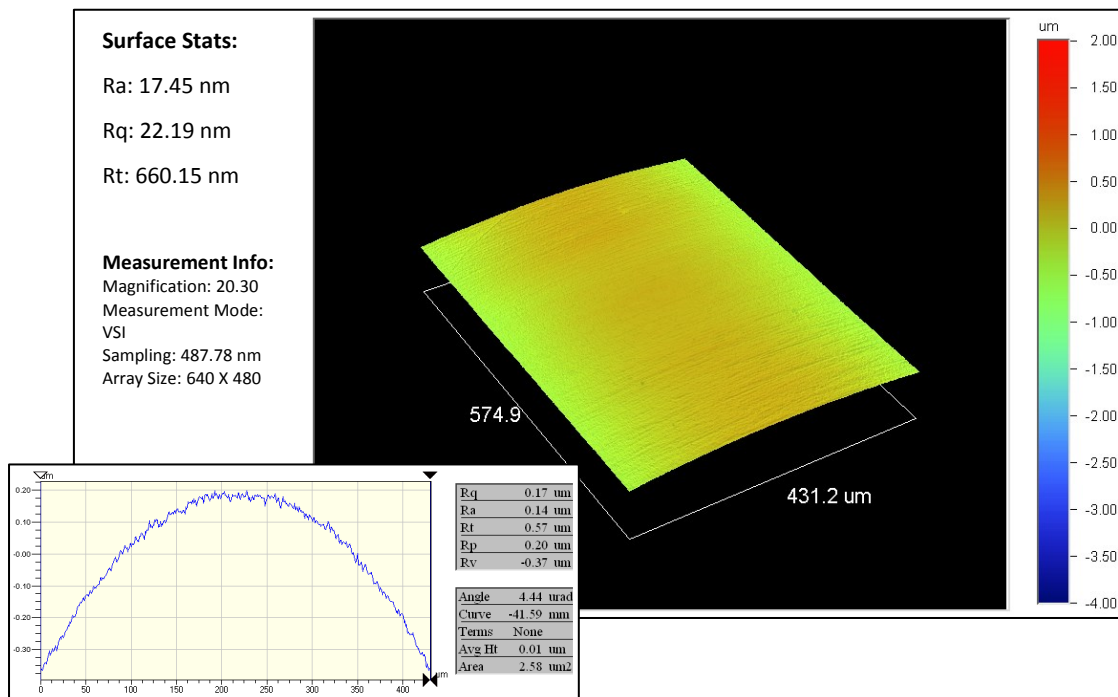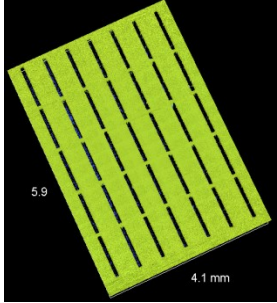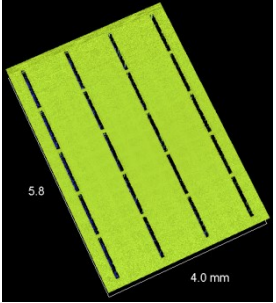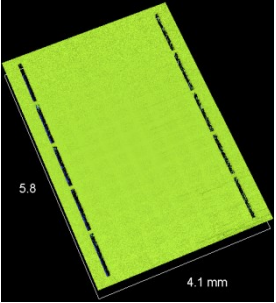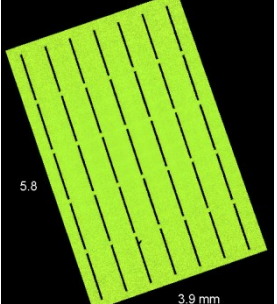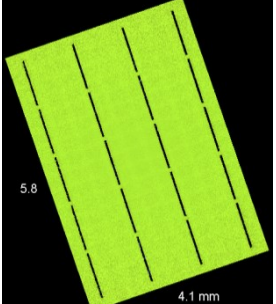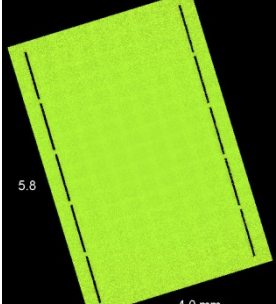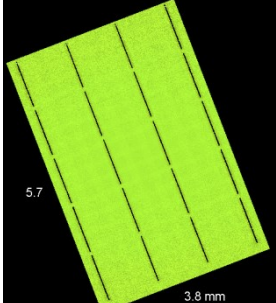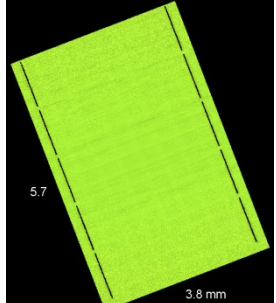
FIGURE 5.1: Three dimensional surface plot of the convex AISI 52100 steel specimen used for the parametric study; roughness average Ra=17 nm, curvature radius 41.6 mm.

A new batch of fused silica specimens was laser textured for the parametric study. Pocket shape and orientation were held constant (*i.e.* grooves transversal to the direction of sliding), while the separation (gap between pockets), depth and breadth of the pockets were varied to obtain the patterns presented in tables 5.1 to 5.3. To determine optimal density, three different separations were tested (*i.e.* 500 μm, 1100 μm and 3300 μm) while keeping depth and breadth constant. The matrix employed for texture density tests is presented in table 5.1. Two separate tests were performed to assess the impact of pocket depth: one to compare 3 μm against 8 μm depths, and another to compare 8 μm against 20 μm patterns (table 5.2). Finally, three different pocket breadths were compared, while keeping density and depth constant: 20 μm, 80 μm and 300 μm. An important observation is that the pattern comprising 300 μm wide textured features was the only one with pockets wider than the elastic contact area (usually 180–200 μm wide). The geometry together with visual exemplifications of the textured patterns employed for the pocket breadth comparisons are exhibited in table 5.3.

TABLE **5.1**: Geometry and visual exemplification of the selected textured patterns employed for pocket density comparisons.

Density Comparison No.	Specimen geometry		
1	*Breadth Depth Separation* **80μm×8μm×500μm**	*Breadth Depth Separation* **80μm×8μm×1100μm**	*Breadth Depth Separation* **80μm×8μm×3300μm**
2	*Breadth Depth Separation* **40μm×7μm×500μm**	*Breadth Depth Separation* **40μm×7μm×1100μm**	*Breadth Depth Separation* **40μm×7μm×3300μm**
3	–	*Breadth Depth Separation* **20μm×20μm×1100μm**	*Breadth Depth Separation* **20μm×20μm×3300μm**

TABLE 5.2: Geometry and visual exemplification of the selected textured patterns employed for pocket depth comparisons.

TABLE 5.3: Geometry and visual exemplification of the selected textured patterns employed for pocket breadth comparisons.

All textured specimens detailed above, as well as the non-textured reference were subject to tests at varying crank angle velocities, between 0.15 Hz and 6 Hz. Velocity was manipulated in order to place the reciprocating bearing under the full range of lubrication regimes (*i.e.* boundary, mixed and the transition between mixed and full film) without the need to vary the temperature and consequently the viscosity of the fully formulated oil. A lubricant temperature of 60ºC was set for the entire parametric study, representing the optimal level at which all lubrication regimes required could be achieved given the velocity limitations of the test rig. The viscosity properties of the lubricant at this selected temperature are presented in table 5.4.

TABLE **5.4**: Properties of the fully formulated engine oil at 60°C used during the test session

Oil Temperature [ºC]	Oil properties			Load, W [N]
	Dynamic viscosity, η [mPa·s]	Kinematic viscosity, ν [mm^2/s]	Density, ρ [g/cm^3]	
60	35	42	0.841	70

5.3　Results and discussion

Over the full set of tests, friction data were recorded as a function of crank angle along the entire stroke. However, for optimum visualisation of the impact of surface texture geometry on friction under different lubrication regimes, the results are graphically depicted throughout this chapter as master Stribeck curves. This approach has two key advantages: *i)* it allows the determination of the optimum functioning regime for each geometrical parameter; *ii)* it allows the matching between tests performed in this study and a real IC engine scenario, enabling the author to define a set of criteria for varying pocket spacing, depth and breadth along the stroke in a real IC engine. To draw the master Stribeck curves corresponding to each different scenario, friction data captured for all tested specimens between 30º and 150º crank angle were plotted against speed × viscosity, as presented in figures 5.2 and 5.4 to 5.8. As previously mentioned, this

visualisation allows the squeeze film effects before and after reversal point to be removed.

5.3.1   Influence of texture density on friction force

The parametric study started by varying texture density. Figure 5.2 illustrates the variation in friction coefficient for three textured specimens comprising pockets of constant breadth (80 μm) and depth (8 μm), while varying the spacing between two consecutive lines of features from 500 μm to 1100 μm and finally 3300 μm.
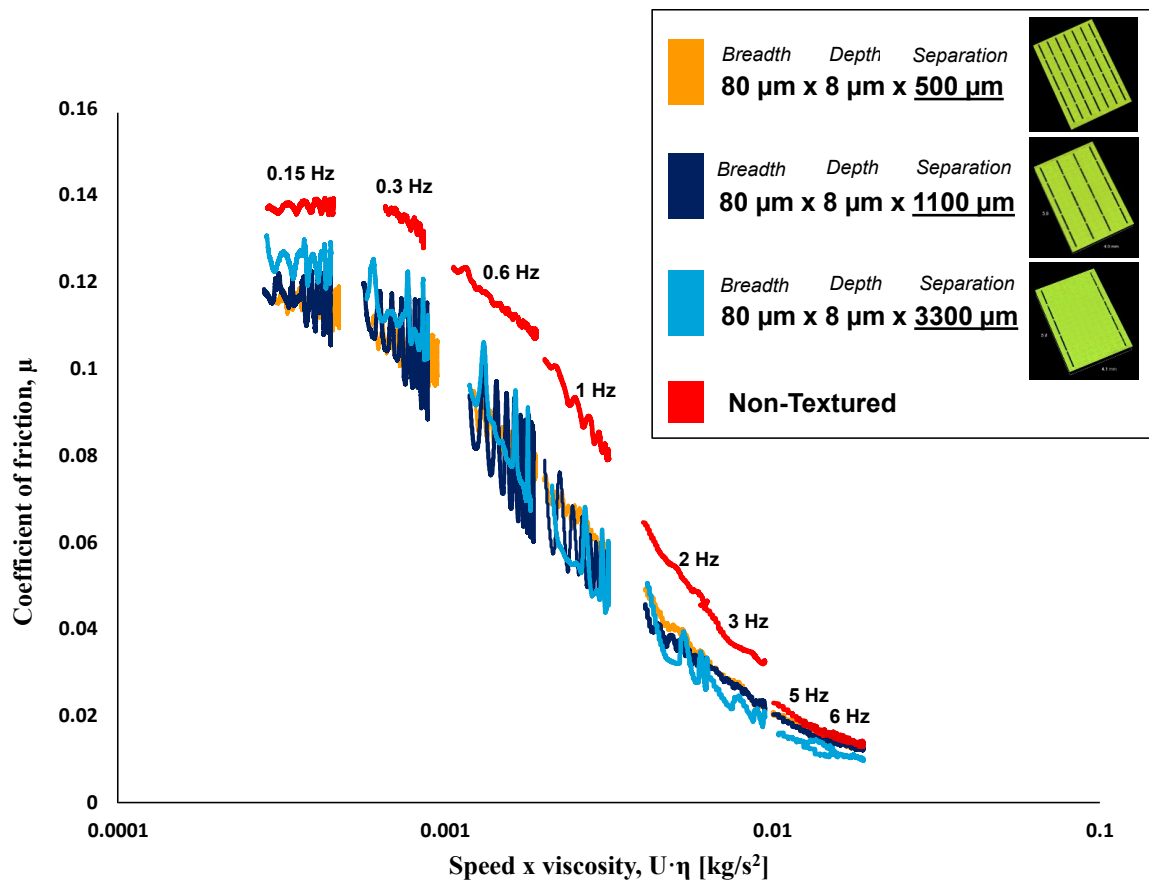
FIGURE 5.2: Master Stribeck curves showing friction behaviour for three textured specimens with different pocket spacing (500 μm, 1100 μm and 3300 μm) and the non-textured reference. Pocket breadth: 80 μm, pocket depth: 8 μm.

Observations of the resulting friction coefficient curves leads to the conclusion that a denser laser texture is desired when the bearing runs under boundary lubrication regime (*i.e.* crank angular velocities of 0.15 Hz and 0.3 Hz), whereas as the speed increases and

the bearing moves first towards the mixed and then the transition between mixed and full film regime a sparser textured area is preferable to reduce friction. It can be observed in figure 5.2 that the textured pattern which performs best under boundary regime (*i.e.* 500 µm gap between pockets) displays the highest friction coefficient of all textured patterns at the transition between mixed and hydrodynamic regime and vice versa.

This conclusion is verified by observing the variation in friction force along the stroke shown in figure 5.3. Here, it can be seen that during the first 30º crank angle, (where due to low velocity, the contact is in the transition between boundary and mixed regime) the denser 1100 µm spaced specimen generates lower friction when compared with the sparser, 3300 µm spaced, specimen. However, as velocity increases towards the middle of the stroke between 30º and 150º crank angle where the bearing is shifted towards the transition between mixed and full film regime, it can observed that the sparser textured specimen shows a lower friction response than the denser one.
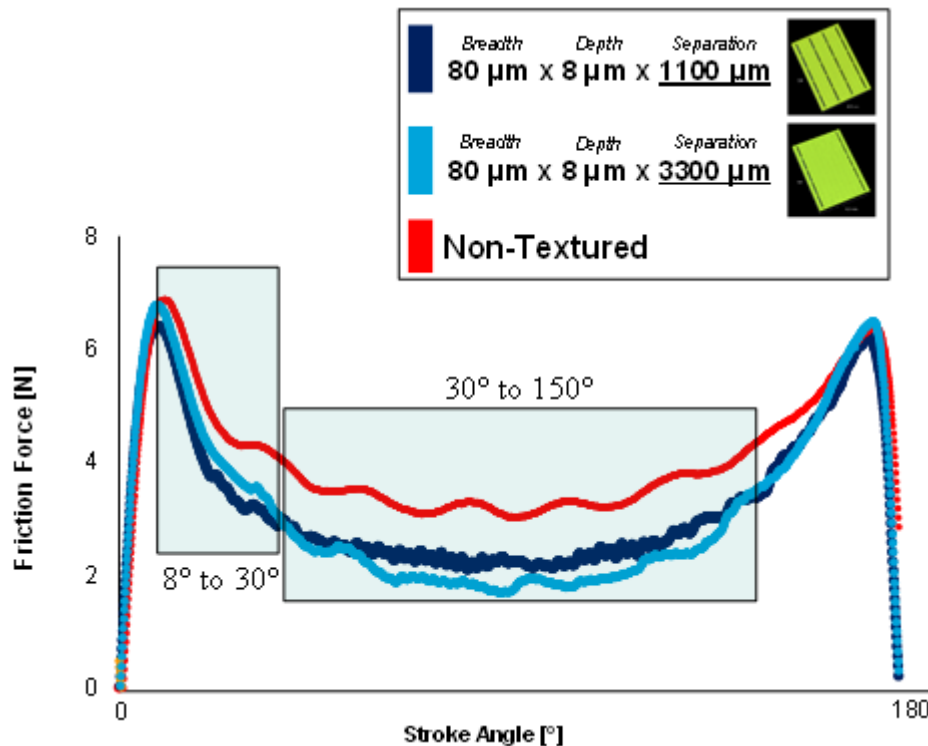
FIGURE 5.3: Friction behaviour along one stroke for two textured specimens with different pocket spacing (1100 µm and 3300 µm) and the non-textured reference.

The real world implication of these findings is that, to achieve maximum friction reduction in an IC engine, denser textured features must be applied close to top and bottom dead centres (where as detailed in Appendix B the piston ring–liner bearing operates in the boundary and mixed regimes during the power stroke) and sparser pockets towards the middle of the piston's stroke, where speed increases and the bearing approaches a full film regime.

To verify this preliminary conclusion, two additional sets of tests were performed employing different pocket geometries. Figure 5.4 illustrates master Stribeck curves plotted for three textured specimens with the same spacing values (500 µm, 1100 µm and 3300 µm), again holding pocket breadth and depth constant at 40 µm and 6 µm respectively.
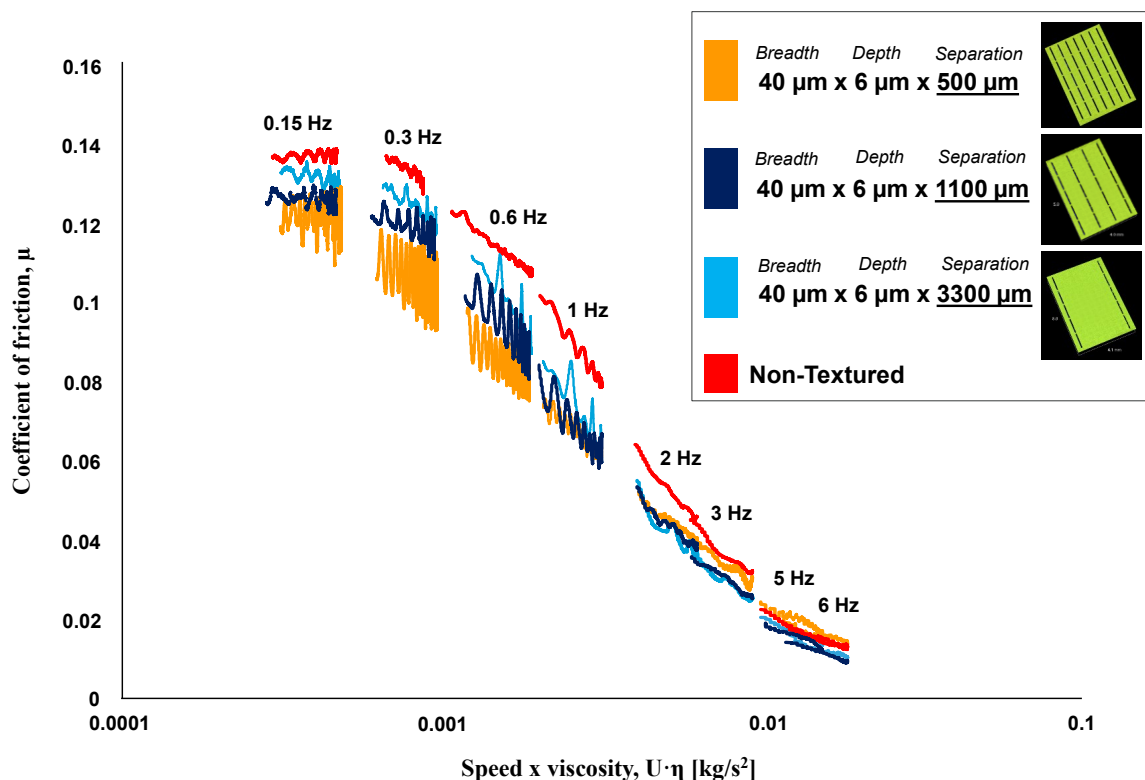
FIGURE 5.4: Master Stribeck curves showing friction behaviour for three textured specimens with different pocket spacing (500 µm, 1100 µm and 3300 µm) and the non-textured reference. Pocket breadth: 40 µm, pocket depth: 6 µm.

Similar friction behaviour as shown in figure 5.2 can be observed, with the denser pattern again exhibiting the lowest friction coefficient when running under boundary and mixed regimes. Moreover, as previously shown in Chapter 4, as soon as the full film regime is reached, the densest textured pattern exhibits a higher frictional response when compared with the non-textured reference.

Finally, the influence of pocket spacing was confirmed by employing two textured specimens with shallower (20 μm breadth) and deeper (20 μm depth) pockets. Although only the 1100 μm and 3300 μm pocket spacing were tested (due to financial limitations the texturing of the 500 μm spacing pattern was not possible), similar findings regarding the criteria of pocket spacing variation along the stroke were achieved: denser texture is desired when the bearing runs in boundary regime, while sparser texture is preferable when the contact operates at the transition between mixed and hydrodynamic regime (figure 5.5).
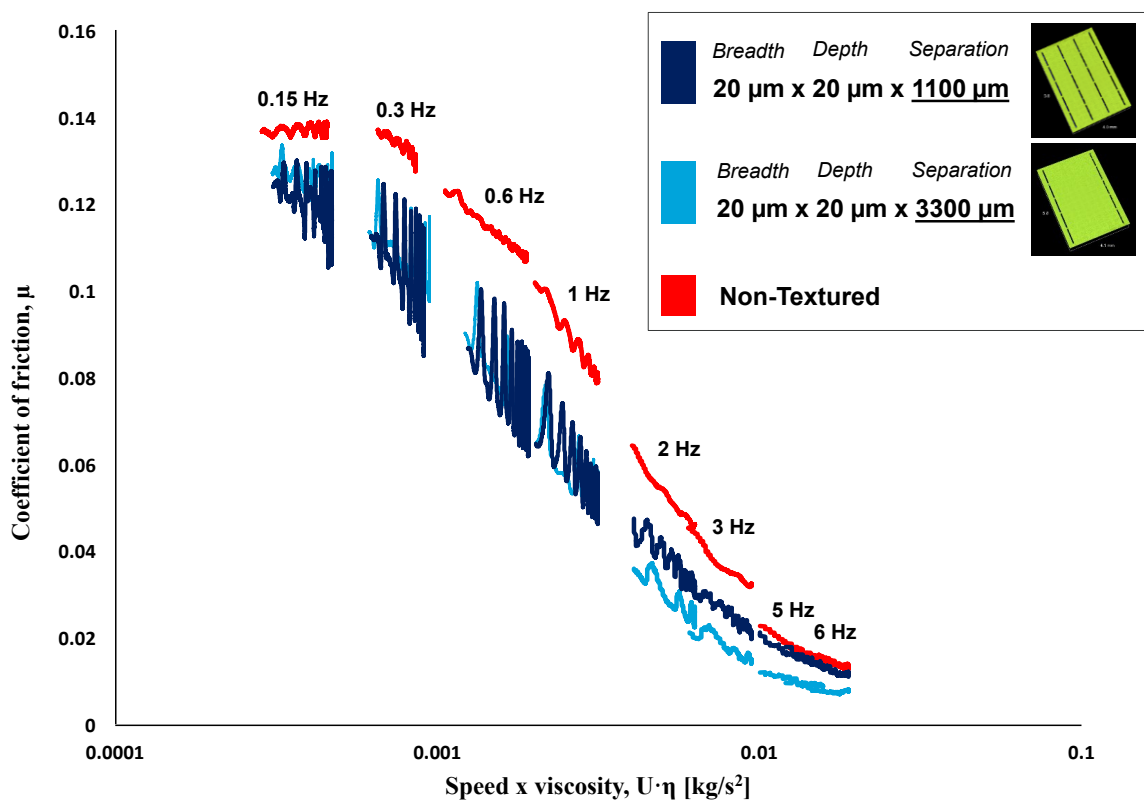
FIGURE 5.5: Master Stribeck curves showing friction behaviour for two textured specimens with different pocket spacing (1100 μm and 3300 μm) and the non-textured reference. Pocket breadth: 20 μm, pocket depth: 20 μm.

5.3.2   Influence of pocket depth on friction force

Once the pocket spacing criteria along the stroke have been established, the research focused on the influence of pockets depth on friction force. Two separate sets of tests were performed employing specimens of constant pocket breadth and spacing and variable depths. Figure 5.6 illustrates the friction variation for two identically spaced patterns (1100 µm), with features of the same breadth (20 µm), but with two different pocket depths: 8 µm and 20 µm. The deeper pattern prove optimal when the bearing runs in boundary and at the transition between boundary and mixed regime. However, on the steep part of the Stribeck curve, as soon as a film forms between the counterpart surfaces, deeper texture becomes detrimental when compared with shallower pockets.
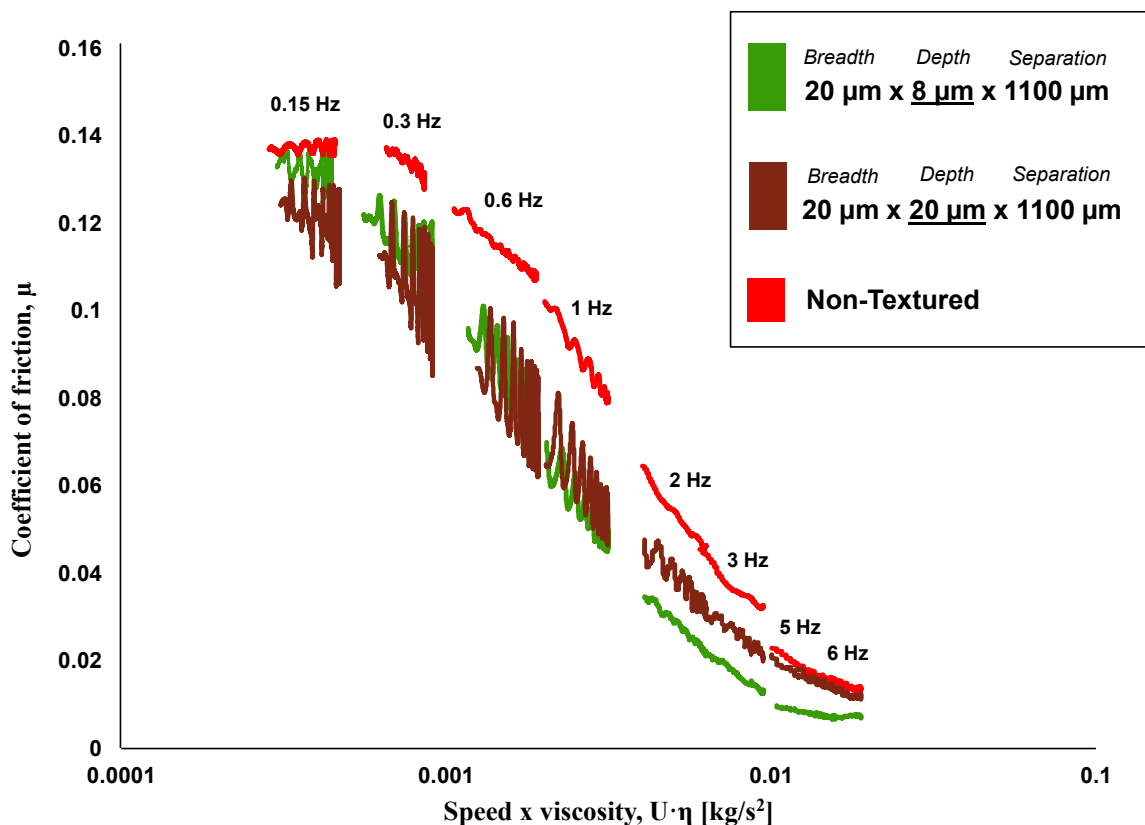
FIGURE 5.6: Master Stribeck curves showing friction behaviour for two textured specimens with different pocket depths (8 µm and 20 µm) and the non-textured reference. Pocket breadth: 20 µm, pocket spacing: 1100 µm.

When comparing textured patterns comprising features with depths of 3 µm and 8 µm (constant breadth, 80 µm, and constant pocket spacing, 500 µm), superior friction

performance along the entire Stribeck curve was recorded for the deeper pattern (8 μm), as illustrated in figure 5.7. Another observation is that at the transition between mixed and full film regime (crank angular velocity: 6 Hz), the shallower pattern resulted in higher friction than the non-textured reference, while the effect on friction of the deeper pocketed area is close to undistinguishable when compared with the non-textured sample.
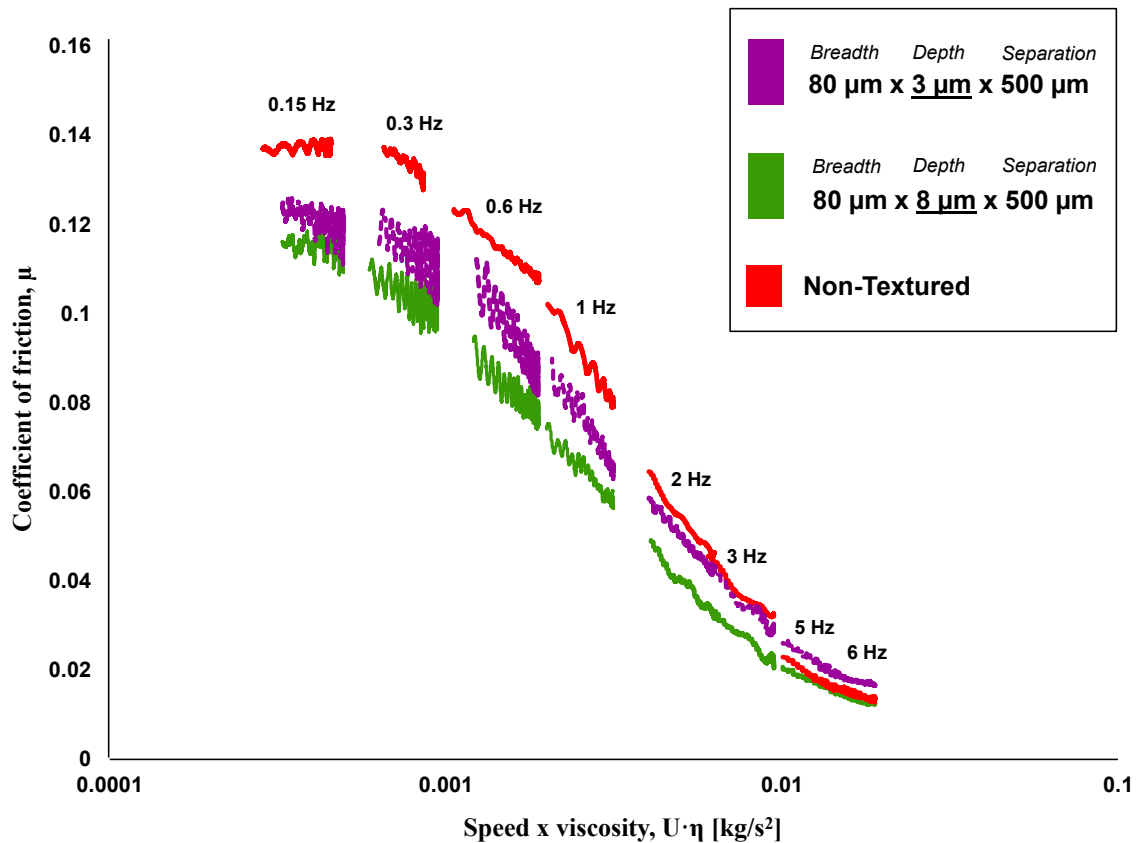
FIGURE 5.7: Master Stribeck curves showing friction behaviour for two textured specimens with different pocket depths (3 μm and 8 μm) and the non-textured reference. Pocket breadth: 80 μm, pocket spacing: 500 μm.

As only three depth values were tested in the current research, additional investigations are required to accurately identify the optimum pocket depth, which will likely be a value between 3 μm and 20 μm.

This friction reduction behaviour observed in figures 5.6 and 5.7, as well as the previously demonstrated impact of pocket spacing on frictional response, suggested a correlation between friction force and the amount of oil which can be trapped within

pockets – the higher the quantity of lubricant fed by the textured pattern to the contact area, the lower the friction force when running in boundary and mixed conditions. As a result of this finding, it was decided to extensively investigate the oil replenishment mechanism, with results presented in Chapter 8.

5.3.3   Influence of pocket breadth on friction force

Finally, the influence of pockets breadth on friction is explored in figure 5.8. Here, friction coefficient curves are plotted for three different textured patterns: two which exhibit pocket breadths smaller than the elastic contact area (20 µm and 80 µm) and one with a feature breadth greater than the elastic contact area (300 µm).
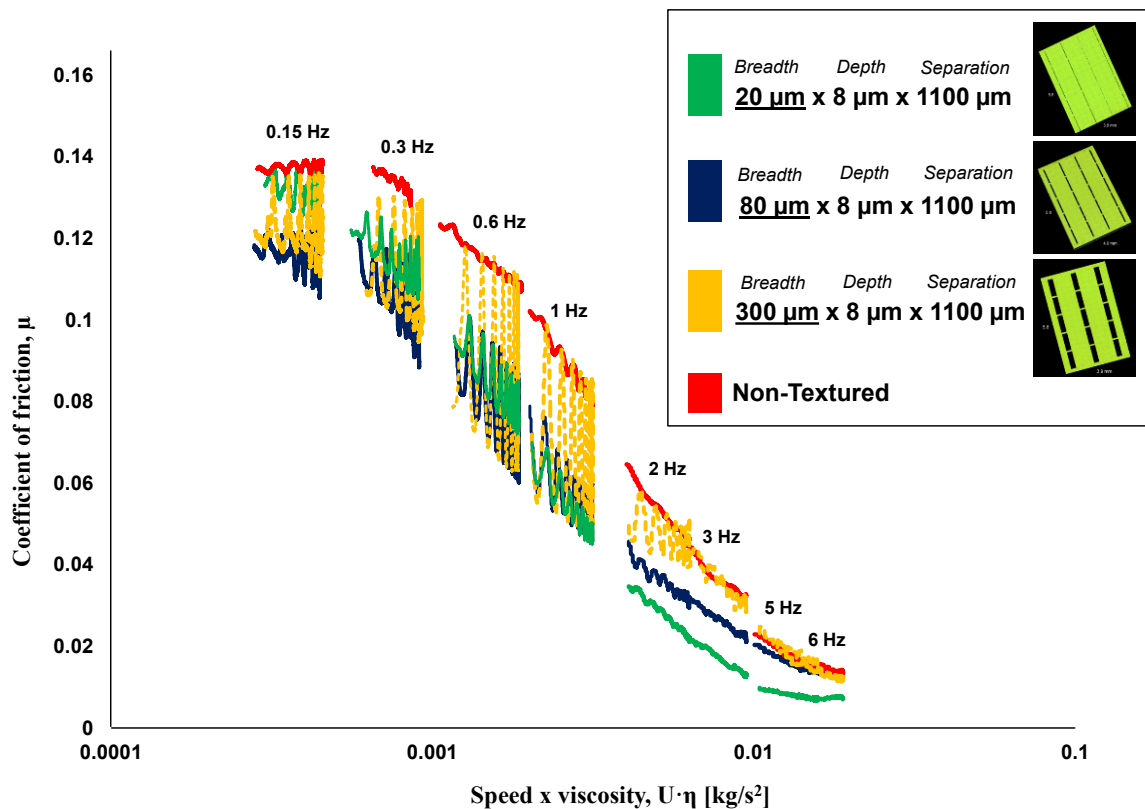
FIGURE 5.8: Master Stribeck curves showing friction behaviour for three textured specimens with different pocket breadths (20 µm, 80 µm and 300 µm) and the non-textured reference. Pocket depth: 8 µm, pocket spacing: 1100 µm.

These reciprocating sliding tests revealed that the sample comprising features with a breadth of 80 μm exhibited the lowest friction coefficient when the bearing ran in boundary and at the transition between boundary and mixed lubrication regime, while the 20 μm wide features showed significant decreases in friction, compared to all other specimens, when running at the transition between mixed and full film regime.

Although the friction coefficient corresponding to pockets wider than the elastic contact area (300 μm breadth) was lower throughout the test procedure when compared with the non-textured reference, this exhibited higher friction along the Stribeck curve when compared with the 80 μm breadth pockets. Moreover, significant friction peaks were recorded every time a line of pockets entered the contact, a behaviour which is explained in detail in Chapter 7.

Future work will determine the optimum pocket breadth applicable especially when the bearing runs under boundary conditions, with a value situated between 80 μm and 300 μm.

Concerning the application of surface texture to real IC engines, it can be concluded that pockets breadth should be graded along the stroke, as wider pockets show superior performance under boundary conditions while narrower pockets operate better at the transition between mixed and full film lubrication regime.

5.4 Conclusions

A series of fused silica specimens comprising geometric variations of the optimally performing textured shape identified in Chapter 4 (*i.e.* grooves normal to the direction of sliding) were employed to identify the criteria for varying pocket depth, breadth and density along the stroke to further reduce friction force. Key conclusions from this parametric study include:

- In agreement with findings presented in Chapter 4, all textured surfaces proved beneficial under boundary and mixed lubrication conditions; conversely, when approaching the full film lubrication regime, the tribological performance of

laser surface textures becomes negligible or even detrimental when compared with the non-textured reference.

- Densely textured micro-features showed highest effectiveness under mixed and boundary regimes, while sparser texture patterns exhibited maximum friction reduction at the transition between mixed and thick film regimes (see figure 5.9 for the schematic representation). This behaviour was observed in all the different pocket spacing tests and led to the conclusion that in real IC engines dense textured patterns are desired immediately before the top and bottom dead centres are reached.
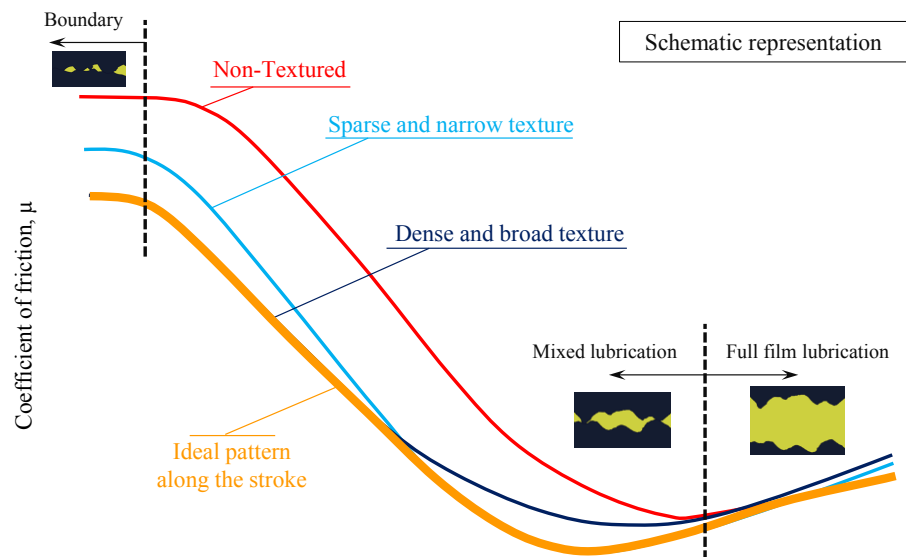
FIGURE 5.9: Schematic representation of master Stribeck curves explaining criteria for varying pocket spacing along the stroke.

- Pocket depth shows an inverse correlation with friction coefficient under boundary and at the transition between boundary and mixed regime, and is positively correlated to friction on the steep part of the Stribeck curve. In the latter instance, deeper textures become detrimental when compared with shallower ones.
- 80 µm wide pockets reduce friction coefficient to a minimum when the bearing runs in boundary and at the transition between boundary and mixed lubrication regime, whilst pockets of the 20 µm showed a significant decrease in friction as the full film regime is approached. In agreement with the conclusions of Chapter 4, pockets must be entirely entrapped within the elastic contact area - 300 µm

wide pockets result in frequent peaks in friction, on average delivering inferior tribological results.

- The implication on real IC engine texturing is that geometry positioning should vary according to the alternating lubrication regimes along piston stroke.

It should be noted that the conditions tested in this chapter closely replicate those in a piston-liner contact, with texture applied to the liner surface. Numerous other texture configurations and contact conditions are possible (such as texturing that has zero velocity in relation to the moving contact), where these conclusions may not be relevant.

Chapter 6

SIMULTANEOUS MEASUREMENTS OF LUBRICANT FILM THICKNESS AND FRICTION FORCE

6.1   Introduction

One of the key aims of this project was to establish the connection between the variation in friction force from textured to non-textured specimens and the corresponding changes in lubricant film thickness that occur when the contact operates under various lubrication regimes. As a result, film thickness was measured using a modified version of the ultra-thin film optical interferometry approach, enabling film thicknesses of <50 nanometres to be measured under mixed lubrication conditions. As detailed in section 6.2, this involved using the out-of-contact curvature of the specimens in place of a spacer layer and analysing multiple interference fringes to avoid fringe ambiguity. Tests were performed on both a textured sample (with features oriented normal to the direction of sliding) and a non-textured reference sample, while angular velocity, applied normal load and lubricant temperature were controlled in order to study the effect of varying lubrication regime, as typically occurs in internal combustion engines. These results are important in providing film thickness data to validate piston-ring lubrication models and also in helping to understand the effect of surface roughness on texture performance.

6.2   Determination of film thickness using a multiple wavelength, out of contact, ultrathin-film interferometry approach

The piston-liner contact frequently operates in the mixed and boundary lubrication regimes with film thickness less than 100 nm. Using interferometry, it is not possible to measure such thin films directly, since values in this range do not provide a sufficiently large path difference between the light rays to cause interference. To ensure that the optical gap between the sliding surfaces is greater than ½ the wavelength of light, and hence cause interference fringes, a *"spacer layer"* is typically applied to the contacting surface of the transparent specimen. The invisible spacer layer, which increases the measured film thickness by virtue of having a refractive index close to that of the test lubricant and its thickness, determined prior to testing, is subtracted from each test measurement. In this work, however, a silica spacer layer had to be avoided since it would alter the topography of the pocketed surface of the transparent specimen.

Furthermore, due to the sliding nature of the contact, operating under mixed lubrication conditions, any surface coatings present would be removed rapidly due to wear. Therefore, a modification was devised, in which the effect of the spacer layer was reproduced by using the out-of-contact curvature of the ring specimen – *i.e.*, as shown in figure 3, the measurement location was chosen outside the contact area so that each measurement was a composite of the lubricant film thickness and the 400 to 700 nm gap caused by the curvature of the ring specimen. The required curvature of the ring specimen was achieved by machine grinding a slope on to each end of the pin specimen prior to testing.
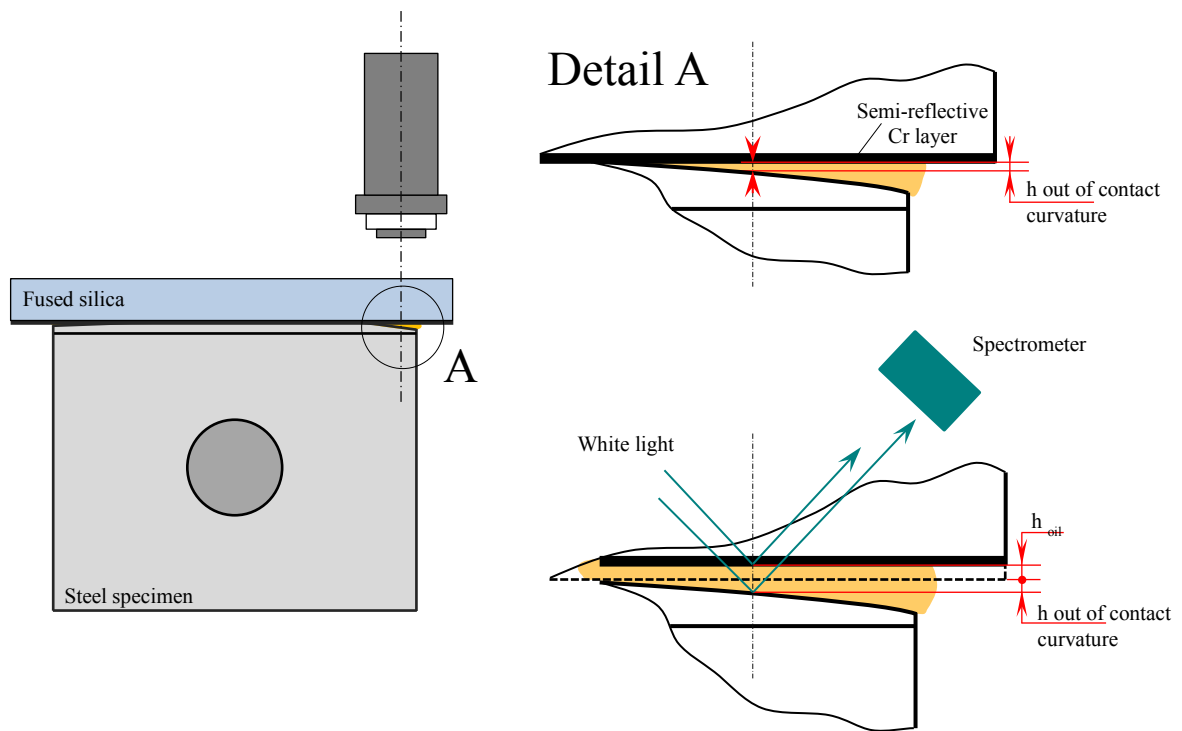
FIGURE 6.1: Principle of ultrathin film interferometry with out of contact curvature.

A challenge to overcome here is that, whereas a spacer layer's approximate thickness is known a priori, the out-of-contact gap is not known and therefore the fringe order is not available to be used in the film thickness calculation. To overcome this problem, a second modification was made, whereby the film thickness was calculated based on the difference in wavelength between adjacent interference fringes. The equation to enable this calculation is obtained as follows.

Constructive interference occurs when the light beam, reflecting off the lower surface of the oil film, has travelled an integer number of wavelength further than the beam reflected of the upper surface according to

$$h = \frac{(N-\phi)\lambda_N}{2\,n\,\cos\theta} \qquad (6.1)$$

where h is the spatial thickness of the oil film, n is its refractive index, λ_N is the wavelength associated with the Nth order fringe, θ is the angle of incidence of the oil and ϕ is any phase change that occurs on reflection (expressed as number of wavelengths).

If white light containing a broad range of wavelengths is used, then, for the same film thickness, h, Equation 1 will be satisfied for several different values of N. For example, some smaller wavelength, λ_{N+1}, will result in the $N^{th}+1$ interference fringe according to

$$h = \frac{(N+1-\phi)\lambda_{N+1}}{2\,n\,\cos\theta} \qquad (6.2)$$

If Equations 1 and 2 are equated and rearranged, an expression for h is obtained in which the fringe order and the phase change are absent

$$h = \frac{\lambda_N\,\lambda_{N+1}}{2\,n\,(\lambda_N-\lambda_{N+1})} \qquad (6.3)$$

This relationship is useful since it enables the film thickness to be calculated from the wavelengths of any two adjacent interference fringes without requiring knowledge of the phase difference or fringe order (hence overcoming the issue of "wavelength ambiguity" that is sometimes discussed (*e.g.* see [107]). All that is needed in practice to obtain film thickness values with this approach is an intensity-wavelength image from the spectrometer that shows more than one interference peak. Usually, this condition is satisfied when large film thicknesses are measured (since they allow many wavelengths to interfere). The out-of-contact measurement method, described above, produces sufficiently large thickness (*i.e.* hundreds of nm) and makes this possible.

It should be noted that Equation 3 can also be used to calculate film thickness based on two adjacent destructive interference fringes.

In order to measure film thickness in this way, knowledge was required of the out of contact gap at each angular position along the stroke (since it varied slightly due to imperfections in the fused silica specimen and differences in alignment between the contacting surfaces). To achieve this, successive images were recorded prior to each test, under quasi static conditions (*i.e.* reciprocating at a speed of 0.1 Hz) and with the relevant normal load applied. A frame rate of 200 Hz was used here, resulting in 6 film thickness measurements for every degree of crankshaft's revolution. In this way, interference images were captured throughout four consecutive strokes (two crank revolutions) and were subsequently processed automatically using a custom Matlab code. This processing consisted of a) averaging, b) calibrating out erroneous spectral intensity variations, c) identifying the wavelengths that corresponded to adjacent interference peaks and d) applying Equation 3 to give film thickness. The resulting variation in gap height with angular position was then stored to be used in the subsequent test (this is analogous to the spacer layer thickness being recorded in conventional thin film interferometry). Each test involved increasing the speed to the required value, acquiring images at the same out of contact location, and processing with the same Matlab code (described above) to give the film thickness variation along the stroke. Then, to obtain the in contact film thickness, the quasi static film thickness was subtracted from each test measurement at the correct angular position (*i.e.* the out of contact gap was removed from the measured thickness). This was possible, since the angular position at which each image was acquired was recorded, alongside film thickness, thanks to the trigger system and the rotary encoder.

In summary, the optical interferometry technique was selected and modified for this research for two main reasons: *i)* it is now believed that texture is most effective under mixed lubrication conditions ([10,19,22,92]) where film thicknesses are in the nanometre range and hence this technique is most effective, *ii)* the use of conventional LIF techniques were not possible for such textured surfaces, as measurements are distorted by additional light escaping from inside the pocket which is nearly an order of magnitude deeper than the contact film thickness.

6.3   Test specimens and experimental procedure

Real-time measurements of frictional force were acquired simultaneously with film thickness using a LabView programme. Fully formulated SAE 40 oil was supplied to the reciprocating contact, and its temperature and consequently viscosity were controlled accurately. Table 6.1 shows the lubricant properties for three distinct temperatures, selected in order to place the reciprocating bearing in various lubrication regimes. In one set of tests the speed was varied between 1 Hz and 3 Hz for a constant load of 10 N, while in a second set, progressive loads (10 N, 30 N and 50 N) were applied for a constant speed of 3 Hz. In addition to the repeated out-of-contact-film thickness calibration described in Section 6.2, isometric load cell calibrations were performed before and after each test sequence (as previously detailed in Section 3.5.1).

TABLE **6.1**: Properties of the fully engine formulated lubricant at the desired temperatures selected for this study.

Oil Temperature [ºC]	Oil properties		
	Dynamic viscosity, η [mPa·s]	Kinematic viscosity, v [mm^2/s]	Density, ρ [g/cm^3]
15	274	315	0.8689
45	62	73	0.8502
80	19	23	0.8283

A 10×10×2 mm rectangular steel pad (AISI 52100) was employed throughout this testing session. One surface of the 2 mm width side was ground at a 40 mm radius in the sliding direction to produce a convex form. Accurate measurements of both friction and film thickness relied on high quality finish, which was achieved (as depicted in figure 6.2) by polishing the surface with a synthetic short nap cloth and a 0.25 µm monocrystalline water based diamond spray. The roughness parameters of the steel specimen measured without taking into account the 40 mm curvature are also presented in figure 6.2.

Surface Stats:

Ra: 13.87 nm

Rq: 17. 82 nm

Rt: 580.68 nm

Measurement Info:

Magnification: 11.02

Measurement Mode: VSI

Sampling: 898.31 nm

Array Size: 640 X 480
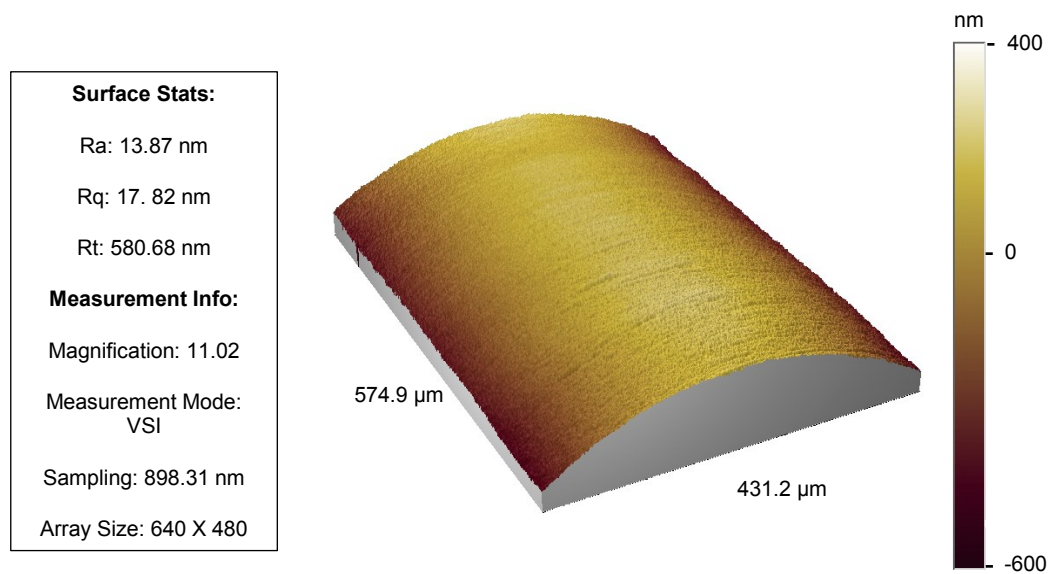
FIGURE 6.2: Three dimensional surface topography of the cylindrical steel specimen as obtained by the Veeco Wyko NT9100 optical profiler.

The three-dimensional optical profile of the counterpart fused silica textured sample is shown in figure 6.3, as recorded by a Veeco Wyko NT9100 optical profiler. The dimensions of the pockets were 7.5 µm in depth; 80 µm in breadth; 500 µm separation (gap between two lines of pockets in the direction of travel).

Again, the pocket shape was selected based on the previous experimental work presented in Chapter 4, which showed that transverse grooves normal to the direction of sliding exhibit the lowest friction force under mixed and boundary lubrication regimes when compared with other textured patterns such as chevron, crosshatch and grooves inclined or parallel to the direction of sliding. The geometric parameters of the textured area were selected according to findings presented in Chapter 5, were it is shown that a larger pocket breadth and denser texture pattern exhibited the optimal friction performances under mixed and boundary regimes. This selection will allow a better visualisation of the impact of surface texture on film thickness under low lambda ratios conditions.
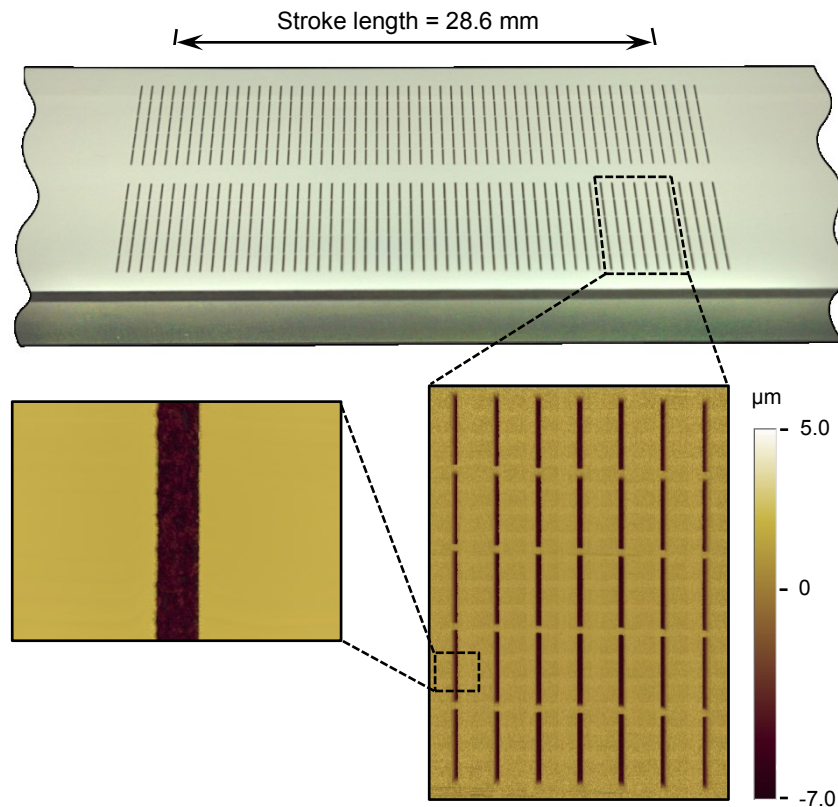
FIGURE 6.3: Two dimensional surface plot of the laser surface textured fused silica non-textured specimen.

Before starting the simultaneous film thickness-friction force test sequence, measurement repeatability and stability over time were assessed for each of the two parameters, as previously detailed in Section 3.9.

6.4   Results and discussion

The graphs shown in this section clarify the relationship between friction response and stroke angle, as well as oil film thickness and stroke angle, both as a function of applied normal load and sliding speed. The section is divided up according to the test temperature, since the lubricant temperature (and hence its viscosity) controls the lambda value and therefore the lubrication regime under which the contact is operating. For each lubrication regime, two series of tests were performed. First, the angular velocity was

varied while keeping normal applied load constant and second, the applied load was varied while keeping the crank angular velocity constant.

For each test, a comparison between the textured and non-textured specimens is presented. Both friction force and film thickness curves display cyclic fluctuations, as the sliding speed varies along the stroke length.

6.4.1 Results from full film regime – nominal lambda for non-textured specimen varying between 3.6 and 7.9

Results from the full film lubrication regime are shown in figure 6.4 and figure 6.5. Here, simultaneous friction force and film thickness test data are plotted for a constant oil temperature of 15°C (oil viscosity of 273.6 mPa·s) while varying the crank angular velocity (figure 6.4) and normal applied load (figure 6.5). These tests show the friction force increasing towards the middle of the stroke in an approximately sinusoidal fashion. This occurs because under such conditions, friction arises due the shearing the oil layers inside the contact, and is approximately proportional to the varying sliding velocity. This has been noted previously in Chapter 4, and is in good agreement with observations by Costa and Hutchings [13]. Also in agreement with hydrodynamic/elastohydrodynamic theory, it can be observed that both friction and film thickness increase with reciprocating frequency and hence entrainment speed.

From figure 6.4 (as well as 6.5) it can clearly be observed that the presence of surface texture in the full film regime results in higher friction compared with the non-textured case. These friction results support the conclusions from previous study presented in Chapter 4, where it was shown that in the full film lubrication regime the surface texture is detrimental, no matter which of the tested pocket geometries or patterns are used. Furthermore, the film thickness measurements in figures 6.4 and 6.5 show that this friction increase is caused by an increase in shear rate. The measured friction is also in agreement with those obtained by Kovalchenko et al. [19], Pettersson et al. [30] and

Costa et al. [13], in that the presence of surface texture does not significantly reduce friction force when a bearing is fully lubricated.
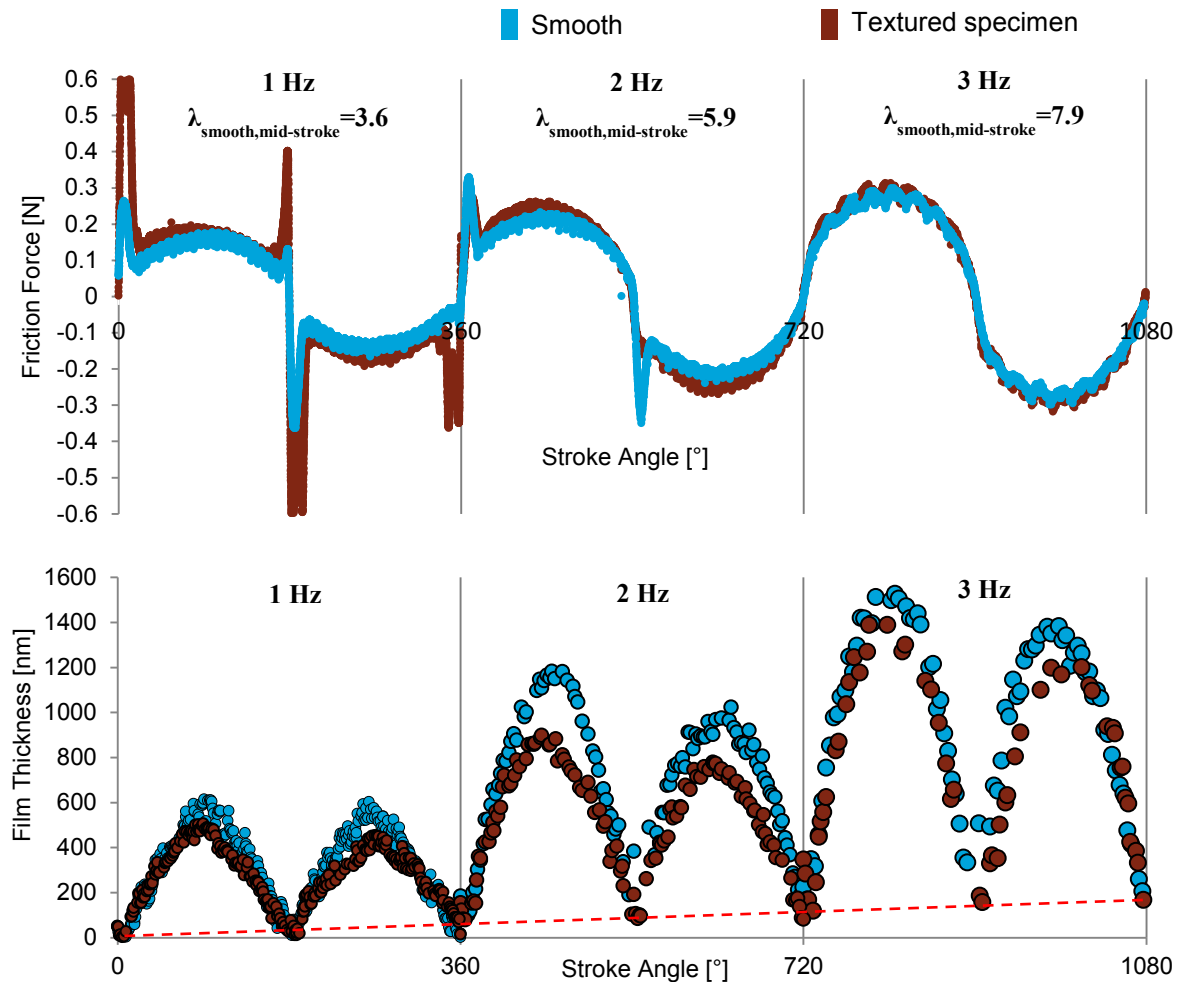
FIGURE 6.4: Simultaneous measured friction force and film thickness comparisons between textured and non-textured samples under full film lubrication regime (test conditions: crank angular velocity: 1, 2 and 3 Hz, normal load: 10 N, oil temperature: 15°C).

Figure 6.5 shows how friction force and film thickness vary with applied normal load, when the angular speed is held constant at 3 Hz. Although friction is seen to increase with applied load, the coefficient of friction reduces again according to hydrodynamic theory (*i.e.* F α u/h and h α w$^{-0.5}$, therefore μ α w$^{-0.5}$). This is confirmed by a simple analysis of the data in figure 6.5, which shows that the coefficient of friction at mid-stroke is approximately proportional to the load raised to the power 0.5.

150

Similarly to figure 6.4, figure 6.5 again shows that surface texture has a detrimental effect on film thickness in the full film regime.
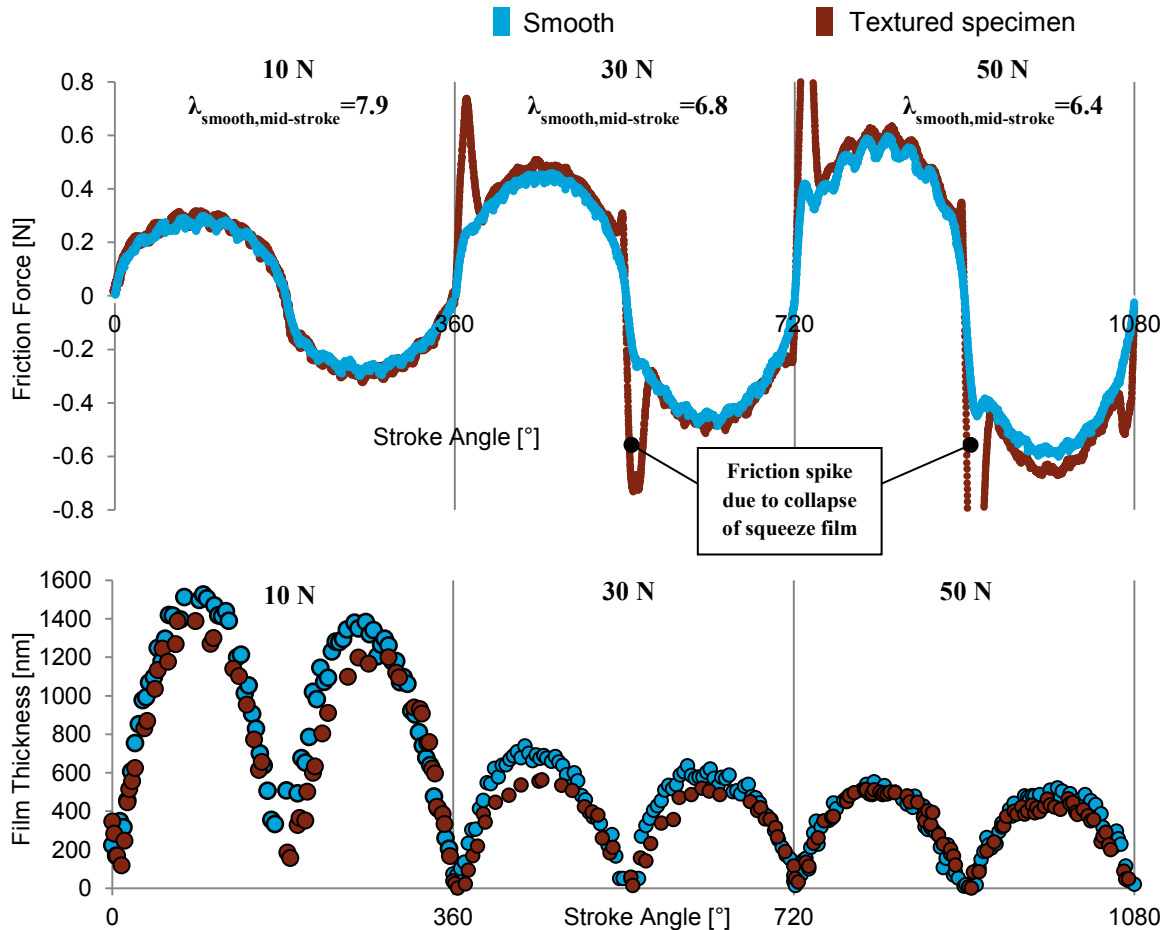
FIGURE 6.5: Simultaneous friction force and film thickness comparisons between textured and non-textured samples under the full film lubrication regime (test conditions: crank angular velocity: 3 Hz, normal load: 10, 30 and 50 N, oil temperature: 15°C).

The detrimental effect of texture features being present at the reversal point, and protruding outside the contact area, is demonstrated by figures 6.4 and 6.5. Here, pockets act to collapse the squeeze film, thus causing a pronounced friction spike as the contact enters into mixed/boundary regime.

Figure 6.5 also shows that, although for the textured specimen the friction spike after reversal is significantly higher than that of the smooth specimen, the friction force falls rapidly to the same level as, or even below, the non-textured value as the contact

accelerates (test condition: 30 N and 50 N). However, towards the middle of the stroke, the friction response of the textured specimen increases above the non-textured value.

A final detail to be noted from figure 6.4 is the variation of film thickness at the end of the stroke. As the reciprocating speed increases, the minimum film thickness at reversal increases accordingly (figure 6.4, dotted line). This demonstrates that, at high reciprocating speeds, an appreciable lubricant film remains at the reversal point and there is insufficient time to for it to be squeezed out of the contact area before the acceleration of the pad in the subsequent stroke begins to build the film thickness. This squeeze film behaviour at reversal can be seen clearly in figure 6.6, which is a zoomed-in plot of figure 6.4 (test conditions 1 Hz – 10 N), for the non-texted specimen over the first 30° of stroke angle. Here, the minimum film thickness is reached at 7° of crankshaft revolution after the reversal point. This is when the rate of film reduction due to the lubricant being squeezed out from the contact is outweighed by the increasing thickness due to hydrodynamic entrainment. The film thickness in figure 6.6(a) was used to calculate the strain rate (u/h), which is shown in figure 6.6(b), alongside the measured friction force. As expected, the maximum friction coincides with the maximum strain rate (since, under hydrodynamic conditions, friction is proportional to u/h).
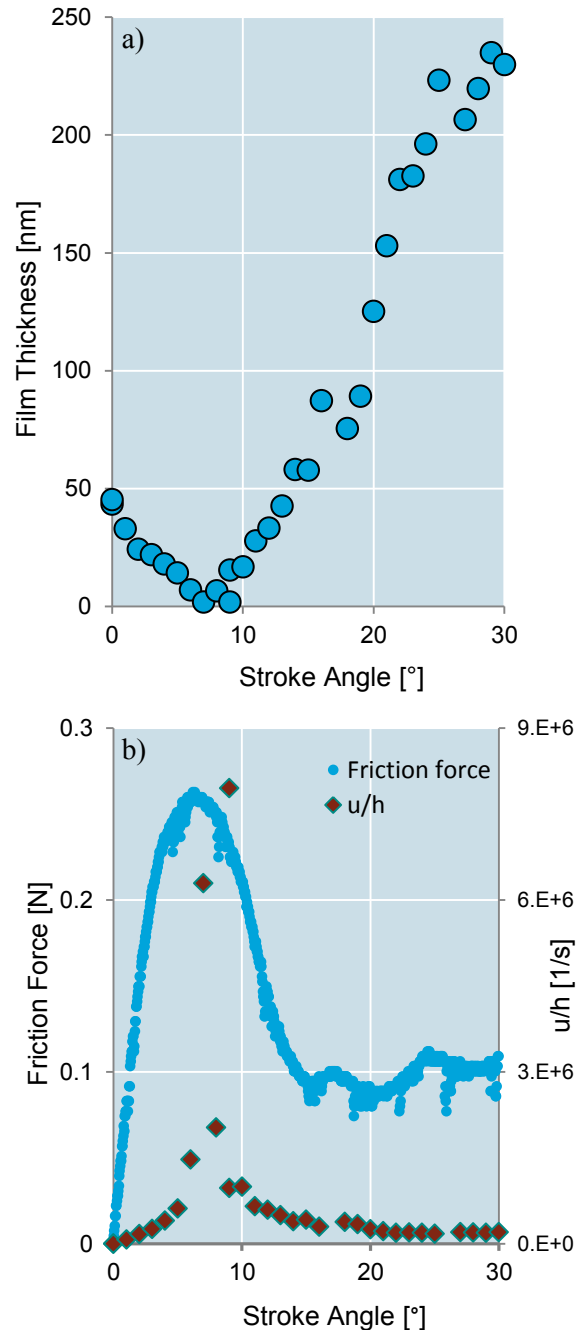
FIGURE 6.6: Oil film thickness (a) and corresponding friction force (b) captured for the non-textured specimen (test condition: crank angular velocity: 1 Hz, normal load: 10 N, oil temperature: 15°C).

A final remark relating to squeeze film effects is that the film thickness peaks are not symmetrical about the maxim value. In fact, it can be seen that the film thickness during deceleration is greater than during acceleration. This is because, during deceleration, squeeze effects prevent the film falling to its steady-state value, while, during acceleration, the converse effect prevents the film thickness reaching its steady-state value (the behaviour has been predicted recently by Medina et al [104]).

6.4.2   Results from mixed regime – nominal lambda for non-textured specimen varying between 1.3 and 2.8

When the lubricant temperature is increased to 45°C (oil viscosity: 61.73 mPa.s), the bearing contact under investigation passed from the full film lubrication regime towards the mixed regime (as the lambda value reduced). As shown previously in Chapter 4, friction values obtained around the centre of the stroke are not affected by squeeze effects and may therefore be plotted onto a master Stribeck curve. When this is done for both smooth and textured specimens, it can be seen that the latter has the effect of shifting the Stribeck curve towards the left, and this was previously attributed to an increased oil film thickness in the mixed regime (see figure 6.10). This hypothesis has been confirmed in the current study by the simultaneous measurement of friction force and oil film thickness for the test conditions corresponding to the transition from full film to mixed lubrication (figure 6.7 and figure 6.8).

As depicted in figure 6.7, the friction force for the non-textured specimen reduces with increasing reciprocating speed as a result of the contact moving from the mixed to the full film regime. The textured specimen on the other hand is less affected by the variation in reciprocating speed and as a result, there is a cross over between the friction results for the two specimens – at both 1 and 2 Hz the textured specimen outperforms the non-textured, while at 3 Hz, the reverse is true. This is because at 1 and 2 Hz, the contact is operating in the mixed regime, where texture is known to be effective, while at 3 Hz the contact is operating in the full fill regime, where texture is detrimental. The corresponding film thickness results are in complete agreement with the friction results, in that the higher friction between textured and non-textured is invariably accompanied

by a lower film thickness – *i.e.* in the mixed regime, texture increases film thickness and hence reduces asperity contact and, in turn, friction; while in the full film regime, texture reduces film thickness and hence increases shear rate and, in turn, friction.
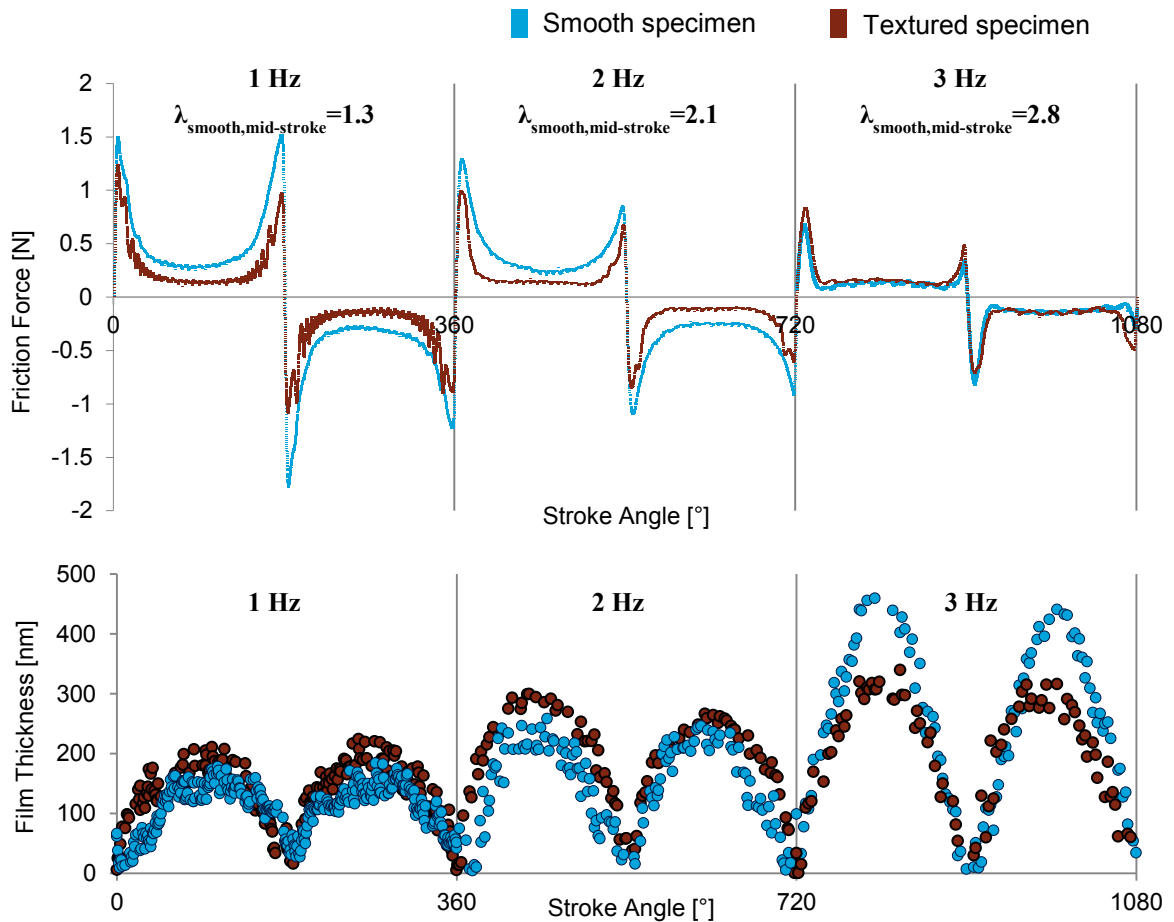
FIGURE 6.7: Simultaneous friction force and film thickness measurements, comparing textured and non-textured samples and showing the transition from mixed to full film lubrication (test conditions: crank angular velocity: 1, 2 and 3 Hz, normal load: 10 N, oil temperature: 45°C). Measurements repeatable to within: 1 Hz - 9 nm; 2 Hz - 16 nm; 3 Hz - 21 nm.

Figure 6.8 shows the effect of applied load for the oil at 45°C. Here, the transition from full film to mixed lubrication can again be seen, however, unlike figure 6.7, the beneficial effects of texture in the mixed regime are markedly less pronounced. The behaviour is tentatively attributed to the sliding speed effecting, not only the lubrication regime, but also the frequency with which the pockets are entrained into to the contact. As will be explored in Chapter 7, the pocket entrainment frequency is believed to be a key parameter in controlling the effectiveness of surface texture friction reduction.

154
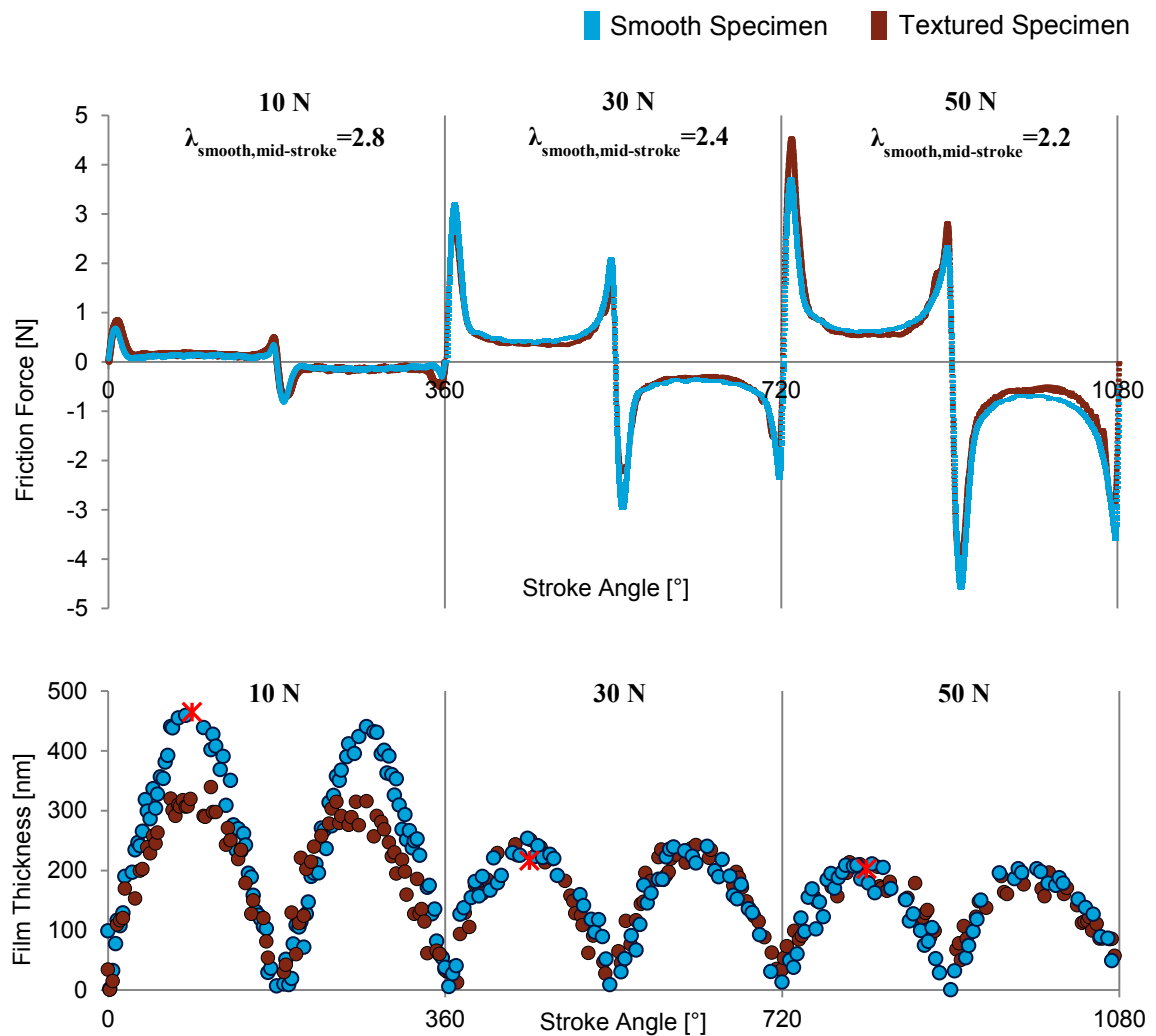
FIGURE 6.8: Simultaneous friction force and film thickness measurements, comparing textured and non-textured samples and showing the transition from full film to mixed lubrication (test conditions: crank angular velocity: 3 Hz, normal load: 10, 30 and 50 N, oil temperature: 45°C). Red asterisks denote film thickness, calculated according to[102,108].

A large change in film thickness is evident in figures 6.7 and 6.8 when comparing the 3 Hz-10 N ($\lambda_{smooth, mid-stroke}$ = 2.8) test condition to all other test conditions (in both figures 6.7 and 6.8). This can be attributed to a change in elastohydrodynamic lubrication regime – specifically, the bearing is running under rigid-isoviscous lubrication conditions for the 3 Hz-10 N test and under piezoviscous-elastic conditions for the 30 N and 50 N tests. This change in lubrication regime was verified by applying Johnson's method [109] to each set of test conditions and was further confirmed when the calculated film thicknesses (based on the appropriate lubricant regime) agreed closely with the experimental values in figure 6.8 (see red asterisks on the figure).

6.4.3 Results from mixed/boundary regime – nominal lambda for non-textured specimen varying between 0.9 and 1.2

Finally, the oil temperature was increased to 80°C (oil viscosity: 18.85 mPa.s) and friction force was recorded simultaneously with the oil film thickness response (figure 6.9). Angular velocity was kept constant at 3 Hz, while the applied normal load was varied from 10 N, to 30 N and 50 N. Here, friction reductions of up to 41% were recorded when comparing the textured and non-textured specimens. Although oil film thickness measurements were difficult under these extreme testing conditions due to vibration, data captured during four consecutive strokes were averaged and plotted against stroke angle.
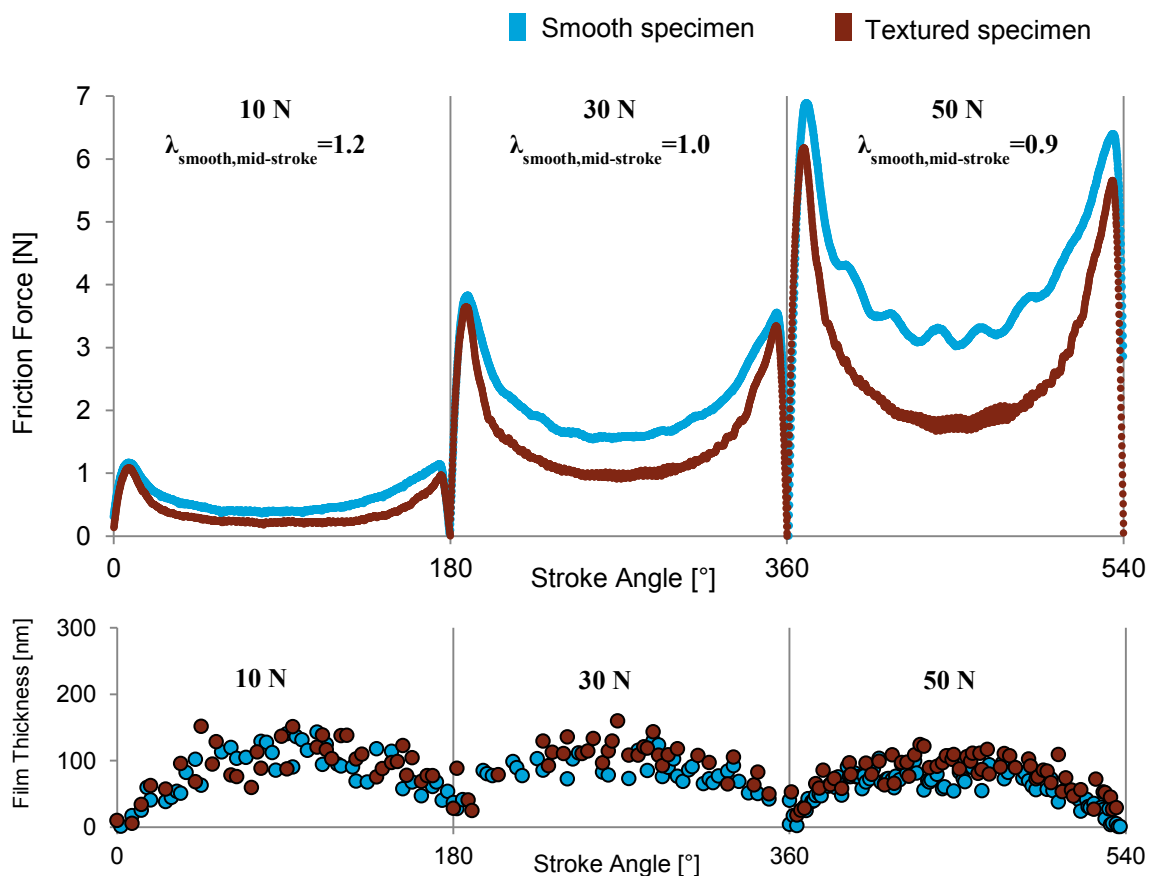
FIGURE 6.9: Simultaneous friction force and film thickness measurements, comparing textured and non-textured samples in the mixed lubrication regime (test conditions: crank angular velocity: 3 Hz, normal load: 10, 30 and 50 N, oil temperature: 80°C). Measurements repeatable to within: 10 N - 12 nm; 20 N - 10 nm; 30 N - 5 nm.

It can be seen that there is only a slight (~20 nm) difference in film thickness between the textured and non-textured specimens. At first sight, this is surprising, given the large

difference in friction force between the two. However, it should be noted that these contacts are operating in the mixed lubrication regime, where friction is highly sensitive to film thickness changes, due to the steep gradient of the Stribeck curve.

6.4.4   Summary of Results

The method described above, of plotting mid-stroke friction force from different reciprocating tests onto a single master Stribeck curve, was applied to the data in figures 6.5, 6.8 and 6.9. The result of this is shown in figure 6.10 (for a range of loads and an angular velocity of 3 Hz), where it can be seen clearly that the effect of texture is to reduce friction in mixed and boundary regime. In addition, at 45 °C the transition between mixed and full film lubrication occurs and this further explains the reversal in texture vs. non-textured performance, observed in figure 6.7.
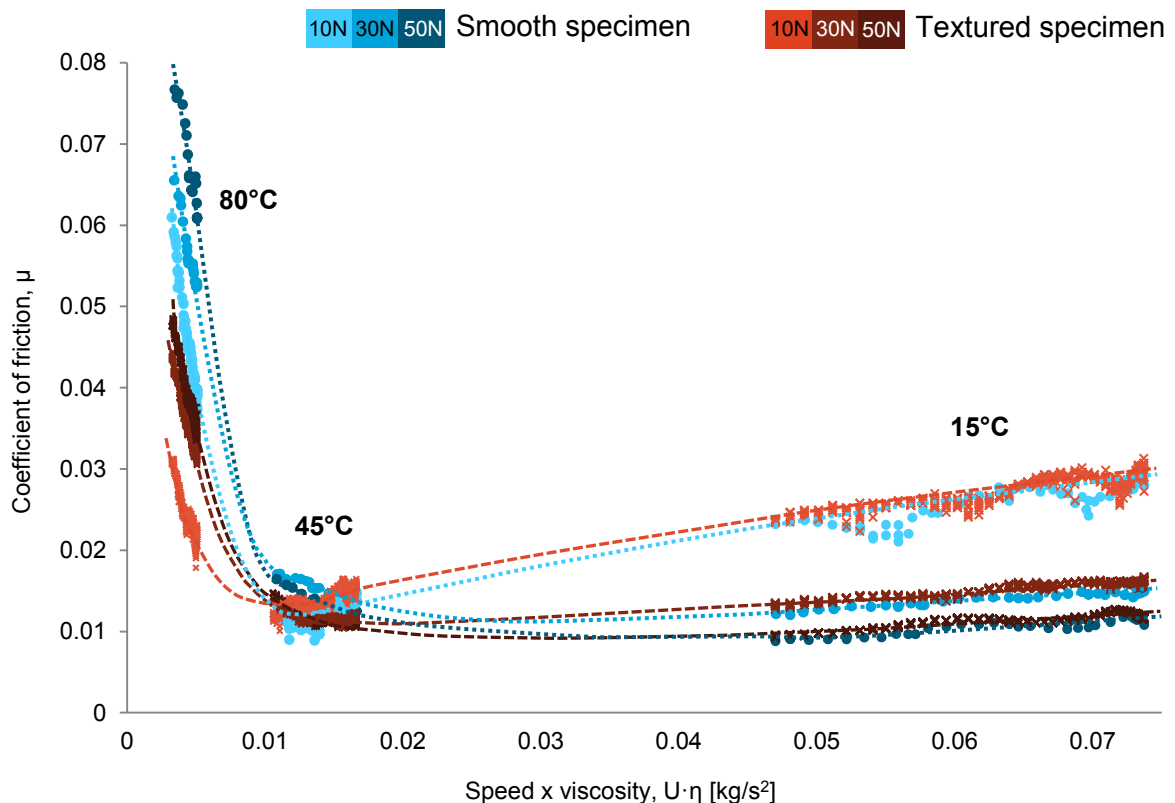
FIGURE 6.10: Stribeck curves showing friction behaviour the following oil temperatures: 15°C, 14°C and 80°C. Sliding velocity was kept constant, while load was varied from 10N to 30N and 50N.

For a better understanding of the influence of texture in the mixed regime, friction data recorded for all three test conditions presented in figure 6.9 (oil temperature: 80°C, oil viscosity: 18.85 mPa.s) were plotted against film thickness in figure 6.11 (to avoid transient squeeze film effects, only data captured between 8° and 90° is plotted). Despite the scatter it can be seen that both textured and non-textured friction values show nearly identical dependence on film thickness. This shows that, under the conditions tested, texture-induced friction reduction results entirely from the increase in film thickness.
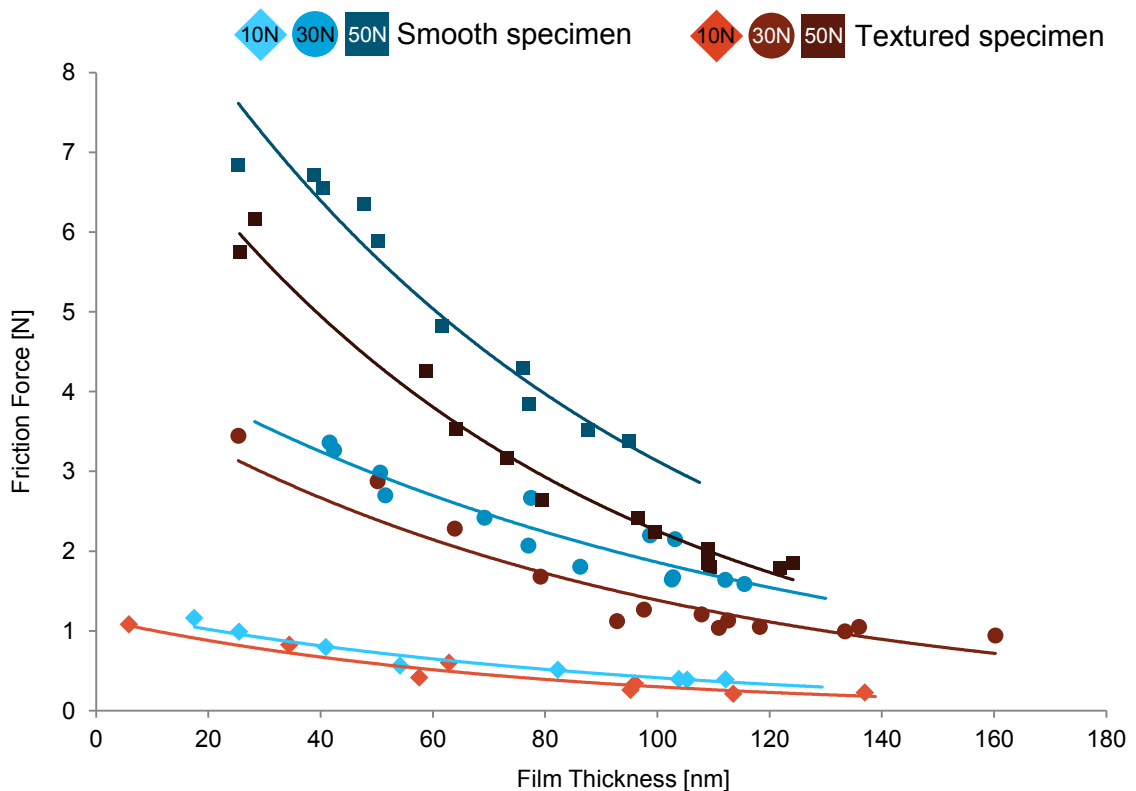
FIGURE 6.11: Friction force variation vs. oil film thickness for three different loading conditions: 10 N, 30 N and 50 N (crank angular velocity: 3 Hz, oil temperature: 80°C).

6.5 Conclusions

The research described in this chapter contributes to the field of tribology research in two ways. Firstly, it demonstrates how a modified version of ultrathin film interferometry can be measure transient changes in film thickness under sliding, mixed lubrication conditions. This approach, which uses the out-of-contact curvature of the specimens in

order to negate the need for a spacer layer and analyses multiple interference fringes remove fringe ambiguity, enabled film thickness to be measured in a reciprocating line contact, replicating the piston ring-liner pairing. The validity of the technique was confirmed by a comparison with standard HL and EHL theory and its key benefits include:

- The ability to study transient film behaviour in detail. For instance, the squeeze effect was seen to preserve the film thickness at reversal so that the minimum lubricant thickness occurred after 8° to 10° of angular revolution into the subsequent stroke and coincided with the peak in friction force. This can be used to test hypotheses regarding optimum ring geometry [78].

- The production of data to validate of transient piston ring modelling, such as [104].

The second contribution of the study is its evaluation of the beneficial and detrimental effects of laser surface texture by simultaneously measuring friction force and lubricant film behaviour in a line contact placed under different lubrication regimes.

Considering that an IC engine's piston transits all three lubrication regimes over one power stroke [99], these findings provide information to inform design decisions regarding the application of surface texture. Key conclusions include:

- Under full film lubrication conditions, the effect of surface texture is to reduce film thickness, which causes an increase in lubricant shear rate and hence increases friction. These friction increases are minor (<12%).

- Under mixed and boundary conditions, the effect of surface texture is to increase film thickness, causing a reduction in asperity contact and hence reduces friction. Although this film thickness increase is small (~28%), its effect on friction is significant (~41% in this study), due to steep gradient of the Stribeck curve in this regime.

Chapter 7

TRANSIENT FRICTION BEHAVIOUR OF A LASER TEXTURED, RECIPROCATING CONTACT

7.1   Introduction

It was shown in previous chapters that rectangular pockets produced by laser surface texturing can reduce friction by more than 50% in a simulated piston-liner paring operating under boundary/mixed lubrication conditions. To achieve this benefit, pockets must be oriented normal to the direction of sliding in order to become entirely entrapped within the elastic contact zone. To shed light on the underlying mechanisms responsible for the reduction in friction, this chapter introduces measurements of the transient friction response as individual pockets pass through the reciprocating sliding contact. Tests were performed at two lubricant temperatures and over a wide range of crank angular velocities, and results were compared to those using a non-textured, reference specimen. In addition, the impact of pockets at reversal was assessed for various lubrication conditions, key conclusions regarding feature location at reversal being drawn.

The results of this chapter contribute to the existing body of tribological knowledge as they help understand the mechanisms through which surface texture acts to reduce friction force. Both the transient and the overall effect of pockets were investigated and mechanisms characteristic to each lubrication regimes are explained in what follows.

7.2   Test specimens and experimental procedure

The effects of pockets in reciprocating sliding bearings were investigated by employing two fused silica specimens; one textured and one non-textured (figure 7.1). The pockets were 1 mm in length, 80 μm in breadth, 8 μm deep and spaced at 3.3 mm. The 3.3 mm separation between each line of pockets was specifically selected so that the effect on friction force of individual pockets could be observed as they passed through the contact. A higher pocket density would result in a friction signal in which individual pockets could not be distinguished, while a sparser spacing would not allow for the compound effect of subsequent pockets to be observed.
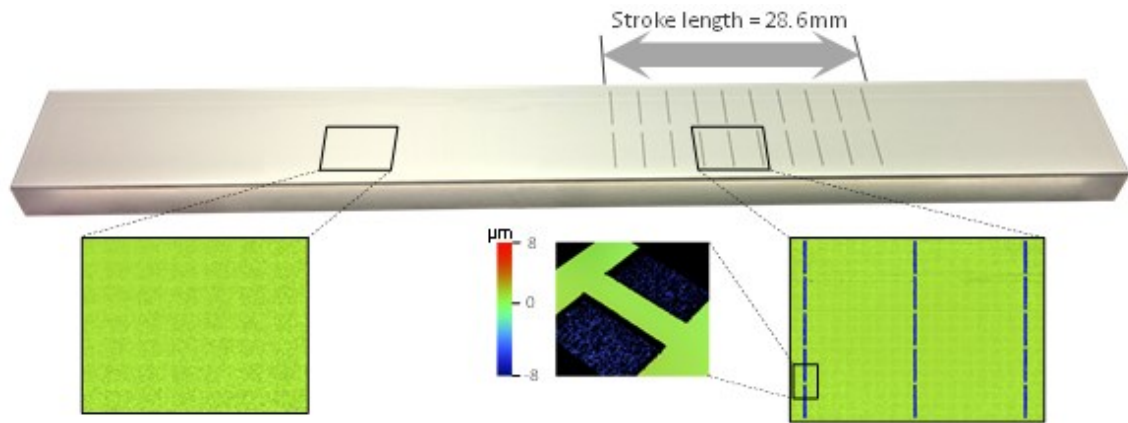
FIGURE 7.1: Surface topography of the textured and non-textured fused silica specimens as obtained by the Veeco Wyko NT9100 optical profiler.

The counterpart AISI52100 steel specimen was mirror-polished as described previously, with the overall finish and surface roughness depicted in figure 7.2.
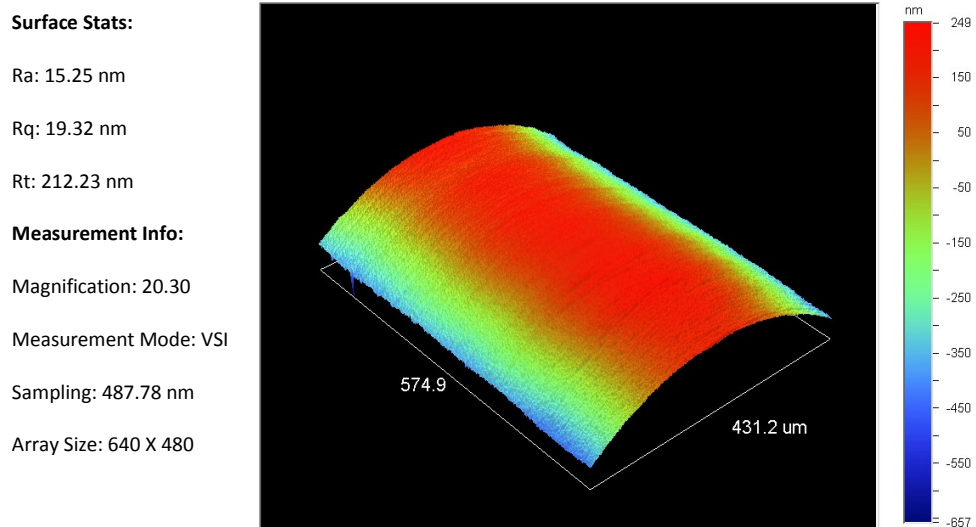
FIGURE 7.2: Three dimensional surface profile of the convergent-divergent steel specimen employed throughout the study of friction reduction mechanisms.

In order to assess the transient friction response of each pocket, as well as the compound effect of successive pockets passing through contact under all lubrication conditions, it was not sufficient to vary only the test velocity. For this reason, temperature was also varied throughout the testing programme, using the same fully formulated engine oil at temperatures, and hence viscosities, accurately maintained at the values shown in Table 1. The 10ºC temperature was employed in order to place the bearing under full film

lubrication regime, while the 80ºC helped assess the friction reduction mechanisms under mixed and boundary lubrication conditions. All tests were carried out at an operating normal load of 70 N, applied using dead weights.

TABLE 7.1: Properties of the fully engine formulated lubricant at the desired temperatures selected for this study.

Oil Temperature [ºC]	Oil properties		
	Dynamic viscosity, η [mPa·s]	Kinematic viscosity, ν [mm^2/s]	Density, ρ [g/cm^3]
10.0	401	460	0.8720
80.0	19	23	0.8283

7.3   Results and discussion

7.3.1   Overall steady state friction response

Transient friction tests were performed under the sets of conditions shown in Table 7.2, producing the series of friction versus crank angle plots, presented in Sections 7.3.2 and 7.3.3. The same series of reciprocating friction tests were conducted for both textured and non-textured fused silica configurations, while varying engine speed from 0.15 Hz to 5 Hz.

TABLE 7.2: Complete testing session followed for both the plain and textured specimens.

Load, W [N]	Oil Temperature [ºC]	Crank angular velocity, [Hz]					
70	10.0	-	0.3	0.6	1	3	5
	80.0	0.15	0.3	0.6	1	3	5

The use of two significantly different lubricant viscosities and a wide range of speeds meant that the lubrication regime, in which the contact operated, varied from boundary to mixed to full film. Therefore, before interpreting these results, it is useful to identify in which lubrication regime the contact was operating for during each test. This is done by fitting the friction data onto a single Stribeck master curve, as shown in Fig. 7.3. To

achieve this, friction coefficient is plotted against speed × viscosity for both plain and textured specimens, using that same data that is later shown in figures 7.4-7.6. As detailed in Chapters 4 to 6, squeeze film effects were eliminated by selecting only friction data from crank angles between 40° and 140°. The plot shows how the presence of texture has the effect of shifting the Stribeck curve to the left and reduces friction in the mixed regime by as much as 82%.
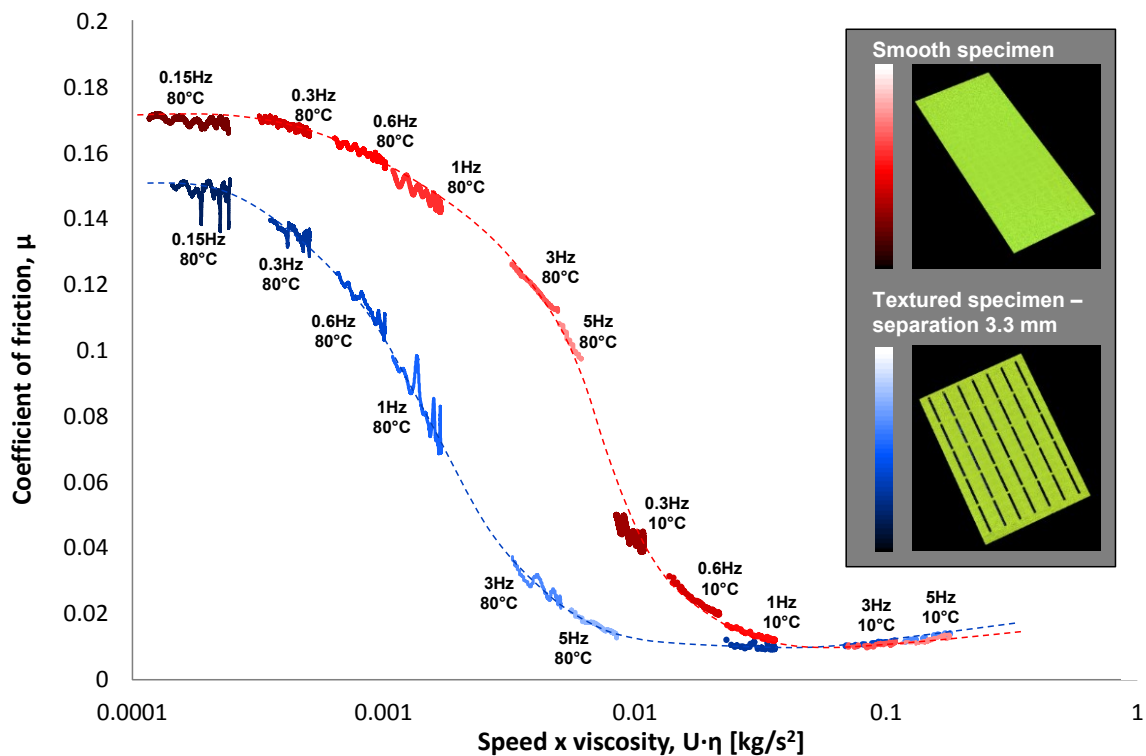
FIGURE 7.3: Stribeck curves showing friction behaviour for the two fused silica specimens used in this study.

7.3.2 Transient response of friction to pockets in the boundary and mixed lubrication regimes

Figures 7.4 and 7.5 presents the variation in friction force along a single stroke for the plain and the textured silica specimen, respectively, both at a constant oil temperature of 80ºC (oil viscosity: 18.8 mPa·s). Under these conditions, the contact is operating predominantly in boundary and mixed conditions.
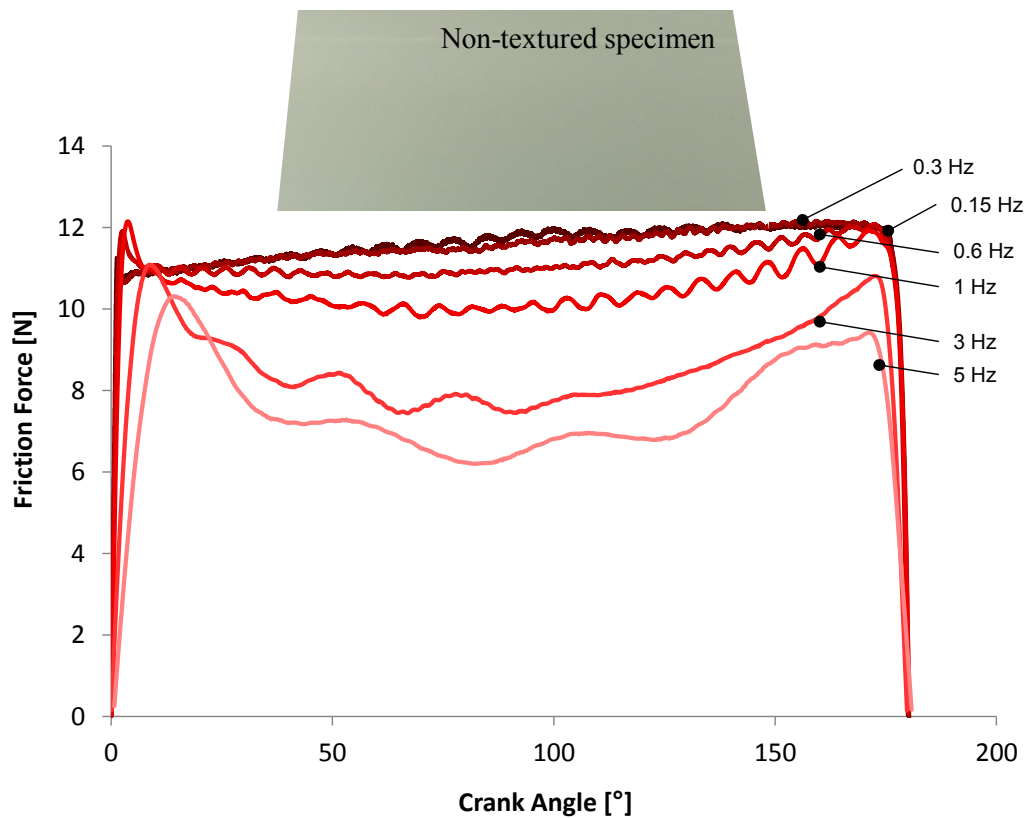
FIGURE 7.4: Friction force comparison between different crank angular velocities – plain specimen (test conditions: normal load: 70N, oil temperature: 80°C).

Figure 7.5, which presents the most insightful data in this friction reduction mechanisms study, plots the friction force variation, obtained using the textured specimen against crank angular velocity between 0.15 Hz and 5 Hz at 80ºC. It should be noted that, since figure 7.5 shows friction force versus crank angle, the length of time associated with each plot reduces as the angular velocity increases (*e.g.* at 0.15 Hz it takes 3.33 seconds to travel 180º, while at 5 Hz it takes 0.1 seconds).

Despite some noise in the signal, caused by fluctuations in load (see section 3.2 – figure 3.6(c) for details), it is immediately noticeable that individual pockets produce various transient effects on friction as they pass through the contact area. For crank angular speeds of 0.15 Hz and 0.3 Hz, friction force is reduced when pockets pass, however the opposite occurs when the speed is between 0.6 Hz and 3 Hz, with individual pockets temporarily increasing friction force. Lastly, when the angular speed is increased to 5 Hz, the features passing through contact have no significant local effect on frictional response.
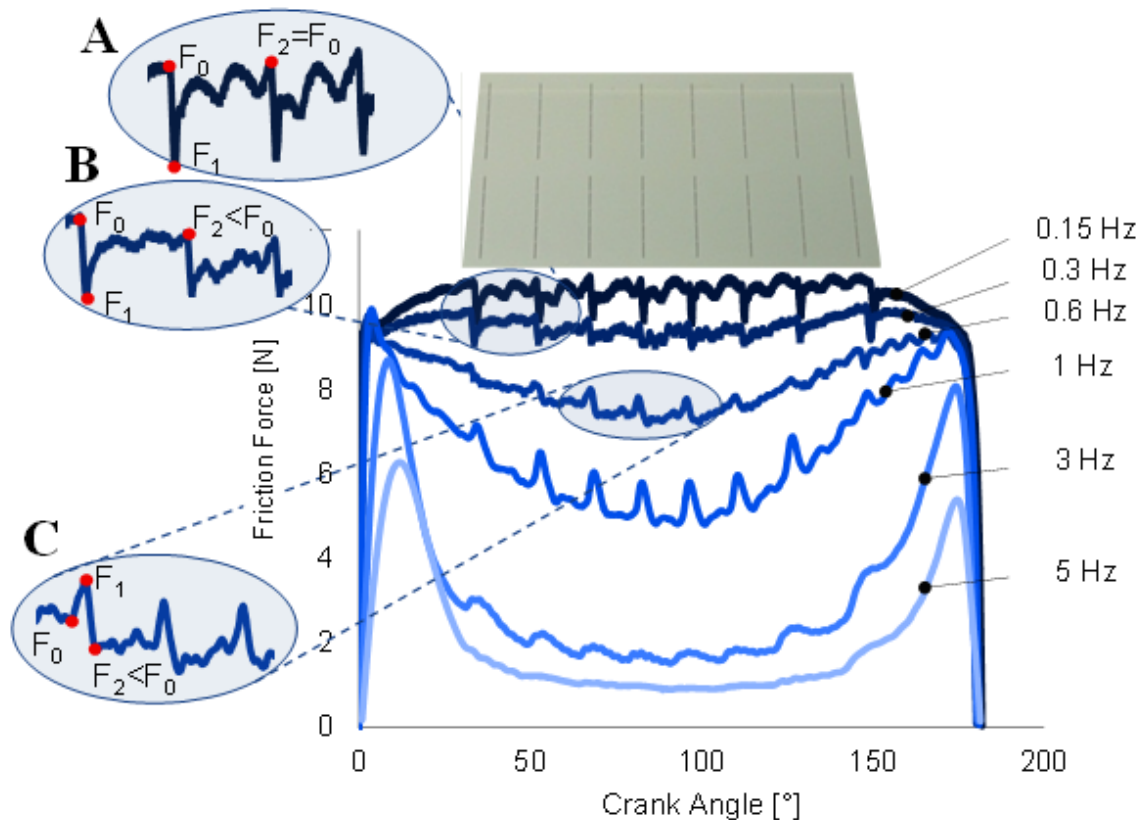
FIGURE 7.5: Friction force measurements for various crank angular velocities, using the textured fused silica specimen (normal load 70N, oil temperature: 80°C).

From figure 7.5 – detail A it can be seen that, while running in the boundary lubrication regime (0.15 Hz crank angular velocity, 80 °C), friction force decreases abruptly as soon as a pocket leaves the contact, before gradually returning to its initial value (F_0). This behaviour is in agreement with previous findings presented in Chapter 6 which showed that textured features act to increase lubricant entrainment into the contact, and hence reduces asperity friction. It then follows that the subsequent gradual increase in friction can be attributed to the oil film being steadily squeezed out of the contact. This mechanism results in a friction force that repeatedly returns to a constant maximum value along the entire stroke. The corresponding results for the non-textured case (the 0.15 Hz angular velocity plot in Fig. 7.4), shows a friction force value that, at the beginning of the stroke, is similar to that of the textured specimen. However, the non-textured frictional response then increases continuously throughout the stroke, reaching its maximum close to the reversal point. This behaviour of the non-textured specimen has also been observed by previous

166

researchers [110,111] and in this case demonstrates the beneficial effect of texture in relieving friction build up.

Further analysis of the textured specimen's frictional response (figure 7.5 – detail B) reveals that, at a crank angular velocity of 0.3 Hz, the bearing has shifted from the boundary lubrication regime towards the initial part of the mixed regime (figure 7.3). The same friction reduction characteristics as the 0.15 Hz case are observed, *i.e.* a rapid reduction in friction that coincides as each pocket enters the contact followed by a gradual increase. However, at this velocity, the period of time between pockets entering contact is half that of the 0.15 Hz case and therefore the friction force does not have time to return to its initial value (F_0) before the next pocket arrives. A stepwise reduction in friction is thus observed, with a minimum value at mid-stroke. The "downward-steps" until mid-stroke, followed by the "upward-steps" for the remainder of the stroke, are correlated with the approximately sinusoidal sliding speed that reaches its peak mid-stroke. In comparison, the plain specimen, tested under the same load and angular velocity, remains in the boundary lubrication regime throughout the entire stoke, with no change in friction force between 0.15 Hz and 0.3 Hz.

For angular velocities of 0.6 and 1 Hz, a different transient variation in friction is observed with the textured silica specimen (figure 7.5 – detail C). As soon as the pocket enters contact, the friction force increases from F_0 to F_1. Then, as the pocket leaves the contact, the friction force descents to a value F_2, which is lower than the initial, value F_0. The step-like behaviour is preserved throughout the stroke but, in contrast to the boundary lubrication case, the instantaneous friction force does not reduce until the pocket leaves the sliding contact. When comparing the plain and textured bearing under these conditions, it is obvious that the latter is already midway through the mixed lubrication regime (for a crank angular velocity of 1 Hz), whereas the former has hardly left the boundary regime. This transient friction peak that is observed is likely to be caused by an instantaneous collapse of the oil film due to the order of magnitude reduction in contact area as the pocket is entrained. This leaves the ring specimen momentarily in contact with the area surrounding the pocket, before the action of the pocket leaving the contact boosts film thickness. This peak is not noticeable at lower speeds, most probably due to the

plateauing of the Stribeck curve (*i.e.* at very low speeds there is no oil film to collapse). The difference in friction between the plain and textured bearings increases further at higher speeds, when the latter is operating on the steepest region of the Stribeck curve. In this case, reductions of up to 82% are recorded when friction from the textured specimen is compared to that of the plain reference specimen for a crank angular velocity of 5 Hz. Another interesting observation is that the transient effect of individual pockets on friction gradually disappears as the contact approaches the full film regime (*i.e.* the conditions under which friction is insensitive to changes in film thickness).

In the boundary and mixed regime, an overall transient response to pocket entrainment can be inferred from the above results is 1) film thickness decrease due to contact area reduction, followed by 2) film thickness increase, followed by 3) decay in due to squeeze action – a process which agrees qualitatively with recent modelling predictions of load support variation during pocket entrainment [104]. This process is suggested based on the fact that the measured variations in friction result from changes in film thickness. This is justified by the experimental study presented in Chapter 6, which demonstrated that the friction reduction due to presence of surface texture in the mixed lubrication regime does indeed result from an increase in film thickness.

7.3.3 Transient response of friction to pockets in the mixed and full film lubrication regimes

Figure 7.6 shows the relationship between friction force and crank angle for the same specimens, at a constant oil temperature of 10 °C (oil viscosity: 401.3 mPa·s) – conditions which favour mixed to full-film conditions.

When the bearing is operating in the mixed regime, close to the bottom of the Stribeck curve, the friction reduction due to pocket entrainment becomes less pronounced. This is shown in figure 7.6(a) and is consistent with previous findings from Chapters 4 to 6. A spike in friction, attributed to the film collapsing as the contact moves over the pocket, is again evident (figure 7.6(a) – 0.3 and 0.6 Hz), and has a high magnitude due to the gradient of Stribeck curve in this region (*i.e.* there is a large amount of film that the pocket can

collapse). At higher speeds (1 Hz) the effect on friction of individual pockets becomes indistinct. This is due to a combination of factors including the flatting of the Stribeck curve in this region and possibly the reduction in the time each pocket covers the contact.

When the bearing is in the full film lubrication regime (figure 7.6(b)), the smooth specimen begins to outperform the laser surface textured one, exhibiting lower friction forces along the entire stroke. As observed in figure 7.6(b) (for test velocity: 3 and 5 Hz), the difference between the two samples (now with the non-textured sample showing lowest friction) increases as the speed increases and the contact is moved towards the right of the master Stribeck curves.
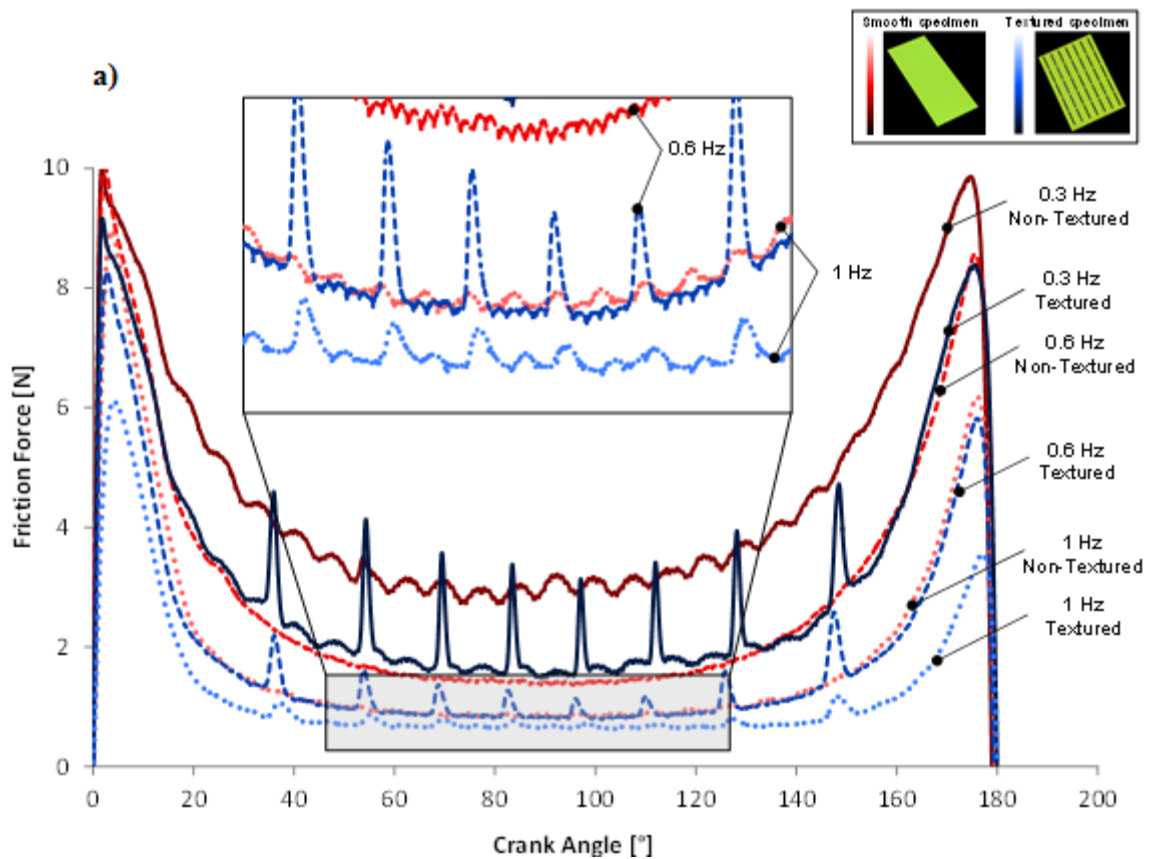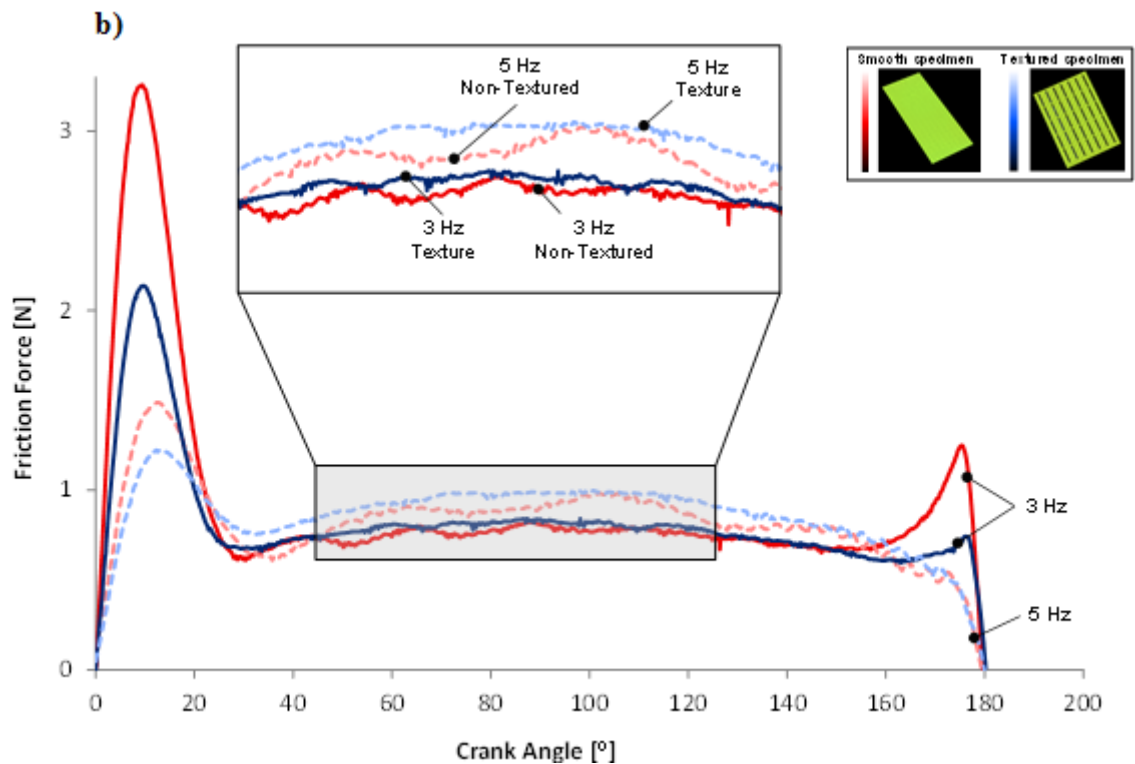
FIGURE 7.6: Friction force comparison between textured and non-textured samples for various crank angular velocities: a) 0.3 Hz, 0.6 Hz and 1 Hz; b) 3 Hz and 5 Hz (test conditions: oil temperature: 10 °C; normal load 70 N).

7.3.4 Influence of texture around reversal

If the location of the mid-stroke and the stroke length of a reciprocating bearing are known, the question arises as to where along the stroke should the texture be applied in order to minimise friction. For instance, the texture could cover the entire sliding distance, be positioned only along the central region, or only towards the end of the stroke. The current research suggests the latter case is optimal since this is where the contact operates in the boundary regime. However, it is possible that texture may have undesired effects if it positioned very close to reversal. Defining the optimal position of texture in this way is important since this can enable the maximum reduction in friction for the minimum manufacturing cost.

Test results presented throughout this chapter demonstrate additional effects on friction response when comparing the textured specimen with the non-textured reference. Firstly, in many cases, the textured specimen shows lower friction than the non-textured case,

even before the textured region reaches the contact (*e.g.* friction traces, at 3 Hz, between 10 and 30° in figure 7.6(b)). This difference may in part be due to the action of the texture bringing lubricant into the cavitated region, to prevent starvation at reversal (as suggested in Chapter 4 and by [67]). However, it is also likely to be caused by difference in squeeze film thickness at reversal between the textured and non-textured cases – *i.e.* the compound effect of multiple pocket entrainments builds a thicker film that is more persistent at reversal so that, when the speed subsequently increases, the contact slides further down the Stribeck curve.

Comparing the friction variation along the first 30°s of crank angle in figures 7.4 (non-textured specimen) and 7.5 (textured specimen), suggests that pockets should be placed immediately before/after reversal in an actual piston-liner to achieve the beneficial effects described above.

To verify this hypothesis it was decided to run a separate set of tests particularly focused on assessing the effects of pockets on friction force at the end of the stroke, both while placing the reciprocating bearing under the full film regime, as well as under mixed lubrication conditions.

Influence of pockets at reversal under full film lubrication conditions

In order to study the influence of texture location on friction, reciprocating sliding tests were performed on two textured specimens, both with a pattern of grooves perpendicular to the sliding direction. In order to place the bearing under hydrodynamic lubrication conditions, the lubricant temperature was held constant at 15°C (oil viscosity 273.6 mPa.s).

The first fused silica sample (E1) had pockets only in the central region, (over 22.6 mm out of the 28.6 mm stroke length), leaving a smooth 3 mm area at each end (figure 7.7 (a)). The second specimen (E2) was textured along the entire sliding distance, the reversal taking place exactly on a row of pockets, as depicted in figure 7.7 (b). The two images, captured at the end of the reciprocating stroke, shown in figure 7.7 (a) and (b), were

obtained using the optical interferometry technique, which allowed clear visualisation of the contact between the steel pad and the transparent silica specimen coated with a thin semi-reflective chromium layer. The images display two "dark" zones, one showing the contact area and the other a laser etched pocket, as well as fringes visible outside the contact, representing optical interference caused by varying fluid film thickness.
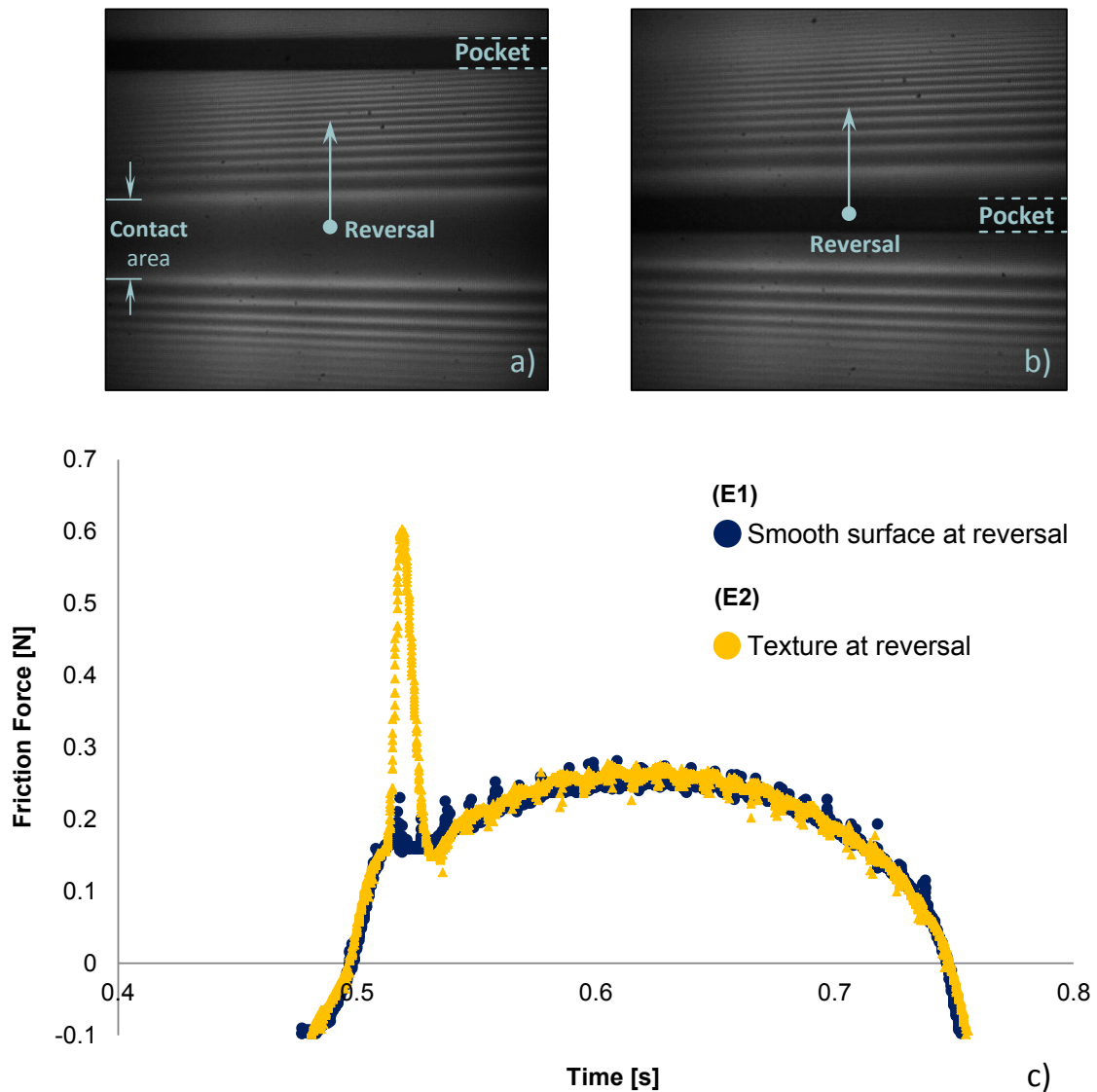
FIGURE 7.7: Influence of texture at reversal: a) Optical image showing texture restricted to the central region - reversal takes place on a smooth area; b) Optical image showing texture applied on the entire sliding distance - reversal takes place with a pocket inside the contact area; c) Friction force profile variation for the same textured specimen (Transverse Grooves) under two different scenarios: (E1) reversal takes place on a smooth surface at the end of the stroke; (E2) reversal takes place on a line of pockets at the end of the stroke.

Figure 7.7 (c) shows that, while both friction curves closely follow the sinusoidal velocity profile, sample (E2), where the reversal takes place on a row of rectangular pockets, displays a significant spike in friction immediately after reversal. This spike in friction ultimately leads to a 13% increase in the average friction force per stroke, when comparing case (E2) with (E1).

If pockets are located at one end of travel and protrude outside the contact, they can act to collapse the oil film, as shown in figure 7.7. Therefore, to maximise the benefit of the pockets, there should be no pockets at the reversal position.

Influence of pockets at reversal under mixed lubrication conditions

As presented previously in Chapter 4 when assessing the mixed and boundary regimes, pockets close to reversal appear beneficial in reducing friction shortly before and after reversal point. To accurately determine the influence of texture location on friction at reversal under mixed lubrication conditions, the lubricant temperature was increased to 45°C (oil viscosity 61.72 mPa·s) and tests were performed employing two fused silica specimens, a textured (F1) and a plain one (F2). The positioning of the reciprocating stroke was selected in such a way that at one end (180° crank angle) the reversal takes place approximately 1 mm before/after the last line of pockets pass through the contact. At the other end, the last line of pockets passes through the contact approximately 2 to 3 mm before/after reversal.

The key finding illustrated in figure 7.8 is that pockets located immediately before reversal generate disproportionately large reductions in friction compared to pockets located elsewhere along the stroke. Pockets in this location increase the minimum film thickness which occurs after reversal (*i.e.* pockets are most beneficial when lubricant entrainment is minimal). As highlighted in figure 7.8 at 180° crank angle, this benefit caries through to the next stroke by means of a boosted squeeze film.
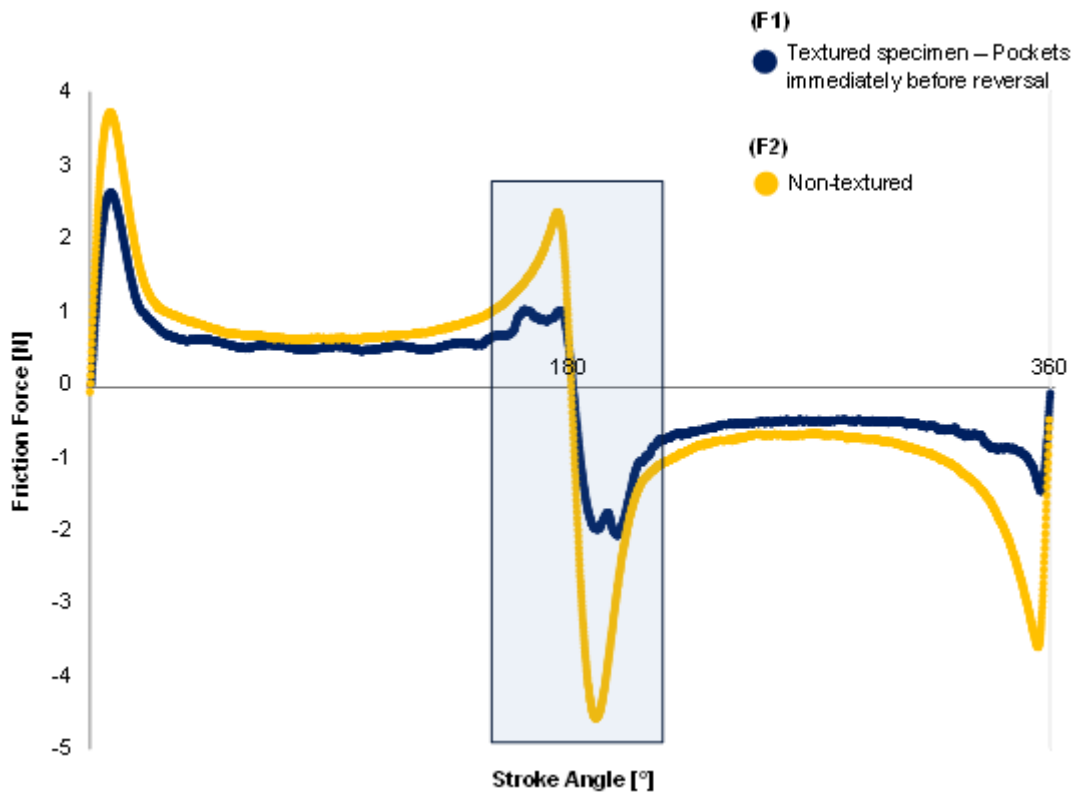
FIGURE 7.8: Friction force profile variation of a textured specimen compared against the plain reference, for different pocket arrangements at the two ends of stroke.

7.4   Conclusions

This investigation aimed to shed light on the underlying mechanisms by which LST affects friction, under conditions that closely matched a piston-liner contact. To do this, the carefully designed reciprocating tribometer was used to obtain the transient friction response to pocket entrainment. The results were compared to those from a non-textured specimen. Key conclusions include:

- Laser surface texture applied on linear bearing surfaces is a powerful means of reducing friction under boundary and mixed lubrication conditions. This is demonstrated by the improvements in friction performance of up to 82% that were shown when comparing the average stroke friction values from the pocketed and plain specimens. Conversely, in the full film regime, texture causes a slight increase in friction. These effects manifests themselves as a leftwards shift of the Stribeck curve, and are indicative of enhanced/reduced fluid film thickness.

174

- When applying texture to a piston liner, it is advisable to locate pockets as close to reversal as possible (though not actually at the point of reversal, since this collapses the film). In addition to the increased lubricant entrainment this affords, it may also reduce starvation due to cavitation.

- In the mixed and boundary regimes, sliding speed has a strong effect on texture performance via two routes. Firstly, the speed determines where on the Stribeck curve the contact is operating and therefore how sensitive the friction force is to changes in film thickness. Secondly, the speed controls the pocket entrainment frequency and hence determines whether the film thickness has time to decay to its steady state value between pocket entrainments. This also has important practical implications regarding the configuration of pockets on piston liners, since the pocket entrainment frequency may be adjusted, according to the varying sliding speed, by gradating the geometric pocket spacing.
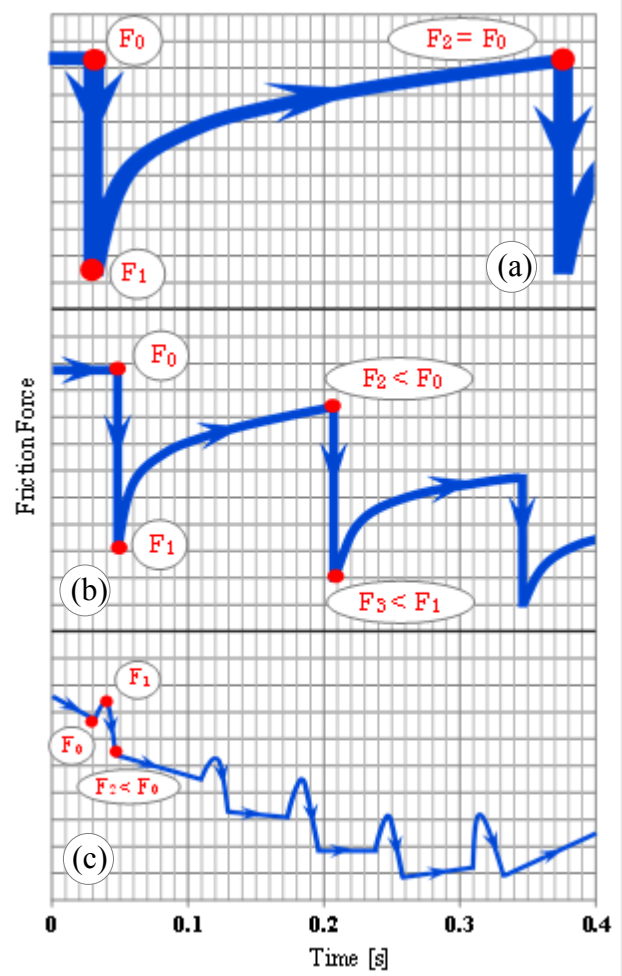
FIGURE 7.9: Schematic representation of the transient effects of pockets passing through contact for different crank speeds: (a) 0.15 Hz; (b) 0.3 Hz; (c) 0.6 Hz.

- In the boundary lubrication regime where the load is supported predominantly by asperity contact, a steep reduction in friction force is observed as each pocket leaves the contact, presumably due to an oil replenishment mechanism (which will be further documented in chapter 8).

175

If the pocket entrainment velocity is sufficiently low, there is time for this addition film to be squeezed out before the next pocket arrives. Although this does not result in a compound reduction in friction, pocket entrainment under these conditions prevents a gradual build up in friction force as is observed with the plain pad.

At higher pocket entrainment speeds, the contact does not have time to recover from subsequent pocket entrainments and as a result the friction reduces in a stepwise fashion (see figure 7.9(a, b)).

The effect of pocket entrainment on friction is modulated by the position on the Stribeck curve that the contact is operating. Therefore, largest reductions in friction are observed when the contact is operating in the steepest region of the Stribeck curve. Conversely, pockets are seen to have minimal effect on friction when the contact is operating in the hydrodynamic regime, where the Stribeck curve is flat. In fact, texture is actually seen to increase friction under these conditions.

- Under mixed lubrication conditions, where the load is supported by a combination of lubricant pressure and asperity contact, the transient friction response shows a peak value as each pocket enters the contact (figure 7.9(c)). It is suggested that this is due to the considerable reduction in contact area as the pocket passes and, as a consequence, the lubricant film is believed to collapse (see figure 7.10 for the schematic representation).

  Even under these conditions, the net effect of pocket entrainment is still to increase lubricant thickness along the stroke (as illustrated in Chapter 6), and significantly reduce the friction below the non-textured case.
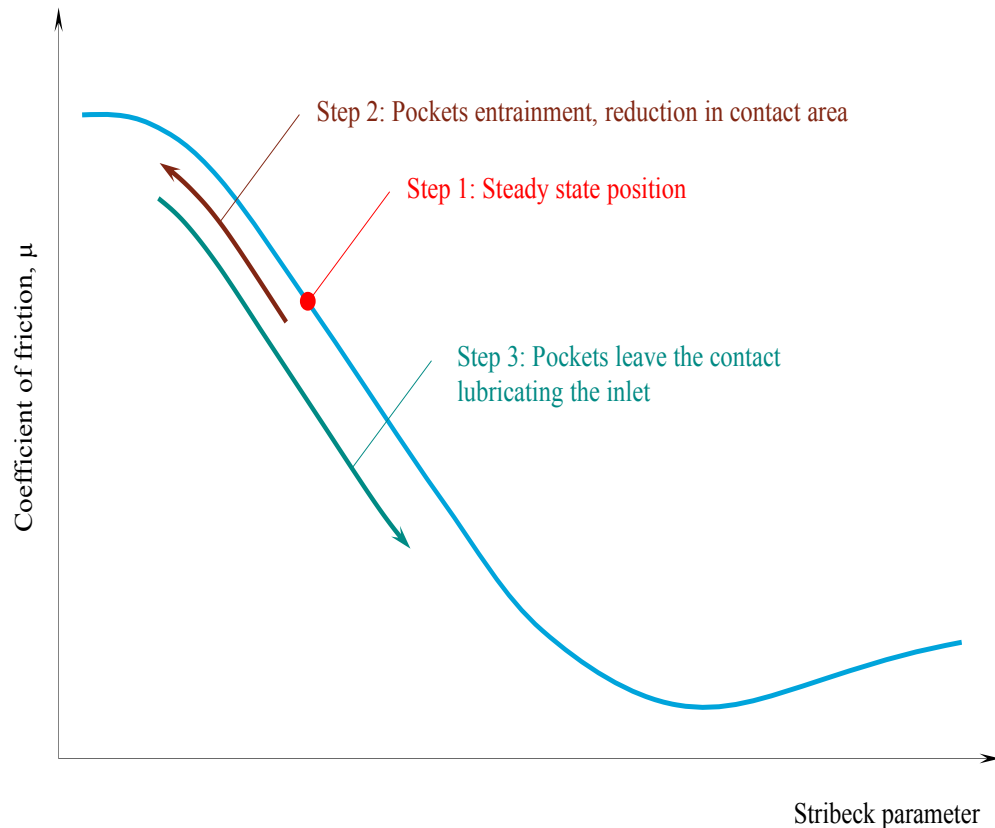
FIGURE 7.10: Schematic representation of the transient effects of individual pocket entrainment.

- When running at high pocket entrainment frequencies in the mixed regime, the effect of successive pockets entering the contact builds up. It is suggested that this causes a beneficial increase in film thickness that carries over to subsequent reciprocations by means of the squeeze film effect. This is supported by the fact that the friction for the textured specimen drops far more rapidly that for the plain specimen, at the start of the reciprocation, before any pockets have entered the contact.

- These results imply that each pocket gives rise to an increase in film thickness that is both short-lived and small in magnitude (we estimate a few tens of nm). However, the resulting effect on friction can be significant (up to 82% in this study) for two reasons: i) provided the pocket frequency is sufficient, each successive pocket entrainment builds the film up without there being time for it to reduce back

to its steady state value ii) when the contact is in the mixed regime the Stribeck curve is at its steepest and is therefore most sensitive to film thickness changes. This has important practical implications in that pocket spacing on piston liners should be varied as a function of reciprocating sliding speed. This also ties in with results from the parametric study in Chapter 5, which showed that pocket density should increase towards the ends of the stroke where the sliding speed decreases (*i.e.* the increased density is required to ensure the short length of time between pocket entrainments is maintained).

Chapter 8

EFFECTS OF SURFACE TEXTURE ON LUBRICANT REPLENISHMENT AND WEAR BEHAVIOURS

8.1   Introduction

The final aim of this study was to understand the interactions between laser-honed surface pockets and wear behaviour in an automotive piston-liner pairing. To do this, the test apparatus previously described in Chapter 3 was used to conduct wear tests under highly loaded conditions. Fused silica specimens with a range of pocket geometries were rubbed against a convex steel pad and the resulting friction and wear data were compared with those from a non-textured specimen. As described in Chapter 2, the majority of investigations into surface texture have, so far, focussed on either friction or wear but not both simultaneously. Since texture is most effective in reducing friction under mixed and boundary conditions, where appreciable surface contract and wear occurs, it seems likely that the effects of pockets on friction and wear are interlinked. The aim of the simple experiments described in this chapter is to explore the relationship between these three parameters.

8.2   Test specimens and experimental procedure

The same type of HPFS Standard Grade fused silica rectangular pads were used as the reciprocating specimens in this final study. Textured patterns, consisting in linear grooves orientated normal to the direction of sliding, were applied to these specimens. The orientation of the pockets was selected based on the previous experimental studies (Chapter 4), which showed that grooves perpendicular to the direction of sliding are most effective in reducing friction under both mixed and boundary lubricated conditions. It is also important that pockets can become entirely trapped within the contact zone, since these perform better than those with pockets that are longer than the contact zone in the direction of travel [13,30,92]. In this study, three different pockets breadths were selected; firstly, two breadths of 40 μm and 80 μm, which are small enough to be completely enclosed within the contact area and secondly, a pocket breadth of 300 μm which is much larger than the elastic contact width.

TABLE **8.1**: Geometry of the selected textured patterns.
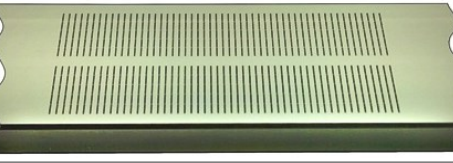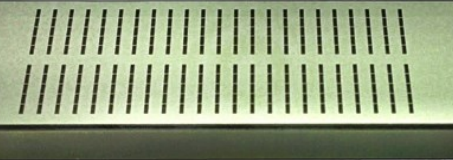
Specimen No.	Surface Texture Geometry			Image	Sample name
	Breadth [μm]	Depth [μm]	Separation [μm]		
1	40	7	500		**40x7x500**
2	80	3	500		**80x3x500**
3	80	3	1000		**80x3x1000**
4	300	7	1100		**300x7x1100**

Table 8.1 summarises the geometries of the selected patterns together with the corresponding images, while figure 8.1 shows an example of an interference image of the contact with an 80 µm breadth pocket close to the inlet of the contact (obtained by viewing the contact through transparent silica specimen with the optical microscope previously described in Chapter 6).
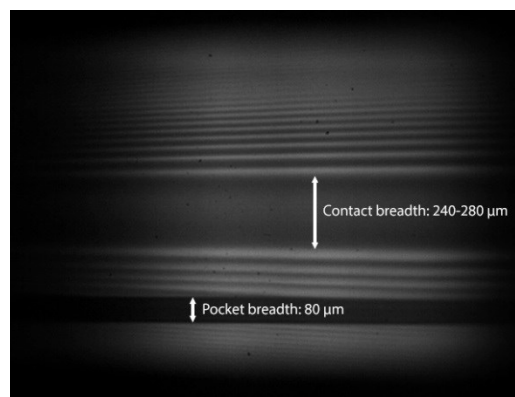
FIGURE 8.1: Interference image of the contact showing a pocket close to the inlet.

The counterpart specimens − all identical AISI 52100 steel pads replicating the top piston ring − are 10 mm long and curved in the direction of sliding resulting in a convergent-divergent form.

In all friction force and wear tests presented in this chapter, a normal load of 155 N was applied and a crank angular velocity of 1 Hz was maintained. Such high load, low speed, conditions were chosen in order to minimise lubricant film thickness, increasing surface contact and wear. Wear was also promoted by using an additive-free mineral oil, which was continuously supplied to the contact region while accurately controlling its temperature, and consequently viscosity, throughout the entire testing session. The lubricant properties alongside all other test parameters are listed in table 8.2.

TABLE **8.2**: Experimental conditions (note: the quoted lambda value is that for the non-texture specimen, calculated from the mid-stroke film thickness at the start of the test. As the test progress and wear takes place, the lambda value will decrease due to roughening of the specimens).

Load, W [N]	Crank angular velocity, [Hz]	Oil Temperature [$^\circ$C]	Oil properties			Time length of the test, t [h]	Initial Lambda Ratio, Λ [-]
			Dynamic viscosity, η [mPa·s]	Kinematic viscosity, v [mm^2/s]	Density, ρ [g/cm^3]		
155	1	80	18.313	22.947	0.798	4	2.65

The fused silica and the steel specimens were consecutively sonicated in toluene and isopropanol before all traces of solvent were removed using a heat gun. Wear tests, each with a duration of four hours were carried out on all the textured specimens presented in table 8.1 as well as the non-textured reference. During each test, the friction force variation for one complete stroke was recorded after one minute and after three minutes, then every five minutes for the first half hour and every ten minutes for the remaining three and a half hours. At the end of the test, the cleaning procedure previously described was repeated and the topography of wear track around the reversal point was recorded using the Veeco Wyco NT9100 optical profiler. The Veeco's area of analysis was a rectangle, 2 mm wide by 3.5 mm long. This rectangle was located such that, at reversal, its short axis coincided with that of the elliptical contact. In this way the region of

highest wear fell within its borders. In the direction of sliding, the rectangle's 2 mm width extend outside the wear track, thus encompassing a non-worn region, which could provide a datum from which the wear volume could be calculated.

8.3   Results and discussion

Many of the studies into the impact of surface texture on wear and frictional response have been conducted on ball-on-plate contact configurations using commercially available pin-on-disc tribometers [11,30,112,113]. These test conditions differ significantly from those found in an actual piston ring-cylinder liner pairing. The test apparatus developed for the present research allows for the friction force variation on every stroke to be plotted as a function of crank angle throughout the wear test. This provides more detailed information than the previously obtained single point measurements. A graphically depicted comparison of the frictional response was thus possible at any time during the test. Figure 8.2 displays the friction force variation, captured for all four textured specimens together with the smooth reference, plotted as a function of crank angle, throughout the entire wear test.

Over the first few cycles of each test (t_0), the smooth pad exhibits the lowest friction force for the majority of the stroke compared with any of the textured specimens. This can be explained as follows. At the start of the test, negligible wear has occurred on any of the sliding pairs and the composite roughness was approximately equal to its initial value of 12 nm. For a mid-stroke film thickness of around 38 nm (calculated by applying Dowson and Higginson's Equation [114] for the non-textured pairing), this roughness gives nominal lambda values in the region of 2.65, showing the bearing contacts are operating in the full film hydrodynamic lubrication regime. This initial predominance of hydrodynamic lubrication is further demonstrated by the flat-bottomed "U" shape of the non-textured friction curve; when considering the sinusoidal nature of the varying entrainment speed, this shape must arise from the contact spending the majority of each reciprocation around the lowest point of the Stribeck Curve. As previously shown in Chapter 4, it is under these full film lubrication conditions, that surface texture can have

the effect of increasing friction, and hence explains why the non-textured specimen performs the best, initially.
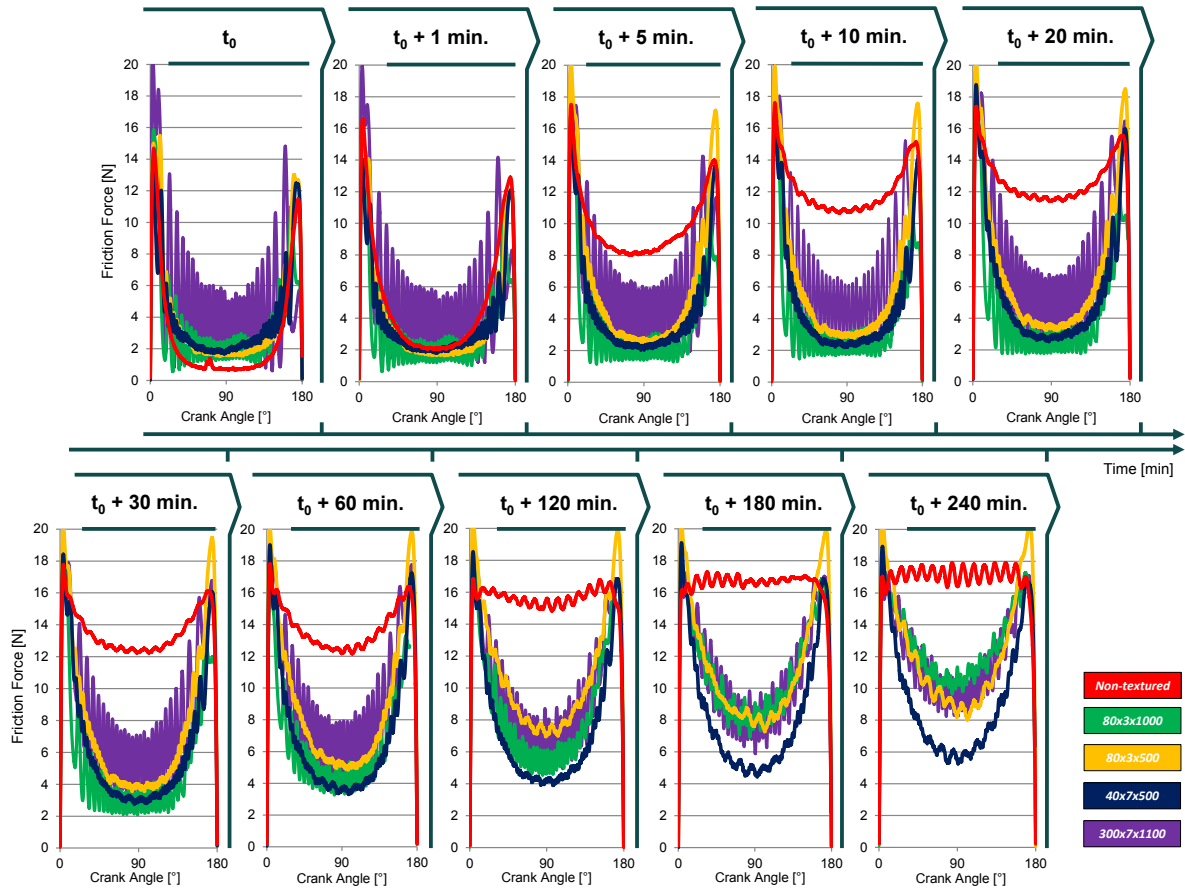
FIGURE 8.2: Friction force comparison between all textured specimen and the smooth reference over the four hour wear tests.

After approximately 5 minutes, and as soon as the first scars of wear appear on its surface, the non-textured reference begins to show the highest friction compared to all of the other textured specimens. This is because the appearance of wear signifies the transition of the contact from full film to mixed lubrication conditions due to an increase in composite surface roughness that is greater than the lubricant film thickness. It is under this regime that surface texture is most beneficial in terms of reducing friction, as proven in Chapters 4 and 5. No further changes in ranking were recorded over the remaining four hours test, with the non-textured specimen continuing to exhibit the highest friction at every time step. Moreover, after approximately three hours of rubbing ($t_0 + 180$ min.), the

non-textured bearing reaches the boundary regime, exemplified by a constant friction force along the entire stroke (*i.e.* the wear has advance to such an extent that the increasing hydrodynamic separation as the bearing accelerates towards mid-stoke is insignificant compared to the roughness).

Further inspection reveals that the most sparsely textured specimen (80×3×1000) displays the lowest friction force at the beginning of the testing sequence and the highest friction force by the end of the fourth hour, when compared with the other pocketed specimens. Conversely, the deepest and most dense pattern (40×7×500) displays the lowest friction from the first hour of the test onwards. This behaviour suggests that deeper and more densely packed pockets are desired towards the end of the stroke (*i.e.* in the boundary and mixed lubrication regime), whereas sparser and more shallow pockets are needed towards the middle of the stroke (*i.e.* in transition between mixed to full film regime), and surface pockets should in fact be avoided when the bearing is operating in full film lubrication regime. These observations are in perfect agreement with results presented in Chapter 5, where all friction data was plotted as Stribeck curves.

For a better visualisation of the above mentioned trends, the mid-stroke friction force, captured between 60° and 120° crank angle, has been averaged and is plotted as a coefficient of friction against sliding time in figure 8.3. Here, significant and constant reductions of up to 70% are evident over the last two hours of tests when comparing the best performing textured pattern (40×7×500) against the non-textured reference.
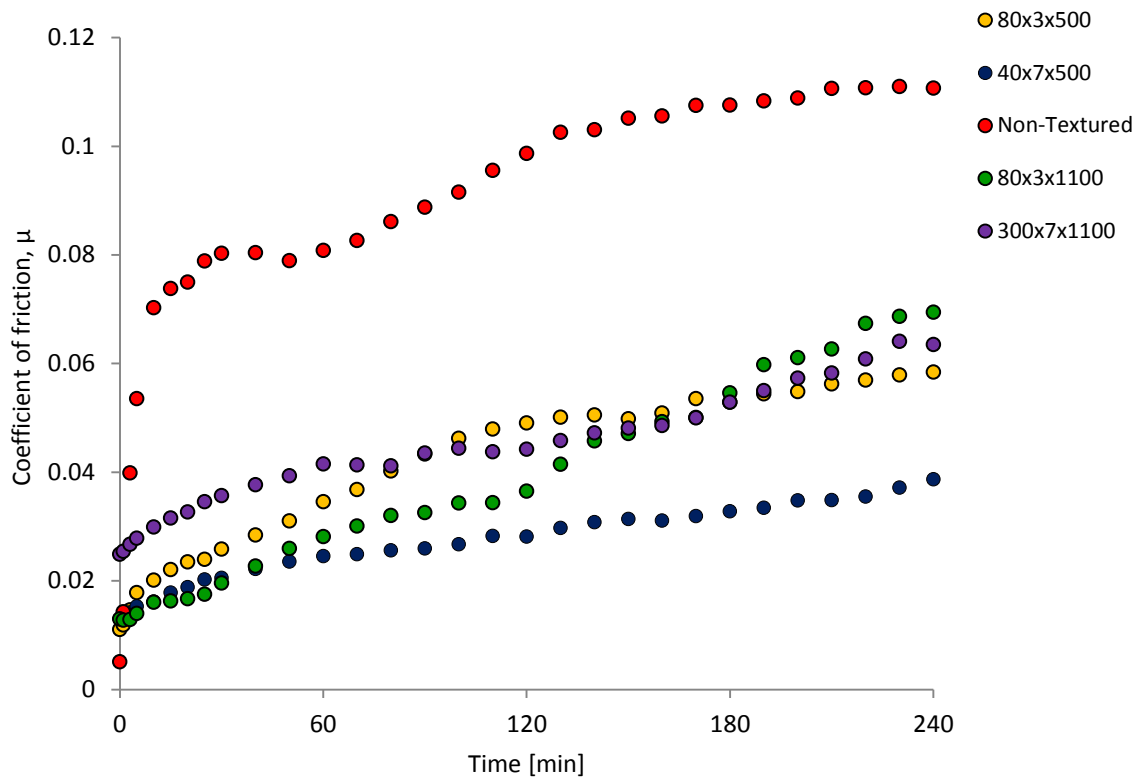
FIGURE 8.3: Variation of coefficient of friction (average values obtained between crank angles of 60° and 120°) with sliding time for all textured and non-textured fused silica specimens.

Figure 8.4 shows the data from figure 8.3 replotted in terms of percentage improvement for the four textured bearings compared with the non-textured reference. Here, the relative change in performance between the non-textured and texture specimens can be clearly observed. In addition to this, it can be seen that the pattern consisting of pockets wider than the contact in the direction of travel (300×7×1100) exhibits slightly higher friction than the other texture geometries over the initial stage of the test (*i.e.* during the first hour). This requirement that pocket should be less wide that the contact in order to provide greatest friction reduction is consistent with previous findings for texture specimens. However, it should also be noted that by the end of the test, there are no discernable differences between the friction performances of the 300 μm breadth pockets and the 80 μm breadth ones.

186
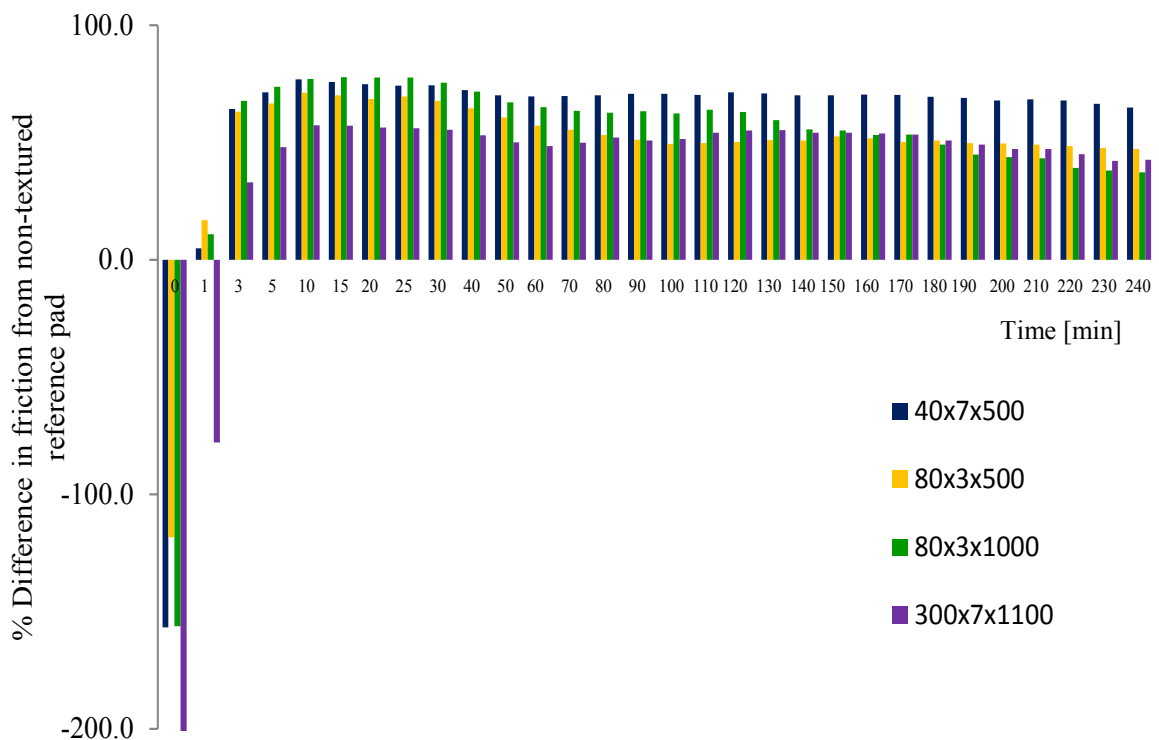
FIGURE 8.4: Percentage difference in friction between each textured specimen and the non-textured reference.

Another key observation from figure 8.2 is the presence of significant peaks in the friction traces from certain pocket configurations. Rather than being experimental noise, these peaks correspond to lines of pockets entering the contact. Upon reaching a line of pockets, the contact area reduces considerably (by a factor of 10, which, under mixed lubrication regime has a significant impact on friction force) and, as a consequence, a local spike in friction is observed. As soon as each pocket leaves the contact, the film thickness increases and friction falls below the initial level. This effect is more pronounced for the specimens with a more sparse texture pattern, *i.e.* 300×7×1100 and 80×3×1000. As the frequency with which pockets enter the contact doubles (*i.e.* with specimens 40×7×500 and 80×3×500), the observation of this local friction effect becomes difficult. This relationship between friction force and the frequency with which textured features pass through a contact is an important topic which will be investigated in future research.

For a better visualisation of this transient effect, the friction force variation of the 80×3×500 textured pad at $t_0 + 1$ *min* was plotted alongside the non-textured reference as a function of distance travelled along the reciprocating stroke in figure 8.5. It can be observed that, although at the beginning of the stroke both pads exhibit similar friction, the first pocket placed immediately after reversal results in a considerable reduction of frictional response.

The friction force shows a temporary increase as each line of pockets enters the contact, however, as soon as they leave the contact, the friction force drops significantly compared with the non-textured pad. This behaviour is consistent with the study into the transient effects of surface texture presented in Chapter 7. Furthermore, since it is now known that the overall reduction in friction that results from multiple pocket entrainments is due to an increase in film thickness (Chapter 6), it seems reasonable to assume that the observed transient variation in friction force is due to a corresponding variation in film thickness, caused by the entrainment of pockets. This assumption is supported by the fact that, in figure 8.5, the optical profile image shows regions of wear that are localised around the edges of the pockets.
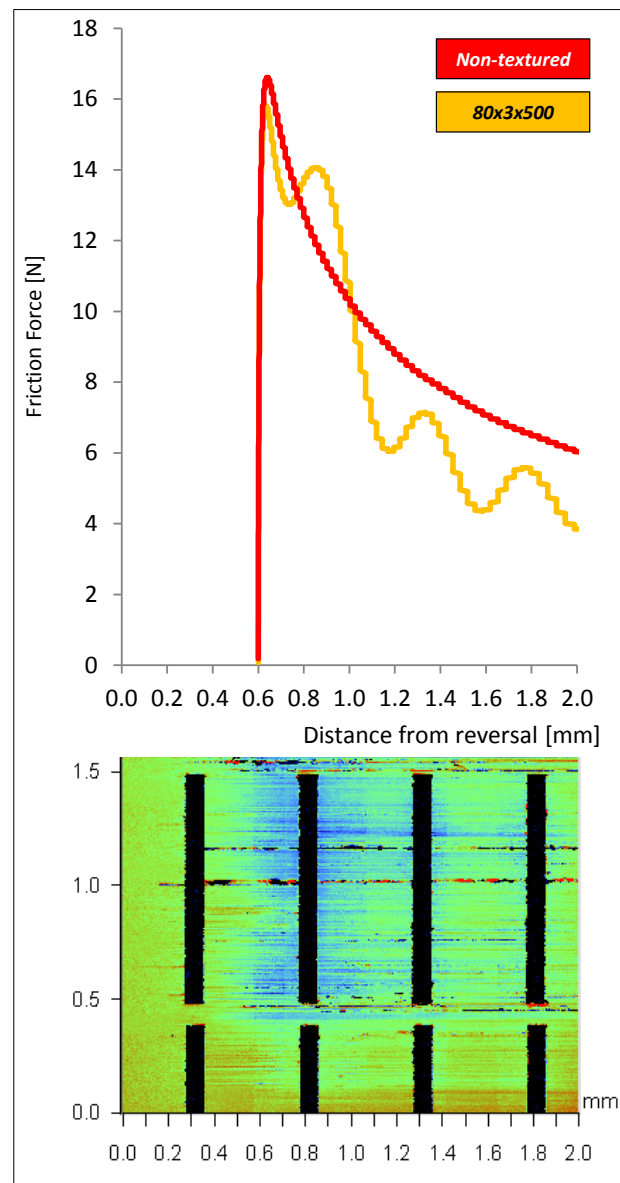
FIGURE 8.5: Friction force and wear topography variation vs. sliding distance at the end of travel.

The counterpart steel specimens were analysed by Veeco Wyko surface profiler and no differences in average mean roughness greater than 5 nm were detected when comparing

the five steel specimens. To exemplify this, figure 8.6 illustrates the surface topography of the steel pads before a test (a), after the four hours long wear test against a non-textured fused silica pad (b), and at the end of the test employing the pocketed specimen 40×7×500. Most probably, this low wear behaviour of the steel pads is due to the hardening process that the specimens underwent prior testing. For this reason, this study focusses on the wear observed on the silica liner specimen, and wearing of the steel ring specimen will be the subject of further testing.
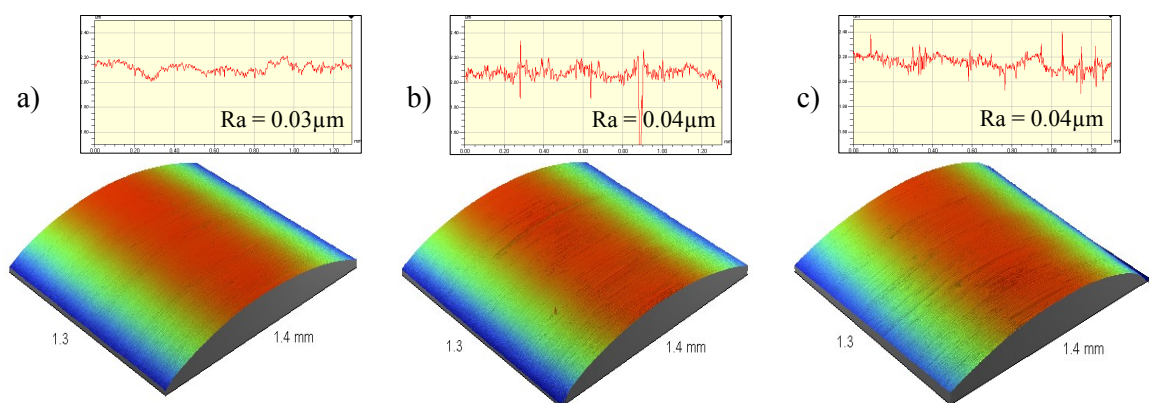
FIGURE 8.6: Three dimensional surface topography of the steel specimens used for the wear study: a) Surface plot captured before the test against the non-textured counterpart; b) Surface plot captured after the test against the non-textured counterpart; c) Surface plot captured after the test against the 40 x 7 x 500 counterpart.

Two-dimensional images of the typical wear tracks on the fused silica pads at the reversal point are shown in figure 8.7. The 3.5×2 mm images were recorded, for all five tested specimens, at the same point along the stroke. This enabled accurate comparisons of the wear tracks and corresponding wear volumes. The first 0.2 mm slice on the horizontal axis, outside of the contacting region was considered the initial, unworn, level and was set as the datum surface before performing the wear measurements. Similar to IC engines and other applications comprising reciprocating bearings, wear occurred almost exclusively towards the end of the strokes due to a significant reduction in speed and hence lubricant entrainment in these regions. Indeed, optical profiles of the worn surfaces indicate that the greatest wear scar depths on the fused silica specimens occurred in all cases on the first 1.5 mm of the reciprocating stroke, immediately after reversal.

Although figure 8.7 presents topography for only one end of stroke, a near identical wear pattern was observed at the other end.
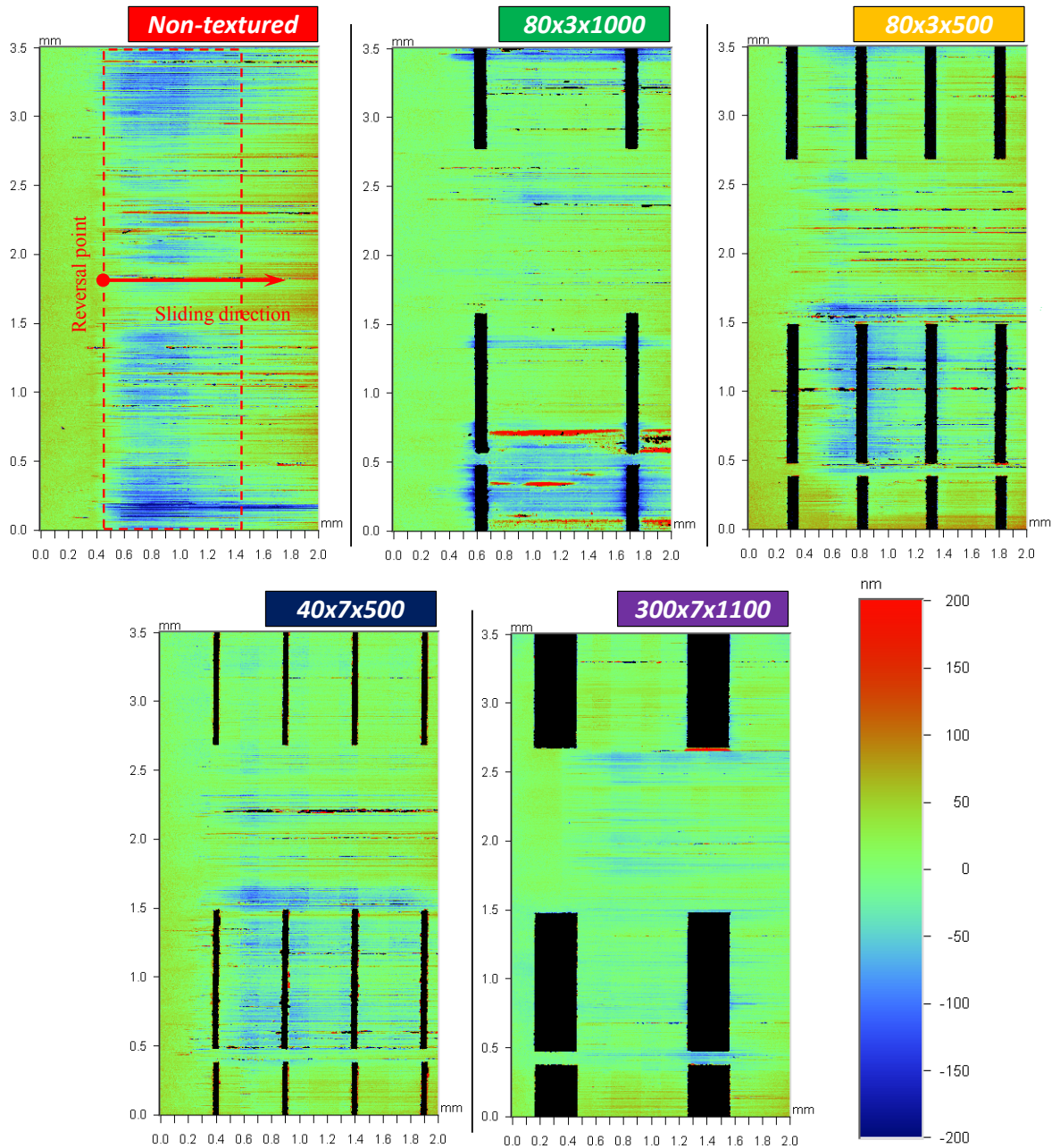
FIGURE 8.7: Two dimensional surface topography plots of all tested specimens as obtained post-test by the Veeco Wyco optical profiler.

Despite similar wear scar dimensions in the direction of sliding (approx. 1.5 mm) for all the specimens, a qualitative and quantitative analysis of the volume of wear removed from the 3.5 mm^2 area around reversal, as indicated in figure 8.7, was performed. This

shows the highest volume of wear for the non-textured specimen, followed by the 80×3×1000 sample, whereas the 300×7×1100 pattern proved most resilient. This ranking of specimen performance leads us to conclude that there is a close connection between the volume of wear removed from the surface and the volume of oil each pattern brings to the contact during one stroke. Figure 8.8 presents this conclusion graphically: for each specimen, the volume of each pocket multiplied by the number of pockets replenishing the contact with each stroke is shown on the left, while the graph on the right displays the volume of wear removed over the four hour test.

It is immediately apparent from figure 8.8 that, as the volume of oil brought into the contact increases from one pattern to the next, the volume of wear observed throughout the test decreases in perfect correlation. The non-textured specimen, with no pockets to replenish the contact area, exhibits the highest wear volume when compared with any of the textured surfaces. The 80×3×1000 pattern on the other hand shows a higher volume of wear removed from the surface when compared with a twice as dense pattern, 80×3×500, which in turn shows lower wear performance when compared with the much deeper 40×7×500 pattern. Finally, the 300×7×1100 textured pattern, which replenishes the contact with a volume of oil at least three times higher than any of the other specimens, exhibited the lowest wear volume throughout the test. It should be noted that this monotonic decrease would not have been observed if wear had been plotted against pocket length, depth or width individually.
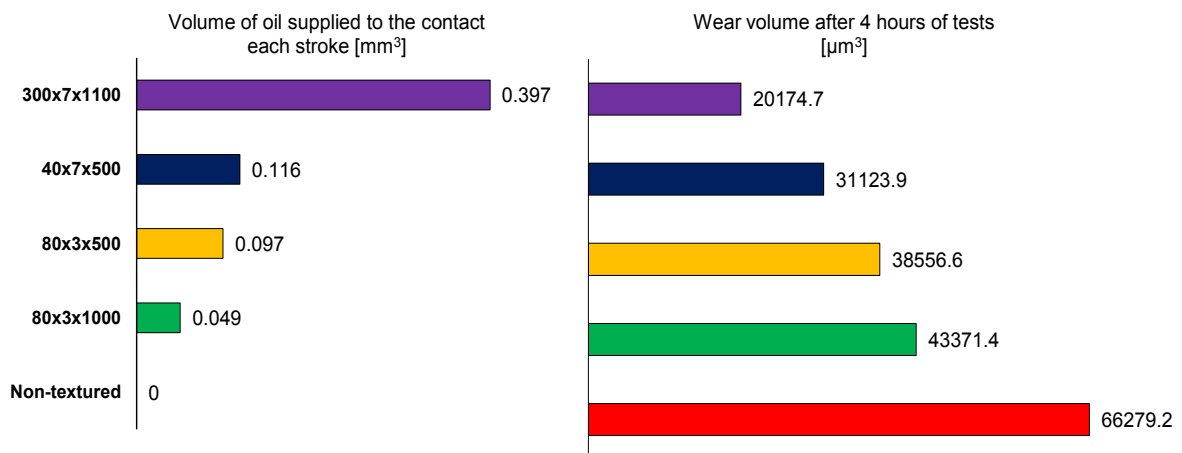
FIGURE 8.8: Correlation between the volume of oil supplied to the contact by the textured pattern each stoke and the wear behaviour.

To show the link between wear and friction behaviour, figure 8.9 plots average friction coefficient over the last 60 minutes of testing alongside final wear volume for different pocket entrainment volumes. Here, a positive correlation can be observed for four out of five specimens – specifically, a lower average friction corresponds to a lower final wear volume. This correlation may at first seem to be due to the fact that pockets cause an increase in film thickness (as presented in Chapter 6), and that this causes a reduction in both friction (as is known to be the case from Chapters 4 and 7), and also wear. However an exception to this trend is the 300×7×1100 pocketed specimen, which showed the lowest wear of all specimens but higher friction than denser pattern samples 40×7×500 and 80×3×500. It is important to note that this exception can be attributed to the 300 μm width pockets, which are larger than the 240 μm long contact. Such wide pockets are known to allow oil to flow from the contact and hence cause a collapse of the film, as showed in Chapter 4. This is an important result and seems to suggest that pockets reduce wear and friction via different mechanisms.
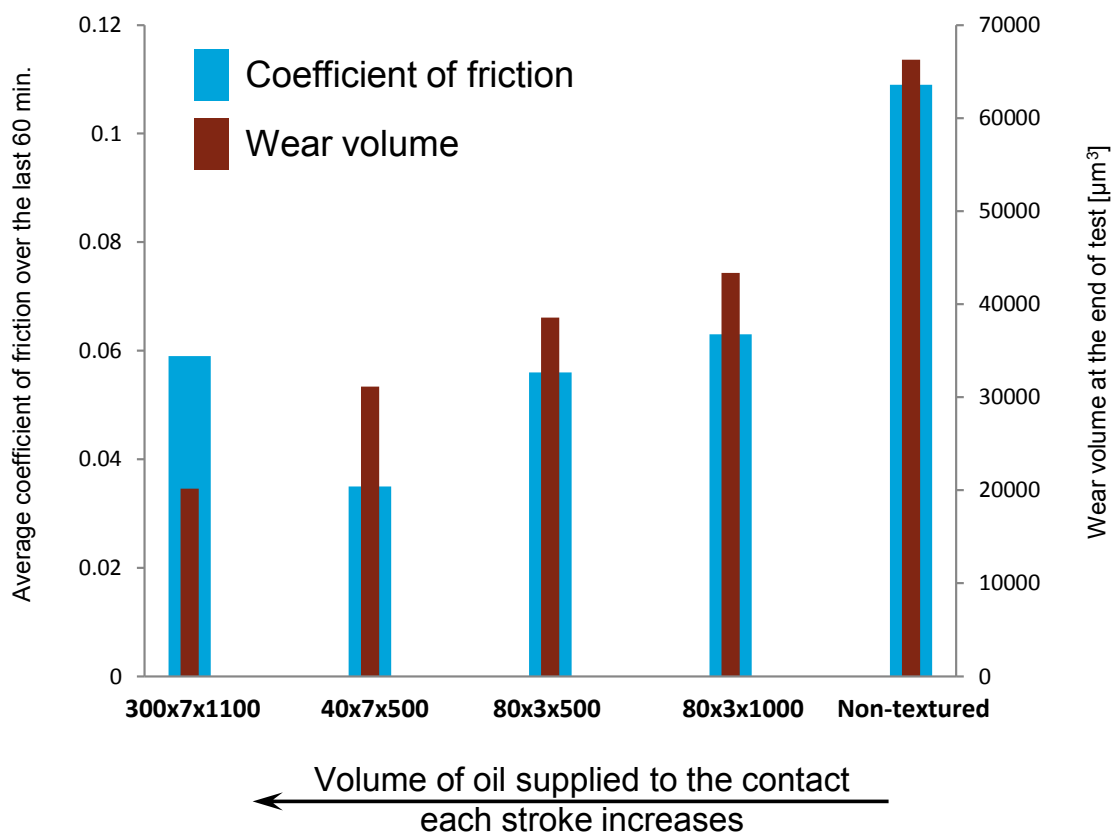
FIGURE 8.9: Correlation between the average coefficient of friction calculated over the last 60 minutes of testing and the final wear volume.

It may be that the additional mechanism with which pockets reduce wear is that of debris trapping and this is supported by the Veeco images of the worn silica pads, which show scoring marks in the direction of sliding that being cut short by the presence of pockets. It is also possible that pockets are reducing wear by replenishing lubricant and reducing starvation, however this mechanism would not explain the discrepancy between wear and friction behaviour. Furthermore, it should be noted that the excess oil was supplied to the contact inlet by means of the lubricant pumps, so that starvation is only likely to result from the ingestion of the cavitated region following reversal.

It should be noted that the fused silica pads used in this chapter will wear differently to steel specimens, however, they were selected so that results presented can be correlated with film thickness and friction results obtained in previous chapters. Similar wear testing of texture surfaces in metal-metal contacts will be the subject of future work.

8.4   Conclusions

The developed test apparatus was employed to assess the effects of laser produced surface texture upon friction and wear behaviour. This involved reciprocating sliding tests on a linear contact replicating the piston ring-cylinder liner pairing for a duration of four hours. Various patterns comprising pockets orientated normal to the direction of sliding were compared against a non-textured reference specimen, and this lead to the following key conclusions:

- For unworn contacts with high lambda values, such as those found at the start of testing, the presence of texture causes an increase in friction compared to the non-textured reference case (this agrees with previous findings on full film conditions).

- As specimens become worn and the contact enters the mixed lubrication regime, surface texture acts to significantly reduce the friction coefficient. Under these conditions, friction reductions of up to 70% were observed when comparing the best performing micro-textured pattern (40×7×500) against the non-textured reference. This suggests that surface texture performance is not only effective on

mirror polished laboratory specimens, but is likely to work on actual machine components where it will limit the deleterious effects of wear on friction.

- Both friction and wear reduce monotonically as the sum of the pocket volumes along the stroke increases. This may aid texture design, since it means that individual pocket width and depth values can largely be ignored, so long as the overall volume is maximised. The only exception to this trend is when the pockets are larger than the contact area. In this case, fiction increases due to a collapse of the lubricant film, while wear reduction remains unaffected and may suggest that pockets reduce wear and friction via separate mechanisms. This supports the theory that, in addition to providing a hydrodynamic film thickness boost, pockets act as reservoirs, which reduce starvation by increasing the supply of lubricant to the contact − particularly after reversal when the cavitated outlet becomes the inlet.

- Considering wear reduction when selecting the optimal pattern is thus an important step but must be complemented with thorough analysis of the frequency at which pockets enter the contact, the relative size of the pockets compared to the contact, and the precise pocket location relative to after reversal point.

Chapter 9

CONCLUSIONS

9.1   Summary

The main goal of this project was to experimentally investigate the effects of laser produced surface texture on friction force and film thickness for a convergent-divergent bearing, operating under different lubrication regimes. This was achieved by means of a recently developed test apparatus that closely simulates an automotive piston ring-liner contact by sliding patterned, plane, fused silica surfaces against a convex steel pad. High sensitivity optical imaging techniques were used to capture both film thickness and cavitation measurements in-situ, and a high resolution detection system to record frictional response.

The initial step in this research was a review of relevant literature to identify apparent gaps in the current knowledge related to textured bearings. This covered areas such as (1) the effects of textured surfaces on sliding friction, wear, lubricant replenishment and static friction; (2) the current level of advancement in film thickness measurements and (3) the understanding of the effects of cavitation within the lubricant on frictional behaviour.

The experimental undertaking was divided into five stages. Firstly, various textured fused silica pads were designed and manufactured with strategically chosen pocket shapes, and compared against a non-textured reference based on frictional performance. Secondly, the transverse groove pattern, deemed most effective, was subsequently parameterised in terms of pocket depth, breadth and area density. Thirdly, an innovative modification of the ultrathin optical interferometry technique, which relies on out-of-contact separation in place of a spacer layer, was employed to investigate film thicknesses for all lubrication regimes with high accuracy. To shed light on the mechanisms responsible for the beneficial or detrimental effect of surface texture under different lubrication regimes, this project adopted a novel approach by observing the individual transient friction response as each pocket passes through the reciprocating sliding contact. Finally, the study pursued to understanding the effects of surface texture on lubricant replenishment and wear behaviour in a lubricated reciprocating contact under highly loaded conditions.

9.2   Achievements

The accomplishments of this project have a direct industrial impact as Ford Motor Company is proceeding with patenting its findings, to be applied in engine trials. The most significant achievements are summarised below:

- Friction force, film thickness and cavitation were all measured in situ and simultaneously for the first time in a transient linear bearing, all parameters being captured with high precision at all points along the reciprocating stroke. This was enabled by a novel tribometer, designed and developed in-house, that accurately simulates the contact between automotive piston ring and liner under precisely controlled conditions.

- The relationship between the benefits of surface texture and operating regime was comprehensively outlined. In low film thickness contacts, surface texture can improve friction performances along the entire length of the stroke. Reductions in friction of more than 82% were achieved when operating in the mixed lubrication regime, if the correct shape, size and location of pockets are chosen. It was concluded that, as the lubricant film decreases and consequently directs the bearing towards the mixed lubrication regime, laser surfaced texture becomes increasingly beneficial. However, surface texture can deteriorate the performance of the convergent-divergent bearing when running in full film friction contacts. In this hydrodynamic lubrication regime, the non-textured reference specimen achieved the lowest average friction along one full cycle. The conclusion that texture

hydrodynamic

mixed

boundary
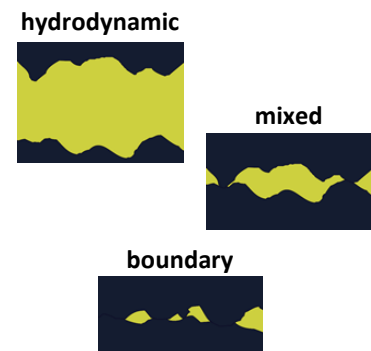
benefits depend on lubrication regime has significant industrial relevance, with clear implication on pocket spacing along the liner according to the lubrication regimes encountered during the piston's stroke.

- A thorough investigation was successfully conducted to identify the criteria for effective pocket shape. Textured samples with rectangular pockets which can be entirely trapped in the contact zone performed better than textured samples comprising pockets longer than the contact zone in the direction of travel. With regard to the pocket orientation, grooves perpendicular on the direction of sliding showed the highest level of effectiveness for all mixed and boundary regime tests.
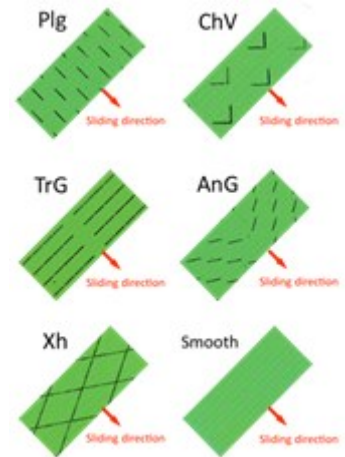
- A parametric study of texturing in transient linear bearings was also conducted throughout the project. It was found that a more densely textured area is desired at the end of stroke (boundary regime) while a sparsely textured area is required when the contact operates in the EHL regime. Similarly, it was found that deeper pockets performed better as the bearing approaches the boundary regime while shallower pockets lead to lower friction at the transition between mixed and hydrodynamic regimes.
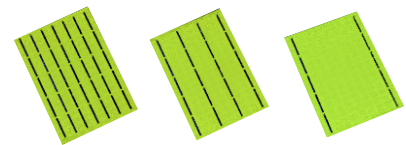
- Valuable insights into the mechanisms by which surface texture acts to reduce friction force were identified and detailed in this study:

a) By analysing the frictional behaviour of individual pocket passing through the contact, it was observed that each feature reduces the friction instantaneously

198
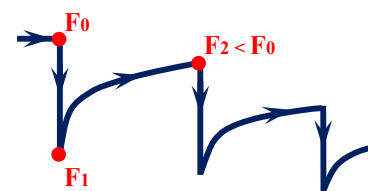
and this phenomenon is followed by a gradual film decay. It was concluded that pocket entrainment frequency is more important than physical spacing. Other industrial considerations (such as the optimum pocket spacing along the piston's stroke) follow on from this.

b) It was observed that surface texture at the end of travel can act to collapse the oil film. While running in the hydrodynamic regime, high friction spikes were observed when pockets were present at the point of reversal. However, under mixed and boundary lubrication conditions, pockets located immediately before reversal cause disproportionate reductions in friction; this benefit caries through to the next stroke.
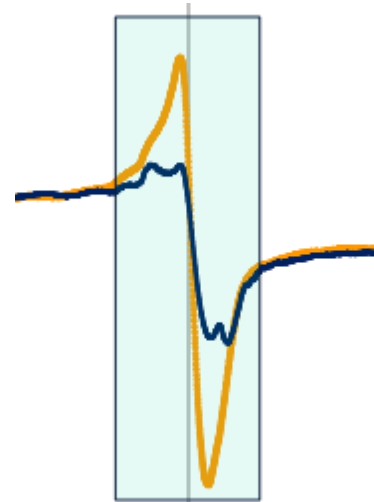
c) Based on previous studies claiming that the cavitated region may reduce lubricant entrainment immediately after reversal, causing starvation, the effect of surface texture on cavitation was qualitatively investigated. It was observed that pockets bring oil into the cavitated region, which may aid lubricant entrainment and hence reduce friction.
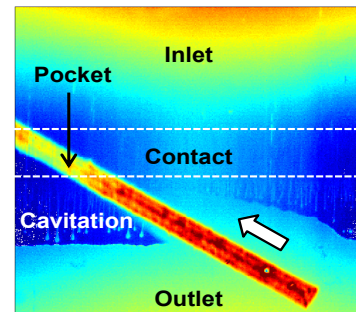
- Transient film thicknesses were measured using a modified version of the ultra-thin film optical interferometry approach and tests were performed for various textured geometries. Measurements showed that under the mixed lubrication regime pockets act to increase the oil film by 10s of a nanometre, causing a reduction in asperity contact. Hence, this led to the
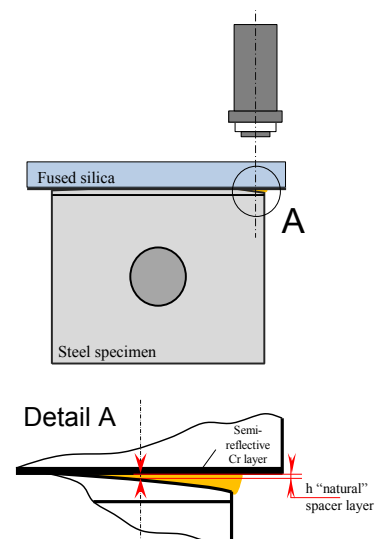
conclusion that enhanced fluid entrainment in mixed lubrication regime has the effect of shifting the Stribeck curve to the left.

- The interactions between laser produced surface texture and wear behaviour were also extensively investigated, leading to significant outcomes. Tests showed that as the specimens became worn and surface roughness increased, the contact progressed further into the mixed and boundary regimes. This lead to a significant improvement in the relative performance of the textured specimens, showing reductions in friction of up to 70%, compared to the non-texture case. Experiments also revealed that pockets can act as micro-reservoirs of oil which replenish the contact area immediately before and after reversal, a region where starvation can occur due to either insufficient lubricant entrainment or cavitated film. A close correlation was found between the wear behaviour in the vicinity of the reversal point and the amount of oil with which each pocket replenishes the contact area. As the volume of oil supplied by each pocket to the contact increases, the wear volume at the reversal drops correspondingly.
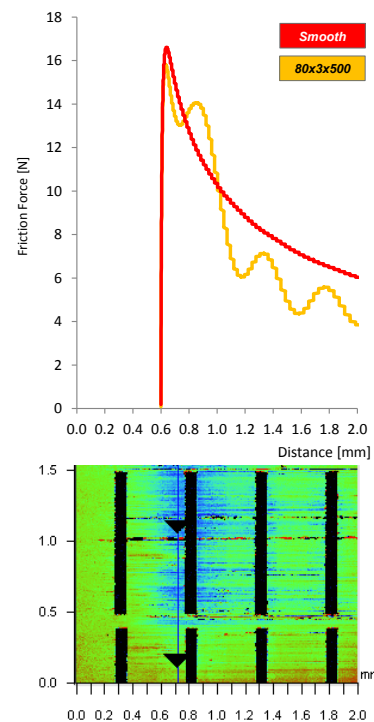
The question remains as to exactly what mechanism is responsible for the film thickness increase as each pocket leaves the contact and so far our experiments have not been able to prove or disprove inlet suction, the Trip effect, or some other hydrodynamic mechanism as being responsible. This problem is being tackled in ongoing work, particularly with the comparison on transient friction variations with outputs from a modelling approach mass conserving solution to Reynolds' Equation.

9.3   Future work

The high-level conclusion of this research is that surface texture can be applied in commercial production facilities as a cost-effective means of increasing fuel efficiency in motor vehicles. Results presented in Chapters 4 to 8 suggest this is possible; however texture lubrication mechanisms must be clearly understood before they can be modelled, optimised and ultimately used in practice. A number of interesting additional questions arose over the course of this research, not addressed due to time and resource constraints. Therefore, the following objectives were set for careful future investigation:

a) **Effects of Lubrication Parameters on Texture Performance.** No study to date has attempted to correlate friction reduction due to surface texture with different tribological parameters. However, such research is now possible thanks to the test apparatus developed for the purpose of this study, which can control/measure the relevant test parameters with sufficient accuracy. The parameters listed below will have to be tested in future work, in order to: *i)* shed light on the mechanisms by which pockets increase film thickness, *ii)* characterise how texture will function under the conditions in an actual engine.

- **Surface roughness** is a key parameter in determining the performance of deliberately applied features, with textured surfaces only outperforming plain ones over a certain range of lambda values (typically < 4, as previously detailed). However the effect of wear on texture friction reduction is not yet understood and neither are the interactions between pockets and wear-debris under piston/liner conditions.

- **Lubricant composition** will also affect the performance of pockets, although this has so far been overlooked. Future experiments can test how *i)* in-contact viscosity, *ii)* shear thinning and *iii)* asperity shear strength interact with surface texture. This can be achieved by varying the lubricant's *i)* pressure viscosity coefficient, *ii)* viscosity modifier content, and *iii)* friction modifier content. As well as shedding light on the mechanisms that occur, this will enable the formulation of lubricants that maximise texture friction reduction.

- **Starvation**, *i.e.* the reduction in film thickness due to inadequate replenishment of lubricant, is believed to be an issue in automotive piston-liner contacts, caused by the rapid reciprocating motion of the contact and the fact that the oil must lubricate multiple ring contacts. Applying texture to the liner surface might alleviate starvation effects in two ways. Firstly, starvation will push the contact towards the mixed and boundary regime where texture is most effective at increasing film thickness. Secondly, the presence of pockets on the contact path has been shown in pin-on-disc tests to limit starvation by providing additional reservoirs of lubricant. These proposed texture benefits should also be confirmed in a reciprocating piston-liner contact under starved lubrication conditions by controlling the flow rate of oil to the contact inlet.

b) **Optimisation of Texture.** It was already demonstrated in this study that friction reductions of more than 80% are possible and a set of criteria for optimum geometry was established (in terms of pocket density, breadth and depth). However, there are a number of novel alterations to further improve texture performance which are worth exploring:

- **Appling texture to the ring** specimen (in addition to the liner) in order to study the interaction between pockets on opposing surfaces (in this study so far, it was only the liner specimen that was textured).

- **Adjusting the piston ring radius** to control the relative dominance squeeze versus hydrodynamic effects and use this to optimise texture friction reduction.

- **Varying the spacing between pockets** along the stroke according to the sliding speed. This is necessary since the current research has shown the time between pockets being entrained into the contact is more important than the physical spacing between pockets (specifically, each pocket should enter the contact before the film has time to recover from the previous pocket).

c) **Expand to Other Components.** There is a real possibility that other mechanical components will benefit from surface texture (particularly those, such as gears and

cams that regularly operate in the mixed and boundary lubrication regimes). The potential for these numerous additional use cases can be assessed by performing short scoping studies by modifying existing standard test equipment such as UMT2 tribometer and PCS Instruments' journal bearing rig.

REFERENCES

[1]   International Energy Agency, World Energy Outlook 2014, Paris, France, 2014. doi:ISBN 978-92-64-20804-9.

[2]   European Parliament, Regulation (EC) no 443/2009 setting emission performance standards for new passenger cars as part of the Community's integrated approach to reduce CO_2 emissions from light-duty vehicles, Off. J. Eur. Union. (2009) 1–15.

[3]   K. Holmberg, P. Andersson, A. Erdemir, Global energy consumption due to friction in passenger cars, Tribol. Int. 47 (2012) 221–234. doi:10.1016/j.triboint.2011.11.022.

[4]   R.I. Taylor, R.C. Coy, Improved fuel efficiency by lubricant design: A review, Proc. Inst. Mech. Eng. Part J J. Eng. Tribol. 214 (2000) 1–15. doi:10.1177/135065010021400101.

[5]   S. Korcek, J. Sorab, M.D. Johnson, R.K. Jensen, Automotive lubricants for the next millennium, Ind. Lubr. Tribol. 52 (2000) 209–220.

[6]   V. Macián, B. Tormos, V. Bermúdez, L. Ramírez, Assessment of the effect of low viscosity oils usage on a light duty diesel engine fuel consumption in stationary and transient conditions, Tribol. Int. 79 (2014) 132–139. doi:10.1016/j.triboint.2014.06.003.

[7]   D.B. Hamilton, J.A. Walowit, C.M. Allen, A Theory of Lubrication by Micro- irregularities, Trans. ASME J. Basic Eng. 88 (1966) 177–185.

[8]   G. Ryk, Y. Kligerman, I. Etsion, a. Shinkarenko, Experimental Investigation of Partial Laser Surface Texturing for Piston-Ring Friction Reduction, Tribol. Trans. 48 (2005) 583–588. doi:10.1080/05698190500313544.

[9]   H. Rahnejat, S. Balakrishnan, P.D. King, S. Howell-Smith, In-Cylinder Friction Reduction Using a Surface Finish Optimization Technique, Proc. Inst. Mech. Eng. Part D J. Automob. Eng. 220 (2006) 1309–1318. doi:10.1243/09544070JAUTO282.

[10]   D. Braun, C. Greiner, J. Schneider, P. Gumbsch, Efficiency of laser surface texturing in the reduction of friction under mixed lubrication, Tribol. Int. 77 (2014) 142–147. doi:10.1016/j.triboint.2014.04.012.

[11]   U. Pettersson, S. Jacobson, Influence of surface texture on boundary lubricated sliding contacts, Tribol. Int. 36 (2003) 857–864. doi:10.1016/S0301-679X(03)00104-X.

[12]   L.M. Vilhena, M. Sedlaček, B. Podgornik, J. Vižintin, a. Babnik, J. Možina, Surface texturing by pulsed Nd:YAG laser, Tribol. Int. 42 (2009) 1496–1504. doi:10.1016/j.triboint.2009.06.003.

[13]   H.L. Costa, I.M. Hutchings, Hydrodynamic lubrication of textured steel surfaces under reciprocating sliding conditions, Tribol. Int. 40 (2007) 1227–1238. doi:10.1016/j.triboint.2007.01.014.

[14]   H. Costa, I. Hutchings, Some innovative surface texturing techniques for tribological purposes, Proc. Inst. Mech. Eng. Part J J. Eng. Tribol. (2014). doi:10.1177/1350650114539936.

[15]   Gehring, Advance Honing Technology, 2013.

[16]   G. Flores, Tribologisch gestaltete Oberflächen durch Laserstrukturieren, 2014.

[17]   G. Ryk, I. Etsion, Testing piston rings with partial laser surface texturing for friction reduction, Wear. 261 (2006) 792–796. doi:10.1016/j.wear.2006.01.031.

[18]   I. Etsion, E. Sher, Improving Fuel Efficiency with Laser Surface Textured Piston Rings, Tribol. Int. 42 (2009) 542–547. doi:10.1016/j.triboint.2008.02.015.

[19]   A. Kovalchenko, O. Ajayi, A. Erdemir, G. Fenske, I. Etsion, The Effect of Laser Surface Texturing on Transitions in Lubrication Regimes During Unidirectional Sliding Contact, Tribol. Int. 38 (2005) 219–225. doi:10.1016/j.triboint.2004.08.004.

[20]   A. Borghi, E. Gualtieri, D. Marchetto, L. Moretti, S. Valeri, Tribological effects of surface texturing on nitriding steel for high-performance engine applications, Wear. 265 (2008) 1046–1051. doi:10.1016/j.wear.2008.02.011.

[21]   W. Wang, Z. Huang, D. Shen, L. Kong, S. Li, The Effect of Triangle-Shaped Surface Textures on the Performance of the Lubricated Point-Contacts, J. Tribol. 135 (2013) 021503. doi:10.1115/1.4023206.

[22]   X. Lu, M.M. Khonsari, An Experimental Investigation of Dimple Effect on the Stribeck Curve of Journal Bearings, Tribol. Lett. 27 (2007) 169–176. doi:10.1007/s11249-007-9217-x.

[23]   A.V. Olver, M.T. Fowell, H.A. Spikes, I.G. Pegg, "Inlet suction", a load support mechanism in non-convergent, pocketed, hydrodynamic bearings, Proc. Inst. Mech. Eng. Part J J. Eng. Tribol. 220 (2006) 105–108. doi:10.1243/13506501JET168.

[24]   M. Fowell, A.V. Olver, A.D. Gosman, H.A. Spikes, I.G. Pegg, Entrainment and Inlet Suction: Two Mechanisms of Hydrodynamic Lubrication in Textured Bearings, J. Tribol. 129 (2007) 336–347. doi:10.1115/1.2540089.

[25]   M. Scaraggi, F.P. Mezzapesa, G. Carbone, A. Ancona, L. Tricarico, Friction Properties of Lubricated Laser-MicroTextured-Surfaces: An Experimental Study from Boundary- to Hydrodynamic-Lubrication, Tribol. Lett. 49 (2012) 117–125. doi:10.1007/s11249-012-0045-2.

[26]   L. Wang, Use of structured surfaces for friction and wear control on bearing surfaces, Surf. Topogr. Metrol. Prop. 2 (2014) 043001. doi:10.1088/2051-672X/2/4/043001.

[27]   K.H. Zum Gahr, M. Mathieu, B. Brylka, Friction control by surface engineering of ceramic sliding pairs in water, Wear. 263 (2007) 920–929. doi:10.1016/j.wear.2006.11.024.

[28]   M. Varenberg, G. Halperin, I. Etsion, Different aspects of the role of wear debris in fretting wear, Wear. 252 (2002) 902–910.

[29]   A. Volchok, G. Halperin, I. Etsion, The effect of surface regular microtopography on fretting fatigue life, Wear. 253 (2002) 509–515. doi:10.1016/S0043-1648(02)00148-5.

[30]   U. Pettersson, S. Jacobson, Friction and Wear Properties of Micro Textured DLC Coated Surfaces in Boundary Lubricated Sliding, Tribol. Lett. 17 (2004) 553–559. doi:10.1023/B:TRIL.0000044504.76164.4e.

[31]   A. Blatter, M. Maillat, S.M. Pimenov, G.A. Shafeev, A.V. Simakin, E.N. Loubnin, Lubricated sliding performance of laser-patterned sapphire, Wear. 232 (1999) 226–230. doi:10.1016/S0043-1648(99)00150-7.

[32]   Y.P. Chiu, An Analysis and Prediction of Lubricant Film Starvation in Rolling Contact Systems, A S L E Trans. 17 (2008) 22–35. doi:10.1080/05698197408981435.

[33]   I. Demirci, S. Mezghani, M. Yousfi, H. Zahouani, M. El Mansori, The Scale Effect of Roughness on Hydrodynamic Contact Friction, Tribol. Trans. 55 (2012) 705–712. doi:10.1080/10402004.2012.694990.

[34]   I. Křupka, M. Vrbka, M. Hartl, Effect of surface texturing on mixed lubricated non-conformal contacts, Tribol. Int. 41 (2008) 1063–1073. doi:10.1016/j.triboint.2007.11.016.

[35]   C. Greiner, M. Schafer, U. Popp, P. Gumbsch, Contact Splitting and the Effect of Dimple Depth on Static Friction of Textured Surfaces, Appl. Mater. Interfaces. 6 (2014) 7986–7990.

[36]   J.N. Anno, J. a. Walowit, C.M. Allen, Microasperity Lubrication, J. Lubr. Technol. 90 (1968) 351–355. doi:10.1115/1.3601568.

[37]   K. Tønder, Dynamics of rough slider bearings : effects of one-sided roughness / waviness, Tribol. Int. 29 (1996) 117–122.

[38]   K. Tønder, Hydrodynamic effects of tailored inlet roughnesses: extended theory, Tribol. Int. 37 (2004) 137–142. doi:10.1016/S0301-679X(03)00043-4.

[39]   D. Gropper, L. Wang, T.J. Harvey, Hydrodynamic lubrication of textured surfaces: A review of modeling techniques and key findings, Tribol. Int. 94 (2016) 509–529. doi:10.1016/j.triboint.2015.10.009.

[40]   A. Ronen, I. Etsion, Y. Kligerman, Friction-Reducing Surface-Texturing in Reciprocating Automotive Components, Tribol. Trans. 44 (2001) 359–366. doi:10.1080/10402000108982468.

[41]   I. Etsion, State of the Art in Laser Surface Texturing, J. Tribol. 127 (2005) 248. doi:10.1115/1.1828070.

[42]   G. Ryk, Y. Kligerman, I. Etsion, Experimental Investigation of Laser Surface Texturing for Reciprocating Automotive Components, Tribol. Trans. 45 (2002) 444–449.

[43]   P. Brajdic-Mitidieri, A.D. Gosman, E. Ioannides, H.A. Spikes, CFD Analysis of a Low Friction Pocketed Pad Bearing, J. Tribol. 127 (2005) 803–812. doi:10.1115/1.2032990.

[44]   M.T. Fowell, S. Medina, A.V. Olver, H.A. Spikes, I.G. Pegg, Parametric study of texturing in convergent bearings, Tribol. Int. 52 (2012) 7–16. doi:10.1016/j.triboint.2012.02.013.

[45]   I. Krupka, M. Hartl, M. Zimmerman, P. Houska, S. Jang, Effect of surface texturing on elastohydrodynamically lubricated contact under transient speed conditions, Tribol. Int. 44 (2011) 1144–1150. doi:10.1016/j.triboint.2011.05.005.

[46]   L. Mourier, D. Mazuyer, F.-P. Ninove, A.A. Lubrecht, Lubrication mechanisms with laser-surface-textured surfaces in elastohydrodynamic regime, Proc. Inst. Mech. Eng. Part J J. Eng. Tribol. 224 (2010) 697–711. doi:10.1243/13506501JET771.

[47]   H.L. Costa, I.M. Hutchings, Effects of die surface patterning on lubrication in strip drawing, J. Mater. Process. Technol. 209 (2009) 1175–1180. doi:10.1016/j.jmatprotec.2008.03.026.

[48]   M. Wakuda, Y. Yamauchi, S. Kanzaki, Y. Yasuda, Effect of surface texturing on friction reduction between ceramic and steel materials under lubricated sliding contact, Wear. 254 (2003) 356–363. doi:10.1016/S0043-1648(03)00004-8.

[49]   Q.J. Wang, D. Zhu, Virtual Texturing: Modeling the Performance of Lubricated Contacts of Engineered Surfaces, J. Tribol. 127 (2005) 722. doi:10.1115/1.2000273.

[50]   Y.-R. Jeng, Impact of Plateaued Surfaces on Tribological Performance, Tribol. Trans. 39 (1996) 354–361. doi:10.1080/10402009608983538.

[51]   N.W. Bolander, B.D. Steenwyk, F. Sadeghi, G.R. Gerber, Lubrication regime transitions at the piston ring-cylinder liner interface, Proc. Inst. Mech. Eng. Part J J. Eng. Tribol. 219 (2005) 19–31. doi:10.1243/135065005X9664.

[52]   S. Mezghani, I. Demirci, H. Zahouani, M. El Mansori, The effect of groove texture patterns on piston-ring pack friction, Precis. Eng. 36 (2012) 210–217. doi:10.1016/j.precisioneng.2011.09.008.

[53]   S. Yuan, W. Huang, X. Wang, Orientation effects of micro-grooves on sliding surfaces, Tribol. Int. 44 (2011) 1047–1054. doi:10.1016/j.triboint.2011.04.007.

[54]   Y. Kligerman, I. Etsion, A. Shinkarenko, Improving Tribological Performance of Piston Rings by Partial Surface Texturing, J. Tribol. 127 (2005) 632–638. doi:10.1115/1.1866171.

[55]   R. Ausas, P. Ragot, J. Leiva, M. Jai, G. Bayada, G.C. Buscaglia, The Impact of the Cavitation Model in the Analysis of Microtextured Lubricated Journal Bearings, J. Tribol. 129 (2007) 868. doi:10.1115/1.2768088.

[56]   R.F. Ausas, M. Jai, G.C. Buscaglia, A Mass-Conserving Algorithm for Dynamical Lubrication Problems With Cavitation, J. Tribol. 131 (2009) 031702. doi:10.1115/1.3142903.

[57]   X. Wang, K. Kato, K. Adachi, K. Aizawa, Loads carrying capacity map for the surface texture design of SiC thrust bearing sliding in water, Tribol. Int. 36 (2003) 189–197. doi:10.1016/S0301-679X(02)00145-7.

[58]   A. Ramesh, W. Akram, S.P. Mishra, A.H. Cannon, A.A. Polycarpou, W.P. King, Friction characteristics of microtextured surfaces under mixed and hydrodynamic lubrication, Tribol. Int. 57 (2013) 170–176.

[59]   D. Yan, N. Qu, H. Li, X. Wang, Significance of Dimple Parameters on the Friction of Sliding Surfaces Investigated by Orthogonal Experiments, Tribol. Trans. 53 (2010) 703–712. doi:10.1080/10402001003728889.

[60]   M. Duarte, a. Lasagni, R. Giovanelli, J. Narciso, E. Louis, F. Mücklich, Increasing Lubricant Film Lifetime by Grooving Periodical Patterns Using Laser Interference Metallurgy, Adv. Eng. Mater. 10 (2008) 554–558. doi:10.1002/adem.200700321.

[61]   A.S. Manzoor, Fluorescence Imaging of Lubricants in Microtextured Bearings, Imperial College London, 2009.

[62]   K. Poser, K.-H. Zum Gahr, J. Schneider, Development of Al2O3 based ceramics for dry friction systems, Wear. 259 (2005) 529–538. doi:10.1016/j.wear.2004.11.007.

[63]   M. Varenberg, a. Peressadko, S. Gorb, E. Arzt, Effect of real contact geometry on adhesion, Appl. Phys. Lett. 89 (2006) 121905. doi:10.1063/1.2356099.

[64]   G.E. Morales-Espejel, Elastohydrodynamic Lubrication of Smooth and Rough Surfaces - PhD Thesis, University of Cambridge, 1993.

[65]   J.A. Greenwood, G.E. Morales-Espejel, The behaviour of transverse roughness in EHL contacts, Proc. Inst. Mech. Eng. Part J J. Eng. Tribol. 208 (1994) 121–132. doi:10.1243/PIME.

[66]   G.E. Morales-Espejel, P.M. Lugt, J. Van Kuilenburg, J.H. Tripp, Effects of Surface Micro-Geometry on the Pressures and Internal Stresses of Pure Rolling EHL Contacts, Tribol. Trans. 46 (2003) 260–272. doi:10.1080/10402000308982625.

[67]   W.W.F. Chong, M. Teodorescu, N.D. Vaughan, Cavitation induced starvation for piston-ring/liner tribological conjunction, Tribol. Int. 44 (2011) 483–497. doi:10.1016/j.triboint.2010.12.008.

[68]   H.G. Elrod, A Cavitation Algorithm, J. Lubr. Technol. (1981).

[69]   G. Guangteng, P.M. Cann, H.A. Spikes, A study of parched lubrication, Wear. 153 (1992) 91–105.

[70]   M. Priest, D. Dowson, C.M. Taylor, Theoretical modelling of cavitation in piston ring lubrication, Proc. Inst. Mech. Eng. Part C J. Mech. Eng. Sci. 214 (2000) 435–446. doi:10.1243/0954406001523092.

[71]   L.K.R. Gümbel, Vergleich der Ergebrusse der rectinerischen Behandling des Lagerschmierangsproblem mitneueren Versuchsergebrussen, Monatsbl. Berliner Bez Ver. Dtsch. Ing. (1921) 125–128.

[72]   H.W. Swift, The stability of lubricating films in journal bearings, J. Inst. Civ. Eng. 233 (1931) 267–288.

[73]   W. Stieber, Das Schwimmlager, Ver. Dtsch. Ing. (1933).

[74]   B. Jakobson, L. Floberg, The finite journal bearing considering vaporization, Trans. Chalmers Univ. Technol. Guthenberg, Sweden. 190 (1957) 1–119.

[75]   K.O. Olsson, Cavitation in Dynamically Loaded Bearings, Trans. Chalmers Univ. Technol. Goteborg. (1965) 308.

[76]   L. Floberg, On journal bearing lubrication considering the tensile strength of the liquid lubricant, Vedmar, L. Trans. Mach. Elem. Div. (1973) 1–26.

[77]   L. Floberg, Cavitation boundary conditions with regard to the number of streamers and tensile strength of the liquid, Dowson, D., Godet, M., Taylor, C.M. Cavitation Relat. Phenom. Lubr. Proc. 1st Leeds– Lyon Symp. Tribol. (1974) 31–36.

[78]   R. Taylor, Squeeze film lubrication in piston rings and reciprocating contacts, Proc. Inst. Mech. Eng. Part J J. Eng. Tribol. 0 (2015) 1–12. doi:10.1177/1350650114564234.

[79]   D. Dowson, E.H. Smith, C.M. Taylor, An experimental study of hydrodynamic film rupture in a steadily-loaded, non-conformal contact, Arch. J. Mech. Eng. Sci. 1959-1982 (vols 1-23). 22 (2006) 71–78. doi:10.1243/JMES_JOUR_1980_022_018_02.

[80]   D. Dowson, Cavitation in lubricating films supporting small loads, Proc. Institutional Mech. Eng. Conf. Lubr. Wear. (1957) 93–99.

[81]   I. Etsion, L.P. Ludwig, Observation of pressure variation in the cavitation region of submerged journal bearings, J. Tribol. 104 (1982) 157–163. doi:10.1115/1.3253174.

[82]   P. Dellis, C. Arcoumanis, Cavitation development in the lubricant film of a reciprocating piston-ring assembly, Proc. Inst. Mech. Eng. Part J J. Eng. Tribol. 218 (2004) 157–171. doi:10.1243/1350650041323340.

[83]   A. Dhunput, M. Teodorescu, C. Arcoumanis, Investigation of cavitation development in the lubricant film of piston-ring assemblies, J. Phys. Conf. Ser. 85 (2007) 012005. doi:10.1088/1742-6596/85/1/012005.

[84]   T. Tang, N. Morris, J. Coupland, L. Arevalo, Cavitation Bubble Measurement in Tribological Contacts Using Digital Holographic Microscopy, Tribol. Lett. 58 (2015). doi:10.1007/s11249-015-0488-3.

[85]   M.T. Kirk, Hydrodynamic Lubrication of "Perspex," Nature. 194 (1962) 965–966.

[86]   P.M. Cann, H. a. Spikes, J. Hutchinson, The Development of a Spacer Layer Imaging Method

(SLIM) for Mapping Elastohydrodynamic Contacts, Tribol. Trans. 39 (1996) 915–921. doi:10.1080/10402009608983612.

[87]   H. a Spikes, P.M. Cann, The development and application of the spacer layer imaging method for measuring lubricant film thickness, Proc. Inst. Mech. Eng. Part J J. Eng. Tribol. 215 (2001) 261–277. doi:10.1243/1350650011543529.

[88]   I. Křupka, M. Hartl, The effect of surface texturing on thin EHD lubrication films, Tribol. Int. 40 (2007) 1100–1110. doi:10.1016/j.triboint.2006.10.007.

[89]   M. Kaneta, H. Todoroki, H. Nishikawa, Y. Kanzaki, Y. Kawahara, Tribology of Flexible Seals for Reciprocating Motion, J. Tribol. 122 (2000) 787. doi:10.1115/1.1310573.

[90]   T. Reddyhoff, J.H. Choo, H. a. Spikes, R.P. Glovnea, Lubricant flow in an elastohydrodynamic contact using fluorescence, Tribol. Lett. 38 (2010) 207–215. doi:10.1007/s11249-010-9592-6.

[91]   C. Myant, T. Reddyhoff, H. a. Spikes, Laser-induced fluorescence for film thickness mapping in pure sliding lubricated, compliant, contacts, Tribol. Int. 43 (2010) 1960–1969. doi:10.1016/j.triboint.2010.03.013.

[92]   S.-C. Vlădescu, A. V. Olver, I.G. Pegg, T. Reddyhoff, The effects of surface texture in reciprocating contacts – An experimental study, Tribol. Int. 82 (2015) 28–42. doi:10.1016/j.triboint.2014.09.015.

[93]   J. Dearlove, W.K. Cheng, Simultaneous piston ring friction and oil film thickness measurements in a reciprocating test rig, SAE Trans. J. Fuels Lubr. 104 (1995) 1452–1462. doi:10.4271/952470.

[94]   R.S. Dwyer-Joyce, T. Reddyhoff, B.W. Drinkwater, Operating Limits for Acoustic Measurement of Rolling Bearing Oil Film Thickness, Tribol. Trans. 47 (2004) 366–375. doi:10.1080/05698190490455410.

[95]   T. Reddyhoff, S. Kasolang, R.S. Dwyer-Joyce, B.W. Drinkwater, The phase shift of an ultrasonic pulse at an oil layer and determination of film thickness, 219 (2005) 387–400. doi:10.1243/135065005x34044.

[96]   E.Y. Avan, R. Mills, R. Dwyer-Joyce, Ultrasonic Imaging of the Piston Ring Oil Film During Operation in a Motored Engine-Towards Oil Film Thickness Measurement, SAE Int. J. Fuels Lubr. 3 (2010) 786–793.

[97]   R.S. Mills, E.Y. Avan, R.S. Dwyer-Joyce, Piezoelectric sensors to monitor lubricant film thickness at piston–cylinder contacts in a fired engine, J. Eng. Tribol. 0 (2012) 1–12. doi:10.1177/135065011246483.

[98]   R.S. Dwyer-Joyce, T. Reddyhoff, J. Zhu, Ultrasonic Measurement for Film Thickness and Solid Contact in Elastohydrodynamic Lubrication, 133 (2011) 1–11. doi:10.1115/1.4004105.

[99]   P.C. Mishra, H. Rahnejat, P.D. King, Tribology of the ring–bore conjunction subject to a mixed regime of lubrication, Proc. Inst. Mech. Eng. Part C J. Mech. Eng. Sci. 223 (2009) 987–998. doi:10.1243/09544062JMES1220.

[100]   M.A. Brown, H. McCann, D.M. Thompson, Characterization of the Oil Film Behaviour Between the Liner and Piston of a Heavy-Duty Diesel Engine, SAE Tech. Pap. Ser. 932784. (1993).

[101]   PCS Instruments, MTM 2 - Mini Traction Machine, (n.d.). http://pcs-instruments.com/wp-content/uploads/2014/03/MTM2.pdf.

[102]   D. Dowson, A. Toyoda, A central film thickness formula in EHD line contacts., in: Proc 5th Leeds-Lyon Symp. Elastohydrodyn. Lubr. Relat. Top., MEP Press, London, 1978.

[103]   K.L. Johnson, Regimes of elastohydrodynamic lubrication, J. Mech. Eng. Sci. 12 (1970) 9–16.

[104]   S. Medina, M.T. Fowell, S.-C. Vlădescu, T. Reddyhoff, I. Pegg, a. V. Olver, et al., Transient effects in lubricated textured bearings, Proc. Inst. Mech. Eng. Part J J. Eng. Tribol. 0 (2015) 1–15. doi:10.1177/1350650115572448.

[105]   D. Dowson, C.M. Taylor, Cavitation in Bearings, Annu. Rev. Fluid Mech. 11 (1979) 35–65. doi:10.1146/annurev.fl.11.010179.000343.

[106]   C.M. Taylor, Film Rupture for a Lubricated Cylinder Lightly Loaded against a Plane, J. Mech. Eng. Sci. 16 (1974) 225–231.

[107]   H.C. Liu, F. Guo, L. Guo, P.L. Wong, A Dichromatic Interference Intensity Modulation Approach to Measurement of Lubricating Film Thickness, Tribol. Lett. 58 (2015) 1–11. doi:10.1007/s11249-015-0480-y.

[108]   B.J. Hamrock, Fundamentals of Fluid Film Lubrication, McGraw Hill Inc, New York, 1994.

[109]   K.L. Johnson, Regimes of Elastohydrodynamic Lubrication, J. Mech. Eng. Sci. 12 (1970) 9–16. doi:10.1243/JMES_JOUR_1970_012_004_02.

[110]   Y. Wakuri, T. Hamatake, M. Soejima, T. Kitahara, Piston ring friction in internal combustion engines, Tribol. Int. 25 (1992) 299–308. doi:10.1016/0301-679X(92)90027-K.

[111]   Y. Tateishi, Tribological issues in reducing piston ring friction losses, Tribol. Int. 27 (1994) 17–23. doi:10.1016/0301-679X(94)90058-2.

[112]   A. Kovalchenko, O. Ajayi, A. Erdemir, G. Fenske, Friction and wear behavior of laser textured surface under lubricated initial point contact, Wear. 271 (2011) 1719–1725. doi:10.1016/j.wear.2010.12.049.

[113]   D. He, S. Zheng, J. Pu, G. Zhang, L. Hu, Improving tribological properties of titanium alloys by combining laser surface texturing and diamond-like carbon film, Tribol. Int. 82 (2015) 20–27. doi:10.1016/j.triboint.2014.09.017.

[114]   D. Dowson, G.R. Higginson, Elasto-hydrodynamic Lubrication, SI Edition, Pergamon Press Ltd., London, 1977.

[115]   I.M. Hutchings, Tribology - friction and wear of engineering materials, Butterworth-Heinemann, Oxford, 1992.

[116]   G. Stachowiak, A.W. Batchelor, Engineering tribology, Butterworth-Heinemann, 2013.

[117]   J.A. Williams, Engineering tribology, Oxford University Press, Oxford, 1994.

[118]   M. Gore, P.D. King, S. Howell-Smith, H. Rahnejat, Measurement of in-cylinder friction using the floating liner principle, Proc. ASME 2012 Intern. Combust. Engine Div. Spring Tech. Conf. (2012) 1–6.

[119]   S. Furuhama, M. Takiguchi, Measurement of Piston Frictional Force in Actual Operating Diesel Engine, SEA Pap. 790855 (1980) 2896–2914.

[120]   S. Furuhama, S. Sasaki, New Device for the Measurement of Piston Frictional Forces in Small Engines, SAE Tech. Pap. Ser. 831284 (1983) 39–50.

[121]   O. Akalin, G.M. Newaz, Piston Ring-Cylinder Bore Friction Modeling in Mixed Lubrication Regime: Part I—Analytical Results, J. Tribol. 123 (2001) 211–218. doi:10.1115/1.1286337.

Appendix A

GLOSSARY OF RELEVANT TRIBOLOGICAL TERMS

This section briefly introduces readers without a tribological background to the basic concepts used throughout the report. For an in-depth understanding of the topic, readers are advised to refer to one of several tribology text books, *e.g.* [115–117].

Tribology is the study of contacting surfaces in relative motion and encompasses friction, lubrication and wear. The word tribology was coined in 1966, after a government commission report highlighted its industrial importance, and is based on the Greek "tribos" (meaning to rub).

Hydrodynamic Lubrication is the mechanism that allows a wide range of bearings to function. Basically, it involves a liquid being entrained (dragged) into a converging gap between two surfaces by the motion of one, or both surfaces. If the liquid is viscous then it will resist this flow and generates a pressure which pushes the two surfaces apart. As a result, components become separated by a low shear strength layer, which provides low friction and prevents surface contact and wear. Components where this mechanism completely separates the sliding surfaces are said to operating in the hydrodynamic regime.

Boundary Lubrication occurs when the two surfaces that make up a contact are moving very slowly, or, if the lubricant viscosity is too low. In these cases the hydrodynamic effect will be negligible and the entire load will be supported by solid-solid contact. This is known as the boundary lubrication regime. It should be noted that this is not the same

as dry lubrication conditions, since the liquid may still provide lubricant means of chemical effects.

Mixed Lubrication occurs at intermediate speeds and viscosities when the pressure generated by the entrained liquid is sufficient to partially separate the sliding surfaces. Under these conditions, the load is supported by a combination of a liquid films and regions of solid-solid contact.

Stribeck Curve. It follows from the above discussion of lubrication regimes that, if friction is measured in a sliding contact as speed is increased from stationary, then the contact will pass through each of the lubrication regimes. First, the contact will be under boundary lubrication and the friction coefficient will be relatively high (0.1). Then as the speed increases the contact will enter the mixed regime and friction will begin to fall with increasing speed as the surfaces become separated. Finally, at higher speeds, the lubricant film will be sufficiently thick that the surface will be completely separated and the contact will be in the hydrodynamic regime. Under these conditions, friction will begin to rise with increasing speed due to the effect of viscous shear. If this variation in friction is plotted against speed (or speed ×viscosity / load) the result is known as a Stribeck curve, as exemplified in figure A.1.
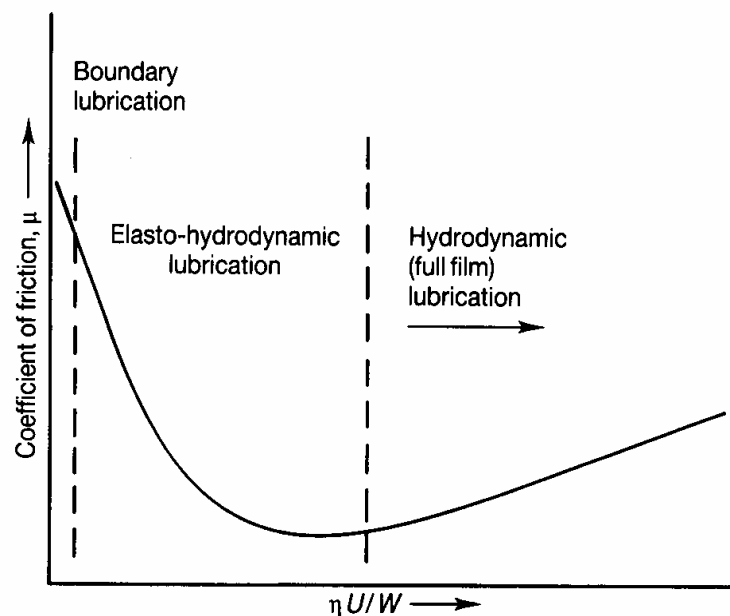
FIGURE **A.1**: Stribeck curve showing coefficient plotted against the product of the absolute viscosity (η) and the rotational speed in revolutions per second (*U*) divided by the load per unit projected bearing area (*W*). [115]

Lambda Ratio is defined as the ratio of the lubricant film thickness to the average out-of-contact roughness of the two surfaces. High values of lambda ratios signify contacts where all the load is supported by the liquid film (hydrodynamic lubrication), whereas low values show that the loads is supported by solid-solid contact. The lambda ratio therefore gives an indication of which lubrication region the contact is operating in.

Elastohydrodynamic Lubrication occurs in counter-formal contacts (*i.e.* contacts in which the gap between contacting surfaces is not constant so that high pressures arise). These high pressure conditions may cause the component surfaces to deform – an effect which aids the hydrodynamic mechanism – in which case the mechanism is known as elastohydrodynamic lubrication. With counter-formal metal components, the contact pressure is sufficiently high to cause a significant increase in lubricant viscosity, which also aids lubrication.

Static Friction is the force which must be overcome when moving an object which is initially stationary. This force is typically greater than that required to maintain the object's motion, *i.e.* kinetic friction, and manifests itself as a spike in friction coefficient at the onset of motion. This reason for the discrepancy between static and dynamic friction is that under static conditions the conjunctions between surfaces have had time to form completely and require a force to be sheared before sliding occurs.

Appendix B

OVERVIEW OF PISTON RING LUBRICATION CONDITIONS

A high-level overview of lubrication regimes found in IC engines over the four strokes is necessary for a better understanding of the tribological conditions present in the piston ring – cylinder liner reciprocating bearing.

The lubrication regimes encountered in the piston ring–liner interface have been identified through a number of experimental techniques. The floating liner method (*i.e.* separating the liner and cylinder using a force sensor, figure B.1(a)) was employed in various studies [110,118–120]. Gore et al. [118] and Wakuri et al. [110] measured the forces exerted by the motion of the piston due to combustion; their results confirmed the generally accepted conclusion that it is the mixed and boundary regimes of lubrication at piston reversals that mostly contribute to parasitic engine losses. Mishra and Rahnejat [99] developed numerical analysis which showed the transient nature of the lubrication regime in the piston ring–cylinder liner conjunction. They compared their results with the numerical predictions of Akalin and Newaz [121] and the experimental findings of Furuhama and Sasaki [120], who determined friction values by employing the same floating liner method on a V2 engine configuration from Chevrolet. The three pieces of work report consistent results, which also match the findings of Gore [118] and Wakuri [110] and lead to the same generic conclusion: the lubrication regimes found at both ends of piston stroke are boundary and mixed regimes - figure B.1(b).

(a)

(b)
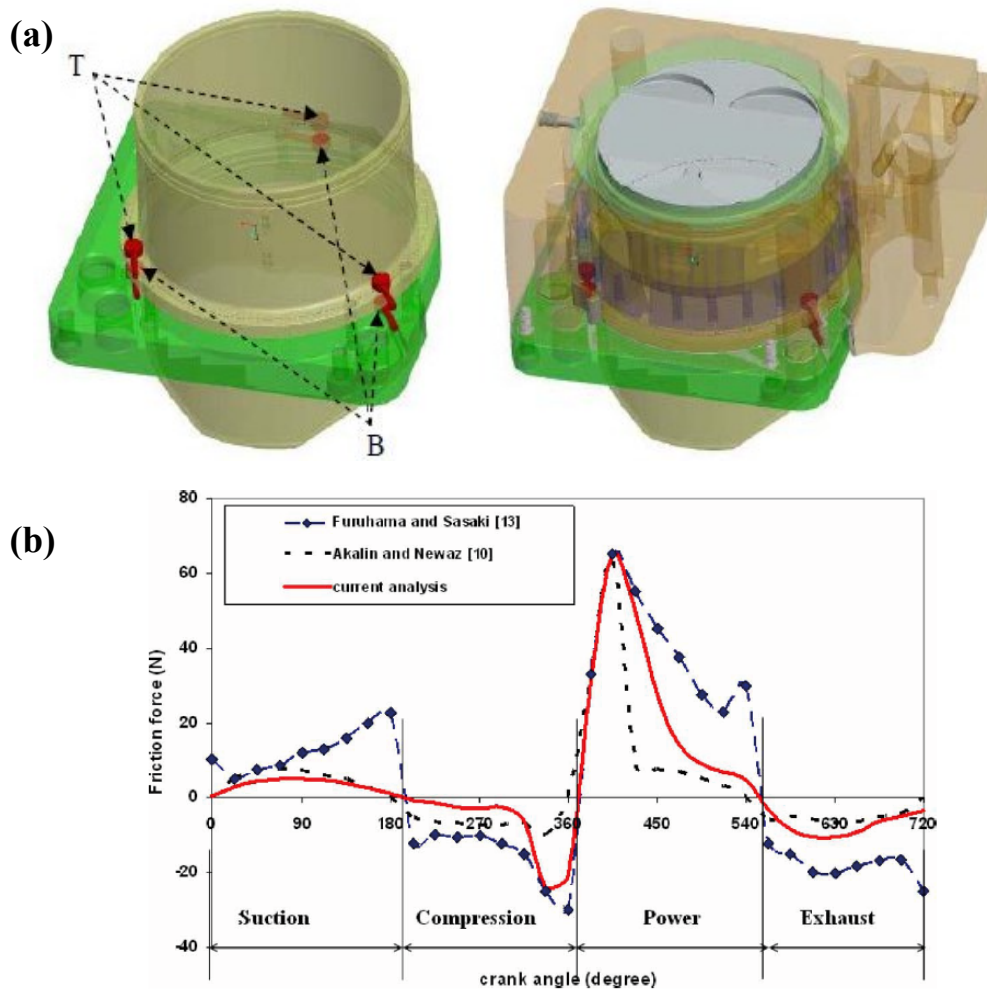
FIGURE B.1: (a) Schematic of the floating liner method; (b) Comparison of Mishra and Rahnejat work with other numerical predictions and experimental measurements [99].

The mixed and boundary lubrications regimes are frequently encountered in various positions along the pistons' stroke of modern IC engines equipped with Start and stop systems, due to the low velocities present every time the engine stops and restarts.

Start and stop (or start-stop) systems in automobiles automatically shut down and start up the internal combustion (IC) engine to reduce the amount of time spent idling. This has the effect of reducing fuel consumption and emissions. According to Wakuda [48], start and stop periods lead to spikes in temperature values caused by dry operating conditions, while Greiner [35] mentions that the tribological system start and stop, where true solid−solid contacts occur, resembles the dead centres of a reciprocating contact.

These observations render the generic research into surface texture under mixed and boundary lubrication conditions extremely relevant to start-stop contacts. Moreover, findings can eventually be applied to contacts such as crank shaft bearings, which nominally operate under full film conditions, a regime where laser produced surface texture proved to have limited impact on reducing friction force.

Appendix C

MATLAB SCRIPT

```matlab
% Run Video_processing_file first (obtain the frames)

clearvars -except frames frames1 frames2 frames3 frames4 frames5


cdir = cd;
cdir2 = cd;

startpixel=1;  % pixel to start  smoothing from
phi_const=0.025;
RI=1.45;

clr=struct('colr',{{'b'; 'r';'g'; 'm' ;'k'}});

h=zeros(1,200);
Nphi=h;
s=h;
locav3=h;

specal=mean(frames(30:150,:,1),1); %where y=30, x=150 and z=1 represents the
first image (see figure C.2 below)
```
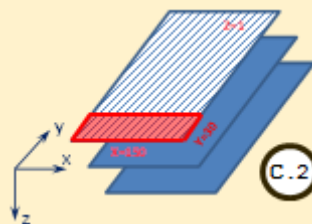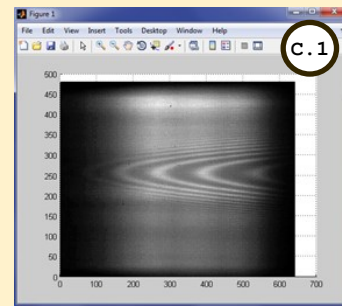
```matlab
specal=specal/max(specal); %it will provide the
average background intensity of the selected area:
30 to 150 pixels (see figures C.3)
use=[50,100,130];

  for p=1:1:200;
        % n=use(p);
        n=p;
        pix=double(frames(:,:,n));

        avgd=mean(pix(250:260,:),1); %average
    intensity variation between pixels 250 and
    260 (see figures C.4)

        smthd=smooth(avgd,startpixel); %smoothens
    the curve previously obtained, for a much
    more accurate determination of the peaks
     (figure C.4 in red)
```
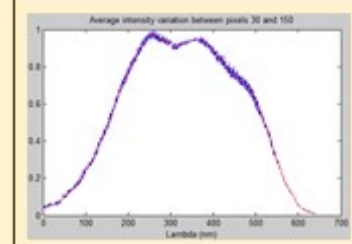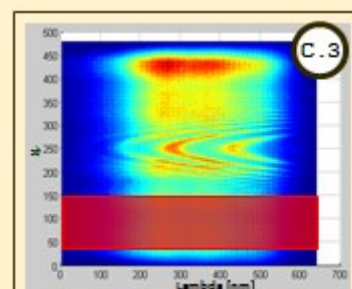
```
smthd=smthd./specal;
figure
plot(smthd)
clear locs

[pk1,pk2,loc1,loc2] = PksLocs(smthd,0.22,100);
%the peaks intensity
should be higher than 0.22, while the minimum
distance between the two peaks has to be greater
than 100nm (figure C.5)

locav=floor(0.5*(loc1+loc2)); %finds the midway
between the two peaks, pk1 and pk2 (figure C.5)
```
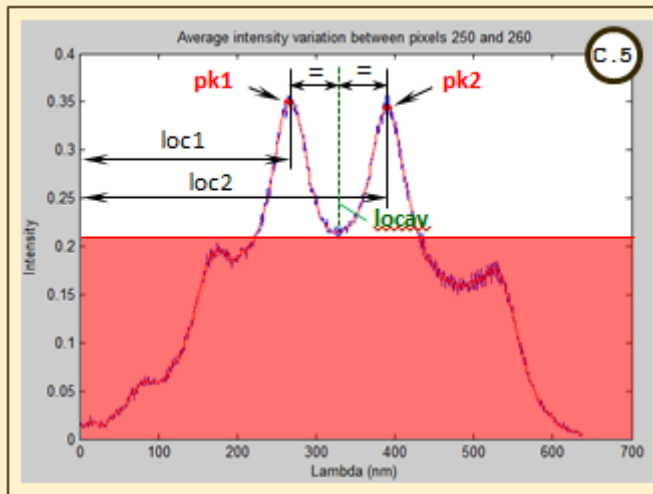

```
avgd2=mean(pix(:,locav-5:locav+5),2); %average
intensity variation between locav-5 and locav+5
(see figure C.6)

[pks,locs2] =
finpeaks(avgd2(218:290),'minpeakheight',0.22,'mi
npeakdistance',30); %finds
the peaks located between pixels 218 and 290 in
avgd2 presented above, with intensity higher
than 0.22 and a minimum distance between the two
peaks greater than 30 (figure C.6)

figure
plot(avgd2(218:290))
title(num2str(n))
locav2=218+floor(0.5*(max(locs2)+min(locs2)));
%finds the midway between the two peaks (figures
C.6 and C.7)

locav3(p)=locav2;
avgd=mean(pix(locav2-5:+locav2+5,:),1); %the new
average intensity variation between locav2 - 5
and locav2 + 5 (see figure C.8)

smthd=smooth(avgd,startpixel);
smthd=smthd./specal; %the new centred average
intensity is divided by the background intensity
(figure C.8)
```
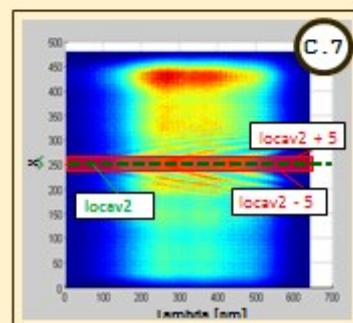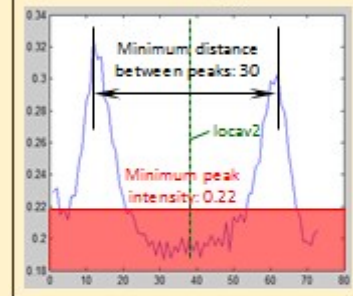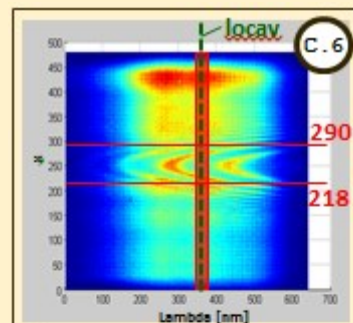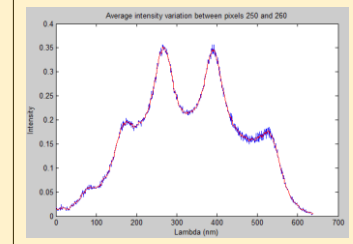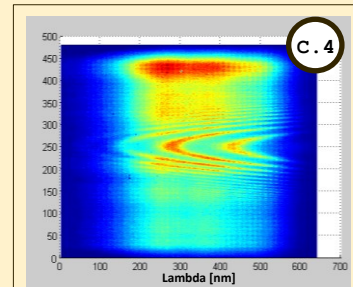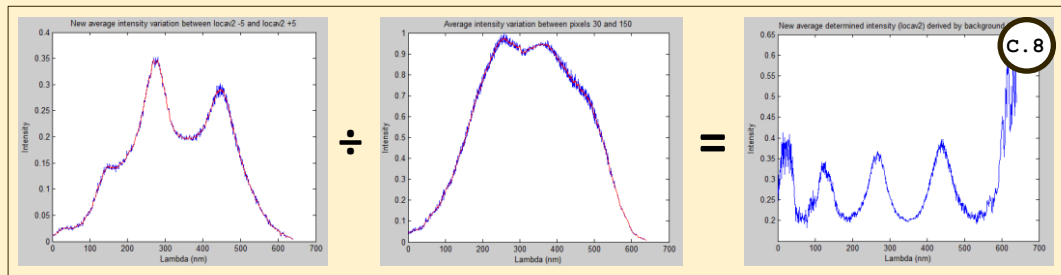
```matlab
figure
plot(smthd)
title(num2str(n))
[pks,locs]=findpeaks(smthd(100:500),'minpeakheight',0.3,'minpeakdistance',
80); %finds all peaks between 100 nm and 500 nm, with an intensity above
0.3 and situated at a minimum distance of 80 nm from each other (fig. C.9)

locs=100+locs;
clear pknum
cd(cdir)

for m=1:1:length(locs)
    pknum(m)=pkft_forVid(smthd,locs (m),20);
end
cd(cdir2)
clear lambdas

[vl1,lc1]=max(pks);
 %% lambdas(1)=pknum(lc1);
pknm300=abs(pknum-350);
[vl1,lc1]=min(pknm300); %finds lc1, the
nearest peak to 350nm (figure C.10)
pknm300(lc1)=1000;
 [vl1,lc2]=min(pknm300); %finds lc2, the
second nearest peak to 350nm (fig. C.10)

lambdas(1)=pknum(lc1); %finding λ1
lambdas(2)=pknum(lc2); %finding λ2
lambdas;
%% pks(lc1)=0;
%% [vl1,lc2]=max(pks);
%% lambdas(2)=pknum(lc2);
lambdas=lambdas*0.4055+353.0750;      %does
the Pixel to λ calibration

Nphi(n)=(min(lambdas))/(max(lambdas)-
min(lambdas));       %finds    the    optical
interference order (fig. C.11)
```
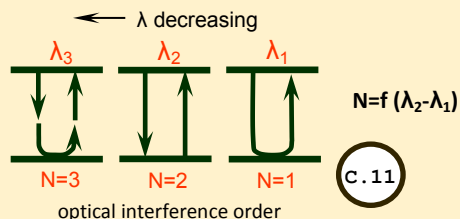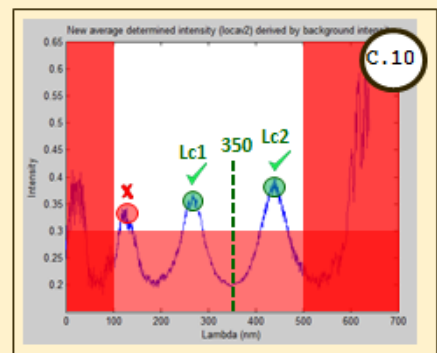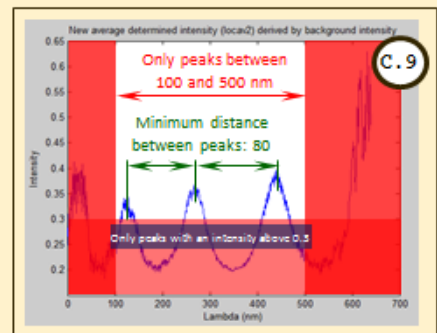


```matlab
h(n)=abs((lambdas(2)*lambdas(1))/(2*RI*(lambdas(2)-lambdas(1)))); %finds
the film thickness value

s(n)=length(pknum);
end
```
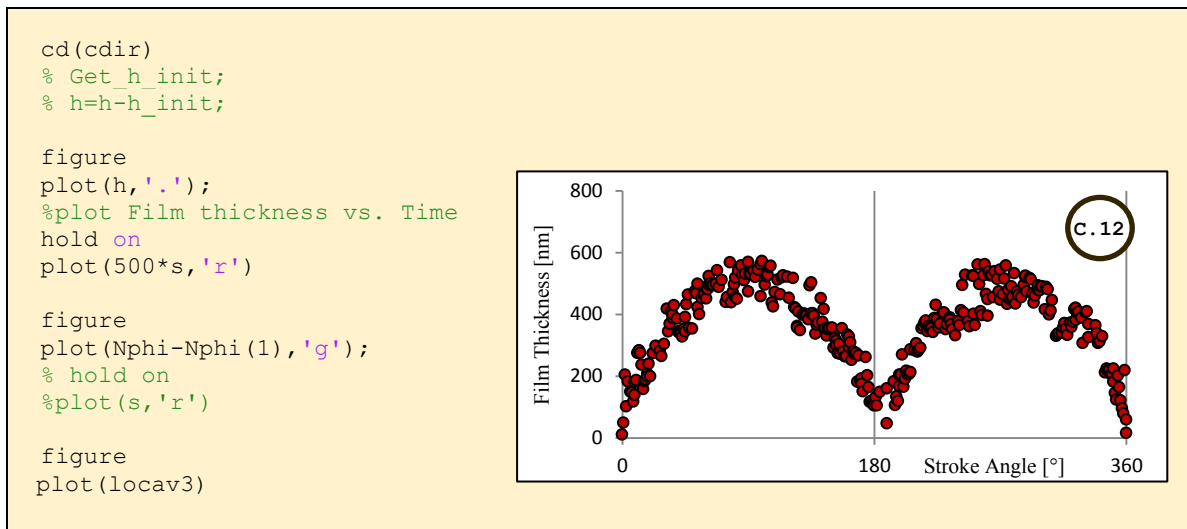
219

```
cd(cdir)
% Get_h_init;
% h=h-h_init;

figure
plot(h,'.');
%plot Film thickness vs. Time
hold on
plot(500*s,'r')

figure
plot(Nphi-Nphi(1),'g');
% hold on
%plot(s,'r')

figure
plot(locav3)
```

FIGURE C.1: Annotated diagram of Matlab script.

Appendix D

LIST OF PUBLICATIONS

Paper No.	Paper Title	Journal Title	Authors	Status
1	"The effects of surface texture in reciprocating contacts - an experimental study"	Tribology International	Sorin-Cristian Vladescu[a], Andrew V. Olver[a], Ian G.Pegg[b], Tom Reddyhoff[a]	Published on 28 September 2014
2	"Transient effects in lubricated textured bearings"	Proc IMechE Part J: Journal Engineering Tribology	Simon Medina[a], Mark T. Fowel[la], Sorin-Cristian Vladescu[a], Tom Reddyhoff[a], Andrew V. Olver[a], IanG.Pegg[b], Daniele Dini[a]	Published on 18 February 2015
3	"The transient friction response of a laser textured, reciprocating contact to the entrainment of individual pockets"	Tribology Letters	Sorin-Cristian Vladescu[a], Simon Medina[a], Andrew V. Olver[a], Ian G.Pegg[b], Tom Reddyhoff[a]	Published on 25 March 2016
4	"Lubricant film thickness and friction force measurements in a laser surface textured reciprocating line contact simulating the piston ring - liner pairing"	Tribology International	Sorin-Cristian Vladescu[a], Simon Medina[a], Andrew V. Olver[a], Ian G.Pegg[b], Tom Reddyhoff[a]	Published on 24 February 2016
5	"Combined Friction and Wear reduction in a piston-liner type contact through laser surface texturing"	Wear	Sorin-Cristian Vladescu[a], Andrew V. Olver[a], Ian G.Pegg[b], Tom Reddyhoff[a]	Published on 6 April 2016
6	"Parametric study of surface texture in reciprocating linear bearings"	–	Sorin-Cristian Vladescu[a], Andrew V. Olver[a], Ian G.Pegg[b], Tom Reddyhoff[a]	To be submitted
7	"Experimental Validation of a Mixed-Lubrication Regime Model for Textured Piston-Ring Liner Contacts"	Materials Performance and Characterization	Francisco J. Profito, Sorin-Cristian Vladescu, Tom Reddyhoff, Daniele Dini	Submitted

PATENT

	Award Title	Authors	Date
1	*"Bearing interface with recesses to reduce friction"*, UK Patent 1512115.5	Sorin-Cristian Vladescu[a], Andrew V. Olver[a], Ian G.Pegg[b], Tom Reddyhoff[a]	2015